Investigation of the steerable parametric loudspeaker based on phased array techniques

Shi, Chuang

2013

Shi, C. (2013). Investigation of the steerable parametric loudspeaker based on phased array techniques. Doctoral thesis, Nanyang Technological University, Singapore.

https://hdl.handle.net/10356/51775

https://doi.org/10.32657/10356/51775

INVESTIGATION OF THE STEERABLE PARAMETRIC LOUDSPEAKER BASED ON PHASED ARRAY TECHNIQUES SHI CHUANG 2013

NANYANG TECHNOLOGICAL UNIVERSITY

INVESTIGATION OF THE STEERABLE PARAMETRIC LOUDSPEAKER BASED ON PHASED ARRAY TECHNIQUES

SHI CHUANG

SCHOOL OF ELECTRICAL & ELECTRONIC ENGINEERING

2013

INVESTIGATION OF THE STEERABLE PARAMETRIC LOUDSPEAKER BASED ON PHASED ARRAY TECHNIQUES

SHI CHUANG

School of Electrical & Electronic Engineering

A thesis submitted to the Nanyang Technological University
in partial fulfillment of the requirement for the degree of
Doctor of Philosophy

2013

Acknowledgements

First and foremost, I would like to thank my supervisor, Associate Professor Gan Woon Seng, for his continued guidance and encouragement throughout my Ph.D. candidature. He created a fully supportive environment to initiate and pursue this research work, and provided me the chance to become a researcher and explore the world.

Sincere thanks to Dr. Tan Ee Leng, Dr. Ji Pei Feng, and Mr. Ji Wei for their generous sharing of knowledge and assistance in technical problems. I am also grateful to the lab technicians, Mr. Yeo Sung Kheng and Mr. Ong Say Cheng, for their friendly logistical and administrative support over the past four years.

Next, I must thank all my friends from DSP Lab, past and present, Dr. Wang Liang, Dr. Nguyen Dinh Quy, Dr. Nay Oo, Mr. Wang Tong Wei, Mr. Mu Hao, Mr. Kaushik Sunder, Mr. Rishabh Ranjan, Mr. He Jian Jun, Mr. Phyo Ko Ko, and Mr. Chen Chiu Hao. They have made the lab a warm, interesting and exciting place to study and work.

I would also like to extend special thanks to my dear wife Wan Jia Ling for her understanding and support, especially towards the end of the thesis writing. I deeply appreciate her tolerance for my impatience, and am thankful for her time spent accompanying me and helping to proofread.

Last but not least, thanks to Dad, Mum, and Jia Ling's parents. All of you have been great parents who unconditionally provide for my needs and pray for my wisdom and health. Thanks be to God for putting me in my lovely family and for giving me the ability to accomplish this thesis. To him be the glory.

Table of Contents

Acknowledgements..... I

Table of Contents..... III

Summary..... VII

List of Figures..... X

List of Tables..... XVIII

List of Abbreviations and Acronyms..... XX

List of Symbols..... XXII

Chapter 1 Introduction..... 1

1.1 Research Area and Motivation..... 1

1.2 Objective..... 6

1.3 Major Contributions of the Thesis..... 7

1.4 Organization of the Thesis..... 9

Chapter 2 Parametric Array and Parametric Loudspeaker..... 12

2.1 Parametric Array..... 12

2.2 Applications of the Parametric Array..... 20

2.3 Parametric Loudspeaker..... 24

2.4 Preprocessing Methods for the Parametric Loudspeaker..... 25

2.5 Applications of the Parametric Loudspeaker..... 30

2.6 Conclusions..... 34

Chapter 3 Steerable Parametric Loudspeaker..... 36

3.1 Directivity Control Methods for the Parametric Loudspeaker..... 37

3.2 Structures for the Steerable Parametric Loudspeaker..... 42

3.3 Simulation Framework for the Steerable Parametric Loudspeaker... 47

3.4 Measurement Setup for the Steerable Parametric Loudspeaker..... 52

3.5 Conclusions..... 56

Chapter 4 Grating Lobe Elimination in the Steerable Parametric Loudspeaker 57

4.1 Derivation of the Grating Lobe Elimination..... 58

4.2 Simulation Results..... 63

4.3 Measurement Results..... 71

4.3.1 Column configuration..... 73

4.3.2 Block configuration..... 76

4.4 Conclusions..... 81

Chapter 5 Generating Dual Beams from a Single Steerable Parametric Loudspeaker..... 83

5.1 Dual-Beamsteering Structures for the Steerable Parametric Loudspeaker..... 84

5.2 Grating Lobe Elimination in the Symmetric Structure..... 89

5.3 Simulation Results..... 94

5.4 Measurement Results..... 101

5.5 Conclusions..... 112

Chapter 6 Product Directivity Models for the Parametric Loudspeaker..... 114

6.1 Product Directivity Models..... 115

6.2 Measurement Results..... 118

6.3 Discussion on Envelopes of the Product Directivity Models..... 126

6.4 Conclusions..... 132

Chapter 7 Analysis and Calibration of System Errors in the Parametric Loudspeaker..... 134

7.1 Analysis of System Errors in the Parametric Loudspeaker..... 135

7.1.1 Conventional array errors..... 136

7.1.2 Steering angle error..... 138

7.2 Calibration Method for the Steerable Parametric Loudspeaker..... 141

7.3 Measurement Results..... 144

7.4 Discussion on Applying the Calibration Data with Different Preprocessing Techniques..... 153

7.5 Conclusions..... 159

Chapter 8 Conclusions and Future Works..... 160

8.1 Conclusions..... 160

8.2 Future works..... 163

Author's Publications..... 165

References..... 167

Appendix A Rayleigh Distance and Absorption Distance of the Parametric Loudspeaker..... 203

Appendix B Configurations of the UTAs in the Measurements..... 205

Appendix C LabVIEW Program for the Steerable Parametric Loudspeaker..... 207

Appendix D Photos of the Measurement Setups..... 209

Summary

This thesis focuses on the directivity control of the parametric loudspeaker based on phased array techniques. The principle of the parametric loudspeaker is derived from the parametric array effect. This nonlinear acoustical phenomenon happens when two primary frequency (PF) waves propagate in the same direction. Due to the nonlinearity of air, new frequency components are generated, including the difference frequency (DF), the sum frequency (SF), and other higher harmonics. When the two PF waves are close in frequency, only the DF wave falls within the audible range, but the other secondary waves, as well as the PF waves, remain inaudible to humans. Still, the DF wave inherits the directivities of the PF waves. Hence, the parametric loudspeaker can produce a highly directional sound beam with a relatively small emitter as compared to other acoustical devices.

Furthermore, the directivity control of the parametric loudspeaker can provide more flexibility in its applications. However, till now, there has not been any in-depth investigation into applying phased array techniques in the steerable parametric loudspeaker. Due to the nonlinear effects involved in the process of the parametric loudspeaker, some considerations must be put into the simulation framework and the measurement setup. Thus, this thesis begins with an overview of theories, techniques, and applications of the parametric array and the parametric

loudspeaker. Next, the state-of-the-art methods of controlling the directivity of the parametric loudspeaker are reviewed and evaluated. In particular, the parametric loudspeaker adopting phased array techniques to achieve directivity control is analyzed for its delay response and a simulation framework is proposed. The measurement setup is carefully examined to prevent the interference caused by the nonlinearity of the receiving system, especially when there is no acoustical filter placed in front of the microphone.

An interesting phenomenon is noticed during the experimental measurement. The spatial Nyquist criterion indicates that the non-aliasing spacing between neighboring loudspeakers is half the wavelength of the reproduced sound in a conventional linear loudspeaker array. The diameter of the ultrasonic transducer is normally wider than the wavelengths of the PF waves. Hence, spatial aliasing is expected to be observed in the PF beampatterns. However, in the measured DF beampatterns, grating lobes are rarely observed. This phenomenon is termed as the grating lobe elimination. If the steerable parametric loudspeaker takes advantage of this grating lobe elimination effect, its non-aliasing spacing can be extended to more than one and a half wavelength of the PF wave. This finding is extendedly applicable in another scenario when dual beams of audible sound are generated simultaneously from a single parametric loudspeaker.

Besides the spatial aliasing problems, mismatches are observed between the simulated and measured beampatterns. They are mainly due to the inaccuracy of the product directivity principle and errors incurred during actual implementations.

For this reason, the original theory behind the product directivity principle is revisited. A transformation from the ultrasonic transducer array to an equivalent Gaussian source array is proposed by minimizing the differences in overall spatial performance. As a result, the radii of the Gaussian sources are incorporated into the proposed product directivity models. At the same time, since the cause of system errors is primarily a result of the frequency characteristics of the ultrasonic transducers, a beamsteering structure is proposed to incorporate the spacing error, the weight error, the delay error, and the steering angle error. A combination of the Monte Carlo method and the nonlinear least-squares method is utilized to calibrate the steerable parametric loudspeaker based on a proposed structure. Comparative results show that the simulated DF beampatterns using the proposed models and the calibration method achieve improved matches to the measured beampatterns.

In conclusion, several practical issues of applying phased array techniques in the steerable parametric loudspeaker are investigated in this thesis. Spatial aliasing and mismatching between simulation and measurement results are addressed. In this thesis, measurement results are presented to verify and support the derived equations and proposed methods. Thus, the feasibility of developing the steerable parametric loudspeaker based on phased array techniques is proven in practice. A few guidelines are also provided, which can then be applied in many applications of the steerable parametric loudspeaker.

List of Figures

Figure 1.1	Illustration of the sound dome.	2
Figure 1.2	Illustration of the loudspeaker array.	3
Figure 1.3	Illustration of the parametric loudspeaker in the directed mode (to project the red beam) and the reflected mode (to project the blue beam).	5
Figure 1.4	The organization of major contributions in the thesis.	11
Figure 2.1	Nonlinear processes of (a) the parametric transmitting array and (b) the parametric receiving array.	13
Figure 2.2	Geometry of the parametric array using (a) the absorption-limited source and (b) the diffraction-limited source.	15
Figure 2.3	Measurement setup carried out by Bennett and Blackstock (extracted and modified from [BeB75]).	19
Figure 2.4	Block diagram of the parametric loudspeaker.	25
Figure 2.5	Block diagrams of (a) the DSBAM and (b) the SRAM.	26
Figure 2.6	Block diagrams of (a) the SSBAM and (b) the MAM.	29
Figure 2.7	Commercial products of the parametric loudspeaker (extracted and modified from [Gan12]).	33
Figure 3.1	Illustrations of the reflective objects, (a) the quadrilateral	38

reflector and (b) the hemispherical reflector.

Figure 3.2 PF and DF beampatterns when the DF wave is generated at 10 kHz and steered to 10° in the UTA consisting of 16 channels with spacing of 5 mm (extracted and modified from [GYT06]). 41

Figure 3.3 Structure of the steerable parametric loudspeaker using two PF waves to generate the DF wave. 44

Figure 3.4 Structure of the steerable parametric loudspeaker using AM preprocessing methods to generate the DF wave. 46

Figure 3.5 Gaussian directivity varying with (a) radiating frequency and (b) effective radius. 48

Figure 3.6 (a) A uniform linear UTA ($M = 8$, half wavelength spacing) is transformed into (b) an equivalent circular Gaussian source array ($N_{lobe} = 7$). 50

Figure 3.7 Beampatterns of a UTA consisting of 8 channels with Chebyshev weights (20dB attenuation) and its equivalent Gaussian source array. 50

Figure 3.8 Measurement setup for steerable parametric loudspeakers. 53

Figure 3.9 Free-field correction curves for the Brüel &Kjær model 4134 condenser microphone (extracted from [BrK12]). 54

Figure 4.1 Distance functions for $K = 1,\ 2,$ and 3 when $1 < F \le 2$. 60

Figure 4.2 When the UTA consists of 8 channels with spacing twice as 64

large as the wavelength, three cases, (a) spatial aliasing, (b) grating lobe elimination, and (c) partial grating lobe elimination, are plotted.

Figure 4.3 When the UTA consists of 8 channels with spacing one and a half times as large as the wavelength, three cases, (a) spatial aliasing, (b) grating lobe elimination, and (c) partial grating lobe elimination, are plotted. 66

Figure 4.4 Intersection function for $K=2$ when equal weights and Chebyshev weights with 10 dB, 20 dB, 30 dB attenuations are adopted in the UTAs consisting of $M=8$ channels with spacing of (a) $\Lambda=1/2$ and (b) $\Lambda=2/3$. 68

Figure 4.5 Intersection function for (a) $K=1$ and (b) $K=2$ when equal weights and Chebyshev weights with 10 dB, 20 dB, 30 dB attenuations are adopted in the respective UTAs consisting of (a) $M=8$ and (b) $M=16$ channels. 70

Figure 4.6 Channel directivities of (a) the column configuration with spacing of 1 cm and (b) the block configuration with spacing of 2 cm. 72

Figure 4.7 Measurement and simulation results using the column configuration. In the subplots, (a)-(b) show grating lobe elimination; (c)-(d) show partial grating lobe elimination; (e)-(f) show spatial aliasing; for the PF waves, the solid 75

and dash lines represent the measurement and simulation results, respectively.

Figure 4.8 Measurement and simulation results using the block configuration. In the subplots, (a)-(b) show grating lobe elimination; (c)-(d) show partial grating lobe elimination; (e)-(f) show spatial aliasing; for the PF waves, the solid and dash lines represent the measurement and simulation results, respectively. 77

Figure 5.1 Direct structure for dual-beam generation of the steerable parametric loudspeaker. 85

Figure 5.2 Symmetric structure for dual-beam generation of the steerable parametric loudspeaker. 86

Figure 5.3 Geometry of the dual-beam generation using the symmetric structure. 87

Figure 5.4 Angular separation of the dual beams adjusted by the center frequency and the spacing of the UTA. 89

Figure 5.5 Distance function for $K = 1,\ 2,$ and 3 in the symmetric structure. 91

Figure 5.6 Intersection function for $K = 1$ in the symmetric structure when equal weights and Chebyshev weights with 10 dB, 20 dB, 30 dB attenuations are adopted in the UTA consisting of $M = 8$ channels. 93

Figure 5.7	Simulated (a) PF and (b) DF beampatterns when the UTA consists of 8 channels with spacing of 1 cm and the dual beams are generated in the direct structure.	96
Figure 5.8	Simulated (a) PF and (b) DF beampatterns when the UTA consists of 8 channels with spacing of 1 cm and the dual beams are generated in the symmetric structure.	97
Figure 5.9	Simulated (a) PF and (b) DF beampatterns when the UTA consists of 8 channels with spacing of 1.5 cm and the dual beams are generated in the direct structure.	99
Figure 5.10	Simulated (a) PF and (b) DF beampatterns when the UTA consists of 8 channels with spacing of 1.5 cm and the dual beams are generated in the symmetric structure.	100
Figure 5.11	Measured PF and DF beampatterns when the UTA consists of 8 channels with spacing of 1 cm and the dual beams are generated in the symmetric structure at -25 ° and 25 °.	102
Figure 5.12	Measured PF and DF beampatterns when the UTA consists of 8 channels with spacing of 1 cm and the dual beams are generated in the symmetric structure at -40 ° and 10 °.	103
Figure 5.13	Measured PF and DF beampatterns when the UTA consists of 8 channels with spacing of 1.25 cm and the dual beams are generated in the symmetric structure at -20 ° and 20 °.	105
Figure 5.14	Measured PF and DF beampatterns when the UTA consists	106

of 8 channels with spacing of 1.25 cm and the dual beams are generated in the symmetric structure at -30 ° and 10 °.

Figure 5.15 Measured PF and DF beampatterns when the UTA consists of 8 channels with spacing of 1.25 cm and the dual beams are generated in the symmetric structure at -40 ° and 0 °. 107

Figure 5.16 Measured PF and DF beampatterns when the UTA consists of 8 channels with spacing of 1.5 cm and the dual beams are generated in the symmetric structure at -15 ° and 15 °. 109

Figure 5.17 Measured PF and DF beampatterns when the UTA consists of 8 channels with spacing of 1.5 cm and the dual beams are generated in the symmetric structure at -20 ° and 10 °. 110

Figure 5.18 Measured PF and DF beampatterns when the UTA consists of 8 channels with spacing of 1.5 cm and the dual beams are generated in the symmetric structure at -30 ° and 0 °. 111

Figure 6.1 Geometry of two intersecting Gaussian beams. 116

Figure 6.2 Measured PF beampatterns and beampatterns of their equivalent Gaussian source arrays, in which the radii of the Gaussian sources (in cm) are labeled next to the equivalent lobes. 120

Figure 6.3 Comparison between the simulated beampatterns using the PD, APD, EPD, and CPD models versus the measured beampattern of the DF wave at 1 kHz. 122

Figure 6.4	Comparison between the simulated beampatterns using the PD, APD, EPD, and CPD models versus the measured beampattern of the DF wave at 4 kHz.	123
Figure 6.5	Comparison between the simulated beampatterns using the PD, APD, EPD, and CPD models versus the measured beampattern of the DF wave at 8 kHz.	123
Figure 6.6	Comparison between the simulated beampatterns using the envelope method versus the measured beampattern of the DF wave at 1 kHz.	130
Figure 6.7	Comparison between the simulated beampatterns using the envelope method versus the measured beampattern of the DF wave at 4 kHz.	130
Figure 6.8	Comparison between the simulated beampatterns using the envelope method versus the measured beampattern of the DF wave at 8 kHz.	131
Figure 7.1	Structure of the steerable parametric loudspeaker where the spacing, weight, and delay errors are incurred.	136
Figure 7.2	Levels of grating lobe elimination when system errors are incurred in the UTA with 8 channels and spacing of 1 cm.	138
Figure 7.3	Steering angle errors for $M = 4,\ 6,$ and 8 channels in the UTA with spacing of (a) 1 cm and (b) 0.5 cm when equal weights are adopted.	141

Figure 7.4	Flow chart of the proposed calibration method, which is a combination of the Monte Carlo method and the nonlinear least-squares method.	144
Figure 7.5	Comparison between the simulated (before and after calibration) and measured PF beampatterns at (a) 39 kHz and (b) 41 kHz, when their mainlobes are steered to 20 °.	148
Figure 7.6	Comparison between the simulated (before and after calibration) and measured DF beampatterns at 2 kHz, when (a) the PD model and (b) the APD (Envelope) model are applied in the simulations.	149
Figure 7.7	PSNR values of the simulated (a) PF and (b) DF beampatterns before calibration (the cross-validation results are highlighted in the dashed rectangles).	151
Figure 7.8	Improvement of PSNR values of the (a) PF and (b) DF beampatterns after calibration (the cross-validation results are highlighted in the dashed rectangles).	152
Figure 7.9	Directivities of the parametric loudspeakers using (a) the LSBAM and (b) the USBAM in simulations based on the calibration data and the APD (Envelope) model.	157
Figure 7.10	Directivities of the parametric loudspeakers using (a) the DSBAM and (b) the SRAM in simulations based on the calibration data and the APD (Envelope) model.	158

List of Tables

Table 3.1	Delay responses of the DF wave generated from the parametric loudspeaker using different AM preprocessing methods.	46
Table 4.1	Distribution of grating lobes of the DF waves generated using the column configuration with spacing of 1 cm (extracted from Fig. 4.7).	76
Table 4.2	Distribution of grating lobes of the DF waves generated using the block configuration with spacing of 2 cm (extracted from Fig. 4.8).	80
Table 6.1	Normalized amplitudes of the grating lobes and selected sidelobes in the simulated beampatterns using the PD, APD, EPD, and CPD models versus those in the measured beampatterns of the DF waves.	124
Table 6.2	6dB beamwidths (in degree) of the mainlobes in the simulated beampatterns using different PD models and the envelope method versus those in the measured beampatterns of the DF waves.	132
Table 7.1	Calibration data of the weight and spacing distortion	145

factors.

Table 7.2 Calibration data of the phase distortion factors for the PF waves at (39.75 & 40.25) kHz, (39.5 & 40.5) kHz, (38 & 42) kHz, and (36 & 44) kHz. 146

Table 7.3 Interpolated phase distortion factors for the PF waves at (39 & 41) kHz. 146

List of Abbreviations and Acronyms

AM	Amplitude Modulation
ANC	Active Noise Control
APD	Advanced Product Directivity
APD (Envelope)	The Envelope of the Advanced Product Directivities
CPD	Combined Product Directivity
CPD (Envelope)	The Envelope of the Combined Product Directivities
CMUT	Capacitive Micromachined Ultrasonic Transducer
DF	Difference Frequency
DSBAM	Double Sideband Amplitude Modulation
DSP	Digital Signal Processor
EPD	Exponential Product Directivity
EPD (Envelope)	The Envelope of the Exponential Product Directivities
FPGA	Field Programmable Gate Array
IMD	Inter-Modulation Distortion
KZK	Khokhlov–Zabolotskaya–Kuznetsov
LSBAM	Lower Sideband Amplitude Modulation
MAM	Modified Amplitude Modulation
MEMS	Microelectromechanical system

MP	Measured Beampattern (only used in figures and tables)
PD	Product Directivity
PD (Envelope)	The Envelope of the Product Directivities
PF	Primary Frequency
PMD	Product of the Measured PF Directivities
PSD	Product of the Simulated PF Directivities
PSNR	Peak signal to noise ratio
PVDF	Polyvinylidene Fluoride
PZT	Piezoceramic
RSSBAM	Recursive Single Sideband Amplitude Modulation
SF	Sum Frequency
SPL	Sound Pressure Level
SRAM	Square Root Amplitude Modulation
SSBAM	Single Sideband Amplitude Modulation
THD	Total Harmonic Distortion
UTA	Ultrasound Transducer Array
USBAM	Upper Sideband Amplitude Modulation
et al.	et alii (and others)
etc.	et cetera (and so forth)
i.e.	id est (that is)

List of Symbols

a	Effective radius of the Gaussian source
a_1	Effective radius of the Gaussian beam of the lower PF wave
a_2	Effective radius of the Gaussian beam of the higher PF wave
A_i	Effective radius of the i th equivalent Gaussian source, for $i = 1,\ 2,\ \ldots,\ N_{lobe}$
α_0	Attenuation rate
α_1	Attenuation rate at the lower PF
α_2	Attenuation rate at the higher PF
α_d	Attenuation rate at the DF
B_i	Initial pressure level of the i th equivalent Gaussian source, for $i = 1,\ 2,\ \ldots,\ N_{lobe}$
β	Nonlinearity coefficient
c_0	Speed of sound
d	Spacing of the UTA
d_m	Spacing between the m th and $m+1$ th channels in the UTA, for $m = 0,\ 1,\ \ldots,\ M-2$
$D_A(\theta)$	Aperture of the transducer
$D_{diff}(\theta)$	DF directivity (or beampattern)

$D_{diff}(\Lambda, F, \Theta)$	DF directivity (or beampattern) with normalized parameters
$D_G(\theta)$	Gaussian directivity
$D_K(F)$	Distance function
δ	Dissipation factor
δ_D^m	Spacing distortion factor for the m th channel, for $m = 0, 1, \ldots, M-1$
δ_P^m	Phase distortion factor for the m th channel, for $m = 0, 1, \ldots, M-1$
δ_W^m	Weight distortion factor for the m th channel, for $m = 0, 1, \ldots, M-1$
f_1	Lower PF
f_2	Higher PF
f_c	Center frequency (or Carrier frequency)
f_d	DF
$f(t)$	Envelope function
$f_{DSBAM}(t)$	Envelope function of the DSBAM
$f_{SRAM}(t)$	Envelope function of the SRAM
F	Ratio of the higher PF to the lower PF
φ	Boundary of the visible region
$H(\omega, \theta)$	Beampattern of the UTA
$\tilde{H}(\omega, \theta)$	Distorted beampattern of the UTA when system errors occur
$I_K(F)$	Intersection function

k_d	Wavenumber of the DF wave
K	Largest index of the grating lobes of the lower PF wave
L	Number of points in the measured beampattern
λ	Wavelength
Λ	Ratio of the lower PF wavelength to the spacing of the UTA
M	Number of channels in the UTA
n_1	Index of the grating lobes of the lower PF wave
n_2	Index of the grating lobes of the higher PF wave
N_{lobe}	Number of lobes in the beampattern of the UTA
p	Entire sound field
p_0	Amplitude at the source
p_1	Amplitude of the lower PF wave at the source
p_2	Amplitude of the higher PF wave at the source
$p_d(r,\theta)$	Secondary sound field consisting of the DF wave
$p_i(r,\theta)$	Primary sound field consisting of the two PF waves
q_d	Virtual source strength density
r	Distance from the observation point to the source
$R(\omega)$	Euclidean norm of the residual errors between the beampatterns of the UTA and its equivalent Gaussian source array
ρ_0	Density of the medium
S	Cross-sectional area of the PF beams
τ	Retarded time

τ_1 Delay amount of the lower PF wave

τ_2 Delay amount of the higher PF wave

τ_c Delay amount of the carrier wave

τ_d Delay amount of the DF wave

τ_m Delay amount of the m th channel in the UTA, for $m = 0,\ 1,\ \ldots,\ M-1$

$\hat{\tau}_m$ Distorted delay amount of the m th channel, for $m = 0,\ 1,\ \ldots,\ M-1$

τ_{m1} Delay amount of the lower PF wave in the m th channel, for $m = 0,\ 1,\ \ldots,\ M-1$

τ_{m2} Delay amount of the higher PF wave in the m th channel, for $m = 0,\ 1,\ \ldots,\ M-1$

τ_{md} Delay amount of the DF wave in the m th channel, for $m = 0,\ 1,\ \ldots,\ M-1$

τ_m^a Delay amount of the m th channel for the first steering angle in the direct structure, for $m = 0,\ 1,\ \ldots,\ M-1$

τ_m^b Delay amount of the m th channel for the second steering angle in the direct structure, for $m = 0,\ 1,\ \ldots,\ M-1$

θ Incidence angle

θ_0 Steering angle of the UTA

θ_1 Steering angle of the lower PF wave

θ_2 Steering angle of the higher PF wave

θ_a	Steering angle of the first beam of the DF wave
θ_b	Steering angle of the second beam of the DF wave
θ_{ac}	Actual steering angle when steering angel error occurs
θ_i	Angular offset of the i th equivalent Gaussian source, for $i = 1,\ 2,\ \ldots,\ N_{lobe}$
Θ	Normalized angle
Θ_1	Location of the grating lobes of the lower PF wave
Θ_2	Location of the grating lobes of the higher PF wave
w_m	Weight of the *m*th channel in the UTA, for $m = 0,\ 1,\ \ldots,\ M-1$
$\hat{w}_m$	Distorted weight of the *m*th channel, for $m = 0,\ 1,\ \ldots,\ M-1$
ω	Angular frequency
ω_1	Angular frequency of the lower PF wave
ω_2	Angular frequency of the higher PF wave
ω_c	Angular frequency of the carrier wave
ω_d	Angular frequency of the DF wave
z	Coordinate along the beam propagation direction
z_1	Rayleigh distances of the lower PF wave
z_2	Rayleigh distances of the higher PF wave
$\nabla_{\perp}^2$	Laplacian operator

Chapter 1
Introduction

1.1 Research Area and Motivation

Sound is one of the most important modes of communication between humans and their external environments. The demand for creating directional sound is growing in applications that necessitate personal privacy. For instance, in the library, a personal public announcement system is designed to communicate with readers in targeted zones without disturbing others in nearby areas; similarly, in museums or art galleries, directional sound systems can be applied to deliver commentary to the visitors standing within the exhibit's viewing area. There are similar demands for private messaging in vending machines, automatic teller machines, exhibition booths, billboards, and *etc*. to reduce noise pollution in public areas. Directional sound systems can be deployed during teleconferencing as well, where different languages are broadcasted simultaneously to participants from different countries in a common room without any physical partition.

Several techniques have been developed to implement the directional sound system, and each of them has its benefits and drawbacks. One such idea comes from the imitation of optical focusing lens, which can be traced back to ancient China, where some ancient buildings have architectural acoustical features that

focus sounds into specific areas. In Brown's patent [Bro96], an acoustic imaging sound dome is proposed to reflect and focus sound waves to a confined listening area, as shown in Fig. 1.1. The sound dome is effortless to install, but there is difficulty in relocating the sweet spot after installation.

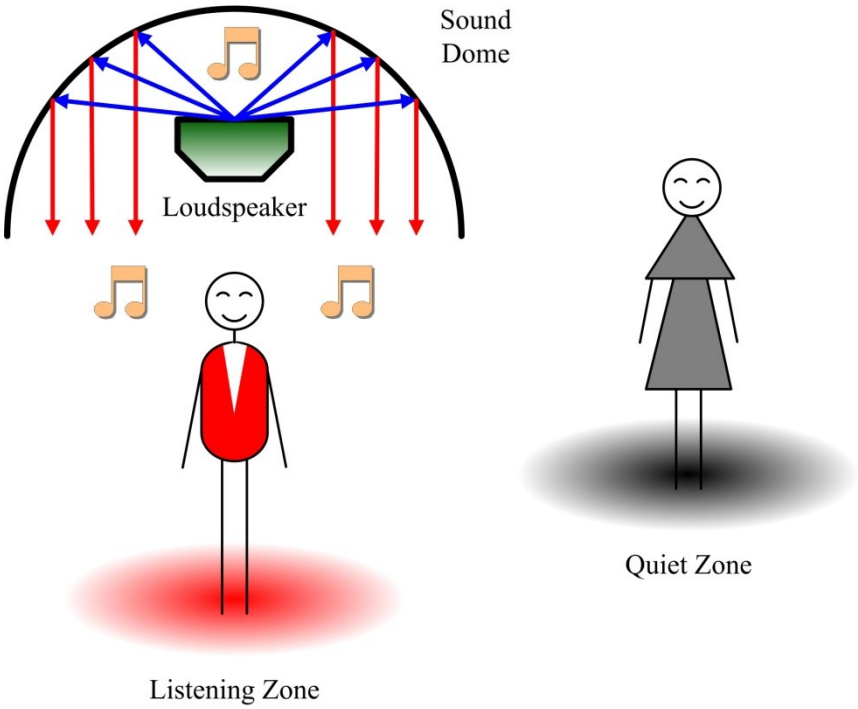

Figure 1.1 Illustration of the sound dome.

Another method of generating directional sound is realized by utilizing loudspeaker array, as shown in Fig. 1.2. Its directivity is controlled by adjusting the phase and gain of every loudspeaker's output in the array. Using phased array techniques, the loudspeaker array has several advantages over the sound dome in its ability to change the steering angle of the audible sound electronically. In 2002, Mizoguchi *et al.* [MKK02] integrated a 16-channel loudspeaker array and face tracking into a novel human machine interface, which they named as the "invisible messenger". It is able to target the sound beam to an intended audience and follow

that audience's movement. However, the directivity of the loudspeaker array depends on the ratio of its aperture size to the reproduced sound's wavelength. Hence, the loudspeaker array normally requires a large scale of several meters to obtain sharp directivities for projecting the low-frequency (<2 kHz) sounds. In later developments of the "invisible messenger", Tamai *et al.* [TKM04] and Shinagawa *et al.* [STM08] used a 128-channel loudspeaker array to generate the sound spot more effectively, but the complexity and cost of the system noticeably increased. Thus, the loudspeaker array is not viable for a range of applications, where the dimension and power consumption of the directional sound system are critical design criteria.

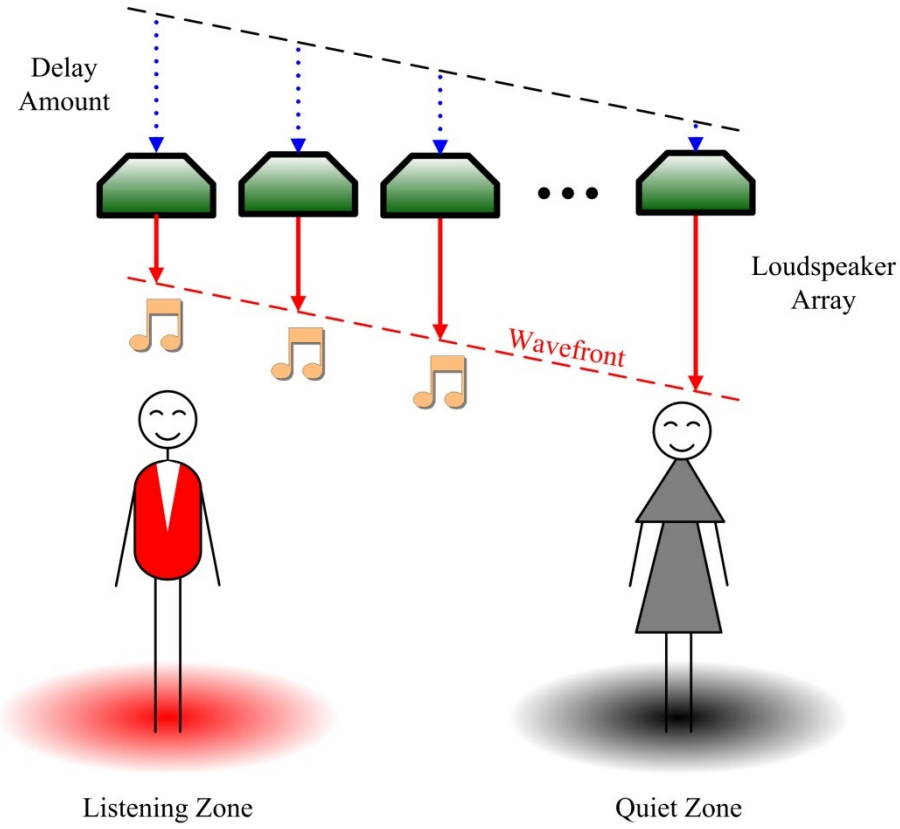

Figure 1.2 Illustration of the loudspeaker array.

The theoretical development and implementation of the parametric array in air provides an attractive and alternative approach to generate directional sounds. A novel type of directional loudspeaker, known as the parametric loudspeaker, is able to project highly directional sounds using a compact ultrasonic emitter, even for the low-frequency sounds. The parametric loudspeaker utilizes an ultrasonic wave beyond human hearing range as a directional carrier to deliver audible sounds to a targeted location. Another advantage of the parametric loudspeaker is that its emitter can be fabricated as an ultrasound transducer array (UTA) to achieve different radiation patterns based on the needs of many applications.

There are two projection modes of using the parametric loudspeaker, namely: (i) directed mode and (ii) reflected mode. It is shown in Fig. 1.3 that besides focusing directly to the listener (in the directed mode), the parametric loudspeaker can also project the sound beam against a surface, thus forming a virtual speaker at the point of reflection (in the reflected mode). In both modes, if the direction of the sound beam generated from the parametric loudspeaker can be further adjusted mechanically or electronically, it will be more readily applied in applications with tracking features.

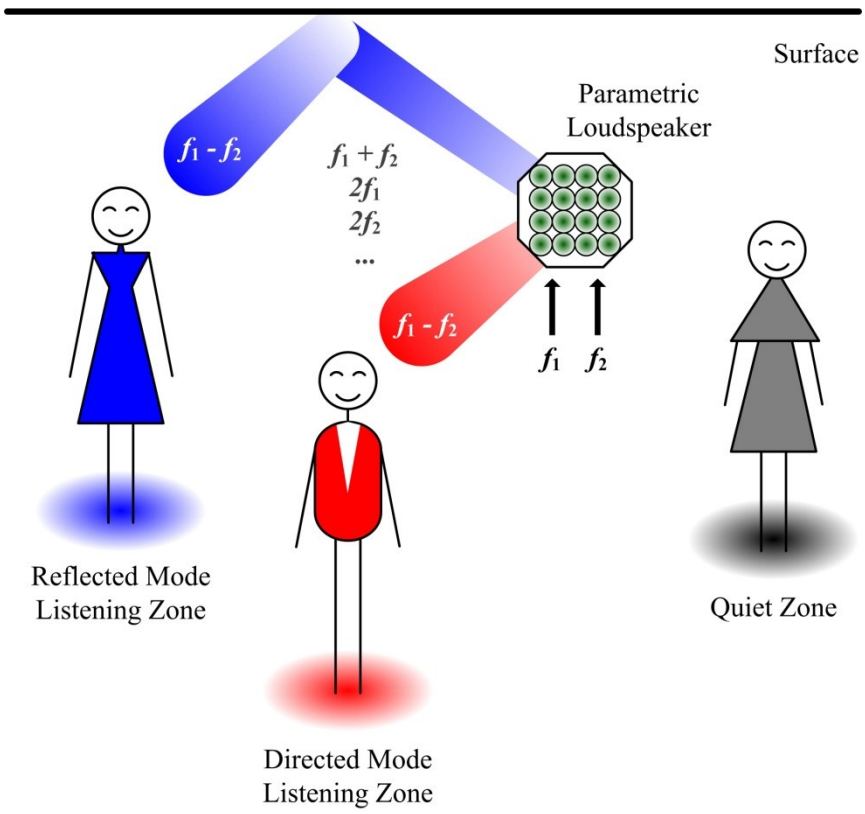

Figure 1.3 Illustration of the parametric loudspeaker in the directed mode (to project the red beam) and the reflected mode (to project the blue beam).

However, there have been few reports on applying mechanical or electronic approaches to steer the directional sound beam [TGY04, OPL05, GYT06, Ols09, TaY10, LBP11, WWH12]. It is noted from these state-of-the-art studies that the relation between the PF and DF beampatterns remains unexplored, and theoretical explanations are vague and insufficient in some descriptions of simulation settings and implementations. Directivity control methods of the parametric loudspeaker have not been investigated thoroughly, and there are still many topics to be explored in this exciting research field. For this reason, this thesis focuses on the directivity control of the parametric loudspeaker using phased array techniques. Simulation and measurement results are always emphasized to link the proposed

structures and theoretical models to the practical implementations of the steerable parametric loudspeaker.

1.2 Objective

The objective of this thesis lies in the following three aspects in the field of the steerable parametric loudspeaker based on phased array techniques.

Firstly, due to the principle of the parametric loudspeaker, the DF directivity is unable to be controlled directly, but can be adjusted indirectly by changing the PF directivities. Therefore, the parametric loudspeaker, which adopts phased array techniques to achieve directivity control, is necessary to be investigated for its theoretical proof and simulation framework. In particular, the measurement setup requires careful examination to exclude errors caused by the nonlinearity of the receiving system in the results.

Secondly, using the simulation framework and measurement setup, the spatial aliasing problem of the steerable parametric loudspeaker is investigated. Different from the conventional loudspeaker array, the parametric loudspeaker transmits PF waves in the ultrasonic range, whose wavelengths are shorter than the diameters of the ultrasonic transducers. The minimum spacing of the UTA in the parametric loudspeaker is at least the radius of the ultrasonic transducer, and thus larger than half the wavelengths of the PF waves. This restriction leads to the occurrences of spatial aliasing in the PF beampatterns. Solution to this spatial aliasing problem is of great importance to the design of steerable parametric loudspeakers.

Thirdly, the spatial performance of the steerable parametric loudspeaker based on phased array techniques is expected to be predictable through simulation. To fulfill this objective, two investigations are carried out in this thesis. The product directivity principle is modified to provide more accurate predictions of the DF beampatterns based on the known PF beampatterns. Next, system errors incurred in the implementation of the steerable parametric loudspeaker are proposed to be calibrated by a combination of Monte Carlo method and nonlinear least-squares method. By using the proposed calibration method, the simulated PF beampatterns result in closer matches to the measurement results, so that the DF beampatterns is able to be further predicted through simulation with improved accuracy using the modified product directivity principle.

1.3 Major Contributions of the Thesis

This thesis focuses on the theoretical development and experimentation of the steerable parametric loudspeaker based on phased array techniques. Its major contributions are highlighted as follows:

I. *Investigation of the feasibility of applying phased array techniques in the steerable parametric loudspeaker*. Firstly, the delay response of the steerable parametric loudspeaker is derived in theory. Secondly, two beamsteering structures are proposed for two PF waves and one modulated carrier wave, respectively. Thirdly, the validation of the product directivity principle is proven by a proposed transformation from the UTA to its

equivalent Gaussian source array. Finally, the measurement setup for the steerable parametric loudspeaker is presented with guidelines on the placement of the microphones.

II. *Discovery of the grating lobe elimination effect in the steerable parametric loudspeaker*. While grating lobes are observed for the PF waves, spatial aliasing seldom occurs for the DF wave. This unique phenomenon of the steerable parametric loudspeaker is termed as grating lobe elimination. It is analyzed based on the simulation and measurement results. The guidelines of designing the steerable parametric loudspeaker are derived, accounting for the occurrence of grating lobe elimination. By choosing the optimized configuration of the UTA and the range of the reproduced DF wave, the non-aliasing spacing of the UTA is extended to more than three times of that given by the spatial Nyquist criterion.

III. *Generation of dual beams from a single steerable parametric loudspeaker*. A symmetric structure is proposed for the steerable parametric loudspeaker to generate dual beams without changing the hardware configuration. The second beam of the DF wave is created from the grating lobes of the PF waves. The angular separation between the two beams is simply adjusted by the center frequency of the PF waves. The grating lobe elimination is still effective in the symmetrical structure. The measurement results show that the symmetrical structure generate higher and more consistent dual DF beams with less power consumption compared to the other direct methods.

IV. *Proposal of three modified product directivity models*. Three modifications of the product directivity principle are proposed for the DF wave, namely (i) the advanced product directivity, (ii) the exponential product directivity, and (iii) the combined product directivity. Configurations of the Gaussian source arrays that are equivalent to the PF beampatterns are incorporated into the proposed product directivity models. The comparison between the simulation and measurement results shows that the DF beampatterns are more accurately predicted by the proposed models than the original product directivity model, especially in the vicinities of the first sidelobes.

V. *Array calibration for the steerable parametric loudspeaker*. A structure for the steerable parametric loudspeaker with the system errors taken into account is proposed. Hence, the distorted beampatterns with four types of system errors, namely the spacing error, the weight error, the delay error, and the steering angle error, are analyzed. A combination of the Monte Carlo method and the nonlinear least-squares method is also proposed to solve the calibration equation of a steerable parametric loudspeaker. The cross-validation results show significantly improved matching accuracies between the simulated and the measured beampatterns.

1.4 Organization of the Thesis

This thesis consists of eight chapters, and its organization is as follows. In Chapter 2, the historical progress of studies on the parametric array is reviewed.

The model equations and applications, under water and in air, are presented. In particular, various aspects of the parametric loudspeaker, which is an application of the parametric array in air, are introduced, including its theoretical principle, implementation, preprocessing techniques, and applications in different scenarios. In Chapter 3, the state-of-the-art directivity control methods for the parametric loudspeaker are reviewed. The structure of the steerable parametric loudspeaker based on phased array techniques is proposed. Next, the simulation framework and the measurement setup are discussed for the steerable parametric loudspeaker. In Chapter 4, as a unique feature of the steerable parametric loudspeaker, the grating lobe elimination is analyzed in theory and verified by the measurement results. It is found that the non-aliasing spacing for the UTA in the steerable parametric loudspeaker can be increased beyond what is limited by the spatial Nyquist criterion under specific conditions. This significant finding is further extended to the case of dual-beam generation in Chapter 5. Without modification to the hardware and the UTA's configuration, two audible beams are generated simultaneously from a single steerable parametric loudspeaker. For the dual-beam generation, the grating lobe elimination is still valid in theory and also verified by the measurement results. In Chapter 6, the fundamentals of the product directivity principle are revisited and three modified product directivity models are proposed. The measurement results show the effectiveness of the proposed models, which are of importance for the future design of the steerable parametric loudspeaker. In Chapter 7, the system errors, which are occurred in the steerable parametric

loudspeaker, are taken into account. A structure is proposed to include the system errors, based on which analysis and calibration process of the system errors is carried out. Finally, Chapter 8 concludes this thesis and discuses some suggested future works based on the current contributions.

Figure 1.4 shows how these chapters are linked to the major contributions and publications of the author. As illustrated in the figure, the main body of this thesis spans two disciplines: array signal processing and nonlinear acoustics. In Chapters 4, 5, and 7, the problems of spatial aliasing and system errors, which are classic for the antenna array in array signal processing, are addressed for the parametric loudspeaker to present new observations and approaches. In Chapters 3 and 6, the product directivity models are derived and the measurement setup is discussed for the parametric loudspeaker, when the UTA is adopted as the ultrasonic emitter to transmit the PF waves. In this case, the phased array techniques can be applied to the parametric loudspeaker.

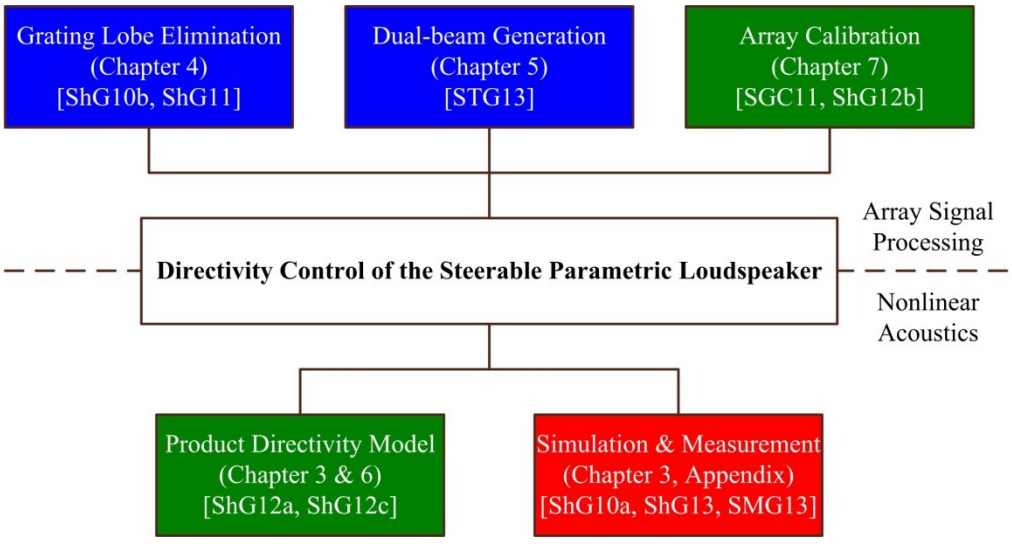

Figure 1.4 The organization of major contributions in the thesis.

Chapter 2
Parametric Array and Parametric Loudspeaker

In this chapter, the fundamental principles and model equations of the parametric array are described in Section 2.1. Several applications of the parametric array are introduced in Section 2.2. In particular, the parametric loudspeaker is explained in Section 2.3, including its mechanism and implementation. Preprocessing methods to reduce the harmonic distortion caused by the parametric array effect itself are presented in Section 2.4. Scenarios where parametric loudspeakers are deployed to reproduce directional sound beams are presented in Section 2.5. Finally, Section 2.6 summarizes this chapter.

2.1 Parametric Array

The theoretical studies on the scattering of sound by sound [InP56, Wes57a, Wes57b, BeB60] led to the subsequent development of the parametric array that was first theoretically explained by Westervelt [Wes63]. The parametric array is able to create a sound beam due to the nonlinear interaction as illustrated in Fig. 2.1(a). When a sound beam consists of two PF waves at f_1 and f_2 propagating in the same direction, the DF and SF waves are generated along with other higher harmonics. Virtual sources are excited along the propagation path, and formed an

end-fire array. Thus, the parametric array is able to act like a highly directional transmitter. Similarly, as illustrated in Fig. 2.1(b), when a carrier wave f_c is transmitted to a specified direction and another existing wave f_d happens to be propagating in the same direction, the DF and SF waves are generated between the carrier wave and the existing wave. In such a case, the DF and SF waves can be measured to calculate the intensity of the existing wave. This described operation of the parametric array can be applied as a directional receiver. The parametric receiving array is functionally same as a parametric amplifier [Wes60], which led to the naming of this nonlinear acoustic interaction as "parametric acoustic array" or "parametric array" for short.

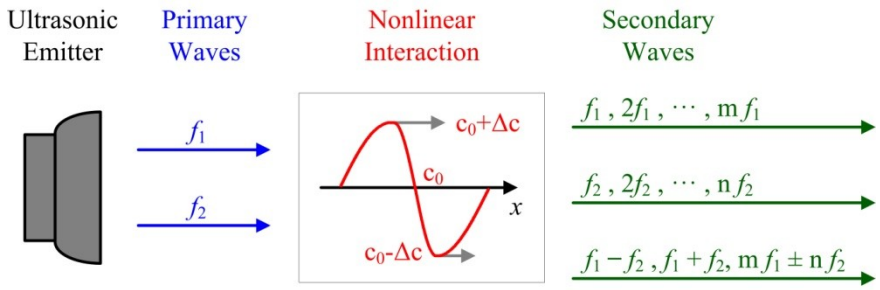

(a) Parametric Transmitting Array

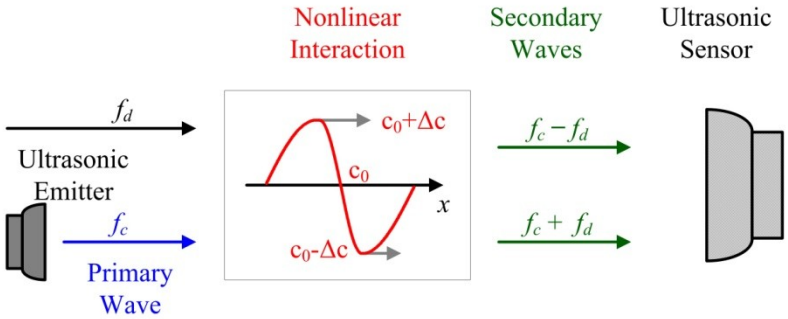

(b) Parametric Receiving Array

Figure 2.1 Nonlinear processes of (a) the parametric transmitting array and (b) the parametric receiving array.

Generally, the parametric array are categorized into three types of sources: the absorption-limited source (shown in Fig. 2.2(a)), the diffraction-limitation source (shown in Fig. 2.2(b)), and the saturation-limitation source. The types of sources are further determined by three distances, namely, the Rayleigh distance, the absorption distance, and the saturation distance [MoM81, VBG98, KiS02, Ols06]. The Rayleigh distance is defined as the distance from the emitter to the transition between the near-field region and the far-field region. Hence, the wavefront of the PF wave is planar within the Rayleigh distance, but spreads spherically when it travels beyond the Rayleigh distance. The absorption distance determines the length traveled by the PF waves before they terminate to generate the secondary waves. Hence, the absorption distance indicates the length of the virtual source array. The saturation distance indicates the region of the saturation effect, which occurs when the amplitude of the PF wave is sufficiently high. In this case, harmonics and shock formations are generated in the PF beam.

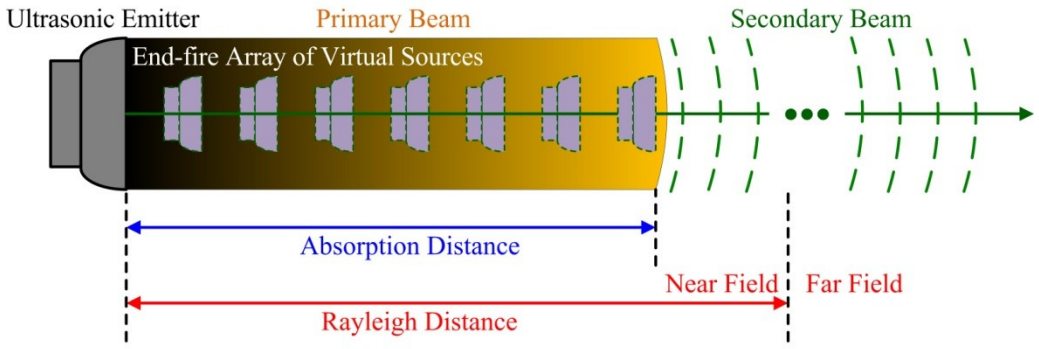

(a) Absorption-limited Source

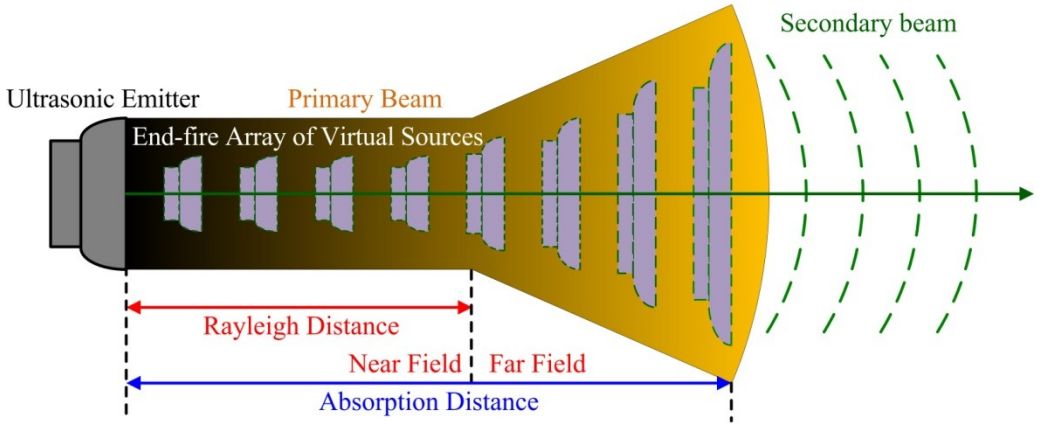

(b) Diffraction-limited Source

Figure 2.2 Geometry of the parametric array using (a) the absorption-limited source and (b) the diffraction-limited source.

When the absorption distance is shorter than the Rayleigh distance, it is the absorption-limited case, where the nonlinear effect terminates within the near-field as illustrated in Fig 2.2(a). In this case, the DF wave is generated from the plane, collimated PF waves. When the absorption distance is longer than the Rayleigh distance, the virtual source array extends to the far-field as illustrated in Fig 2.2(b), resulting in the diffraction-limited case. Moreover, if the absorption distance is much longer compared with the Rayleigh distance, the near-field generation of the secondary waves is negligible. Although the PF waves spread spherically in the

far-field, as long as the PF beam is narrow, the PF waves still give similar parametric array effect as the Westervelt's equation [Ber65b]. When the SPLs of the PF waves are beyond a certain limitation, the saturation effect happens within the near-field of the source. This results in the saturation-limited case, where the PF waves can be assumed to be plane waves in the near-field [Mer75, JTG11a].

In Westervelt's derivation [Wes60, Wes63], the PF waves are assumed to have equal amplitudes of p_0 at the source and equal attenuation rates of α_0 during propagation. Hence, the primary sound field p_i consisting of two PF waves is given as

$$p_i(r,0) = p_0 e^{-\alpha_0 r}\left\{\cos\left[\omega_1\left(t-r/c_0\right)\right]+\cos\left[\omega_2\left(t-r/c_0\right)\right]\right\}, \tag{2.1}$$

where r is the distance from the observation point to the source; c_0 is the speed of sound; and ω_1 and ω_2 are the angular frequencies of the two PF waves.

It is also assumed that the PF waves are collimated and the distance between the source and the observation point is farther than the absorption distance, which is proposed as the reciprocal of the attenuation rate. Therefore, the DF wave is obtained as

$$p_d(r,\theta) = -\frac{i\beta p_0^2 \omega_d^2 e^{-i\omega_d\left(t-r/c_0\right)}}{8\pi\rho_0 c_0^4 r\left[i\alpha_0 + k_d \sin^2\left(\theta/2\right)\right]}, \tag{2.2}$$

where β is the nonlinearity coefficient [Bey98]; ρ_0 is the density of the medium; ω_d and k_d are the angular frequency and the wavenumber of the DF wave, respectively.

The experimental verification of the Westervelt's equation was reported in

[BWB60, BeB62]. A circular transducer was used to transmit two collimated PF waves at 13 MHz and 14 MHz underwater. Due to the high absorption coefficient of water, the formation of virtual sources was restricted to the near-field of the transducer, and fulfilled Westervelt's assumptions. The experimental results showed the expected trends of the SPL and the 3dB beamwidth of the DF wave along the axis of propagation, in spite of the SPL and the 3dB beamwidth being found lower and narrower than the predictions of the Westervelt's equation.

The finite aperture effect was brought out by Berktay [Ber65b] to explain the cause of the mismatch between Bellin and Beyer's experimental results and the predictions of the Westervelt's equation. The PF waves are assumed to be plane and collimated. Thus, the primary sound field is given by

$$p_i(r,0) = p_1 e^{-\alpha_1 r}\cos\left[\omega_1\left(t - r/c_0\right)\right] + p_2 e^{-\alpha_2 r}\cos\left[\omega_2\left(t - r/c_0\right)\right], \qquad (2.3)$$

where p_1 and p_2 are the amplitude of the two PF waves; α_1 and α_2 are the attenuation rate for the two PF waves.

Due to the finite aperture formed by the cross-section of the virtual source array, the DF wave is given by

$$p_d(r,\theta) = \frac{\beta p_1 p_2 \omega_d^2}{8\pi\rho_0 c_0^4 r}\frac{1}{\sqrt{\left(\alpha_1 + \alpha_2 - \alpha_d\cos\theta\right)^2 + k_d^2\sin^4\left(\theta/2\right)}} D_A(\theta), \qquad (2.4)$$

where α_d is the attenuation rate for the DF wave; $D_A(\theta)$ is the aperture of the transducer, which can be either circular [Ber65b] or rectangular [NaT65, Ber65a], in the far-field.

The self-demodulation process of a pulsed carrier, which was also proposed by Berktay, was proven by the experiment carried out by Moffett *et al.* [MWB70,

MWB71]. Due to the nonlinear effect, the modulated PF wave interacts with itself and creates the frequency component same as the envelope function without the carrier frequency. When the wavefront of the modulated PF wave is assumed to be planar, the primary sound field on the propagation axis is presented in the form of

$$p_i(r,0) = p_0 e^{-\alpha_0 r} f(t - r/c_0)\cos\left[\omega_c (t - r/c_0)\right]. \tag{2.5}$$

Here, ω_c is the angular frequency of the carrier wave, and $f(t)$ is the envelope function with unity amplitude that varies slowly. The frequency components of the envelope function are assumed to be much lower than the carrier frequency. Hence, the self-demodulated wave on the propagation axis is given by

$$p_d(r,0) = \frac{\beta p_0^2 S}{8\pi\rho_0 c_0^4 r(2\alpha_0)} \frac{\partial^2}{\partial t^2}\left[f^2(t - r/c_0)\right], \tag{2.6}$$

where S is the cross-sectional area of the PF beams.

In the early studies of parametric array, many experiments had been carried out to validate the parametric array effect under a variety of conditions [MuB69, MBK71, BWT72, MuW72]. Until 1975, the earliest acknowledged evidence of the parametric array effect in air was obtained by Bennett and Blackstock [BeB75]. In their experiment, two PF waves at 18.6 kHz and 23.6 kHz were transmitted using a circular piston transducer, as shown in Fig. 2.3. The PF waves were collinear and spherically spreading. The DF wave was observed at 5 kHz as expected. It was noted by Bennett and Blackstock in their measurement that the spurious difference frequency signals dominated the result in the near-field when there was no acoustical filter placed in front of the microphone. However, when

the PF waves were sufficiently attenuated at longer distance, the parametric array effect took over. The spurious DF signals were proven to be greatly suppressed by a dome-shaped acoustical filter, which was made from a thin clear plastic material. This experimental work presented an attractive yet challenging method to create sound beams in air. However, no attention is paid to the potential of the parametric array to reproduce audible signals during that period.

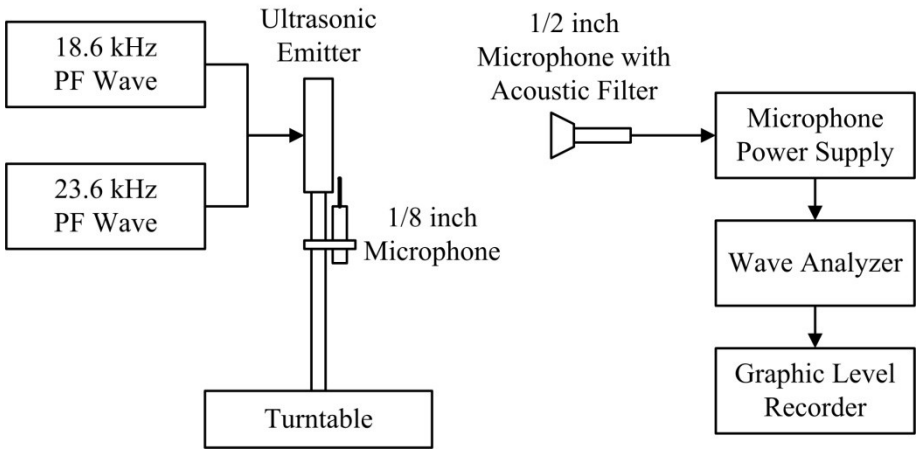

Figure 2.3 Measurement setup carried out by Bennett and Blackstock (extracted and modified from [BeB75]).

Till now, there are numerous model equations [Bar72, BeL74, MoM77, ChS81, ZhC98, HaM98, ZhW99, KAA04, JTC11, JSC11] that are investigated to describe the propagation of the finite-amplitude sound beam. However, the most widely-used model equation is still the Khokhlov–Zabolotskaya–Kuznetsov (KZK) equation [ZaK69, Kuz71], which is derived under a parabolic approximation and valid when the sound field is in the vicinity of the propagation axis. The KZK equation includes the combining effects of diffraction, absorption and nonlinearity in the propagation of the finite-amplitude sound beams [HaM98, Ham98], which

are expressed by the first, second and third terms on the right hand side of KZK equation, respectively. The KZK equation is given as

$$\frac{\partial^2 p}{\partial z \partial \tau} = \frac{c_0^3}{2}\nabla_\perp^2 p + \frac{\delta}{2c_0^3}\frac{\partial^3 p}{\partial \tau^3} + \frac{\beta}{2\rho c_0^3}\frac{\partial^2 p^2}{\partial \tau^2}, \tag{2.7}$$

where p is the sound pressure; δ is dissipation factor corresponding to thermoviscous absorption; z is the coordinate along the beam propagation direction; $\nabla_\perp^2$ is the Laplacian operator that operates on the X-Y plane perpendicular to the axis of the beam; and $\tau = t - z/c_0$ is the retarded time.

The KZK equation is normally solved by numerical methods in frequency domain [ABT84, KHA89, KTK92] or time domain [Lee93, ALH93, KiS02]. The analytical solution to the KZK equation is achievable in the far-field when the Gaussian beams are used for the PF sources. Furthermore, it was found that any axial-symmetric sound field could be expressed in the form of a superposition of Gaussian beams with different radii and locations along the same axis [WeB88, KSS06]. Thus, the second harmonic sound field of an axial-symmetric source can be simplified to a linear combination of that of the equivalent Gaussian beams [DSL96, Din00, SYG03, YSG04, YSG05].

2.2 Applications of the Parametric Array

The parametric array is useful for applications that demand highly-directional sources within a restricted space. Sonar is one of the earliest applications of the parametric array [Ber65c, BMK09, Ost09]. There are three significant advantages

of the parametric array sonar: wide bandwidth, narrow beamwidth, and absence of sidelobes [HRO98]. Since the Doppler effect can be integrated with the parametric array effect, the parametric array Doppler sonar is developed to measure motions at deep ocean [Kri77] or vibrations in air without contacting the surface [MRB98]. The parametric sonar is also adopted in detecting the depth of the sea [Nic71] or the bottom topography [KGK10]. Due to its sharp directivity, the parametric sonar is ideally deployed to measure the properties of the seabed [Hin99, GrK10] and to monitor the contaminated sediments with high resolution [GRH91].

As low-frequency transmission and long-range reception are achievable with the parametric source in a compact size, it is also advantageous in applications of underwater communication [CZW96, LVE96, KCD00]. For instance, the video signal is processed and coded before being transmitted by the parametric source, of which the aperture is only ten inches in diameter. The DF band is then received at the bottom of the lake, which is about 4000 meters down from the surface. The received DF band can be decoded and displayed on a screen [BMK09].

In a medical tomography system, the parametric array effect is considered to improve the resolution of the diagnostic image in two methods. In the first method, two PF waves are transmitted through the tissue, which is a nonlinear medium, and the generated DF wave is received. The DF wave reflects the nonlinearity of tissue. Therefore, the tomogram of the scanned tissue is reconstructed from the DF data [NHC86, CSW88, ZCG01, ZGZ02]. Alternatively, second harmonics are also generated from the parametric array forming in the tissue, and can be measured to

provide the data for reconstruction [ARP97]. Since the second harmonics have narrower beams and lower sidelobes than the DF wave, images formed with this technique provide better border definition and tissue contrast. Microbubbles, as contrast agents, have been introduced to increase the contrast between the target and the surrounding tissue. The microbubbles are released into the blood, and once they are excited by an external fundamental frequency wave, energy of the second harmonic wave can be detected to form the image. The parametric array can be potentially used as the ultrasound source for the microbubble excitation as well, due to its narrow-beam characteristics in [VGV11].

The parametric array has been proven to be an efficient and inexpensive replacement of the conventional acoustical transducer array. It is widely applied in various industries. For example, in high-energy neutrino interaction [ABC09], the parametric array generates the neutrino-like signals in the calibrator system. It is also utilized to excite different types of materials in nondestructive/noncontacting testing. The responses are detected and the attenuations in the materials are extracted [GCS89]. Thus, the materials are classified based on the measured responses [KSL00]. It was reported by Lee *et al.* [LKM06, LKM07, LKM09] that PF waves at 95 kHz and 134.5 kHz were transmitted to generate the DF wave at 39.5 kHz, and an enhanced spatial resolution was achieved for ultrasound ranging in air and underwater.

When the parametric array is used as a directional receiver [BeA69, KIC85], it behaves like a parametric amplifier as illustrated in Fig. 2.1(b). The application

of such parametric receiver in air is known as the parametric microphone [Mer09]. When an ultrasonic wave is sent over a long distance through a room, it can be modulated by any audio wave that exist in the same room, due to the nonlinear interactions. By recording the modulated ultrasonic wave, the audio waves are able to be recovered. Thus, it can be implemented in the virtual acoustical sensing, with no requirement of placing a real microphone at the desired measuring point. However, the performance of the parametric microphone is sensitive to the phase noise, which prevents it from being widely used in practice.

A well-known application of the parametric array in air is the parametric loudspeaker. By inheriting the advantages of the parametric array, the parametric loudspeaker possesses a variety of useful characteristics. Unlike the conventional loudspeaker, which transmits nearly omnidirectional sound waves and requires a much larger aperture to create a sound beam, the parametric loudspeaker allows a highly directional and controllable sound beam to be generated using a relatively small emitter. The diameter of the emitter used in the parametric loudspeaker can be shorter than the wavelength of the reproduced sound wave. The first parametric loudspeaker, also known as the "audio spotlight", was demonstrated by Yoneyama *et al.* [YFK83] in 1983, who derived from the Westervelt's equation and found that the demodulated wave showed a rate of 12 dB/octave with reference to frequency increment. This frequency response, which is similar to a high-pass filter, can also be derived from the second-time derivative factor in the Berktay's far-field solution shown in (2.6).

2.3 Parametric Loudspeaker

The fundamental theory of parametric loudspeaker is based on the parametric array effect. When two PF signals at close frequencies are fed to the parametric loudspeaker and transmitted into air, as shown in Fig. 2.1, the acoustic energy of the PF signals transfers into new frequency components, such as the DF, the SF, and other high order harmonics. The frequency components in the ultrasonic range decay rapidly with the propagation distance due to the absorption effect in air, but the DF wave, being lower in frequency and audible to humans, is less attenuated and yet increased within the absorption distance due to the virtual end-fire array formed by the excited air molecules in front of the ultrasonic transducer array.

The implementation of a parametric loudspeaker consists of three components: the processor, the amplifier, and the ultrasonic emitter [GYK12]. As shown in Fig. 2.4, the processor performs the preprocessing methods and modulates the audible frequency components into the ultrasonic range. The processor is usually a digital signal processor (DSP) [CHX05, LYM06, LiH10] or a field programmable gate array (FPGA) [KGC04, WWH12], and can also be partially or fully replaced by analog circuits with the same functions [OPL05, Nip12]. The Class-D type amplifier, which is able to operate in the ultrasonic range, is commonly used to drive the ultrasonic emitter, which is made up of a polyvinylidene fluoride (PVDF) film [CrN01, Rit06] or an array of piezoceramic (PZT) transducers [Mur09, Nip12]. Microelectromechanical system (MEMS) techniques have also been used to fabricate the transducers that are customized for the parametric loudspeaker

[RoM02, LXX11, MSH11]. The PF waves at 48.5 kHz and 53.5 kHz transmitted from the capacitive micromachined ultrasonic transducer have achieved sufficient power intensity to create a narrow sound beam at 5 kHz over several meters [WKW09].

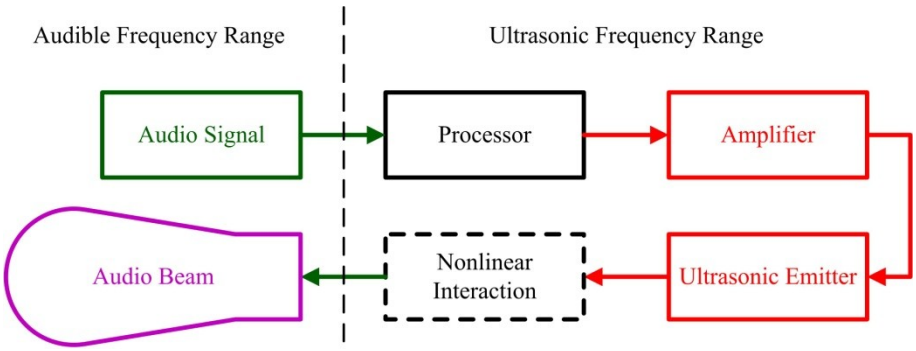

Figure 2.4 Block diagram of the parametric loudspeaker.

2.4 Preprocessing Methods for the Parametric Loudspeaker

In the invention of "audio spotlight", Yoneyama *et al.* [YFK83] derived that the frequency response of the reproduced sound showed a slope of 12 dB/octave, and the second harmonic distortion ratio was proportional to the modulation index, when the double sideband modulation (DSBAM) was used, as shown in Fig. 2.5(a). Since then, several preprocessing methods have been proposed to equalize the frequency response of the reproduced sound and reduce harmonic distortions to an acceptable sound quality level. In 1984, Kamakura *et al.* [KYI84] discovered that the square operator on the envelope function in (2.6) resulted in significant distortions. Hence, they proposed the pre-distorted envelope function, which was the square root of the DSBAM. This preprocessing method is known as the square

root amplitude modulation (SRAM), of which the diagram is shown in Fig. 2.5(b). The SRAM can substantially suppress the second harmonic component of the demodulated signal in the parametric loudspeaker.

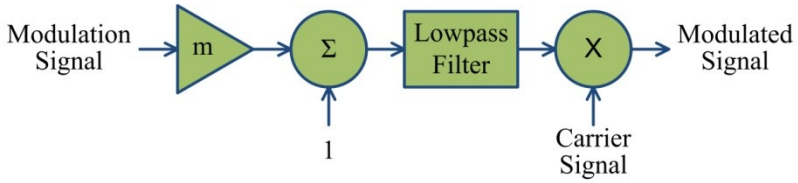

(a) Double Sideband Amplitude Modulation (DSBAM) [Yoneyama *et al.* 1983]

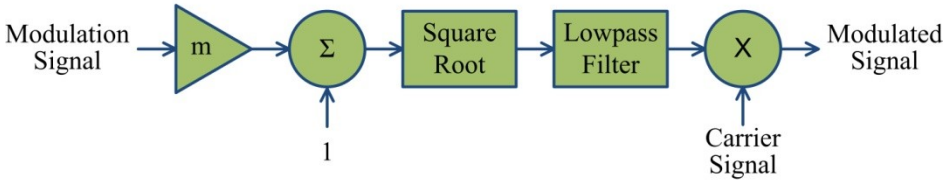

(b) Square-root Amplitude Modulation (SRAM) [Kamakura *et al.* 1984]

Figure 2.5 Block diagrams of (a) the DSBAM and (b) the SRAM.

A variant of the SRAM was also proposed by Kamakura *et al.* [KAK91, AKK91, KAS06] that reduced the average power consumption of the parametric loudspeaker to one third of that when the DSBAM was used, and yet reproduced similar sound quality as the SRAM. The double integral operator was introduced into the SRAM as an equalizer to further reduce the harmonic distortions [KPH98, Pom99, KGE02, KiK02]. In Pompei's measurement [Pom99], the SRAM with double integral operator reduced the total harmonic distortion (THD) to less than 5% over most audible frequencies. However, the necessity of inserting the double integral operator before the SRAM requires further studies, since the ultrasonic transducer behaves similar to a low-pass filter in its frequency response, which can partially compensate for the 12 dB/octave frequency dependence derived from

the second-time derivative factor in the Berktay's far-field solution [HaB00]. Thus, the double integral operator is only recommended for preprocessing when the frequency response of the ultrasonic transducer is relatively flat across a wide frequency range.

A drawback of the SRAM is that the square root operator extends the modulated signal to infinite bandwidth in frequency domain. Hence, the SRAM and its variants suffer from the limited bandwidth of the typical ultrasonic transducer that is designed to achieve sufficiently high SPL in a narrow frequency range due to the current fabrication technique [KPH98]. Kim and Sparrow [KiS02] proposed to use a low-pass filter before the SRAM that compensated the frequency response of the 12 dB/octave slope derived from the Berktay's far-field solution. Another high-pass filter was adopted after the SRAM to remove any audio component generated by the square root operator to avoid aliasing. A truncated SRAM was proposed by Wang *et al.* [WCL07] that added a band-pass filter after the SRAM. Similarly, band-pass filters were also used to approximate the frequency responses of the ultrasonic transducers [JiG12].

To overcome the bandwidth requirement of the SRAM, the single sideband amplitude modulation (SSBAM) was investigated by several researchers [AKK91, JYT07, WXC08, BKS08, WLX09]. The diagram of the SSBAM is shown in Fig. 2.6(a). There are two types of SSBAM, known as the lower sideband amplitude modulation (LSBAM) and the upper sideband amplitude modulation (USBAM), depending on the sign of the multiplier on the Hilbert transformed branch. When a

sine wave is used as the input of the SSBAM, the THD is equal to zero in theory. However, measurement results of the SSBAM show that the THD values differ from the theoretical prediction, due to certain assumptions made in the Berktay's far-field solution [Mer75, WKW09, JTG11a]. Aoki *et al.* concluded that the SSBAM was preferred in terms of the harmonic reduction when the initial SPL was small, and the DSBAM outperformed the SSBAM when PF waves have large amplitudes. An energy-efficient variant of the SSBAM, namely the dynamic single sideband modulation, was proposed by Sakai *et al.* [SaK08]. In this method, the amplitude of the carrier signal was determined by the envelope of the audio signal. Thus, the power consumption of the parametric loudspeaker, as well as the ultrasonic exposure to the users, was reduced.

The core of the SSBAM is the quadrature modulation. Liew [Lie02] revisited this method and proposed the modified amplitude modulation (MAM). The MAM consists of a pre-distorted term that is modulated with the orthogonal carrier, and it can be expressed as a class of preprocessing methods by using different orders of the Taylor expansion of the pre-distortion term, as shown in Fig. 2.6(b). Thus, the MAM is adaptable to the bandwidth of the ultrasonic emitter [TJG10]. The MAM possesses the advantages of both the SSBAM and the SRAM. Hence, it is able to achieve a close THD level as the SSBAM (which is zero in theory), while the inter-modulation distortion (IMD) level of the MAM is greatly reduced compared with other preprocessing methods [YJG07, TJG08, TGY08, JGJ10, TJG10, JTG11a].

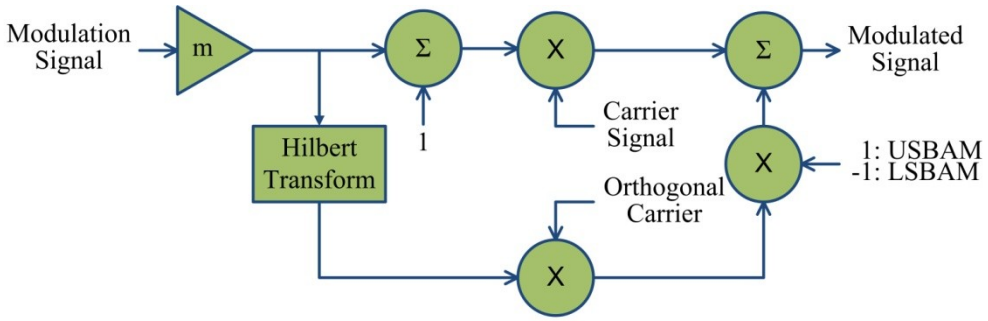

(c) Single Sideband Amplitude Modulation (SSBAM) [Kamakura *et al.* 1985]

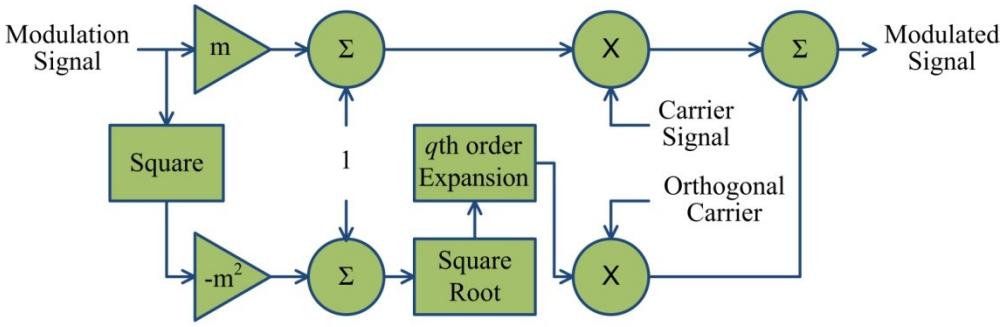

(d) Modified Amplitude Modulation (MAM) [Liew 2002]

Figure 2.6 Block diagrams of (a) the SSBAM and (b) the MAM.

Another attempt at improving the SSBAM was known as the recursive single sideband amplitude modulation (RSSBAM) that was first conceptualized by Croft *et al.* [CrN01, CSN03]. As a recursive algorithm, its performance depended on the total iteration times and the model equation used in each iteration [LeG06, JGT10]. Since all model equations are derived under different assumptions, there is always a trade-off for the RSSBAM between high fidelity and computational complexity. Alternatively, the adaptive Volterra filters can be utilized to model the nonlinear process of the parametric loudspeaker effectively by system identification [LYG02, JTG11b, JiG12]. It is observed in both simulation and measurement results that the harmonic distortions of the parametric loudspeaker are merely generated from the quadratic nonlinearity in the propagation of the PF waves. This observation

validates the assumption made in most analyses of the RSSBAM that the nonlinear demodulator can be simplified by a square operator.

2.5 Applications of the Parametric Loudspeaker

A functional application of the parametric loudspeaker is to create personal listening zones in public areas. For instance, the parametric loudspeaker is able to be deployed in advertising applications that project messages to targeted persons [IYI07], and it can also be applied in entertainment electronic products, such as interactive sound visualization systems [WEL07, NOS09, KHT11] or immersive audio systems [JoG09, JBG10, MaS10, Gre10, TaG12 ATT12, SKI12]. In one particular setup in a gaming booth, a pair of parametric loudspeakers was installed to project directional binaural sound to the gamer [GTK11]. This setup confines sound to a predetermined sound zone. The gamer within the zone can enjoy playing without overly disturbing other visitors standing outside the sweet spot.

The parametric loudspeaker can also be integrated into the mobile phone and other portable devices [NYO05, NYN06, LXX11]. Although the dimension and power consumption of existing prototypes are not satisfactory due to the current technologies, the development of the MEMS transducers is expected to deliver breakthrough solutions in the future. Another similar application of the parametric loudspeaker operating in its near-field is a conceptual earphone driven by the ultrasound vibration [OMW03]. The verification was conducted in an auricular cartilage of a pig, and self-demodulation effect was observed in this experiment. A

major difference between this earphone and the air-borne parametric loudspeaker is that the nonlinear effect taking place in the cartilage contributes to most of the reproduced sound.

In a human-computer interaction application, the parametric loudspeaker was used in a teleconference scenario together with a synthetic talking head, which provides lip actions synchronized to the speech [SvO05]. Improved intelligibility of the spoken output in a noisy environment was verified by subjective tests. In another similar application, the parametric loudspeaker also worked effectively in a new human-humanoid communication system to improve the accuracy of speech recognition when people and the humanoid speak simultaneously [NaT05].

Due to its ability to create highly directional sound beams, the parametric loudspeaker is helpful to traffic applications in reverberant fields, such as in a tunnel [AKK94] or an underground passage [MBM06]. A drawback with using conventional loudspeakers is that the reproduction of severe echo in the tunnel deteriorates the broadcasted information. When the parametric loudspeaker is used, the speech articulation is greatly improved. In the road navigation system, voice instructions can be delivered directionally to the pedestrians using the parametric loudspeaker without emitting sound pollution [AKK94, MBM06, MBK07, NWN08, KaS08, MBK10]. The instructions may contain the traffic conditions, nearby tourist attractions, and the location of the nearest assembly area. However, the maximum SPL of the parametric loudspeaker is limited by the saturation effect in air. Thus, it is not suggested to be deployed in a heavy traffic noise environment

[PRH10].

Moreover, the parametric loudspeaker is studied to replace the conventional loudspeaker as the control source in applications of the active noise control (ANC) system [BZH05, KZH06, KPZ06, TaT09a, TaT10a, TaT10b, KoI11]. When the conventional loudspeaker is used as the control source to minimize the SPL at a specified point, increased SPL around the control point is unwanted yet observed. By using the parametric loudspeaker, the suppression of SPL at the control point is still achieved efficiently, while the SPL around the control point is not affected. Furthermore, the parametric loudspeaker can be operated in the reflected mode. Thus, when the parametric loudspeaker is used as the control source, the control point is allowed to be invisible to the source point, which is impossible for the conventional ANC system [TaT09b, SMN10, KMN10, TaT11].

An emerging usage of the parametric loudspeaker is to detect landmines buried in the soil and hidden weapons on a suspicious person. For the landmine detection, a focused low-frequency sound beam is projected to the ground from the parametric loudspeaker, and the landmine buried in the soil scatters the acoustic energy. The scattered energy causes ground motions, which are captured by the noncontacting vibrometer. Therefore, the resonance pattern of the landmine is first analyzed and then different types of landmines can be identified [WSM05, HaR05]. Moreover, similar methods are applied to detect concealed weapons on persons [HAH05, AMH05, Cos05, RuH08, HiR09]. A remarkable advantage of using parametric loudspeaker for noncontacting detection applications is its light

weight and small size over other acoustic sources.

In addition, the usage of the parametric loudspeakers has been proven to be safe to humans in both near-field and far-field. The burden on the human's endocrine system caused by the parametric loudspeaker was measured to be even lower than that caused by the conventional loudspeaker [LKT10, LKS11a, LKS11b]. A variety of commercial products of the parametric loudspeaker available on the market are shown in Fig. 2.7, which range from ceiling mounted to portable and handheld devices.

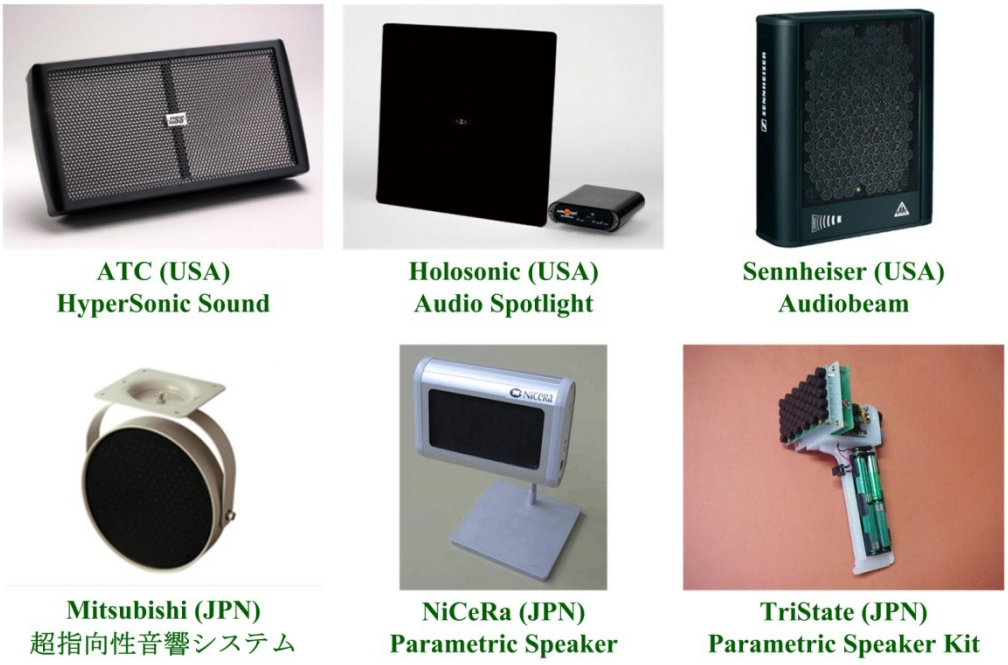

Fig. 2.7 Commercial products of the parametric loudspeaker (extracted and modified from [Gan12]).

2.6 Conclusions

This chapter focused on the introduction and review of the principle and applications of the parametric array. The parametric loudspeaker, which is also an application of the parametric array in air for audio beam generation, was discussed. Generally, the parametric array is a nonlinear acoustical effect that produces new frequency components in the propagation of the primary waves. It is advantageous in creating a narrow beam without obvious sidelobes, at a low frequency, and for a wideband signal with a relatively small sized source. Hence, the parametric array has been deployed in the applications of sonar, echo sounder, bottom topography, underwater communication, medical tomography, and as an inexpensive replacement to the conventional transducer array in a variety of industries. In particular, one of the most attractive and well-known applications is the parametric loudspeaker, which inherits the advantages of the parametric array that can generate a highly directional sound beam with an almost constant amplitude over a range of a few meters. Several researchers have proposed different preprocessing methods to equalize the frequency response and reduce the harmonic distortion of the sound reproduced from the parametric loudspeaker. A variety of applications have also used the parametric loudspeaker and taken advantage of its unique features, such as creating personal audio zone in entertainment systems, providing enhanced cue in 3D audio scenarios, replacing the conventional loudspeaker as the control source in the ANC system, traffic

navigation, generating directional sound beams for human-computer interaction, security check and landmine detection. For all these applications, it is suggested that a steerable sound beam would be an important add-on feature for the parametric loudspeaker to be installed freely and meet the latest demand of interactive and immersive applications. The details of creating a steerable sound beam will be introduced and discussed in the following chapters.

Chapter 3
Steerable Parametric Loudspeaker

As mentioned in the previous chapter, there is an increasing interest in generating controllable directional sound beams from the parametric loudspeaker to support interactive applications, such as multilingual teleconferencing and immersive 3D audio for entertainment [GTK11]. A steerable parametric loudspeaker was used by Tanaka *et al.* [TaT09a] as the control source in an ANC system, which transmitted the directional anti-noise sound wave towards a moving target. Due to the narrow directivity of the parametric loudspeaker, it reduces acoustical disturbances to the surroundings, when compared with the conventional loudspeaker. Therefore, the directivity control has been proven valuable to the parametric loudspeaker. However, there have only been few attempts of developing such techniques using either mechanical or electronic approaches.

Hence, existing directivity control methods for the parametric loudspeaker are reviewed in Section 3.1. In particular, the steerable parametric loudspeaker, which adopts array signal processing techniques, is discussed in Section 3.2. Simulation framework for predicting the spatial performance of the steerable parametric loudspeaker is proposed in Section 3.3. In Section 3.4, the measurement setup for the steerable parametric loudspeaker is shown and explained in detail. Finally,

Section 3.5 summarizes and concludes this chapter.

3.1 Directivity Control Methods for the Parametric Loudspeaker

Pompei and Wooh [PoW02, Pom02] investigated the shape of the individual transducer with the objective of suppressing grating lobes. The transducer arrays consisting of rectangular elements, diamond elements, and circular elements were analyzed and compared. An optimum shape of the transducer was also proposed to be given by the truncated sinc function. In spite of being potentially useful for parametric loudspeakers, the optimum shape is difficult to be fabricated. On the other hand, Gadsby [Gad05] found that more than nine transducers in a column did not significantly reduce the beam divergence in his simulation of the PF beampattern. Olszewski *et al.* [OlL06a] examined different array configurations and attempted to find out an optimum setup of the UTA. It was concluded that when sufficient mounting space was available, the ring array was recommended for its improved directivity at lower frequencies.

A hybrid system was also proposed by Olszewski *et al.* [OPL05, Ols09], which consisted of four louvers that were tilted mechanically in unison to the desired direction. To further fine tune the steering angle, phased array techniques were deployed to realize beamsteering in a limited angular range. By using this method, sufficient acoustic power is delivered to the steering angles beyond the louver's beamwidth. But the hybrid system suffers structurally from interfering reflections, high cost and being bulky in size. Another parametric loudspeaker

consisting of pre-steered segments was presented by Olszewski and Linhard [OlL06b]. These pre-steered segments were installed at the ceiling of the room to transmit multiple beams to different directions at the same time. This multi-beam system allows different audio contents to be delivered to respective directions, but the power consumption dramatically adds up.

The directivity of the parametric loudspeaker working in the reflected mode is controllable by using different reflective objects [HMN09, MIT10]. Therefore, the secondary sound field is diffused to different directivities. The sound reflected by the quadrilateral object resulted in a steered angle, which is perpendicular to the sound beam, while the hemispherical reflector widens the directivity of the DF wave generated from the parametric loudspeaker. This observation of the hemispherical reflector agrees with the conclusion of an earlier experiment carried out by Olszewski and Linhard [OlL06c], who stated that the presence of a listener's head in the near-field of the parametric loudspeaker leads to a broadened DF beampattern similar to that of a conventional loudspeaker.

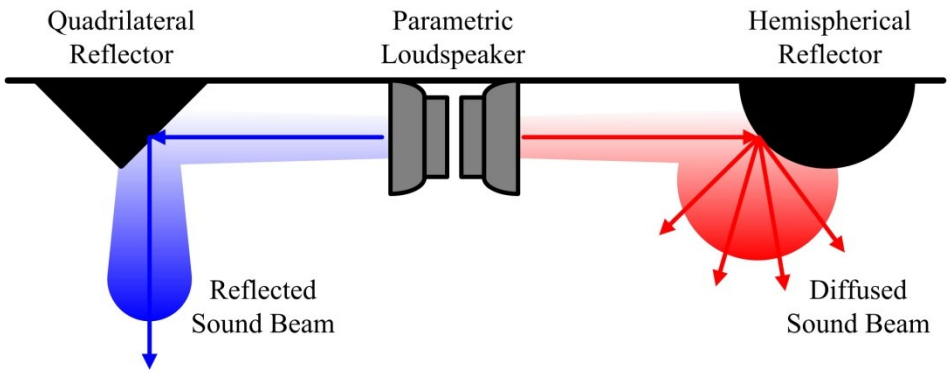

Figure 3.1 Illustrations of the reflective objects, (a) the quadrilateral reflector and (b) the hemispherical reflector.

Among the models describing the beampattern of the parametric loudspeaker [VKT00, YHW11], the product directivity principle stated by Darvennes and Hamilton [DaH90] provides a convenient theoretical basis for the digital control of the parametric loudspeaker's directivity. In their study on the scattering of sound by sound, the DF wave generated from two non-collinear Gaussian beams was derived based on the nonlinear parabolic wave equation. When the Gaussian beams are restricted to moderate source separations and interaction angles, the far-field directivity of the DF wave is given by the product of the PF directivities. In the experiment carried out by Ishimaru *et al.* [IsH02] and Ji *et al.* [JYG09], it was further verified that by using two ultrasonic beams at various angles and locations, it was able to create a localized sound spot due to the nonlinear effect in air.

According to the product directivity principle, the phased array techniques are applicable to adjust the PF beampatterns and indirectly achieve the control of the DF beampatterns. A digital beamforming approach was previously proposed by Tan *et al.* [TGY03, YTG05]. In their proposed structure, the ultrasonic transducers are treated as bifrequency Gaussian sources. Hence, based on the product directivity principle, the constant-beamwidth beamformer is achieved by adjusting the first null of the lower PF wave to coincide with the first sidelobe of the higher PF wave. To extend this method to the broadband case, the weights of the PF wave can be designed as a group of frequency-dependent functions. [Tan04, YGT05].

Subsequently, the digital implementation of the beamsteering algorithm in the parametric loudspeaker was investigated in [TGY04, GYT06]. It was realized that the sampling frequency used in the digital processor limited the range of steering angles. Tan *et al.* proposed a method that applied different delays to the two PF waves. Thus, the PF waves are steered to two different directions, so that the resultant DF wave is steered to the direction predicted by the product directivity principle. Since the carrier wave (one of the PF waves at 40 kHz shown in Fig. 3.2) is able to be generated digitally with arbitrary delays, it can be readily steered to any direction. Another PF wave (at 30 kHz and 50 kHz as shown in Fig. 3.2) is designed to achieve a relatively wide beamwidth. Hence, as a result of the product directivity principle, the DF wave can be steered to the exact direction determined by the carrier wave, and the limited range of the steering angle of the DF wave is resolved. However, the resultant mainlobe of the DF wave is attenuated from the maximum output, as shown in Fig. 3.2, as a result of the separation between the mainlobes of the two PF waves. This suppressed output of the DF wave results in reduced power efficiency.

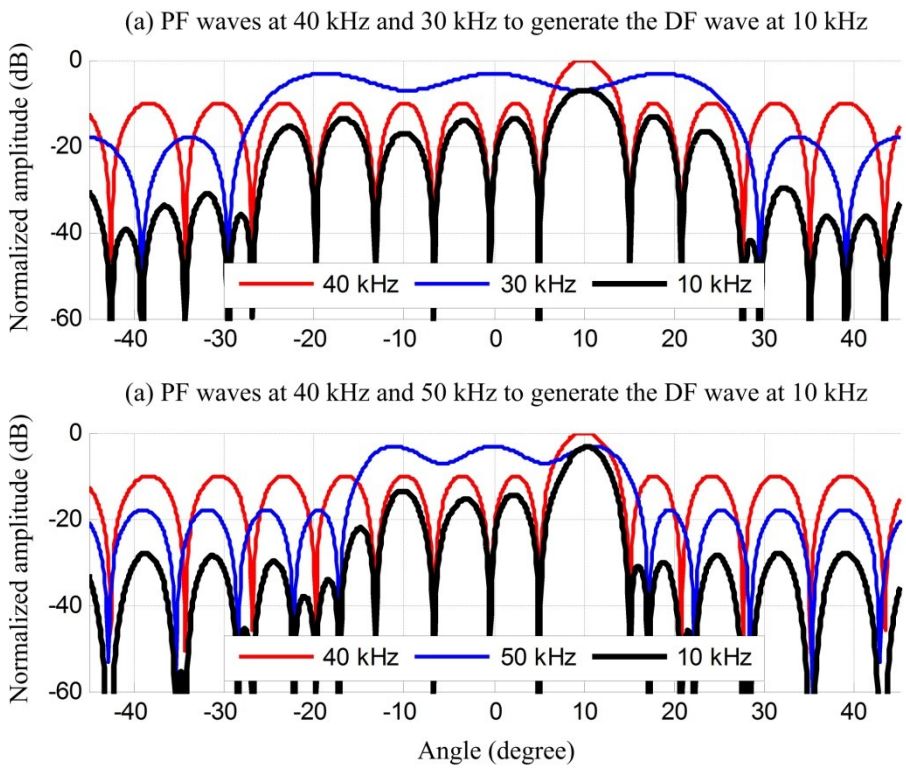

Figure 3.2 PF and DF beampatterns when the DF wave is generated at 10 kHz and steered to 10° in the UTA consisting of 16 channels with spacing of 5 mm (extracted and modified from [GYT06]).

Lee *et al.* [LBP11] proposed to use the complex weights, instead of the time delays, to achieve various transmitting beampatterns in the parametric loudspeaker. In [WWH12], an FPGA implementation of the steerable parametric loudspeaker, which adopted fractional delay filters, was described. Another FPGA-based parametric loudspeaker, which implemented the delta-sigma modulator to control the steering angle of the sound beam, was introduced by Takeoka and Yamasaki [TaY10]. In the latter case, the modulated signal was quantized into a serial bit stream at a sampling frequency of 1.4 MHz. Taking advantage of the simple delay units implemented in the FPGA, 576 PZT transducers were controlled individually,

and a fine angle resolution of about 2° was achieved.

3.2 Structures for the Steerable Parametric Loudspeaker

From the past literature, there are two commonly used methods of achieving the steerable sound beam in the parametric loudspeaker: (1) a system that delays the modulated signal of each channel; and (2) a system that delays the modulating signal of each channel before mixing with the carrier signal. However, no experimental results and theoretical derivations have yet been carried out for these two methods. In addition, the relation between the phases of the PF waves and the DF wave remains unexplored. Therefore, a discussion is presented in this section to link the theoretical and practical aspects of the steerable parametric loudspeaker.

It is assumed that the delay amounts τ_1 and τ_2 are applied to the two PF waves at frequencies f_1 and f_2, respectively. The rest of the assumptions are kept to be the same as what Westervelt assumed in his derivation [Wes63]. Thus, the primary sound field on the propagation axis is described as

$$p_i(r,0) = p_0 e^{-\alpha_0 r}\left[\cos\omega_1\left(t-\tau_1-r/c_0\right)+\cos\omega_2\left(t-\tau_2-r/c_0\right)\right]. \tag{3.1}$$

Virtual sources of the audio signal occur in the PF beam due to the nonlinear acoustical interaction in air. The virtual source strength density is presented by

$$q_d = \frac{\beta p_0^2}{\rho_0^2 c_0^4} e^{-2\alpha_0 r}\frac{\partial}{\partial t}\cos\left[\omega_d\left(t-r/c_0\right)-\left(\omega_2\tau_2-\omega_1\tau_1\right)\right]. \tag{3.2}$$

If the PF source is assumed to be circular, the DF sound pressure on the axis

at a distance of r can be calculated analytically. If it is further assumed that $\omega_2 > \omega_1$ without loss of generality and $\omega_d = \omega_2 - \omega_1$, the DF sound pressure on the propagation axis is given by

$$p_d(r,0) = \frac{\beta P_0^2 a^2}{8\rho_0 c_0^4 \alpha r} \frac{\partial^2}{\partial t^2} \cos\left[\omega_d\left(t - \tau_2 - r/c_0\right) - \omega_1\left(\tau_2 - \tau_1\right)\right]. \tag{3.3}$$

From (3.3), it is found that if the delay amounts of the two PF waves are equal ($\tau_1 = \tau_2$), the DF wave generated from the parametric array obtains the same delay amount. If the delay amounts of the two PF waves are different and the two PFs are very closely spaced in frequency, the initial phase of the resultant DF wave is approximated as the average phase of the PF waves.

The above statement is verified by a series of studies carried out by Kamakura *et al.* [KSN08, AKH08, KNA09, NHK12]. In their simulations and experiments, two sets of parametric loudspeakers were used, and the two PF waves were chosen at 38 kHz and 40 kHz. When using the in-phase excitation, the initial phases of all the PF waves were 0°. When using the out-of-phase excitation, the initial phase of the 40 kHz wave in one parametric loudspeaker was changed to 180°, but the initial phases of the rest of the PF waves were kept at 0°. The results showed that the amplitude of the 40 kHz wave was reduced significantly by the out-of-phase excitation. However, the amplitude of the DF wave was less sensitive to the phase changing of the PF waves. Based on (3.3), the in-phase excitation of the PF waves generates a DF wave with an initial phase of 0°, but the out-of-phase excitation of the PF waves generates a DF wave with an initial phase of 92.3°. Therefore, the reduction in the amplitude of the DF wave by the out-of-phase excitation is

estimated to be 3.2 dB.

A beamsteering structure is proposed in Fig. 3.3 for the steerable parametric loudspeaker based on phased array techniques. The weight of the m th channel is denoted as w_m for $m = 0, 1, 2, \ldots, M-1$, and M is the number of channels in the UTA. The same amount of delay is applied to the two PF waves in each channel, which is given by

$$\tau_m = m\frac{d}{c_0}\sin\theta_0, \tag{3.4}$$

for $m = 0, 1, 2, \ldots, M-1$. The output of every channel drives a group of PZT transducers depending on different configurations of the UTA, whose spacing and steering angle are given by d and θ_0, respectively. Based on (3.3), since the PF waves are delayed in the same amount in each channel, the amount of delay of the generated DF wave is given by (3.4) too. Therefore, due to the delay-and-sum beamforming theory for the plane wave [JoD93], the wavefront of the DF wave is also steered to θ_0.

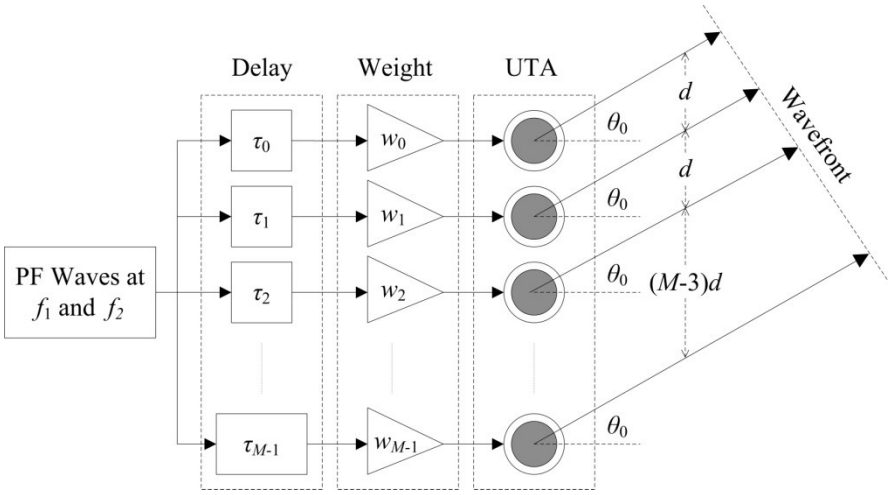

Figure 3.3 Structure of the steerable parametric loudspeaker using two PF waves to generate the DF wave.

If the amount of delay applied to the two PF waves are different and given by

$$\tau_{m1} = m\frac{d}{c_0}\sin\theta_1 \tag{3.5}$$

and

$$\tau_{m2} = m\frac{d}{c_0}\sin\theta_2, \tag{3.6}$$

respectively, the resulted delay amount for the DF wave is given by

$$\tau_{md} = m\frac{d}{c_0}\left(\sin\theta_2 + \omega_1\frac{\sin\theta_2 - \sin\theta_1}{\omega_2 - \omega_1}\right). \tag{3.7}$$

Thus, the wavefront of the DF wave is steered to a direction outside the angular region between θ_1 and θ_2. This result also agrees with the observation made in [DaH90] that the scattered DF wave lies outside the beams of the PF waves.

The analysis of the delay response can be further extended to the parametric loudspeaker using the DSBAM, the USBAM, and the LSBAM. The results are shown in Table 3.1. The amounts of delays applied to the DF wave and the carrier wave are denoted by τ_d and τ_c, respectively. It shows that the delay amount of the DF wave is only related to the envelope function but not to the carrier wave. The structure of the steerable parametric loudspeaker is illustrated in Fig. 3.4 when AM preprocessing methods are included. The audible wave at f_d is fed into the delay-and-sum beamsteering structure. Hence, the preprocessing method is applied to each channel and the modulated carrier waves are transmitted from the UTA. Thus, the wavefront of the generated DF wave, generated from the proposed structure, retains the steering angle of the beamsteering structure.

Table 3.1 Delay responses of the DF wave generated from the parametric loudspeaker using different AM preprocessing methods.

Method	Modulated waves	PF Components	DF wave
DSBAM	$[1+\cos(\omega_d t-\omega_d\tau_d)]\times\cos(\omega_c t-\omega_c\tau_c)$	$\cos(\omega_c t-\omega_c\tau_c)+\frac{1}{2}\left[\begin{array}{l}\cos(\omega_c t+\omega_d t-\omega_c\tau_c-\omega_d\tau_d)\\+\cos(\omega_c t-\omega_d t-\omega_c\tau_c+\omega_d\tau_d)\end{array}\right]$	$\cos(\omega_d t-\omega_d\tau_d)$
SRAM	$\sqrt{1+\cos(\omega_d t-\omega_d\tau_d)}\times\cos(\omega_c t-\omega_c\tau_c)$	$\frac{\sqrt{2}}{2}\left[\begin{array}{l}\cos\left(\omega_c t+\frac{\omega_d}{2}t-\omega_c\tau_c-\frac{\omega_d}{2}\tau_d\right)\\+\cos\left(\omega_c t-\frac{\omega_d}{2}t-\omega_c\tau_c+\frac{\omega_d}{2}\tau_d\right)\end{array}\right]$	$\frac{\sqrt{2}}{2}\cos(\omega_d t-\omega_d\tau_d)$
LSBAM	$[1+\cos(\omega_d t-\omega_d\tau_d)]\times\cos(\omega_c t-\omega_c\tau_c)-\sin(\omega_d t-\omega_d\tau_d)\times\sin(\omega_c t-\omega_c\tau_c)$	$\cos(\omega_c t-\omega_c\tau_c)+\cos(\omega_c t-\omega_d t-\omega_c\tau_c+\omega_d\tau_d)$	$\cos(\omega_d t-\omega_d\tau_d)$
USBAM	$[1+\cos(\omega_d t-\omega_d\tau_d)]\times\cos(\omega_c t-\omega_c\tau_c)+\sin(\omega_d t-\omega_d\tau_d)\times\sin(\omega_c t-\omega_c\tau_c)$	$\cos(\omega_c t+\omega_d t-\omega_c\tau_c-\omega_d\tau_d)+\cos(\omega_c t-\omega_c\tau_c)$	$\cos(\omega_d t-\omega_d\tau_d)$

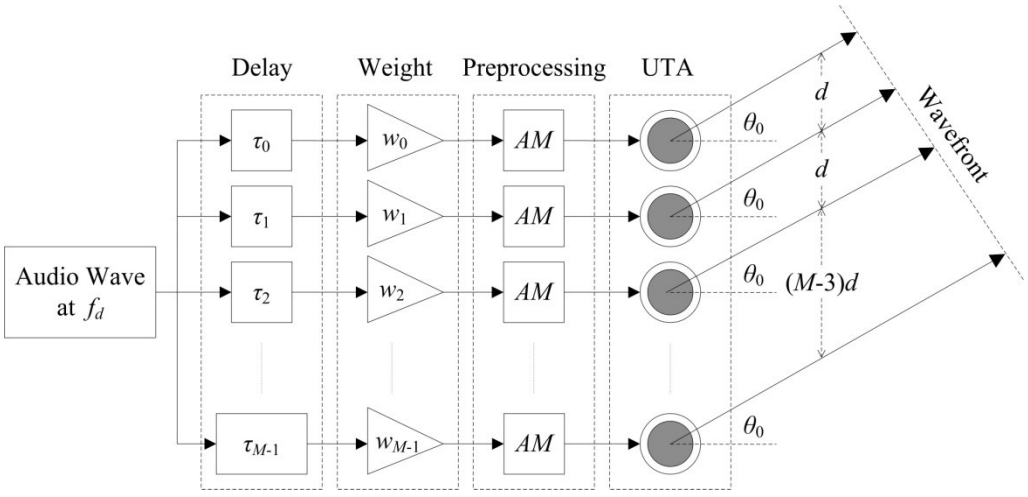

Figure 3.4 Structure of the steerable parametric loudspeaker using AM preprocessing methods to generate the DF wave.

3.3 Simulation Framework for the Steerable Parametric Loudspeaker

The original product directivity principle stated by [DaH90] is only applicable to Gaussian sources. The Gaussian source is an acoustic source with Gaussian amplitude shading, and its directivity function is derived from the KZK equation under the quasilinear approximation [Ham98]. Hence, the Gaussian directivity D_G is given by

$$D_G(\theta) = \exp\left[-\left(\frac{\omega a}{2c_0}\right)^2 \tan^2\theta\right], \tag{3.8}$$

where θ is the angle (in degree) with respect to the axis of the beam; ω is the radiating angular frequency; and a is the effective radius. It is noted from (3.8) that a larger product of the radiating frequency and the effective radius results in a narrower beam. The variation of the Gaussian directivity with the radiating frequency and the effective radius is plotted in Fig. 3.5. Figure 3.5(a) shows that when the radiating frequency increases from 30 kHz to 50 kHz and the effective radius is fixed at 8 mm, the beamwidth of the Gaussian source decreases. Figure 3.5(b) shows another case when the radiating frequency is fixed and the effective radius of the Gaussian source varies from 2 mm, 5 mm to 8 mm. It is observed that the Gaussian directivity gets sharper with higher operating frequency and larger effective radius.

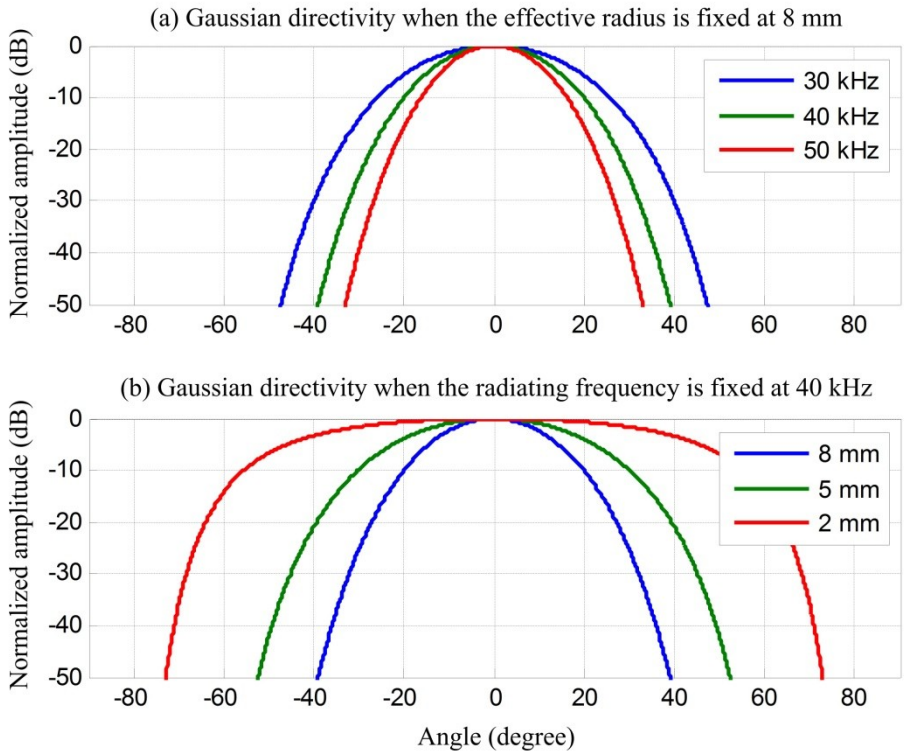

Figure 3.5 Gaussian directivity varying with (a) radiating frequency and (b) effective radius.

The beampattern of the UTA contains one mainlobe, various sidelobes and grating lobes. Thus, it does not fulfill the prerequisite for the product directivity principle that the primary sources are Gaussian beams. However, it is possible to accurately simulate the sound beam of a piston source by the superposition of sufficient Gaussian beams [WeB88, KSS06]. The coefficients are obtained by fitting the Gaussian sources to approximate the piston velocity distribution on the surface of the transducer using a nonlinear least-squares approach. Similarly, since every lobe in the beampattern of the UTA has a bell shape similar to the Gaussian directivity, a transformation is proposed to compute an equivalent Gaussian source array from the beampattern of the UTA. Each Gaussian source in the equivalent

array, having individual effective radius, initial pressure level and angular offset, represents one corresponding lobe in the given beampattern. The beampattern of the UTA is denoted as $H(\omega,\theta)$, and the number of lobes in the visible region is denoted as N_{lobe}. The ith Gaussian source in the equivalent array possesses an effective radius A_i, an initial pressure level B_i, and an angular offset θ_i, for $i = 1,\ 2,\ \ldots,\ N_{lobe}$. Hence, the Euclidean norm of the residual errors over the range of angle θ is given by

$$R(\omega) = \left\| H(\omega,\theta) - \sum_{i=1}^{N_{lobe}} B_i \exp\left[-\left(\frac{\omega A_i}{2c_0} \right)^2 \tan^2(\theta - \theta_i) \right] \right\|_2^2 . \tag{3.9}$$

By minimizing the value of $R(\omega)$, the configuration of the Gaussian source array is solved at each PF wave to result in a beampattern most close to the beampattern of the UTA.

For example, a uniform linear UTA with half wavelength spacing is shown in Fig. 3.6(a). A total of 7 lobes are observed in its beampattern plotted in Fig. 3.7. The configuration of the equivalent Gaussian source array is solved in (3.9) when the PF wave is set at 40 kHz and the Chebyshev weights of 20 dB attenuation are adopted in the UTA. As shown in Fig. 3.6(b) and Fig. 3.7, the Gaussian sources are of different sizes according to the beamwidths of individual lobes, and the axes of the Gaussian sources are located at the peaks of the corresponding lobes. A good matching accuracy is observed between the beampatterns of the UTA and its equivalent Gaussian source array.

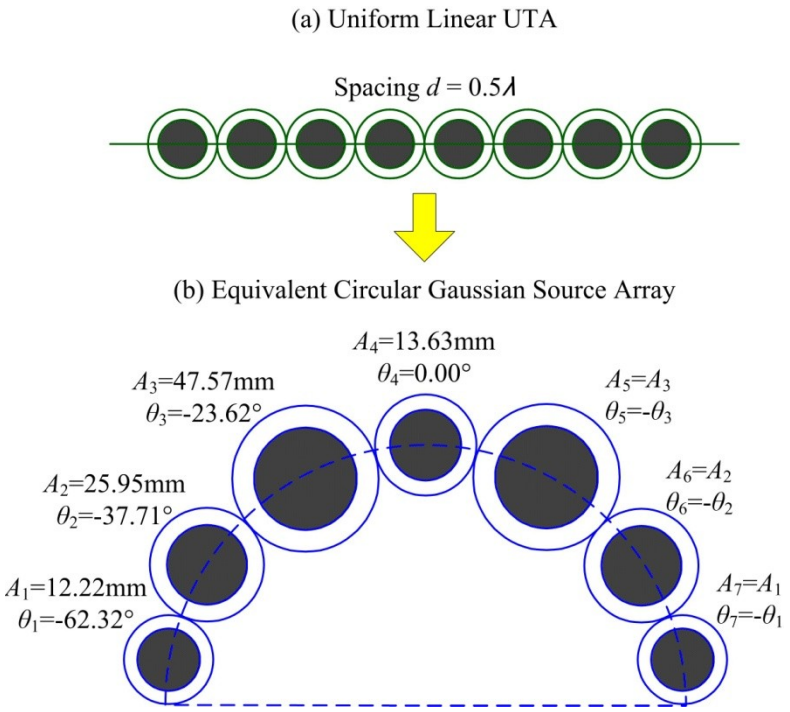

Figure 3.6 (a) A uniform linear UTA ($M = 8$, half wavelength spacing) is transformed into (b) an equivalent circular Gaussian source array ($N_{lobe} = 7$).

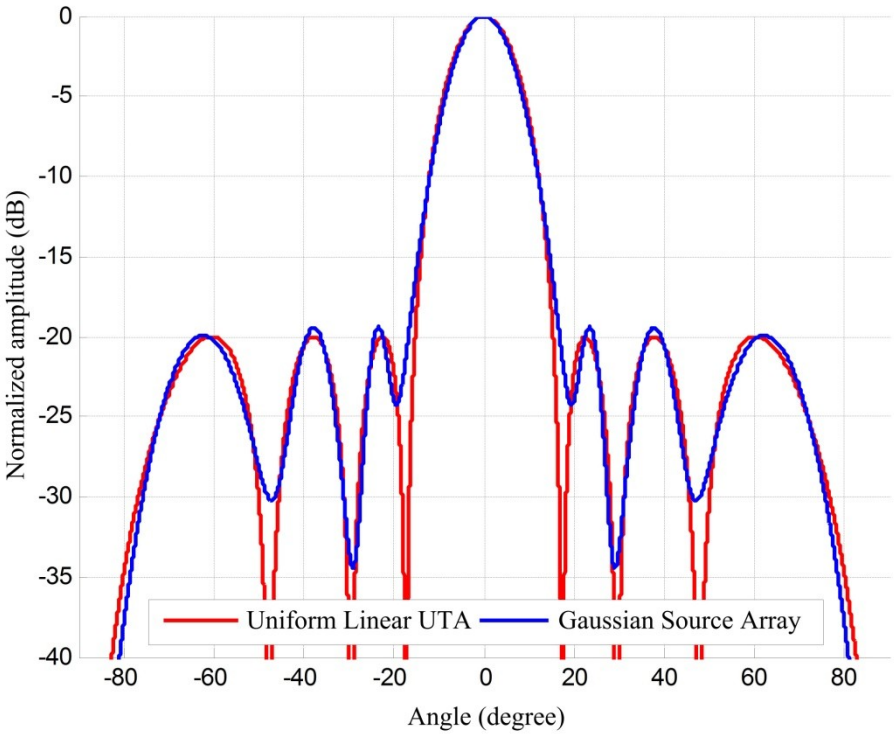

Figure 3.7 Beampatterns of a UTA consisting of 8 channels with Chebyshev weights (20dB attenuation) and its equivalent Gaussian source array.

The equivalent circular Gaussian source array provides a novel observation of the validation of the product directivity principle. The product directivity principle is derived from the Gaussian sources under the quasilinear approximation that is only valid in the vicinity of the propagation axis. Thus, the range of valid angles is limited between ±15° as a result of the constraint imposed by the KZK equation [Ham98]. In particular, if the channels of the UTA are directly assumed Gaussian sources, their propagation axes are parallel. Therefore, the entire range of valid angles of the UTA is limited within an angle of ±15°. But when the UTA is transformed into an equivalent circular Gaussian source array, the propagation axes of Gaussian sources are distributed. Thus, the valid angular range of the circular Gaussian source array is given by the union of the valid ranges of all the Gaussian sources. In this sense, the product directivity principle can always be applied to the parametric loudspeaker.

Hence, the prerequisite of the product directivity principle is fulfilled in the UTA and the validation angle is extended to the entire angular range of the parametric loudspeaker. Moreover, the structure in Fig. 3.3 is suited for theoretical analysis. Using the product directivity principle, the DF beampattern is computed by the product of the PF beampatterns. The PF beampatterns in the UTA are given by

$$H(\omega,\theta)=\left|\sum_{m=0}^{M-1} w_m \exp\left\{ jm\frac{d}{c_0}\omega\left(\sin\theta-\sin\theta_0\right)\right\}\right|, \tag{3.10}$$

where θ is the incidence angle that ranges from -90° to 90° in theory. Thus, the DF beampattern is given by

$$D_{diff}(\theta) = H(\omega_1, \theta) H(\omega_2, \theta). \tag{3.11}$$

3.4 Measurement Setup for the Steerable Parametric Loudspeaker

Measurements are necessary to be carried out to validate the beamsteering theories and algorithms. The setup for the steerable parametric loudspeaker in this thesis is shown in Fig. 3.8. Measurements are conducted in an anechoic chamber with a dimension of 6 m×3 m×3 m. The PF waves are captured by a 1/8 inch microphone (B&K 4138), and the DF waves are measured by a 1/2 inch microphone (B&K 4134). The UTA is mounted on a motorized rotary stage, and the above-mentioned microphones are placed at a location 4 meters away from the UTA. Both the PF and DF beampatterns are measured from -40° to 40° with a resolution of 1°. This angular range is determined by the half-power beamwidth of the PZT transducer (Murata MA40S4S [Mur09]), which is used to assemble all the UTAs in this thesis (shown in Appendix B). In addition, the room temperature is maintained at 20℃ with a relative humidity of 50% in the anechoic chamber, and thus, the sound is estimated to propagate at a speed of 343.21 m/s.

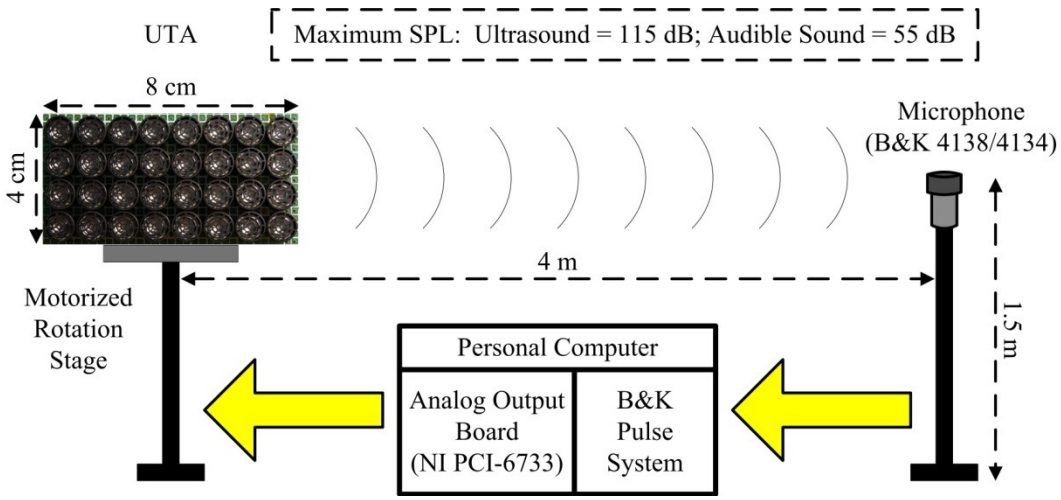

Figure 3.8 Measurement setup for steerable parametric loudspeakers.

An acoustic filter is recommended to be inserted to eliminate the spurious DF signals resulted from the nonlinearity of the receiving system [BeB75, Tod95]. The acoustic filter behaves like a low-pass filter that suppresses the ultrasound significantly, and it also decreases the SPL of the DF wave. In the measurement setup, the UTA is driven directly by the analog output board (NI PCI-6733) without additional amplifiers. Thus, the delays are controlled by the LabVIEW program running on a personal computer. Furthermore, because of the power limitation of the analog output board, the maximum SPL of the DF wave at 4 meter from the UTA is only 55 dB. In the case of far-field measurements, the acoustic filter will not be necessary, as it may cause unwanted drop in the measured SPL of the DF wave.

There are two methods to replace the acoustic filter in the measurement setup. Based on the phase-cancellation and the Gaussian beam expansion technique, Ji *et al.* [JLW12] proposed a method for measuring the performance of preprocessing methods on the axis of the PZT array emitter. Due to the fact that measurements of

the steerable parametric loudspeaker are mostly carried out off-axis and the phase of the PF wave is essential to control the directivity, this method is not suitable for all the cases in this thesis. An alternative technique was reported by Ju and Kim [JuK10]. They suggested taking advantage of the sensitivity characteristics of the condenser microphone, which drops off by almost 20 dB when a 40 kHz wave excites the microphone at an incidence angle of 90° compared to other angles of excitation, as shown in Fig. 3.9. But for the audible range (<10 kHz), the sensitivity does not change more than 4 dB. Hence, the reduced sensitivity in the ultrasonic range is utilized to suppress the ultrasound by placing the microphone perpendicular to the ground, instead of facing the UTA in the measurement setup.

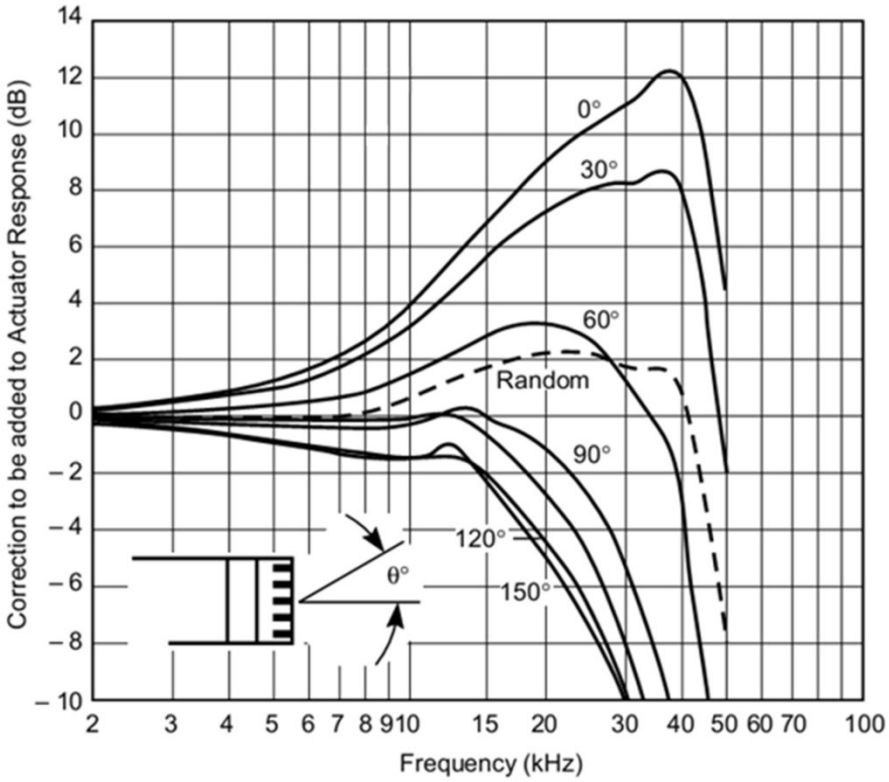

Figure 3.9 Free-field correction curves for the Brüel &Kjær model 4134 condenser microphone (extracted from [BrK12]).

Another concern is the distance between the microphone and the UTA. There are two requirements to be met, if no acoustical filters are placed in front of the microphone in the measurement setup. Firstly, the microphone must be placed in the far-field, due to the basic assumptions of Gaussian sources and beamsteering techniques. Secondly, the microphone must be placed farther than the absorption distance away from the UTA. Bennett and Blackstock [BeB75] measured the DF propagation curves with and without the acoustical filter. When their measuring point was more than a quarter of the absorption distance from the emitter, the amplitudes of the DF wave were almost identical for the filtered and unfiltered cases. In another in-air experiment carried out by Wygant *et al.* [WKW09], the center frequency was set at 51 kHz, and it was found that the DF pressures were at close levels in the filtered and unfiltered measured results when the measured point was more than 3 meter away. Therefore, it is required that the distance between the microphone and the UTA is larger than the absorption distance to prevent the spurious DF signals from affecting the measured results.

In the measurement setup shown in Fig. 3.8, every channel consists of four PZT transducers. Hence, the Rayleigh distance is less than 8 cm when the carrier frequency is 40 kHz (as shown in Fig. A.1). The absorption distance, which is half the reciprocal of the absorption coefficient at 40 kHz, reaches 3.295 meter when the room temperature is 20℃ and the relative humidity is 50% (as shown in Fig. A.2). Hence, when the microphone is placed at 4 meter away, the measuring point is in the far-field of the UTA and farther than the absorption distance away from

the UTA.

3.5 Conclusions

This chapter reviewed different methods of implementing the directivity control for the parametric loudspeaker. The electronic approach to control the sound beam of the parametric loudspeaker opens up a new area of research. It is advantageous over the mechanical approach, in terms of the size of the overall system and the speed of relocating the sound beam. The responses of the DF wave corresponding to different amounts of delays of the PF waves were derived for the parametric loudspeaker. Thus, two structures of the steerable parametric loudspeaker were proposed for two PF waves or one modulated carrier wave, respectively. The validation of the product directivity principle was analyzed and a transformation was proposed for the UTA to find out an equivalent circular Gaussian source array. Based on the equivalent Gaussian source array, the product directivity principle is valid for the whole angular range of the parametric loudspeaker. The measurement setup for the steerable parametric loudspeaker was discussed specifically for the spurious DF signals resultant from the nonlinearity of the receiving system and the microphone's placement to ensure the accuracy of the measured DF wave without an acoustical filter. In the next two chapters, the simulation framework and the measurement setup presented in this chapter will be used to investigate the spatial aliasing problem in the steerable parametric loudspeaker.

Chapter 4
Grating Lobe Elimination in the Steerable Parametric Loudspeaker

Nyquist criterion is a well-known signal processing principle, showing that the sampling frequency must be higher than twice of the cut-off frequency to prevent the occurrence of frequency aliasing. An adaptation of this sampling criterion is applicable to the sensor/transducer array. The spacing between adjacent elements must be less than half the wavelength of the received/transmitted signal to avoid spatial aliasing [JoD93]. In the parametric loudspeaker, the emitter can be built up by an array of PZT transducers, which is grouped into different configurations and driven by several channels (as shown in Fig. B.2). According to the spatial form of the Nyquist criterion, the UTA requires the non-aliasing spacing of 8.5 mm, when consisting of transducers resonating at 40 kHz. The configuration of such narrow non-aliasing spacing is unable to be realized, due to the dimension of the transducers currently available [GYT06]. Therefore, spatial aliasing always occurs in the PF beampatterns, which consists of grating lobes in addition to the main lobe. However, it will be shown in this chapter that grating lobes of the PF waves are not completely inherited by the DF wave through simulation and measurement. This phenomenon, which is known as the grating lobe elimination, occurs under

specific conditions. When the steerable parametric loudspeaker is designed to take advantage of the grating lobe elimination, the non-aliasing spacing of its UTA can be extended to more than what is given by the Nyquist criterion.

Therefore, this chapter is organized as follows. In Section 4.1, the grating lobe elimination in the steerable parametric loudspeaker is analyzed. In Section 4.2, different cases of grating lobe elimination are presented and discussed based on simulation results. Measurement results that verify the grating lobe elimination are presented in Section 4.3. Lastly, Section 4.4 concludes this chapter.

4.1 Derivation of the Grating Lobe Elimination

In order to explore the prerequisites of the grating lobe elimination, the structure of the steerable parametric loudspeaker for two PF waves is used, which is shown in Fig. 3.3. Without loss of generality, the weights are assumed to be symmetric with reference to the center of the UTA. Hence, the DF beampattern based on the product directivity principle is reformulated as

$$D_{diff}\left(\Lambda, F, \Theta\right) = \left|\sum_{m=0}^{M-1} w_m \exp\left(j2\pi m \frac{\Theta}{\Lambda}\right)\right| \cdot \left|\sum_{m=0}^{M-1} w_m \exp\left(j2\pi m \frac{\Theta}{\Lambda} F\right)\right|, \qquad (4.1)$$

where Λ is the ratio of the lower PF wavelength to the spacing of the UTA, given by $\Lambda = \lambda_1 / d$; F is the ratio of the higher PF to the lower PF, given by $F = f_2 / f_1$; and Θ is the normalized angle, given by $\Theta = \sin\theta - \sin\theta_0$.

Therefore, the grating lobes of the PF waves are found at $\Theta_1 = n_1 \Lambda$ for the lower PF wave and $\Theta_2 = n_2 \Lambda / F$ for the higher PF wave, where n_1 and n_2

are the indices. The indices are limited to ensure that their representing grating lobes are in the visible zone, *i.e.* $\left|\Theta_{1,2}+\sin\theta_0\right|<1$. Since the grating lobe elimination of the DF wave is achieved when the grating lobes of the PF waves are far apart, the angular distances between the grating lobes of the PF waves are chosen to quantify the level of the grating lobe elimination. The distance function, which describes the minimum angular distance between grating lobes of the PF waves, is defined as

$$D_K\left(F\right)=\min_{\substack{0\le n_1\le K\\ 0\le n_2\le KF}}\left(\left|n_1\Lambda-\frac{n_2\Lambda}{F}\right|\right), \tag{4.2}$$

where K is the largest index of the grating lobes in the lower PF beampattern. Thus, the largest index of the grating lobes in higher PF beampattern is estimated by KF. Using (4.2), the distance functions for $K=1,\ 2,\ \text{and}\ 3$ are plotted in Fig. 4.1.

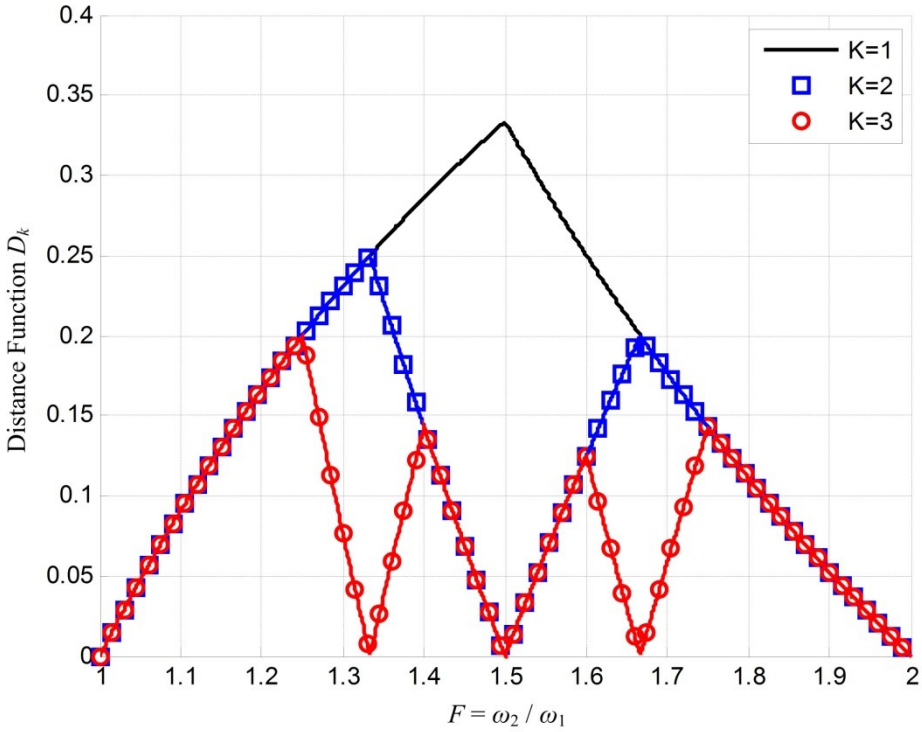

Figure 4.1 Distance functions for $K = 1,\ 2,$ and 3 when $1 < F \le 2$.

Since nulls in the distance function appear when two grating lobes of the PF waves coincide in the same direction, they also imply the occurrence of grating lobes in the DF beampattern due to the product directivity principle. For instance, the second grating lobe of the lower PF wave at 40 kHz coincides with the third grating lobe of the higher PF wave at 60 kHz, and correspondingly, a null appears in the distance function at $F = 1.5$ when $K = 2$. The distance function suggests that the range of F should be constrained between two neighboring nulls to prevent grating lobes of the DF wave. But to ensure the ability of generating low DF wave, the null at $F = 1$ is suggested as the lower bound of the range of F. Based on (4.2), nulls in the distance function are located at $F = n_2/n_1$. Therefore, setting $n_1 = K$ and $n_2 = K+1$ gives the upper bound at $F = 1+1/K$, which

represents the null that is closest to 1. The DF wave is generated from the two PF waves, given by $f_d = f_2 - f_1$. Since $F = f_2 / f_1$, the range of the DF wave is given by $0 < f_d < f_1 / K$. For instance, theoretically, the parametric loudspeaker is able to generate an audible frequency up to 20 kHz (*i.e.* $0 < f_d < 20$ kHz), and the carrier frequency is chosen as 40 kHz (*i.e.* $f_1 = 40$ kHz) because it is a common resonating frequency of commercial ultrasonic transducers. When the USBAM is adopted, the upper sideband can reach as high as 60 kHz (*i.e.* $f_2 = 60$ kHz). Hence, this upper sideband is represented by $F = 1.5$, which is exactly when a null of the distance function occurs for $K = 2$.

The relation between steering angles and numbers of grating lobes in the PF beampatterns is derived from the Nyquist criterion in spatial domain [JoD93]. The range of Λ is approximately given by

$$\Lambda \geq \frac{2 \sin \varphi}{K + 1}, \tag{4.3}$$

where the steering angle ranges between $\pm\varphi$. For example, setting $K = 2$ and $\varphi = 90°$, the non-aliasing spacing of the UTA is less than one and a half of the wavelength of the lower PF wave. In the case when the USBAM is adopted and the carrier frequency is 40 kHz, the non-aliasing spacing of the UTA is 12.75 mm. In another example of K = 2 and φ = 30°, the non-aliasing spacing of the UTA is twice as large as the wavelength of the lower PF wave. Therefore, the non-aliasing spacing is widened to 17 mm when the lower PF wave is at 40 kHz.

As discussed above, the grating lobes of the DF wave appear when there are nulls in the distance function. In addition, grating lobes are suppressed within the

vicinity of nulls in the distance function due to the product directivity principle. Thus, intersection function is proposed to describe the elimination of grating lobes of the DF wave when the distance between the grating lobes of the PF waves is given by the distance function. Intersection function is defined as

$$I_K(F) = \max_{\Theta} \left\{ \left| \sum_{m=0}^{M-1} w_m \exp\left(j\pi m \frac{\Theta}{\Lambda} \right) \right| \cdot \left| \sum_{m=0}^{M-1} w_m \exp\left[j\pi m \frac{F}{\Lambda} \left(\Theta - D_K(F) \right) \right] \right| \right\}. \tag{4.4}$$

One important property of the intersection function is that its values do not change with the value of Λ. This property can be proven as follows. Assume that the Λ is replaced by $\bar{\Lambda} = \mu\Lambda$. Thus, (4.4) is manipulated as

$$I_K(F) = \max_{\Theta} \left\{ \left| \sum_{m=0}^{M-1} w_m \exp\left(j\pi m \frac{\Theta}{\mu\bar{\Lambda}} \right) \right| \cdot \left| \sum_{m=0}^{M-1} w_m \exp\left\{ j\pi m \frac{F}{\mu\bar{\Lambda}} \left(\Theta - D_{K|\Lambda}(F) \right) \right\} \right| \right\}. \tag{4.5}$$

It is noted that the distance function for Λ is also μ times of the distance function for $\bar{\Lambda}$, *i.e.*

$$D_{K|\Lambda}(F) = \min_{\substack{0 \le n_1 \le K \\ 0 \le n_2 \le KF}} \left(\left| n_1 \mu\bar{\Lambda} - \frac{n_2 \mu\bar{\Lambda}}{F} \right| \right) = \mu D_{K|\bar{\Lambda}}(F). \tag{4.6}$$

Substitute (4.6) into (4.5) and define $\bar{\Theta} = \Theta / \mu$, so that the intersection function becomes

$$I_K(F) = \max_{\Theta} \left\{ \left| \sum_{m=0}^{M-1} w_m \exp\left(j\pi m \frac{\bar{\Theta}}{\bar{\Lambda}} \right) \right| \cdot \left| \sum_{m=0}^{M-1} w_m \exp\left\{ j\pi m \frac{F}{\bar{\Lambda}} \left(\bar{\Theta} - D_{K|\bar{\Lambda}}(F) \right) \right\} \right| \right\}. \tag{4.7}$$

Since (4.5) and (4.7) are identical, it is proven that the change of Λ has no influence on the intersection function.

4.2 Simulation Results

Using the structure of the steerable parametric loudspeaker, which is shown in Fig. 3.1, simulations are carried out for the UTA with 8 channels. The spacing is chosen as twice the wavelength of the lower PF wave at 40 kHz (*i.e.* $\Lambda = 1/2$). The higher PF waves are set to 60 kHz (*i.e.* $F = 1.5$), 50 kHz (*i.e.* $F = 1.25$), and 44 kHz (*i.e.* $F = 1.1$). Equal weights are adopted (*i.e.* $w_i = 1$ for $i = 0, 1, 2, \ldots, 7$) and the steering angle θ_0 is chosen as 15°. The simulation results are plotted in Figs. 4.2(a)-(c) for the three cases of higher PF waves. Grating lobes in the figures are indexed from right to left as $1, 2, 3, \ldots$, while the mainlobe is labeled as 0.

In Fig. 4.2(a), the second grating lobe in the lower PF beampattern coincides with the third grating lobe in the higher PF beampattern. Thus, spatial aliasing of the DF wave at 20 kHz occurs at -47.8° (labeled as "1"). In Fig. 4.2(b), grating lobes in the lower PF beampattern coincide with sidelobes in the higher PF beampattern, which result in a few sidelobes of the DF wave at 10 kHz. It is also noted that the sidelobes of the DF wave are lower than the highest sidelobe in the PF beampatterns, due to the occurrence of the grating lobe elimination. In Fig. 4.2(c), the first grating lobe in the lower PF beampattern appears in the direction close to the first grating lobe in the higher PF beampattern. The two grating lobes are spaced closely and result in a sidelobe of the DF wave at 4 kHz, which is lower than the mainlobe but higher than the highest sidelobe in the PF beampatterns. This third case is known as partial grating lobe elimination.

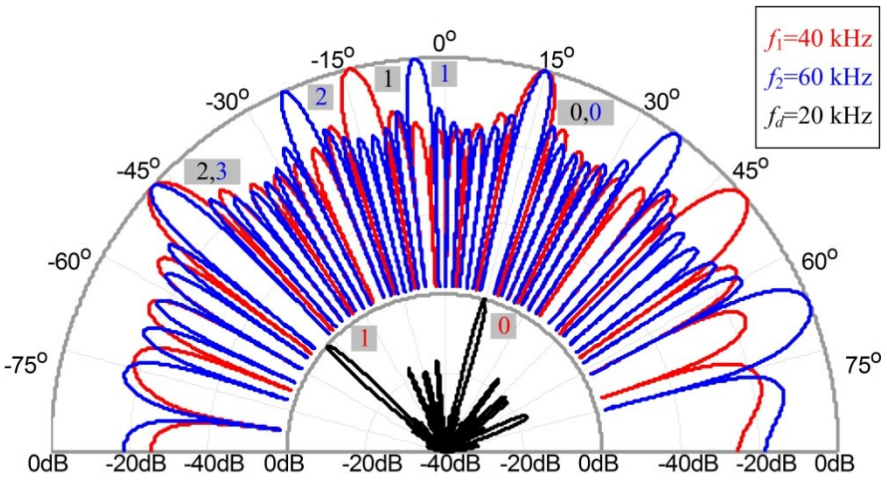

(a) Spatial Aliasing (Λ=0.5;F=1.5)

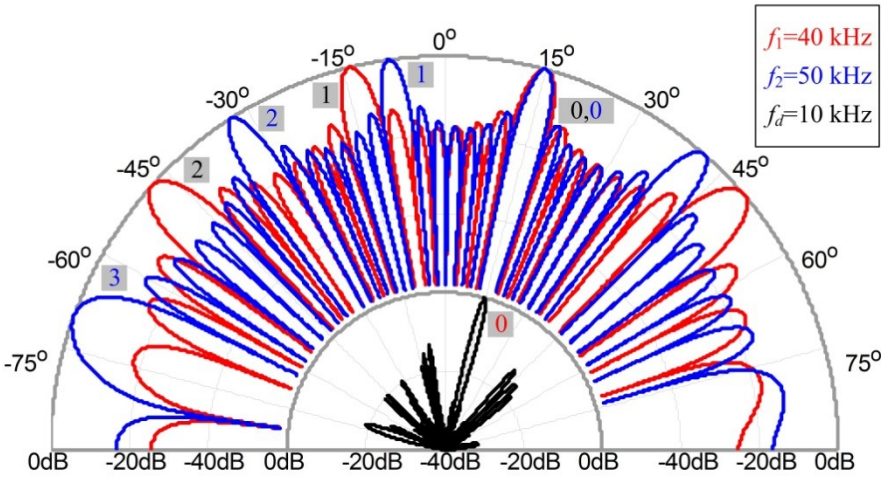

(b) Grating Lobe Elimination (Λ=0.5;F=1.25)

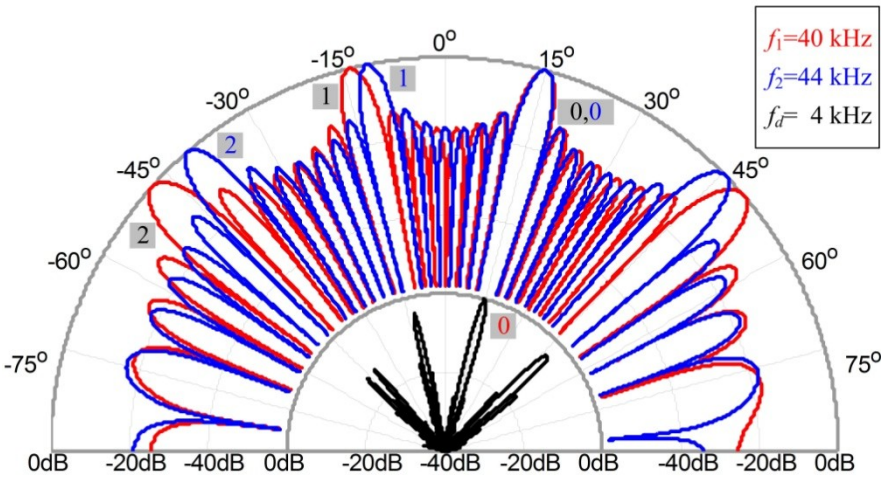

(c) Partial Grating Lobe Elimination (Λ=0.5;F=1.1)

Figure 4.2 When the UTA consists of 8 channels with spacing twice as large as the wavelength, three cases, (a) spatial aliasing, (b) grating lobe elimination, and (c) partial grating lobe elimination, are plotted.

In another scenario, the UTA consists of 8 channels, and the spacing is set to one and a half times the wavelength of the lower PF wave (*i.e.* $\Lambda = 2/3$). The lower PF wave is fixed at 40 kHz. The higher PF waves are set to 60 kHz (*i.e.* $F = 1.5$), 50 kHz (*i.e.* $F = 1.25$), and 44 kHz (*i.e.* $F = 1.1$). Equal weights are still adopted, but the steering angle θ_0 is turned to 35°. The simulation results are shown in Figs. 4.3(a)-(c), corresponding to the cases of spatial aliasing, grating lobe elimination, and partial grating lobe elimination, respectively.

When the spacing of the UTA is changed from two times (in Fig. 4.2) to one and a half times (in Fig. 4.3) the wavelength of the lower PF wave, the number of grating lobes in the PF beampattern is reduced due to the reduced spatial sampling rate. However, according to (4.3), because the steering angle is changed from 15° to 35°, the largest index of grating lobes of the lower PF wave is kept as $K = 2$. In Fig. 4.3(a), the second grating lobe in the lower PF beampattern coincides with the third grating lobe in the higher PF beampattern. Thus, spatial aliasing of the DF wave at 20 kHz occurs at -49.5° (labeled as "1"). In Fig. 4.3(b), the grating lobe elimination occurs. The grating lobes in the lower PF beampattern coincide with sidelobes in the higher PF beampattern, which only result in a few sidelobes of the DF wave at 10 kHz. Fig. 4.3(c) shows another case of partial grating lobe elimination. The first grating lobes in the beampatterns of the lower and higher PF waves appear in close directions. Those two grating lobes result in a sidelobe of the DF wave at 4 kHz, of which the normalized amplitude is -4.3 dB.

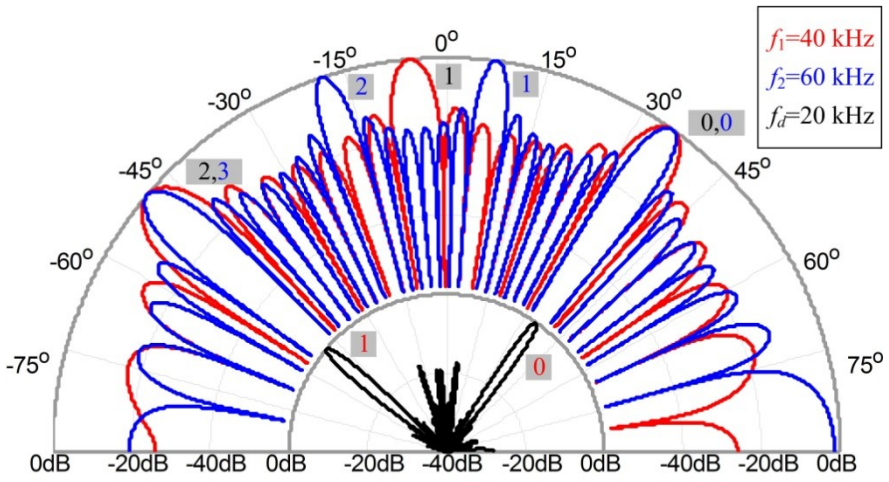

(a) Spatial Aliasing (Λ=0.667;F=1.5)

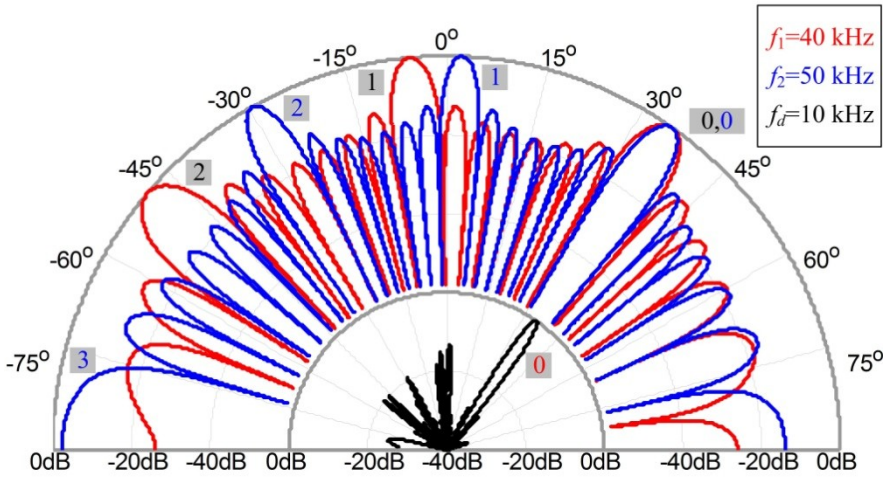

(b) Grating Lobe Elimination (Λ=0.667;F=1.25)

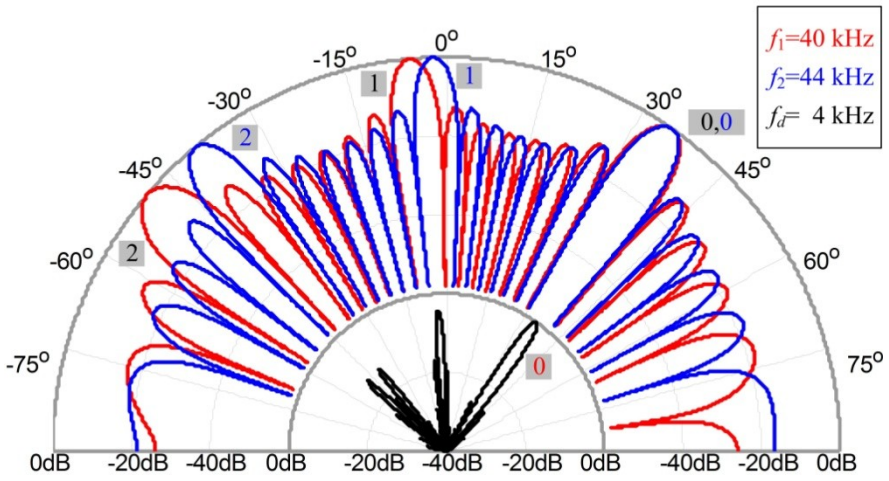

(c) Partial Grating Lobe Elimination (Λ=0.667;F=1.1)

Figure 4.3 When the UTA consists of 8 channels with spacing one and a half times as large as the wavelength, three cases, (a) spatial aliasing, (b) grating lobe elimination, and (c) partial grating lobe elimination, are plotted.

The intersection functions corresponding to Fig. 4.2 and Fig. 4.3 are plotted in Fig. 4.4(a) and Fig. 4.4(b), respectively. Besides the case of equal weights, the intersection functions for the cases of Chebyshev weights of 10 dB, 20 dB, and 30 dB attenuations are included. The horizontal color bars, located at the base of the plots, illustrate the ranges of grating lobe elimination. The yellow bars indicate the ranges of partial grating lobe elimination that lead to sidelobes lower than -6 dB, while the grey bars show the ranges of partial grating lobe elimination that lead to sidelobes higher than -6 dB or even spatial aliasing. In particular, for the case of Chebyshev weights of 30 dB attenuation, because of its wide beamwidth and high attenuation, full grating lobe elimination is not achieved in this simulation.

Furthermore, as Fig. 4.4(a) and Fig. 4.4(b) are identical, it confirms that the range of grating lobe elimination is independent of Λ. However, narrower spacing leads to higher spatial sampling rate and less occurrences of grating lobes. When $\Lambda = 1/2$, there are three grating lobes for the 40 kHz wave (as shown in Fig. 4.2, note that there is one grating lobe on the left side of the mainlobe without a label). When $\Lambda = 2/3$, the number of grating lobes reduces to two (as shown in Fig. 4.3). Hence, the parameter Λ affects the largest index of grating lobes in the lower PF beampattern, and also influences the occurrence of the grating lobe elimination in an implicit way.

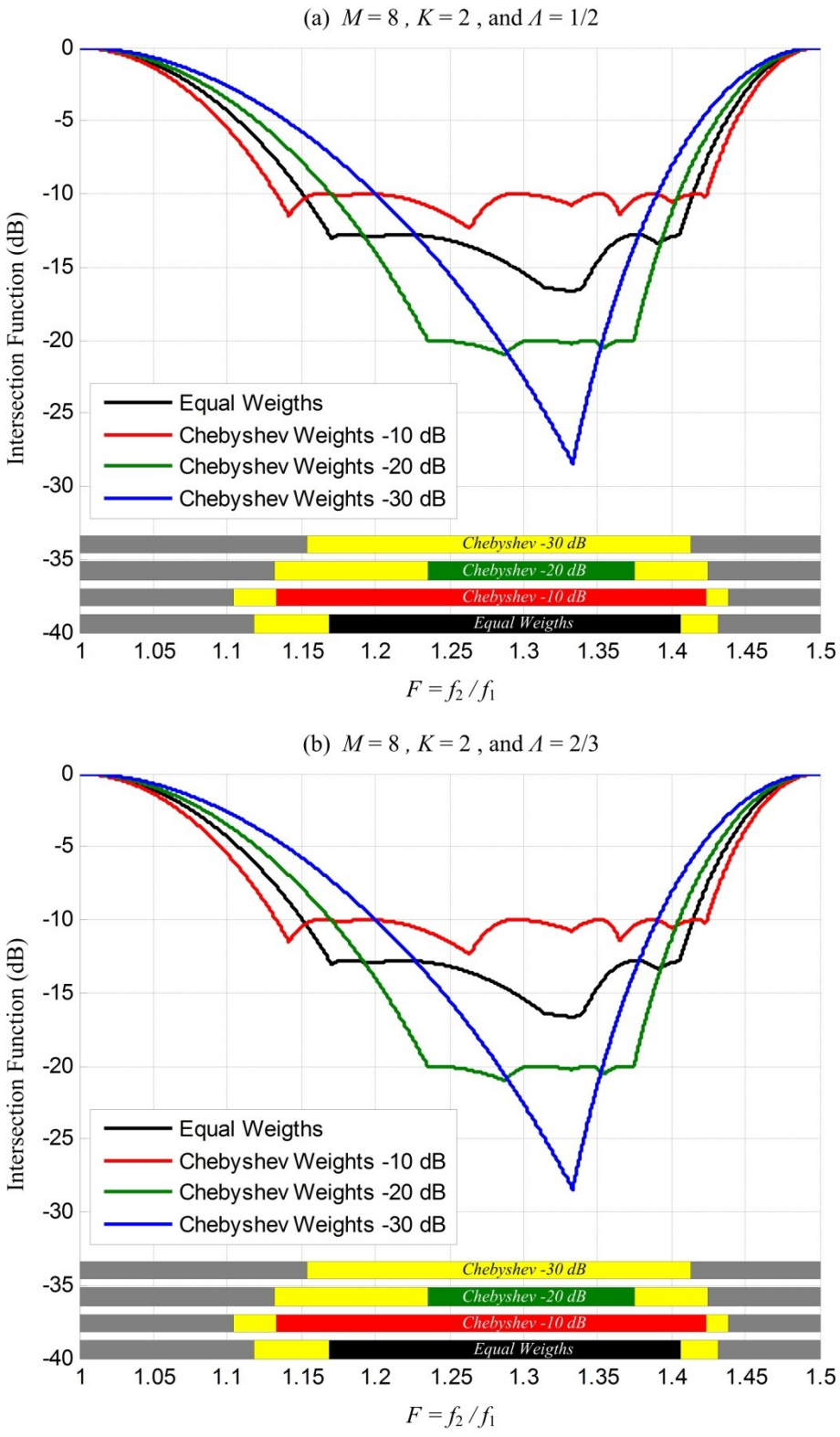

Figure 4.4 Intersection function for $K = 2$ when equal weights and Chebyshev weights with 10 dB, 20 dB, 30 dB attenuations are adopted in the UTAs consisting of $M = 8$ channels with spacing of (a) $\Lambda = 1/2$ and (b) $\Lambda = 2/3$.

In Fig. 4.5(a), K is set to 1 to investigate the intersection function with lesser grating lobes in the PF beampattern. Within the range of $1 < F \leq 1.5$, the lower bounds of grating lobe elimination are obtained. However, the upper bound is close to the null in the distance function, which is located at $F = 2$ as shown in Fig. 4.1. Since the simulation is only carried out between $1 < F \leq 1.5$, the upper bounds of grating lobe elimination are thus given by $F = 1.5$.

In Fig. 4.5(b), the number of channels is doubled to 16. Comparison between Fig. 4.4 and Fig. 4.5(b) suggests that using more channels in the UTA widens the range of grating lobe elimination. Narrower mainlobe of the DF wave is another benefit from the increased number of channels, which results in a higher spatial resolution, but leads to more computational complexity and the usage of more digital-to-analog convertors.

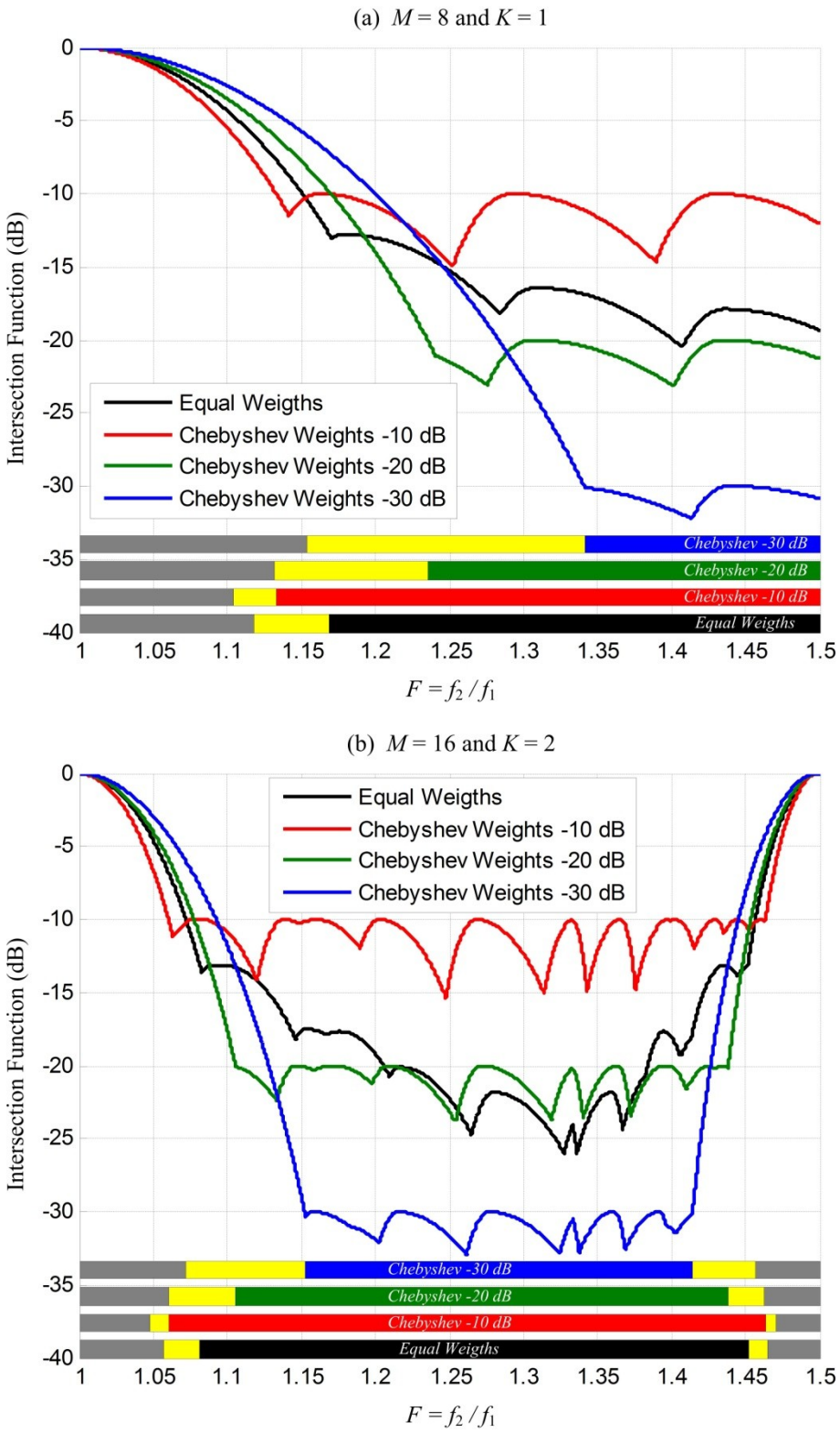

Figure 4.5 Intersection function for (a) $K = 1$ and (b) $K = 2$ when equal weights and Chebyshev weights with 10 dB, 20 dB, 30 dB attenuations are adopted in the respective UTAs consisting of (a) $M = 8$ and (b) $M = 16$ channels.

The comparison among the four groups of weights shows that the case of Chebyshev weights of 30 dB attenuation results in the narrowest range of grating lobe elimination, due to its widest beamwidth and highest attenuation. In contrast, the case of Chebyshev weights of 10 dB attenuation has the widest range of grating lobe elimination. The cases of equal weights and Chebyshev weights of 20 dB achieve the ranges of grating lobe elimination that lie in between. When the range of grating lobe elimination is known, higher carrier frequency leads to wider reproducible range of the DF wave. However, the higher carrier frequency increases both the lower and upper bounds of the reproduced DF wave. Thus, it is still recommended to build the UTA in the steerable parametric loudspeaker with an increased number of channels. With more channels, the steerable parametric loudspeaker achieves a wider range of grating lobe elimination that corresponds to a wider reproducible range of the DF wave.

4.3 Measurement Results

The above simulation results reveal that the Nyquist criterion is no longer applicable to the DF wave generated by the steerable parametric loudspeaker. In order to verify the simulation results, measurements are carried out using the column configuration with spacing of 1 cm and the block configuration with spacing of 2 cm. The measurement setup has been introduced in Section 3.4, and more details are provided in Appendixes B, C, and D. In this chapter, the steering angle is set to -20°. The PF waves are chosen so that three resultant DF waves are

produced at 8 kHz, 4 kHz and 1 kHz. Measurement results of the PF waves are compared with simulation results reported in the previous sections. But for the DF waves, there are two approaches in deriving their beampatterns: (i) using the product of the simulated PF beampatterns and the measured channel directivities (shown in Fig. 4.6); and (ii) using the product of measured PF beampatterns. For comparison, these two approaches are respectively referred as the product of the simulated PF directivities (PSD method) and the product of the measured PF directivities (PMD method) in this and the following chapters.

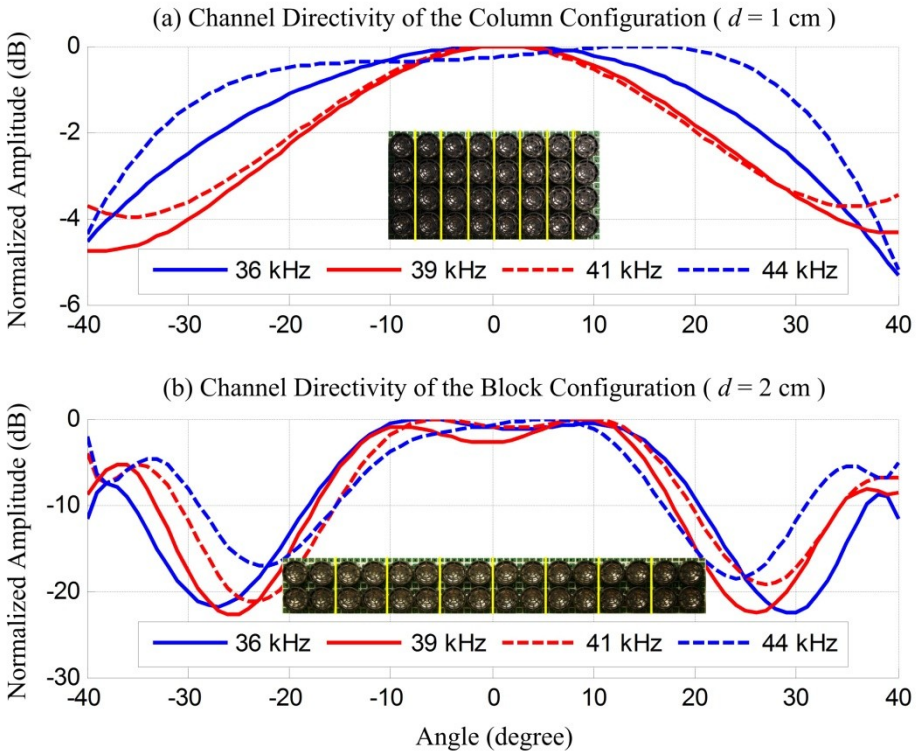

Figure 4.6 Channel directivities of (a) the column configuration with spacing of 1 cm and (b) the block configuration with spacing of 2 cm.

4.3.1 Column configuration

Measurement results, as well as the corresponding simulation results using the column configuration, are shown in Fig. 4.7. Mainlobes are marked as "M" in the PF and DF beampatterns. Grating lobes of the PF wave and the eliminated grating lobes of the DF wave are marked as "G". Figs. 4.7(a)-(b) show a case of grating lobe elimination. The PF waves are set at 36.5 kHz and 44.5 kHz, and the DF wave is formed at 8 kHz. The grating lobes are located at 35° and 24° in the beampatterns of 36.5 kHz and 44.5 kHz, respectively. In the higher PF beampattern, the grating lobe is closer to the mainlobe compared to that in the lower PF beampattern. Due to sufficient angular distance between the grating lobes, grating lobe elimination occurs in the DF wave. The highest sidelobe of the DF wave is an eliminated grating lobe, which is located at 25°. It is also observed that the PSD method provides a high matching accuracy in the vicinity of the eliminated grating lobe, while the PMD method achieves certain overall matching accuracy between the simulated and measured DF beampatterns.

A case of partial grating lobe elimination is shown in Figs. 4.7(c)-(d). The PF waves are set at 38.5 kHz and 42.5 kHz, and the DF wave is generated at 4 kHz. The grating lobes are located at 31° and 26° in the beampatterns of 38.5 kHz and 42.5 kHz, respectively. The two grating lobes are not far apart from each other. Thus, the partially eliminated grating lobe is located at 29° in the DF beampattern. The simulated beampatterns using the PSD and PMD methods generates two similar results for both mainlobe and partially eliminated grating lobe.

The last set of results shows a case of spatial aliasing, as illustrated in Figs. 4.7(e)-(f). The PF waves are set at 39.5 kHz and 40.5 kHz, and thus, the DF wave is resulted at 1 kHz. Both the grating lobes are located at 30° in the beampatterns of 39.5 kHz and 40.5 kHz, respectively. Hence, the two grating lobes result in spatial aliasing. The grating lobe of the DF wave is slightly lower than the mainlobe due to the channel directivity of the UTA. The PSD and PMD methods achieve high matching accuracies between the simulated and measured DF beampatterns in the vicinity of mainlobe and grating lobe. However, outside that vicinity, the PMD method provides a relatively high matching accuracy when compared to the PSD method.

In the above measurement results, when the DF increases, the grating lobes of the two PF waves become further apart in angular distance and full or partial grating lobe elimination occur. However, when the DF decreases, spatial aliasing emerges as a problem. Table 4.1 highlights the locations and suppressions of grating lobes of the DF waves in the column configuration. It shows that the grating lobe (labeled as "G") is reduced by 10.05 dB at the DF of 8 kHz, and by 8.32 dB at the DF of 4 kHz. The measurement results also verify that the product directivity principle is adequate to predict the directivity of the DF wave in the steerable parametric loudspeaker.

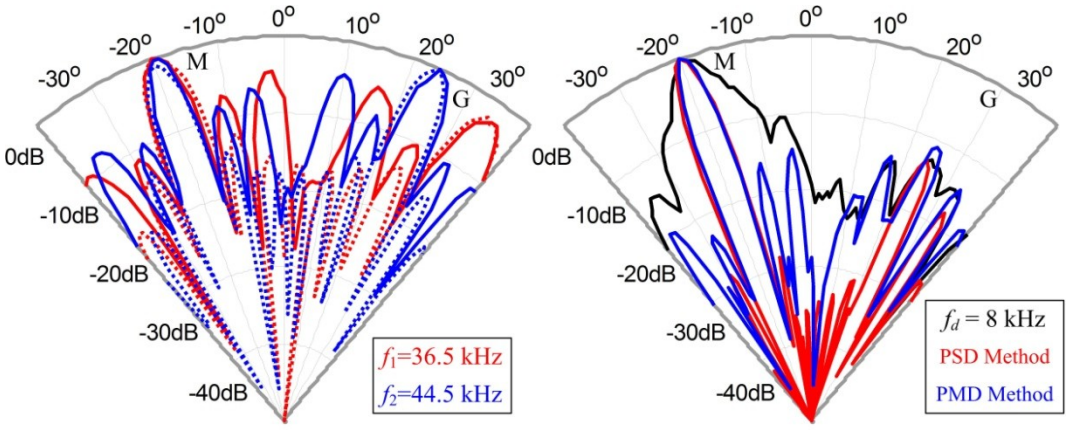

(a) Grating Lobe Elimination (PF Waves)

(b) Grating Lobe Elimination (DF Wave)

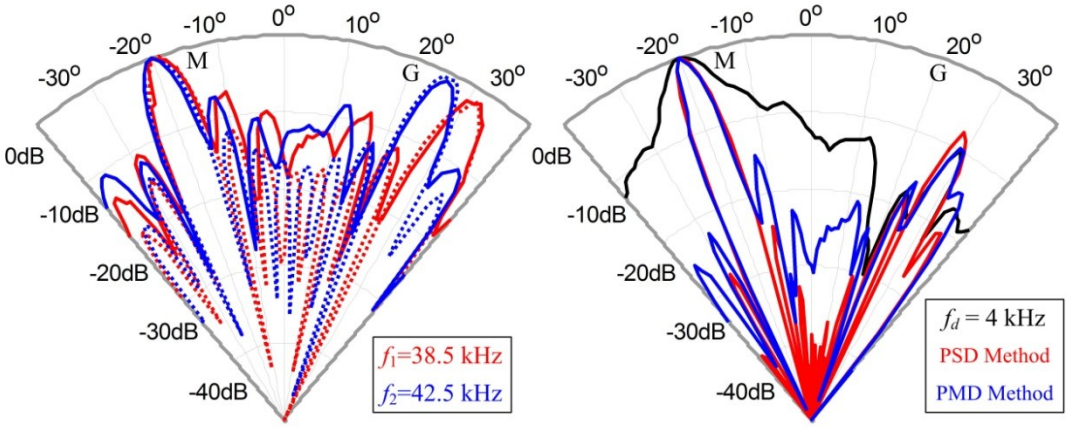

(c) Partial Grating Lobe Elimination (PF Waves)

(d) Partial Grating Lobe Elimination (DF Wave)

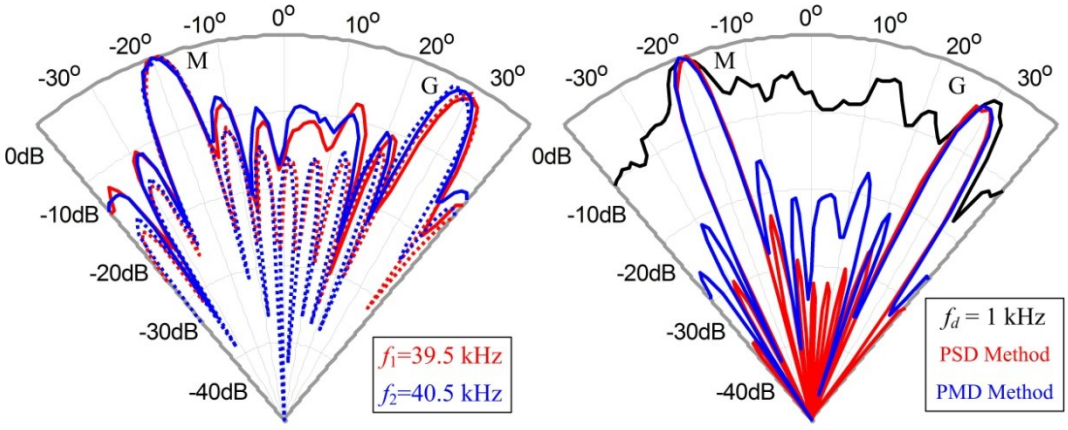

(e) Spatial Aliasing (PF Waves)

(f) Spatial Aliasing (DF Wave)

Figure 4.7 Measurement and simulation results using the column configuration. In the subplots, (a)-(b) show grating lobe elimination; (c)-(d) show partial grating lobe elimination; (e)-(f) show spatial aliasing; for the PF waves, the solid and dash lines represent the measurement and simulation results, respectively.

Table 4.1 Distribution of grating lobes of the DF waves generated using the column configuration with spacing of 1 cm (extracted from Fig. 4.7).

	Location of "G"	Suppression of "G"
8 kHz-MP	25°	10.05 dB
8 kHz-PSD	24°	10.37 dB
8 kHz-PMD	25°	8.13 dB
4 kHz-MP	29°	8.32 dB
4 kHz-PSD	28°	6.12 dB
4 kHz-PMD	29°	7.92 dB
1 kHz-MP	31°	0.35 dB
1 kHz-PSD	30°	2.07 dB
1 kHz-PMD	30°	1.62 dB

4.3.2 Block configuration

The channel directivity of the block configuration is plotted in Fig. 4.6(b). It is noted that there are two sidelobes and two dips located around ±25°. Due to the sharper directivity of the block configuration, the steering angle is suggested to be selected within ±15°. Beyond this range, the mainlobe of the PF wave is largely suppressed by the channel directivity. The measurement results, as well as the corresponding simulation results, are shown in Fig. 4.8.

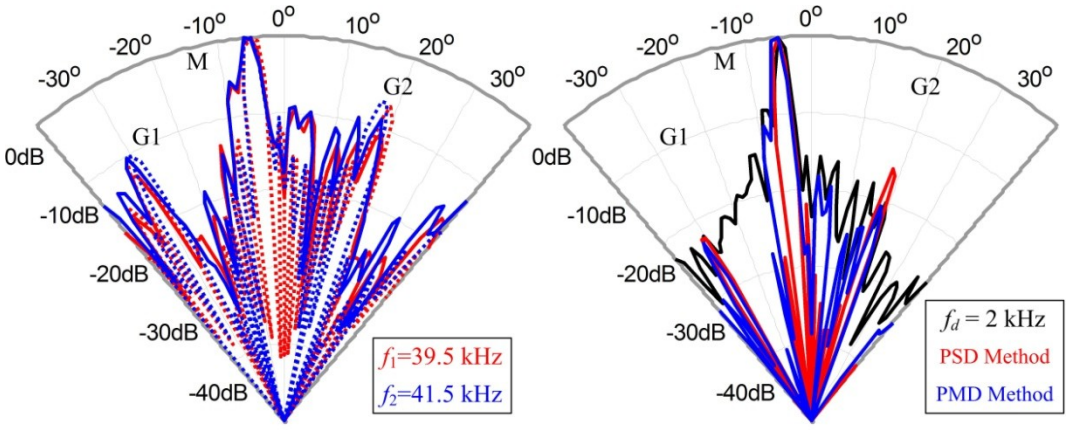

(a) Grating Lobe Elimination (PF Waves)

(b) Grating Lobe Elimination (DF Wave)

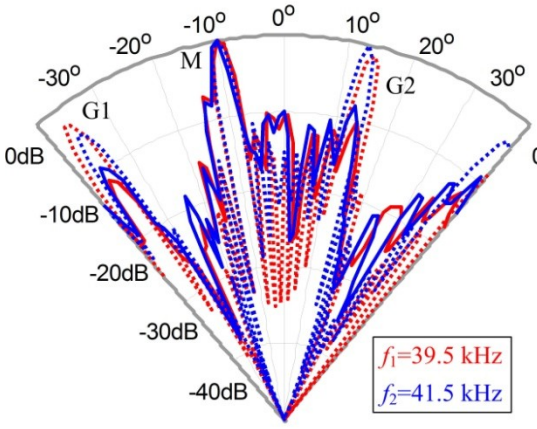

(c) Partial Grating Lobe Elimination (PF Waves)

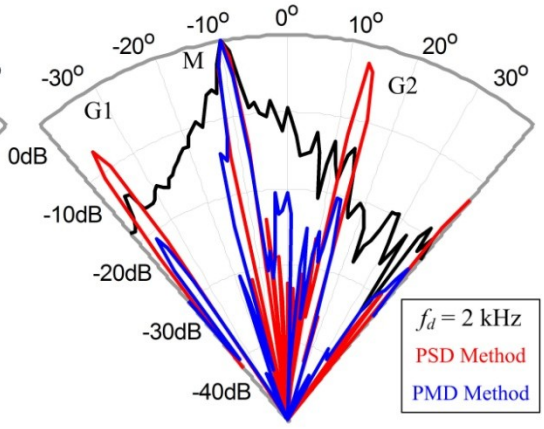

(d) Partial Grating Lobe Elimination (DF Wave)

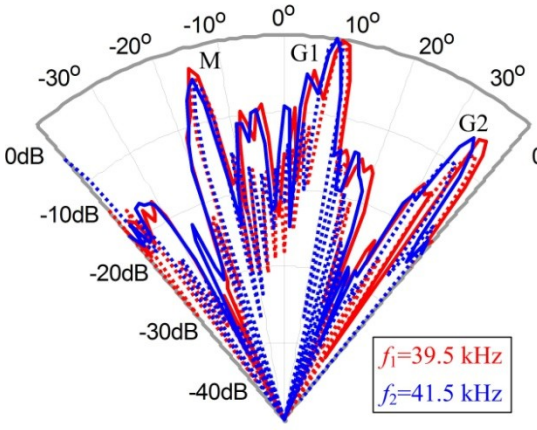

(e) Spatial Aliasing (PF Waves)

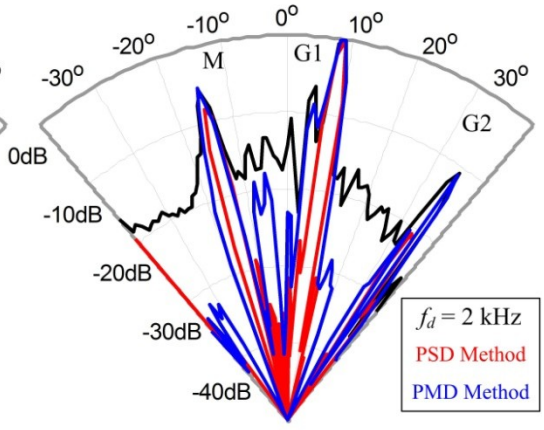

(f) Spatial Aliasing (DF Wave)

Figure 4.8 Measurement and simulation results using the block configuration. In the subplots, (a)-(b) show grating lobe elimination; (c)-(d) show partial grating lobe elimination; (e)-(f) show spatial aliasing; for the PF waves, the solid and dash lines represent the measurement and simulation results, respectively.

Similar to the previous notations, the mainlobes of the PF wave and DF wave are marked as "M". Grating lobes of the PF wave and the eliminated grating lobes of the DF wave are labeled as "G1" and "G2". When the mainlobes are steered to -5°, grating lobe elimination is observed in Figs. 4.8(a)-(b). Grating lobes are located at -32° and 19° in the beampattern of 39.5 kHz, and located at -31° and 18° in the beampatterns of 41.5 kHz. These grating lobes are not sufficiently separated in angular location, but still result in grating lobe elimination due to the troughs in the channel directivity of the block configuration. The PSD and PMD methods provide considerable matching accuracies between the simulated and measured DF beampatterns in the vicinity of the mainlobe as well as the grating lobe.

When the steering angle of the PF waves are increased to -10° (shown in Figs. 4.8(c)-(d)), the grating lobes are observed at 14° and 13° in the beampatterns of 39.5 kHz and 41.5 kHz, respectively. Meanwhile, the other grating lobes are located at -36° in the beampattern of both 39.5 kHz and 40.5 kHz. The angular distance between the two grating lobes of the PF waves remain small. Thus, partial grating lobe elimination occurs because of the channel directivity of the block configuration also. In Fig. 4.8(d), the PMD method provides relatively high matching accuracy between the simulated and measured DF beampatterns in the vicinity of the eliminated grating lobe when compared to the PSD method.

Increasing the steering angle of the PF waves to -15° leads to a significant decrement of the angular distance between the grating lobes, shown in Figs. 4.8(e)-(f). In this case, the grating lobes coincide with each other at 9° in the

beampatterns of 39.5 kHz and 41.5 kHz (labeled as "G1") and result in spatial aliasing. This grating lobe of the DF wave is shown to be higher than the mainlobe. In the same group of measurements, partial grating lobe elimination is also observed for the DF wave at 35°, which is a true elimination that is caused by the angular distance between two grating lobes of the PF waves.

The locations and amplitudes of grating lobes in the block configurations are listed in Table 4.2. The grating lobes are reduced by 11.99 dB ("G1") and 9.41 dB ("G2") by at the DF of 2 kHz. For the case of partial grating lobe elimination, the grating lobe are reduced by 2.69 dB ("G1") and 3.45 dB ("G2") at the DF of 2 kHz. Simulations show fair accuracy in predicting the grating lobe elimination.

Table 4.2 Distribution of grating lobes of the DF waves generated using the block configuration with spacing of 2 cm (extracted from Fig. 4.8).

	Location of "G1"	Suppression of "G1"	Location of "G2"	Suppression of "G2"
-5°-MP	-30°	11.99 dB	19°	9.41 dB
-5°-PSD	-31°	9.73 dB	18°	8.58 dB
-5°-PMD	-31°	10.23 dB	18°	9.98 dB
-10°-MP	-36°	2.69 dB	14°	3.45 dB
-10°-PSD	-36°	2.69 dB	13°	1.32 dB
-10°-PMD	-36°	16.55 dB	13°	10.27 dB
-20°-MP	9°	0 dB	35°	4.98 dB
-20°-PSD	9°	0 dB	34°	10.93 dB
-20°-PMD	9°	0 dB	35°	5.31 dB

However, the grating lobe elimination in the block configuration is observed to be more sensitive to the steering angle and forms two grating lobes in the visible range. In contrast, when the UTA with column configuration is steered to -20°, only one grating lobe is observed in the visible region. It is concluded that the column configuration has a better beamsteering capability and wider range of grating lobe elimination due to the narrower spacing. When the steering angle is small, the block configuration can be designed such that the grating lobes coincide with the troughs in its channel directivity. In this case, the steerable parametric

loudspeaker using block configuration achieves much narrower beam, but with limited range of steering angles.

It is shown in both Fig. 4.7 and Fig. 4.8 that the product directivity principle can predict the major lobes of the DF wave, including the mainlobe, grating lobes and other relatively higher sidelobes. Although majority of the sidelobes are observed in the simulated DF beampatterns, they are not distinguishable in the measurement results. It may be because of the relatively low amplitude of the sidelobes compared to the inherent noise level of the measurement system.

4.4 Conclusions

In this chapter, the spatial aliasing was studied for the steerable parametric loudspeaker. A unique property was observed in both simulation and measurement results. The occurrence of grating lobe elimination depends on the configuration of the UTA and the DF range. An important finding of this chapter shows that the non-aliasing spacing of the UTA in the parametric loudspeaker is extended to more than $K+1$ times of half the wavelength of lower PF wave, where K (usually $K = 2$) is the largest index of grating lobes in the visible region. When the steering angle is in a limited angular range, the non-aliasing spacing is further extended. Taking advantage of the relaxed non-aliasing spacing, the grating lobe elimination allows the steerable parametric loudspeaker to generate a much sharper mainlobe without increasing the number of channels. Two configurations of the UTA were compared. Measurement results showed that the column

configuration allowed the steerable parametric loudspeaker to have better beamsteering capability, but the block configuration led to a sharper mainlobe with restrained steerable range. The grating lobe elimination of the DF wave was shown to be effective in the measurement results for both configurations. In the next chapter, the grating lobe elimination is also observed and analyzed when dual beams are generated from a single steerable parametric loudspeaker.

Chapter 5
Generating Dual Beams from a Single Steerable Parametric Loudspeaker

In the previous chapter, the classic delay-and-sum beamforming has been found to be feasible to electronically steer the sound beam in the parametric loudspeaker. In this chapter, the feature of generating dual beams is integrated into the steerable parametric loudspeaker. The dual beam generation can provide flexibility to a few emerging applications of the parametric loudspeaker, such as a hearing-aid audio system that can create an enhanced hearing spot for the hearing-impaired listener while not affecting other listeners with normal hearing who are sitting near him [TSG12]. Presently, this audio system only allows one fixed enhanced hearing spot in each installation, which limits the listener who may want to move around. Moreover, when there is more than one hearing-impaired listener, more hearing spots are needed so that everyone can be benefit from the enhanced sound quality. To address this problem, a symmetric beamsteering structure is proposed to create an optional second beam using the same hardware and configuration as the previously proposed single-beam parametric loudspeaker. By tuning an adjustable center frequency, the dual beams can deliver identical audio contents to two arbitrary directions with certain angular separation. This proposed method makes

use of the spatial aliasing of the steerable parametric loudspeaker to generate the second beam of the DF wave from the grating lobes of the PF waves. Meanwhile, the remaining grating lobes can still be eliminated by careful selection of the UTA configuration.

This chapter is organized as follows. In Section 5.1, the symmetric structure for the dual-beam generation is proposed and compared with the direct structure. In Section 5.2, grating lobe elimination in the dual-beam parametric loudspeaker is derived. In Sections 5.3 and 5.4, simulation and measurement results verify the effectiveness of the proposed structure for dual-beam generation in the steerable parametric loudspeaker. Finally, Section 5.5 concludes the findings of this chapter.

5.1 Dual-Beamsteering Structures for the Steerable Parametric Loudspeaker

Based on the product directivity principle, when the PF waves are steered to the same direction, the DF wave generated from the nonlinear interaction inherits this steering direction. Thus, a direct method to generate dual beams from a single parametric loudspeaker is to steer the PF waves to the two desired directions θ_a and θ_b at the same time, using the direct structure shown in Fig. 5.1. Two groups of delays (τ_m^a and τ_m^b for $m = 0, 1, \ldots, M-1$) are applied to the PF waves, corresponding to the two desired steering angles of θ_a and θ_b. The delayed PF waves are added together before being weighted. Hence, in the direct structure, each PF beampattern is given by the summation of two beampatterns whose main

lobes are steered to θ_a and θ_b, respectively. The PF beampattern is given by

$$H(k,\theta)=\sum_{m=0}^{M-1} w_m \left\{\exp\left[\, jmdk\left(\sin\theta-\sin\theta_a\right)\right]+\exp\left[\, jmdk\left(\sin\theta-\sin\theta_b\right)\right]\right\}. \quad (5.1)$$

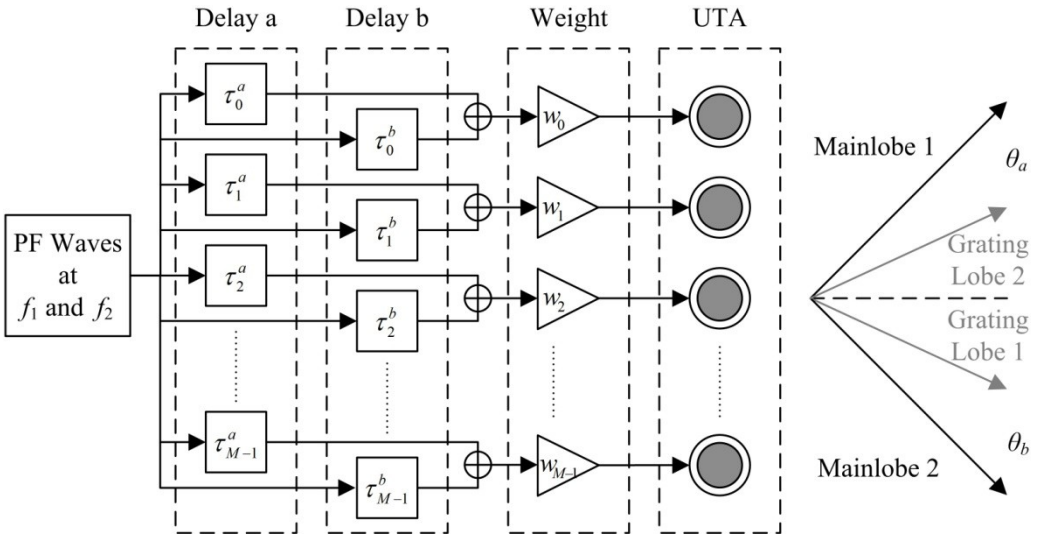

Figure 5.1 Direct structure for dual-beam generation of the steerable parametric loudspeaker.

There are two disadvantages of the direct structure for dual-beam generation. Firstly, the maximum SPL of the DF wave is 12 dB lower than single-beam generation. This is due to the fact that the amplitude of each delayed PF wave is reduced by half of that used to generate a single beam. Secondly, the additional mainlobes and grating lobes of the PF waves in the direct structure significantly increases the complexity of analyzing and solving the spatial aliasing problem.

A new symmetrical structure for dual-beamsteering is proposed, as shown in Fig. 5.2. The second beam of the DF wave is generated from the grating lobes of the PF waves. Two groups of delays (τ_{m1} and τ_{m2} for $m=0, 1, \ldots, M-1$) are applied to the PF waves at f_1 and f_2, respectively. As a result, the mainlobes of

the PF waves are steered to two different angles θ_1 and θ_2, respectively. But the resultant DF wave is steered to the desired steering angle θ_a. At the same time, the grating lobes of the PF waves result in the second beam of the DF wave being steered to the other desired steering angle θ_b. As the mainlobes (leading to the first beam of the DF wave) and the grating lobes (leading to the second beam of the DF wave) are symmetric to the same angle θ_s in the two PF beampatterns, this proposed structure for dual-beamsteering is named as the symmetric structure. The described geometry of the symmetric dual-beam generation is illustrated in Fig. 5.3, and the directivity of the DF wave in the symmetric structure is given by

$$D_{diff}(\theta) = \left\{\sum_{m=0}^{M-1} w_m \exp\left[jmdk_1(\sin\theta - \sin\theta_1)\right]\right\} \times \left\{\sum_{m=0}^{M-1} w_m \exp\left[jmdk_2(\sin\theta - \sin\theta_2)\right]\right\}, \tag{5.2}$$

where the steering angles of the PF waves are θ_1 and θ_2, respectively.

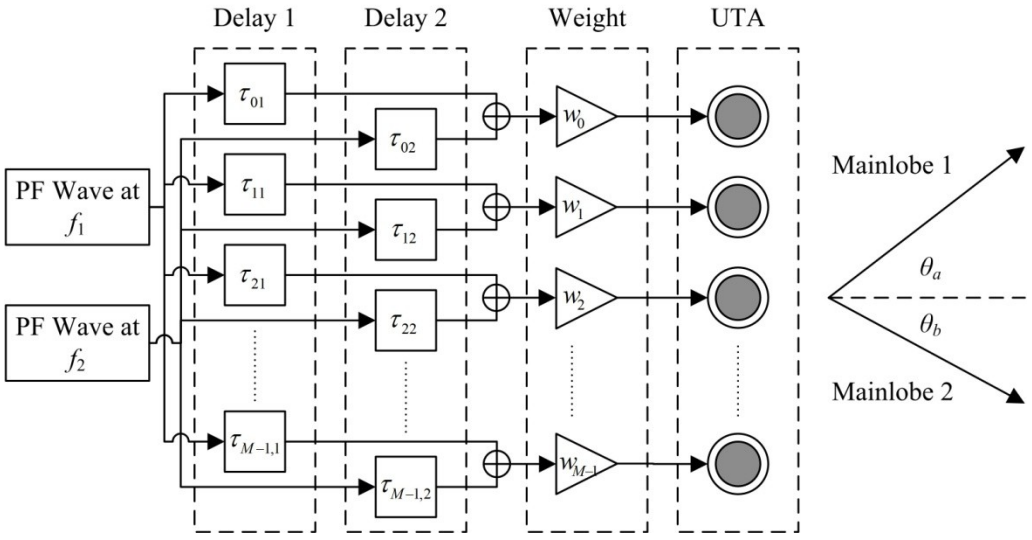

Figure 5.2 Symmetric structure for dual-beam generation of the steerable parametric loudspeaker.

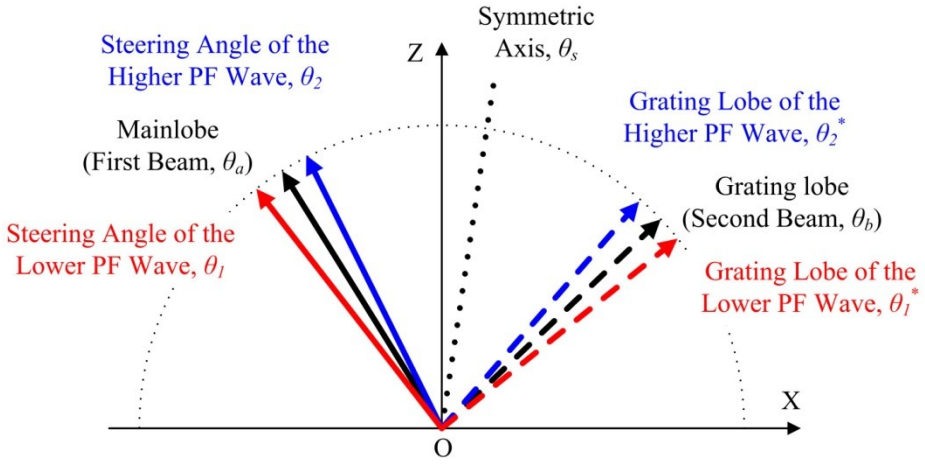

Figure 5.3 Geometry of the dual-beam generation using the symmetric structure.

To compute the two steering angles of the PF waves, it is always assumed that the desired steering angles of the DF wave fulfill the relation of $\theta_a < \theta_b$, without loss of generality. Referring to Fig. 5.3, the symmetric axis of the dual beams of the DF wave is given by

$$\sin\theta_s = \frac{\sin\theta_a + \sin\theta_b}{2}. \tag{5.3}$$

Because the mainlobes and the grating lobes are symmetrical to the same axis, the mainlobes of the PF waves are steered to

$$\sin\theta_1 = \sin\theta_s - \frac{c_0}{2f_1 d} \tag{5.4}$$

and

$$\sin\theta_2 = \sin\theta_s - \frac{c_0}{2f_2 d}, \tag{5.5}$$

respectively.

Applying the product directivity principle to (5.4) and (5.5), the mainlobe of the DF waves is steered to

$$\sin\theta_a = \frac{\sin\theta_1 + \sin\theta_2}{2} = \sin\theta_s - \frac{c_0}{4f_1 d} - \frac{c_0}{4f_2 d}. \tag{5.6}$$

In addition, f_c is the center frequency of the PF waves, *i.e.* $f_c = (f_1 + f_2)/2$. Thus, (5.3) is substituted into (5.6), and a quadratic equation is obtained as

$$(\sin\theta_b - \sin\theta_a) f_c^2 - \frac{c_0}{d} f_c - (\sin\theta_b - \sin\theta_a)\frac{f_d^2}{4} = 0. \tag{5.7}$$

The solution to the quadratic equation of the center frequency is given by

$$f_c = \frac{c_0 + \sqrt{c_0^2 + d^2(\sin\theta_b - \sin\theta_a)^2 f_d^2}}{2d(\sin\theta_b - \sin\theta_a)}. \tag{5.8}$$

Since $c_0 \gg$ $_b - \sin\theta_a) f_d$ is valid when the DF wave is within the speech frequency band, (5.8) can be simplified as

$$f_c = \frac{c_0}{d(\sin\theta_b - \sin\theta_a)} = \frac{c_0}{2d\cos\left(\frac{\theta_a + \theta_b}{2}\right)\sin\left(\frac{\theta_b - \theta_a}{2}\right)}. \tag{5.9}$$

Equation (5.9) shows that the center frequency is the only factor that determines directions of the dual beams when the UTA configuration is fixed.

On the other hand, for a fixed center frequency, it is observed from (5.9) that smaller spacing of the UTA results in a larger angular separation of the dual beams; while larger spacing of the UTA allows the symmetric axis of the dual beams to be closer to the array axis. The curves indicating the angular separation of dual beams are plotted with respect to the UTA's spacing at various center frequencies in Fig. 5.4. The shaded area shows the resonating frequency of the commercial ultrasonic transducer, which typically ranges from 36 kHz to 44 kHz [Mur09, Nip12]. For example, in setting "A" (as indicated in Fig. 5.4), when the spacing is 1 cm and the center frequency is 40 kHz, the angular separation between dual beams achieves 50°. In setting "B", when the spacing and the center frequency

increases to 1.5 cm and 44 kHz, respectively, the angular separation between dual beams reduces to 30°. In setting "C", the center frequency is extended to 60 kHz, and thus, the angular separation between dual beams is further reduced to 20° when the spacing is 1.7 cm, which is approximately three times the wavelength of the center frequency.

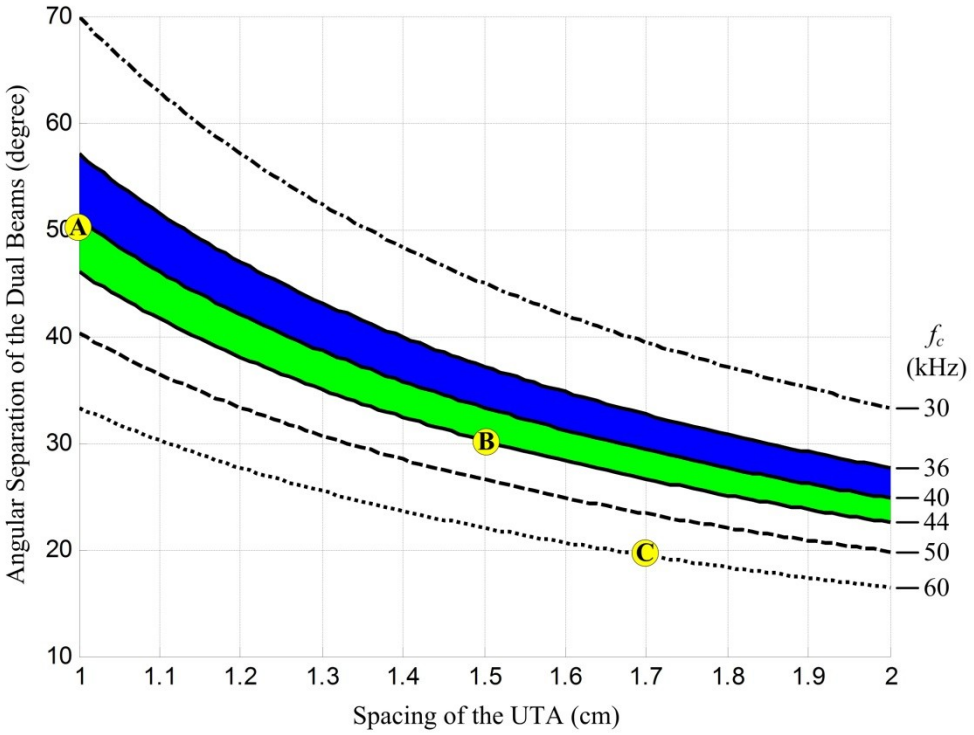

Figure 5.4 Angular separation of the dual beams adjusted by the center frequency and the spacing of the UTA.

5.2 Grating Lobe Elimination in the Symmetric Structure

In this section, the grating lobe elimination is extended from the single-beam to the dual-beam generation using the symmetric structure. As stated in Chapter 4, the grating lobe elimination of the DF wave is achieved when the grating lobes of

PF waves are sufficiently apart in angular distance. In the symmetric structure, the locations of the grating lobes are found at $\Theta_1 = (n_1 - 1/2)\Lambda$ in the lower PF beampattern and $\Theta_2 = (n_2 - 1/2)\Lambda/F$ in the higher PF beampattern. Hence, the distance function that describes the minimum angular distance between grating lobes of the PF waves is adapted for the dual-beam generation and redefined as

$$D_K(F) = \min_{\substack{0 \le n_a \le K \\ 0 \le n_b \le KF}} \left(\left| \left(n_1 - \frac{1}{2} \right) \Lambda - \left(n_2 - \frac{1}{2} \right) \frac{\Lambda}{F} \right| \right). \tag{5.10}$$

When two grating lobes of the PF waves coincide in the same direction, the value of the distance function in (5.10) reduces to 0. Hence, nulls in the distance function indicate the occurrence of grating lobes for the DF wave. It is also noted that $F = 1$ represents the difference frequency of 0 Hz and gives the lower bound of F. The upper bound of F is determined by the adjacent null, which is obtained from the distance function plotted in Fig. 5.5 and formulated as $(2K+3)/(2K+1)$.

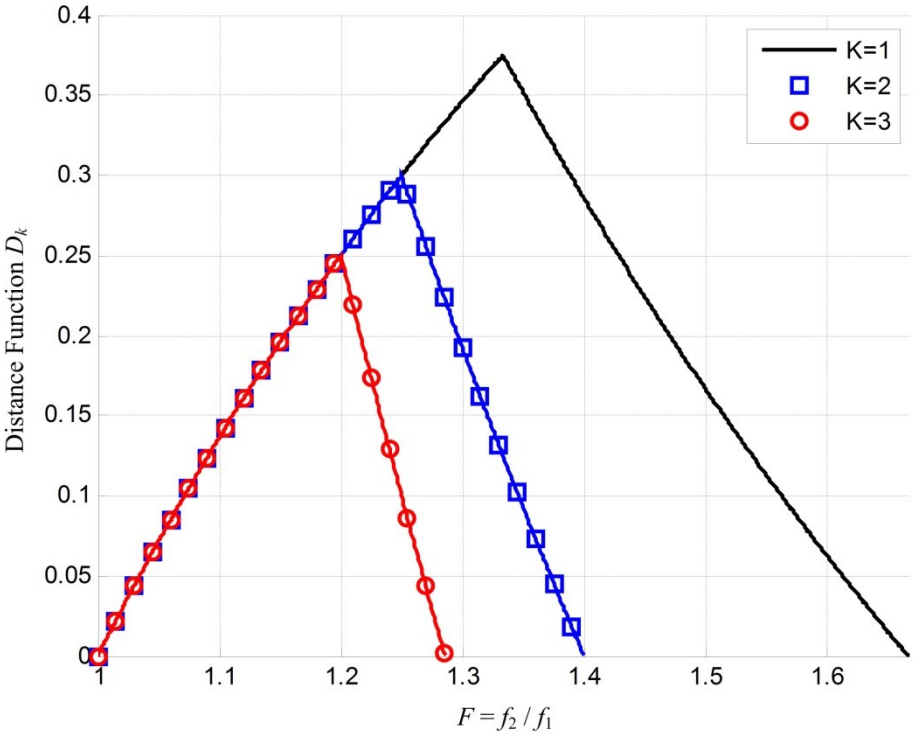

Figure 5.5 Distance function for $K = 1,\ 2,$ and 3 in the symmetric structure.

As discussed, the grating lobes of the DF wave appear when there are nulls in the distance function, while grating lobes of the PF waves are suppressed by each other within the vicinity of nulls in the distance function due to the product directivity principle. However, the mainlobes are also suppressed in the symmetric structure, due to the spatial distance between the mainlobes of the PF waves. Due to the symmetry of the proposed structure, this spatial distance between the mainlobes of the PF waves is always equal to the spatial distance between the first grating lobes of the PF waves. Hence, a new intersection function is proposed to account for the elimination of grating lobes and the suppression of mainlobes of the DF wave in the symmetric structure, *i.e.*

$$I_K(F) = \max_{\Theta}\left\{\left|\sum_{m=0}^{M-1} w_m \exp\left(j\pi m\frac{\Theta}{\Lambda}\right)\right| \cdot \left|\sum_{m=0}^{M-1} w_m \exp\left\{j\pi m\frac{F}{\Lambda}\left[\Theta - D_K(F)\right]\right\}\right|\right\}$$
$$-\max_{\Theta}\left\{\left|\sum_{m=0}^{M-1} w_m \exp\left(j\pi m\frac{\Theta}{\Lambda}\right)\right| \cdot \left|\sum_{m=0}^{M-1} w_m \exp\left\{j\pi m\frac{F}{\Lambda}\left[\Theta - \frac{\Lambda}{2}\left(1-\frac{1}{F}\right)\right]\right\}\right|\right\}. \quad (5.11)$$

Intersection function with different weights are plotted in Fig. 5.6 when the UTA consists of 8 channels and $K=1$. The color bars at the bottom illustrate the range of partial grating lobe elimination that lead to sidelobes lower than -6 dB, while the grey bars show the ranges of partial grating lobe elimination that result in sidelobes higher than -6 dB, including the cases of spatial aliasing. Different colors represent the usages of different weights. Overall, the case of Chebyshev weights with 30 dB attenuation results in the widest range of the -6 dB partial grating lobe elimination in the symmetric structure. It is also observed that when Chebyshev weights with higher attenuation are used in the symmetric structure, the lower bound of the DF wave to achieve the -6 dB partial grating lobe elimination is sacrificed. Moreover, due to the suppression of mainlobes of the DF wave, full grating lobe elimination is unachievable in the symmetric structure.

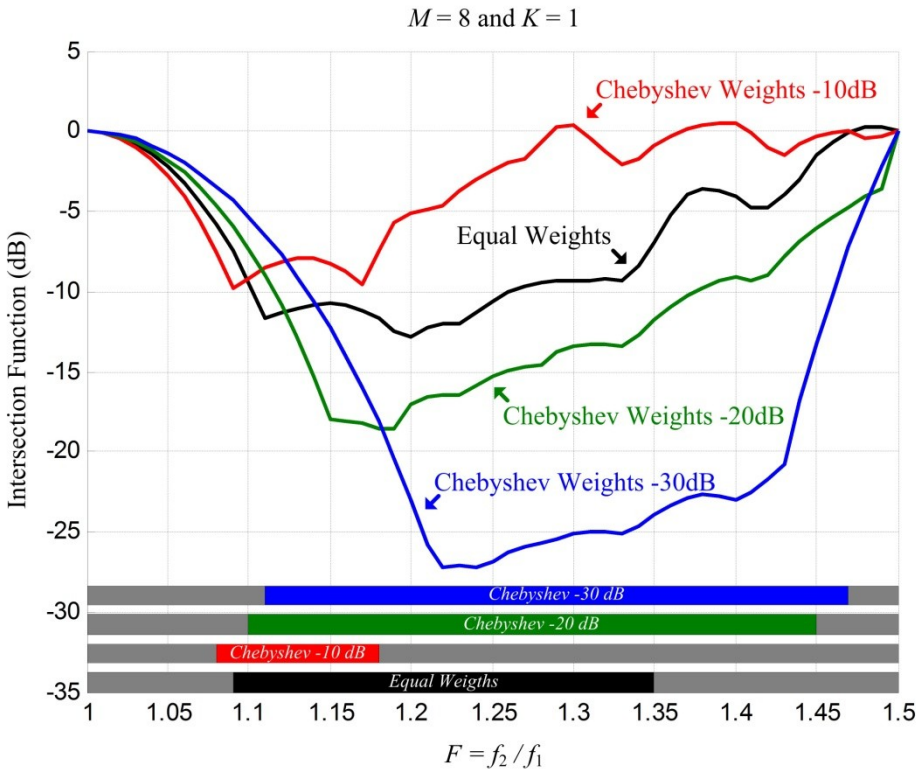

Figure 5.6 Intersection function for $K=1$ in the symmetric structure when equal weights and Chebyshev weights with 10 dB, 20 dB, 30 dB attenuations are adopted in the UTA consisting of $M=8$ channels.

Although the range of F that achieves the grating lobe elimination does not change with the value of Λ, the spacing determines the value of K, which in turn indicates the number of grating lobes in the visible region. Since the upper bound of F is given by $(2K+3)/(2K+1)$, large values of K lead to narrow ranges of the DF wave. Moreover, the relation between the visible range and non-aliasing spacing of the UTA is derived according to the Nyquist criterion, and is given by

$$\Lambda = \frac{\lambda_a}{d} \geq \frac{2\sin\varphi}{(K+2)}, \tag{5.12}$$

where φ indicates the boundary of the visible region. Thus, if the visible region

is between ±45° (i.e. $\varphi = 45°$) and $K = 1$, the spacing must not exceed 2.12 times of the wavelength of the PF wave, and grating lobe elimination occurs when equal weights are applied and $1.1 \le F \le 1.26$; if the spacing is less than 1.41 times of the wavelength of the PF wave, grating lobes of the DF wave do not occur in the visible region between ±45°. Thus, it is suggested that $K = 1$ to ensure sufficient range of the DF wave where grating lobe elimination occurs.

5.3 Simulation Results

Simulations are carried out for comparing the symmetric structure with the direct structure when generating dual beams from a single steerable parametric loudspeaker. The UTA is set to consist of 8 channels and adopt equal weights. The DF waves vary from 0.5 kHz to 10 kHz with frequency interval of 0.5 kHz. The center frequency of the PF waves is fixed to 40 kHz for the direct structure and calculated using (5.9) for the symmetric structure.

In the first group of simulations, the spacing of the UTA is set to 1 cm, and the dual beams are steered to -25° and 25°. The PF beampatterns in the direct structure are shown in Fig. 5.7(a). It is observed that when the PF is low, the mainlobe of the first steering angle appears close to the grating lobe of the second steering angle; but when the PF is high, the mainlobe of the first steering angle overlaps with the grating lobe of the second steering angle. Thus, the mainlobes of the PF wave are interfered as indicated in Fig. 5.7(a). The DF beampatterns in the direct structure are shown in Fig. 5.7(b). It is observed that the steering angles are

inaccurate and the amplitudes of the dual beams are not constant throughout the range of the DF. Both observations are due to the interference of the mainlobes of the PF wave. With the symmetric structure, the beampatterns of the PF waves and the DF waves are plotted in Fig. 5.8(a) and Fig. 5.8(b), respectively. In Fig. 5.8(a), the angular separation between the mainlobe and the grating lobe of the PF wave becomes closer when the PF increases, due to decreasing in the aliasing period. In Fig. 5.8(b), dual beams of the DF wave are accurately steered to -25° and 25°. However, as the DF increases, the angular separation between the mainlobes of the PF waves also increases. Hence, the amplitudes of the dual beams decrease as the DF increases under the symmetric structure, but they are still higher in amplitude than those DF waves generated in the direct structure (in Fig. 5.7(b)). Therefore, the symmetric structure achieves higher amplitude and more consistent dual beams of the DF wave compared to the direct structure.

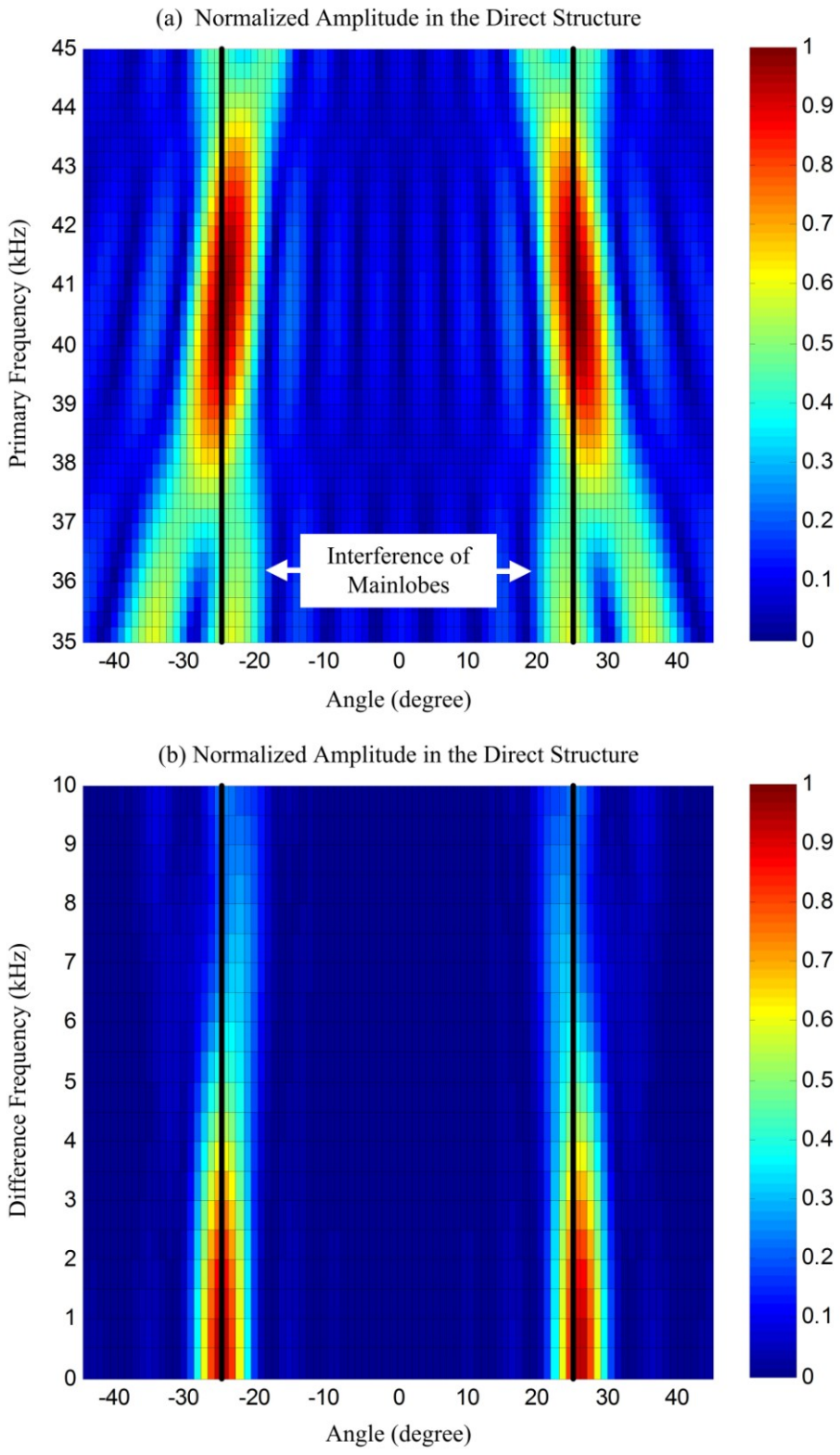

Figure 5.7 Simulated (a) PF and (b) DF beampatterns when the UTA consists of 8 channels with spacing of 1 cm and the dual beams are generated in the direct structure.

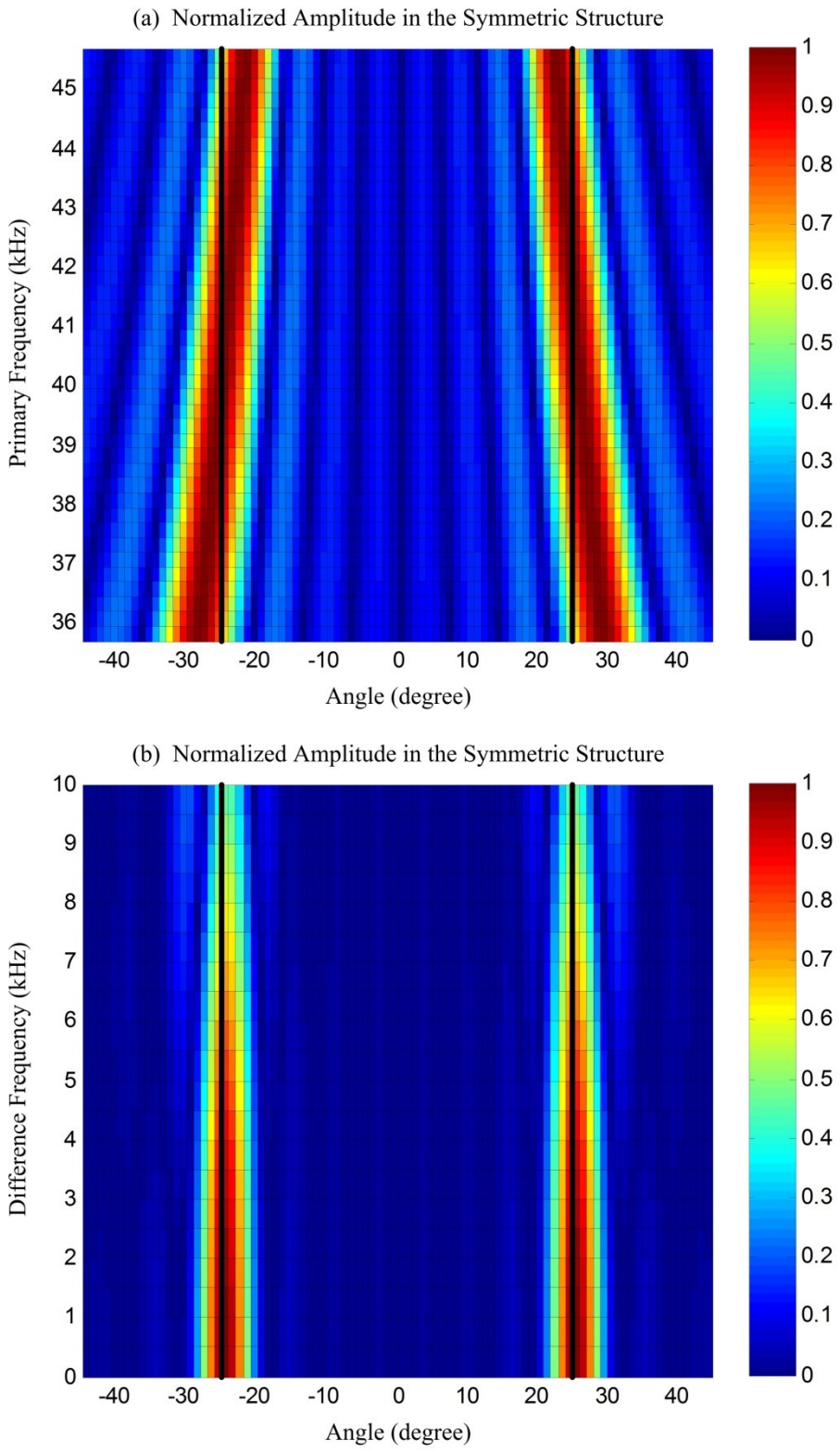

Figure 5.8 Simulated (a) PF and (b) DF beampatterns when the UTA consists of 8 channels with spacing of 1 cm and the dual beams are generated in the symmetric structure.

In the second group of simulations, the spacing of the UTA is set to 1.5 cm and the dual beams are steered to -30° and 0°, respectively. This setting allows the occurrence of two grating lobes of the PF wave in the visible region from -45° to 45°. A more complicated overlapping of mainlobes and grating lobes are observed in the direct structure in Fig. 5.9(a). Due to the interference in the mainlobes of the PF wave, inaccurate steering angles and uneven amplitudes of dual beams are observed in the DF beampatterns in the direct structure, as shown in Fig. 5.9(b). Moreover, for the DF waves generated below 3 kHz, each beam is split into two sidelobes steering to two directions on both sides of the desired direction. The second grating lobes of the PF wave occur in the symmetric structure as shown Fig. 5.10(a). However, in Fig. 5.10(b), grating lobe elimination is observed in the DF beampattern at the direction of around 30°. When the DF increases from 0 to 5 kHz, the amplitude of the grating lobe decreases and subsequently maintains at a level lower than the dual beams, which agrees with the analysis of the intersection functions plotted in Fig. 5.6.

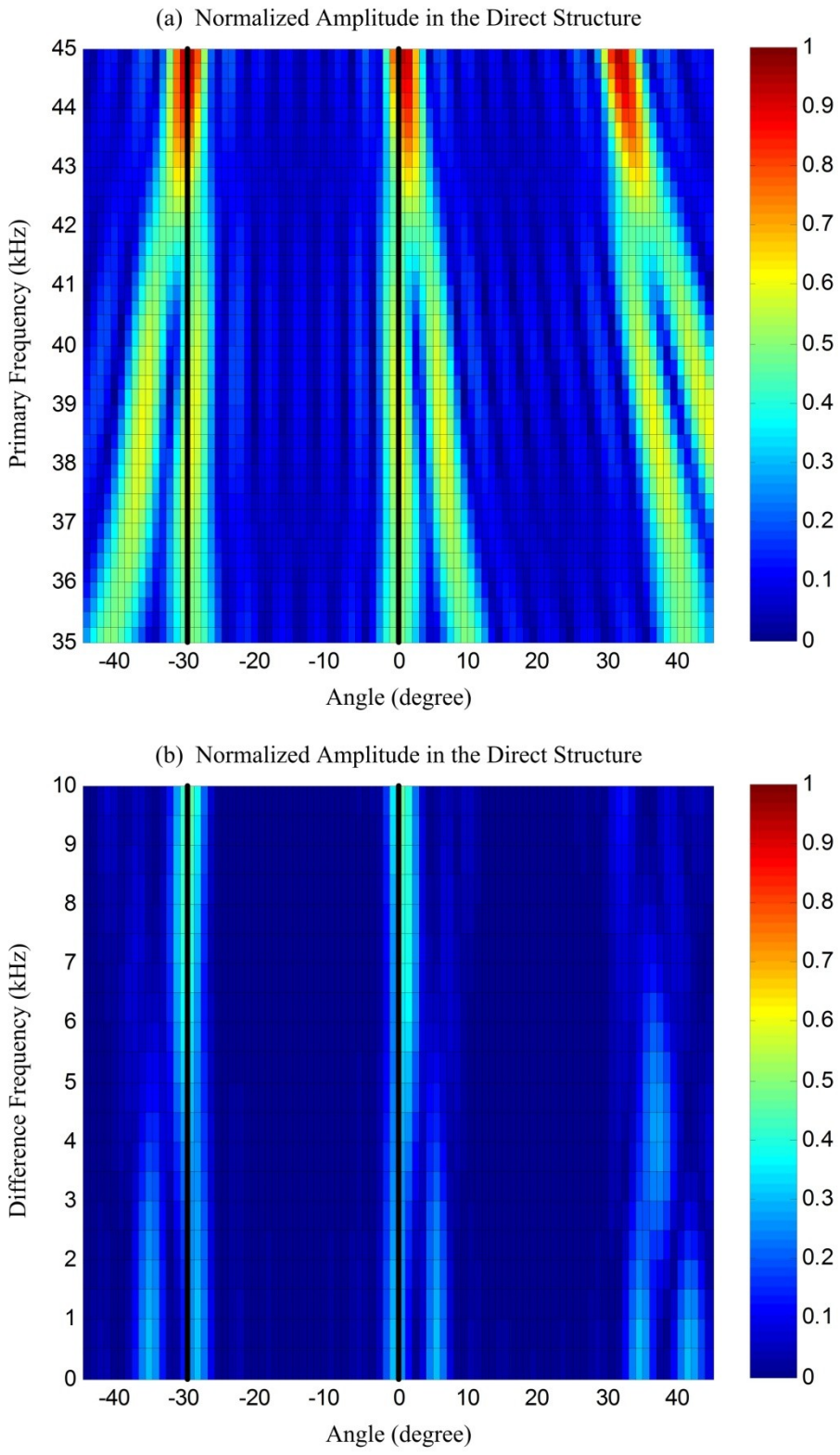

Figure 5.9 Simulated (a) PF and (b) DF beampatterns when the UTA consists of 8 channels with spacing of 1.5 cm and the dual beams are generated in the direct structure.

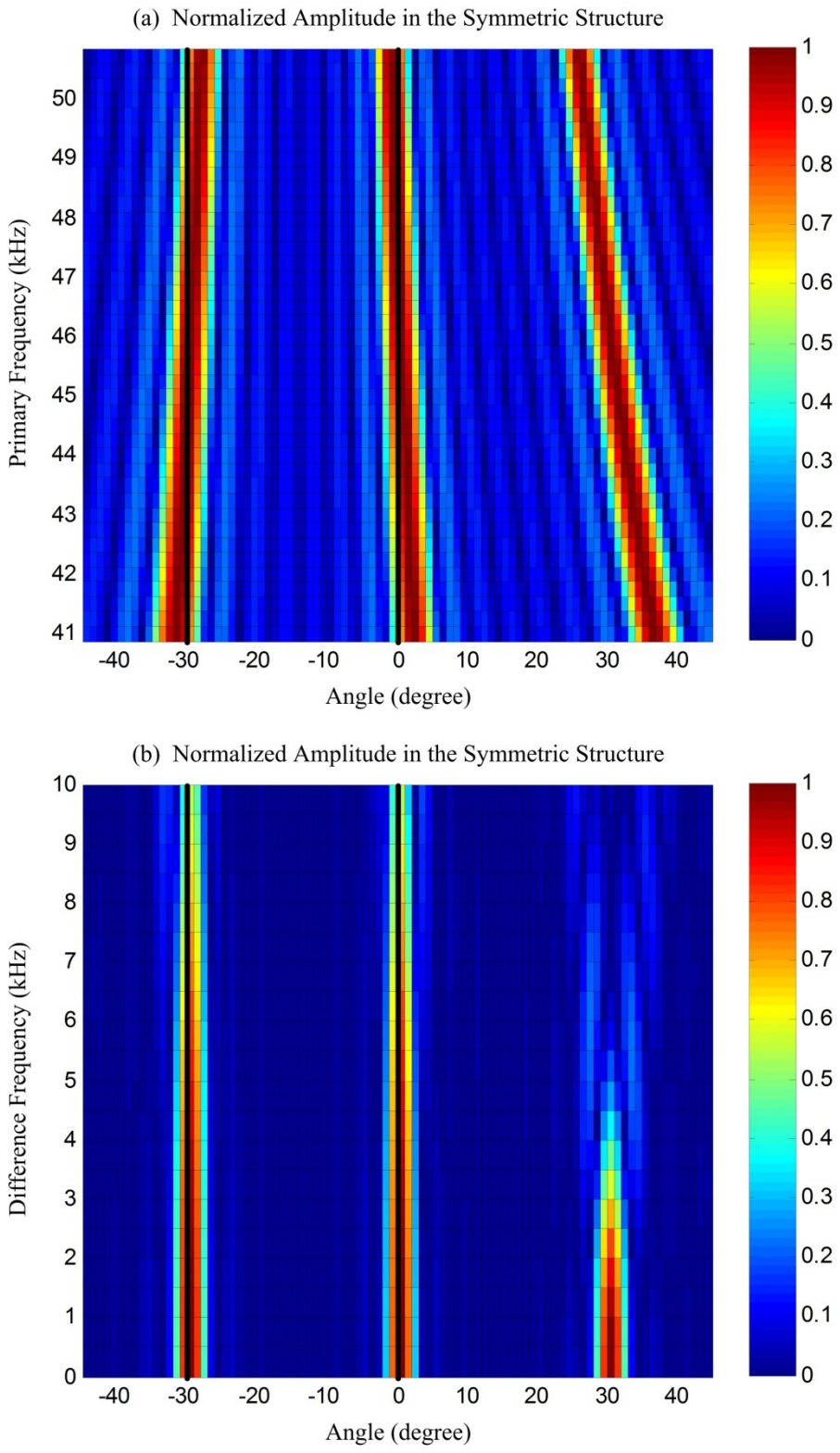

Figure 5.10 Simulated (a) PF and (b) DF beampatterns when the UTA consists of 8 channels with spacing of 1.5 cm and the dual beams are generated in the symmetric structure.

5.4 Measurement Results

The measurement setup has been introduced in Section 3.4, and more details are provided in Appendixes B, C, and D. In this chapter, the measured PF and DF beampatterns are normalized to their maximum SPLs, and thus the maximum normalized amplitudes are given by 0 dB. Firstly, the angular separation between the dual beams is fixed at 50°. When the dual beams are steered to -25° and 25°, the DF beampattern is observed to be symmetric, as shown in Fig. 5.11. However, when the dual beams are steered to -40° and 10°, the dual beams are not at the same amplitude due to the channel directivity of the UTA, as shown in Fig. 5.12. There is only one grating lobe of the PF wave occurring in the visible region that is used for generating the second beam in the symmetric structure. Thus, no grating lobe of the DF wave is observed in Fig. 5.11 and Fig. 5.12.

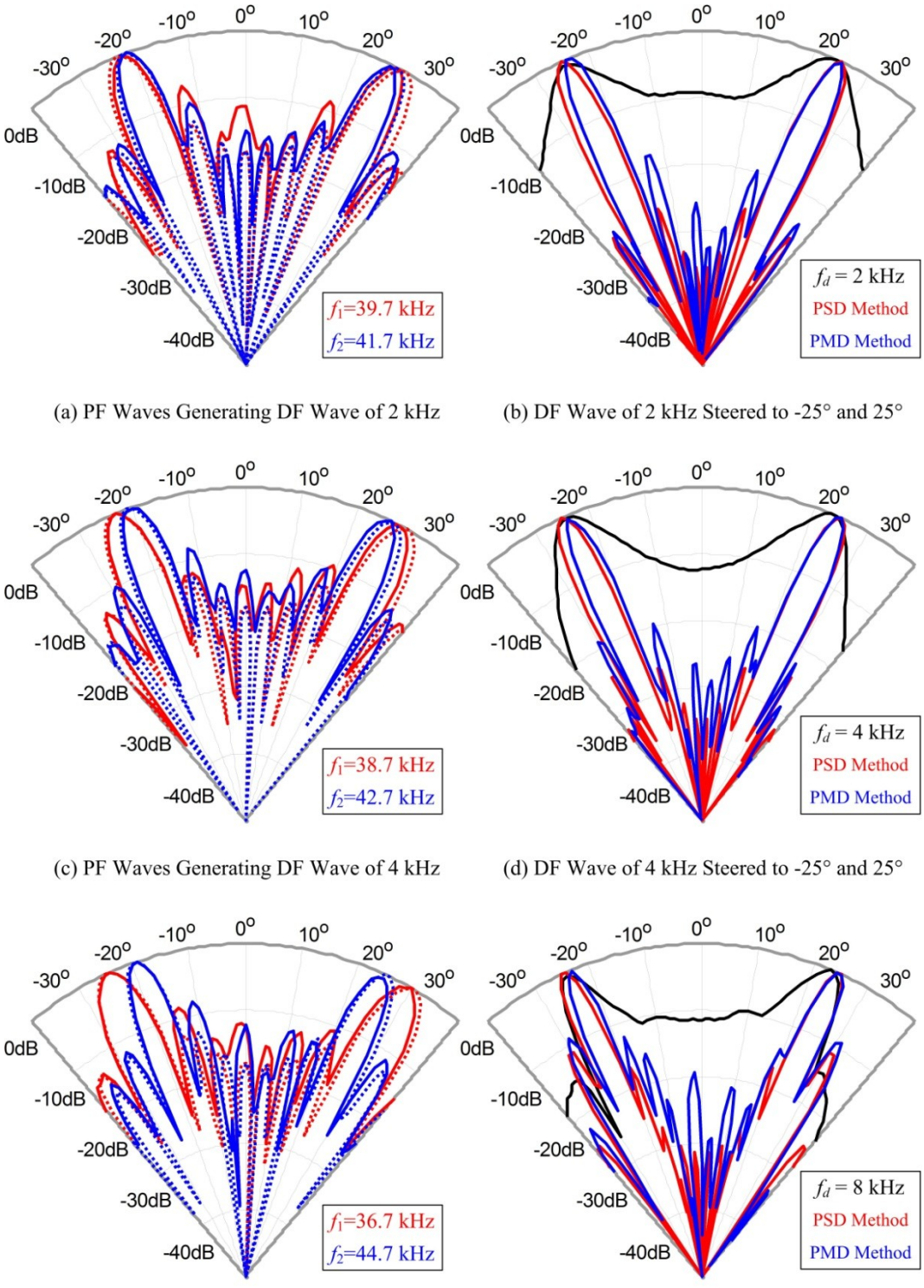

(a) PF Waves Generating DF Wave of 2 kHz

(b) DF Wave of 2 kHz Steered to -25° and 25°

(c) PF Waves Generating DF Wave of 4 kHz

(d) DF Wave of 4 kHz Steered to -25° and 25°

(e) PF Waves Generating DF Wave of 8 kHz

(f) DF Wave of 8 kHz Steered to -25° and 25°

Figure 5.11 Measured PF and DF beampatterns when the UTA consists of 8 channels with spacing of 1 cm and the dual beams are generated in the symmetric structure at -25° and 25°.

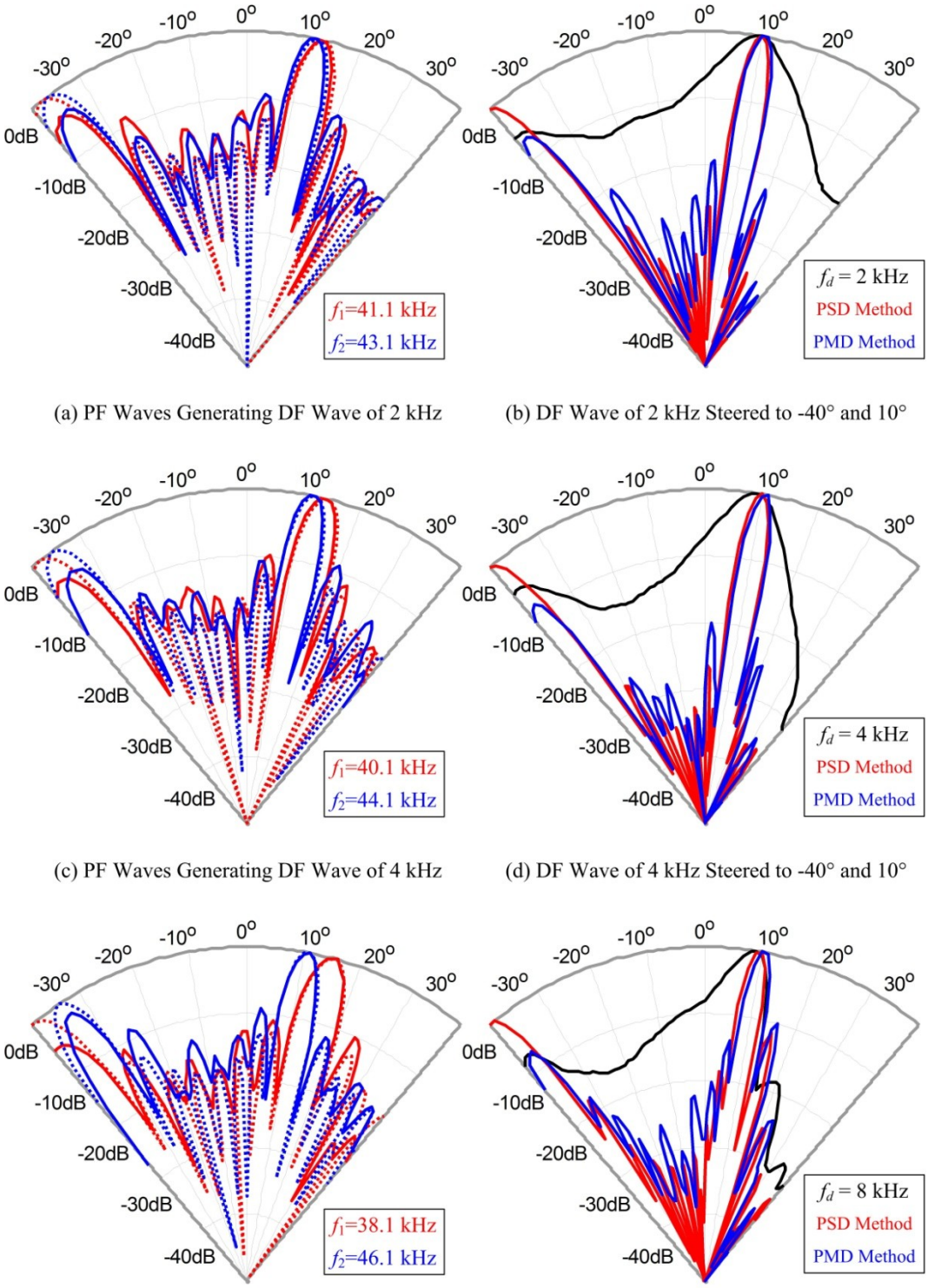

(a) PF Waves Generating DF Wave of 2 kHz

(b) DF Wave of 2 kHz Steered to -40° and 10°

(c) PF Waves Generating DF Wave of 4 kHz

(d) DF Wave of 4 kHz Steered to -40° and 10°

(e) PF Waves Generating DF Wave of 8 kHz

(f) DF Wave of 8 kHz Steered to -40° and 10°

Figure 5.12 Measured PF and DF beampatterns when the UTA consists of 8 channels with spacing of 1 cm and the dual beams are generated in the symmetric structure at -40° and 10°.

Secondly, the spacing of the UTA is increased to 1.25 cm, and the angular separation between the dual beams is fixed to 40°. Similar to the previous set of measurement results, when the dual beams are steered to -20° and 20°, the DF beampattern is observed to be symmetric as shown in Fig. 5.13. When the dual beams are steered to -30° and 10°, the dual beams are not at the same amplitude due to the channel directivity of the UTA, as shown in Fig. 5.14. In particular, when the dual beams are steered to -40° and 0°, two grating lobes of each PF wave occur in the visible region, as shown in Fig. 5.15. The left grating lobes are used for generating the second beam, while the right grating lobes do not coincide with each other and result in grating lobe elimination at the difference frequency. No grating lobe of the DF wave is observed, and thus, the grating lobe elimination is verified in this group of measurements.

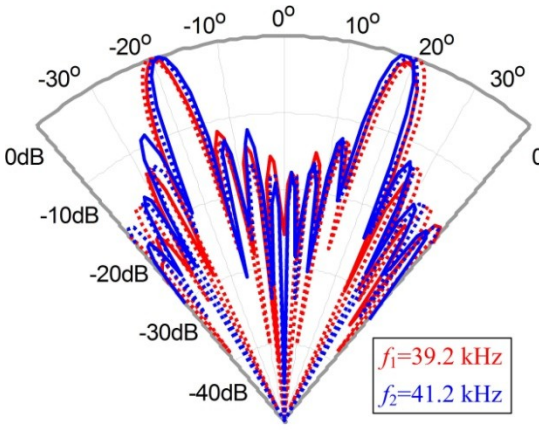

(a) PF Waves Generating DF Wave of 2 kHz

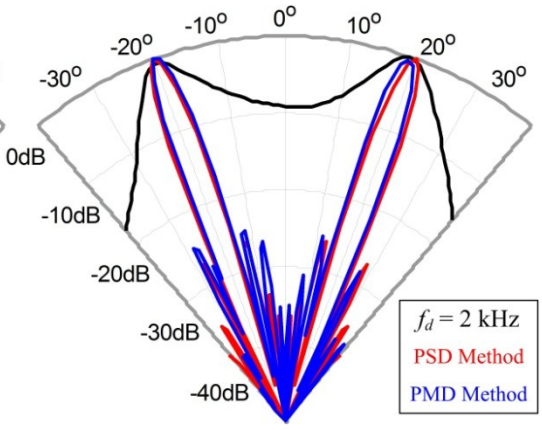

(b) DF Wave of 2 kHz Steered to -20° and 20°

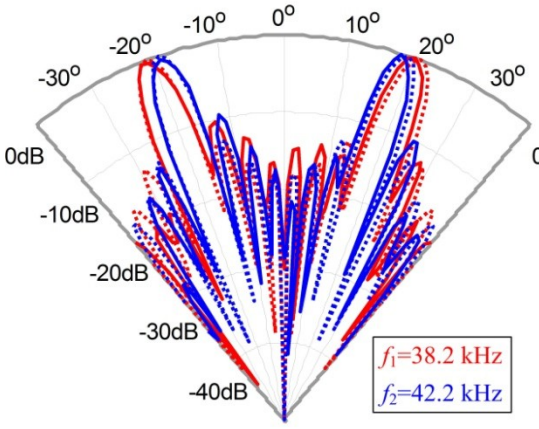

(c) PF Waves Generating DF Wave of 4 kHz

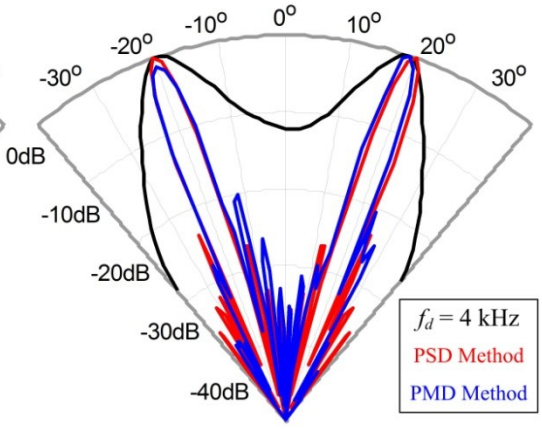

(d) DF Wave of 4 kHz Steered to -20° and 20°

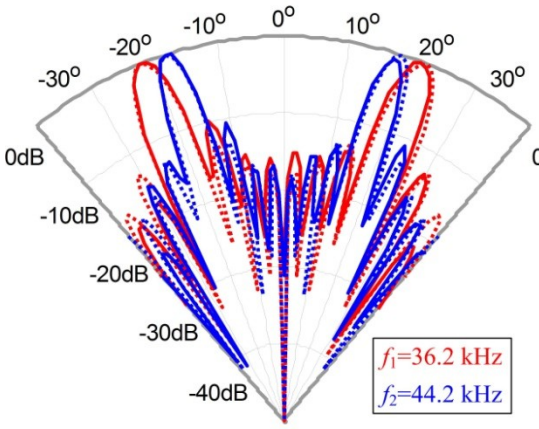

(e) PF Waves Generating DF Wave of 8 kHz

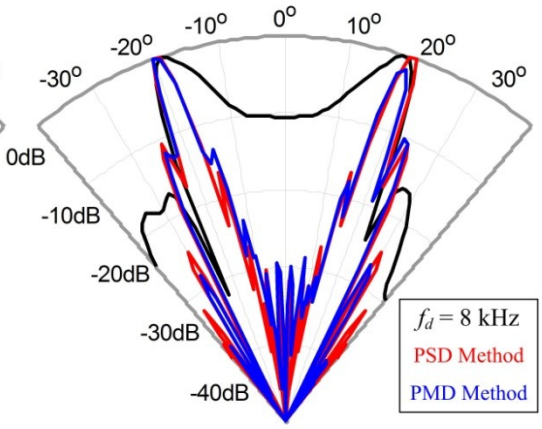

(f) DF Wave of 8 kHz Steered to -20° and 20°

Figure 5.13 Measured PF and DF beampatterns when the UTA consists of 8 channels with spacing of 1.25 cm and the dual beams are generated in the symmetric structure at -20° and 20°.

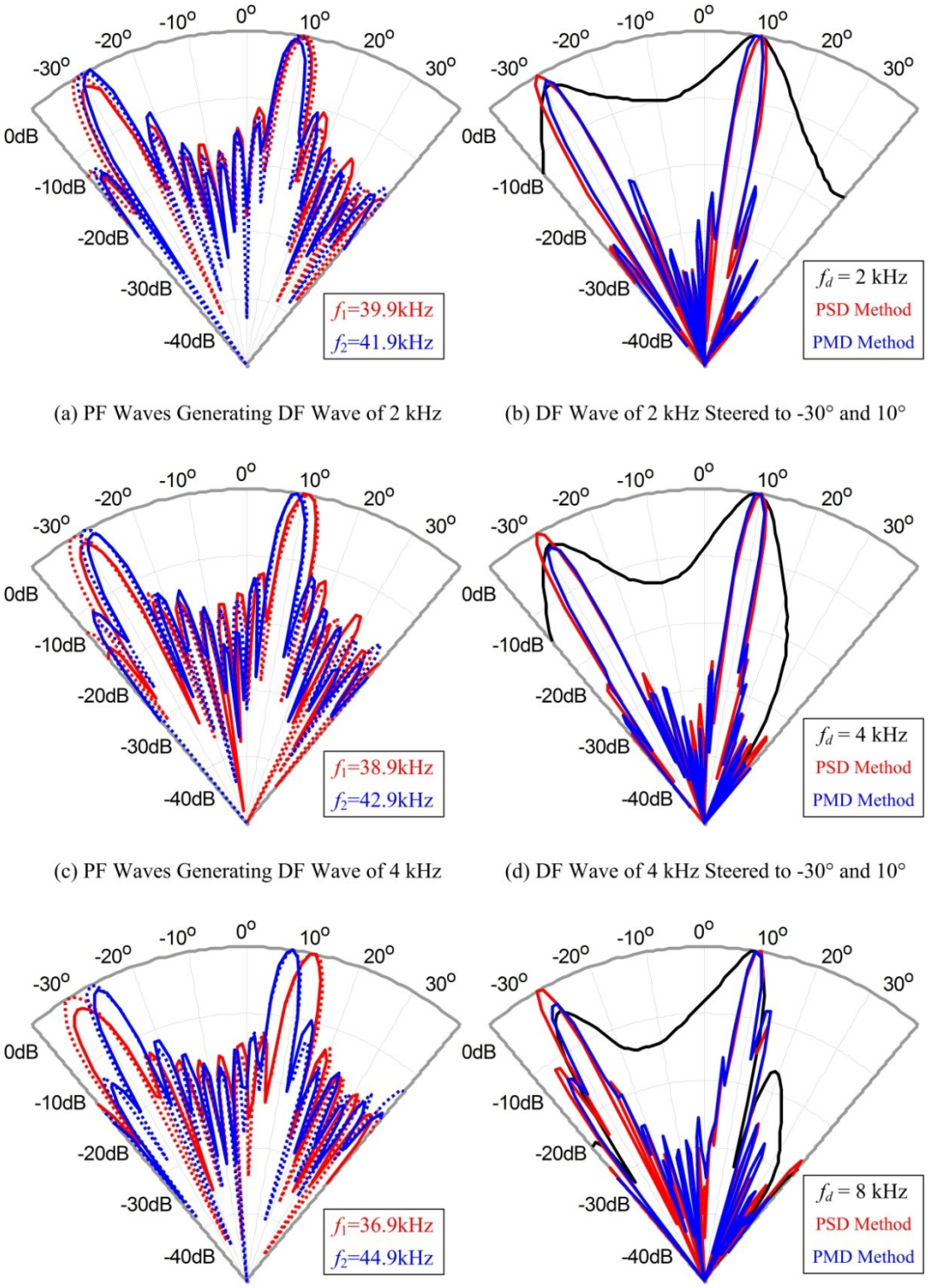

(a) PF Waves Generating DF Wave of 2 kHz

(b) DF Wave of 2 kHz Steered to -30° and 10°

(c) PF Waves Generating DF Wave of 4 kHz

(d) DF Wave of 4 kHz Steered to -30° and 10°

(e) PF Waves Generating DF Wave of 8 kHz

(f) DF Wave of 8 kHz Steered to -30° and 10°

Figure 5.14 Measured PF and DF beampatterns when the UTA consists of 8 channels with spacing of 1.25 cm and the dual beams are generated in the symmetric structure at -30° and 10°.

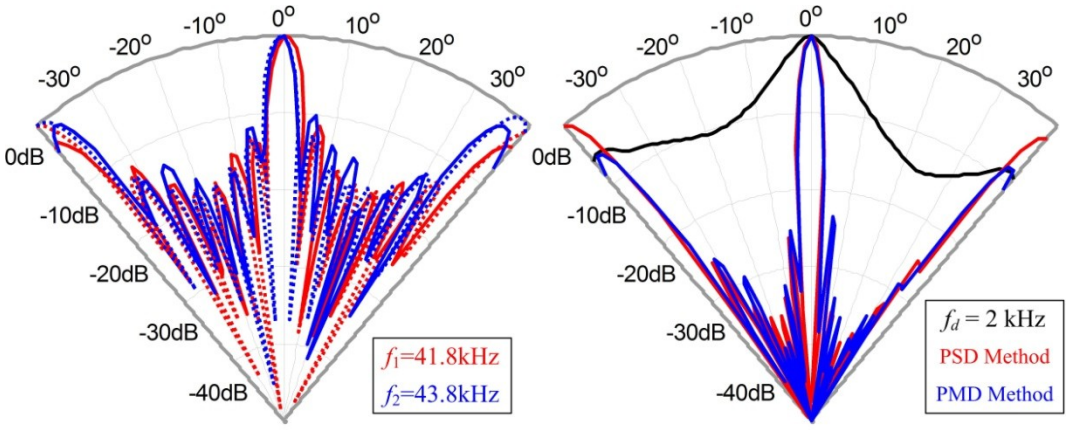

(a) PF Waves Generating DF Wave of 2 kHz

(b) DF Wave of 2 kHz Steered to -40° and 0°

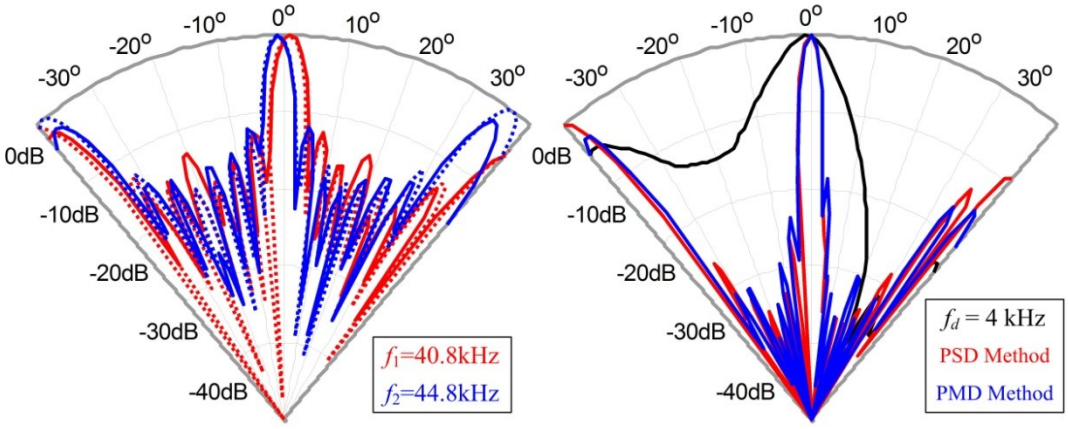

(c) PF Waves Generating DF Wave of 4 kHz

(d) DF Wave of 4 kHz Steered to -40° and 0°

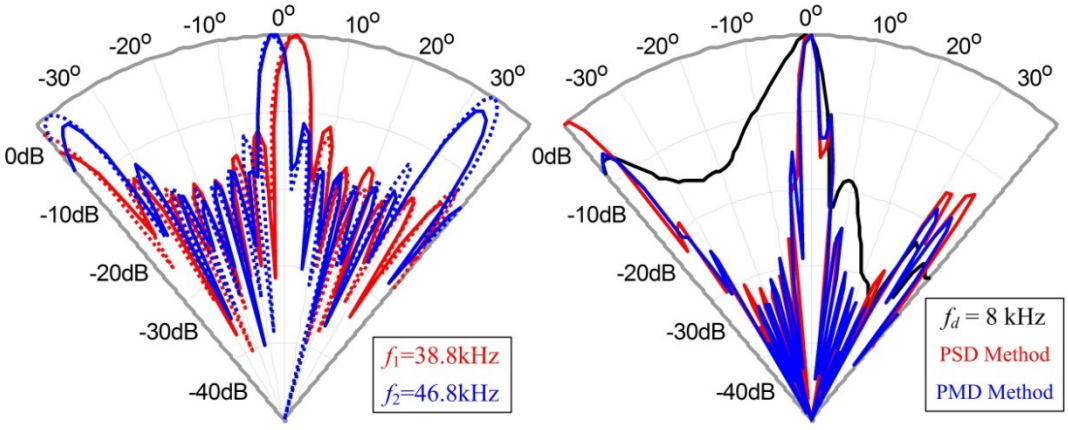

(e) PF Waves Generating DF Wave of 8 kHz

(f) DF Wave of 8 kHz Steered to -40° and 0°

Figure 5.15 Measured PF and DF beampatterns when the UTA consists of 8 channels with spacing of 1.25 cm and the dual beams are generated in the symmetric structure at -40° and 0°.

In the last group of measurements, the spacing of the UTA is further increased to 1.5 cm, and the angular separation between the dual beams is reduced to 30°. Comparing with the two previous groups of measurements, the center frequencies used in this group are around 44 kHz (see Fig. 5.4). The measurement results in this group show a similar trend as the group of measurements obtained from the UTA with spacing of 1.25 cm. When the dual beams are steered symmetrically at -15° and 15°, the DF beampattern is observed to be symmetrical, as shown in Fig. 5.16. However, since the channel directivity of the UTA contributes to the DF beampattern, uneven amplitudes of the dual beams are observed when they are steered asymmetrically to -20° and 10°, as shown in Fig. 5.17. When two grating lobes of each PF wave occur in the visible region, grating lobe elimination is observed for the DF wave. Figs. 5.18(a)-(b) show a case of partial grating lobe elimination of $F = 1.05$, while Figs. 5.18(e)-(f) show a case of full grating lobe elimination of $F = 1.2$. These observations agree with predictions of the intersection function for $K = 1$ when equal weights are adopted in the UTA, as shown in Fig. 5.6. However, Figs. 5.18(c)-(d) show another case of full grating lobe elimination of $F = 1.1$, which is predicted as partial grating lobe elimination by the intersection function. The measured sidelobes resulted from the grating lobe elimination are lower than the simulated ones, which is likely due to the channel directivity involved in the measurements.

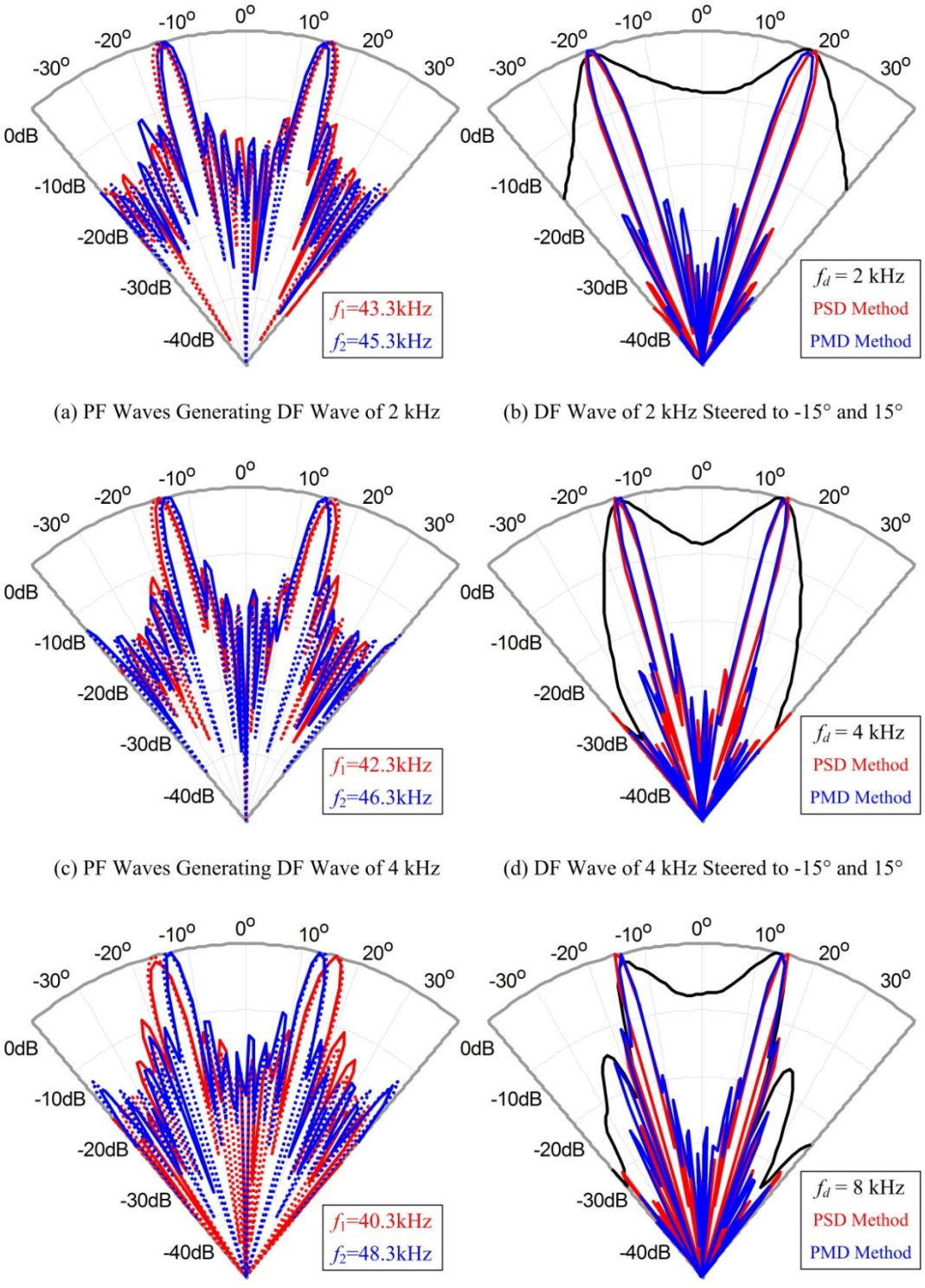

(a) PF Waves Generating DF Wave of 2 kHz

(b) DF Wave of 2 kHz Steered to -15° and 15°

(c) PF Waves Generating DF Wave of 4 kHz

(d) DF Wave of 4 kHz Steered to -15° and 15°

(e) PF Waves Generating DF Wave of 8 kHz

(f) DF Wave of 8 kHz Steered to -15° and 15°

Figure 5.16 Measured PF and DF beampatterns when the UTA consists of 8 channels with spacing of 1.5 cm and the dual beams are generated in the symmetric structure at -15° and 15°.

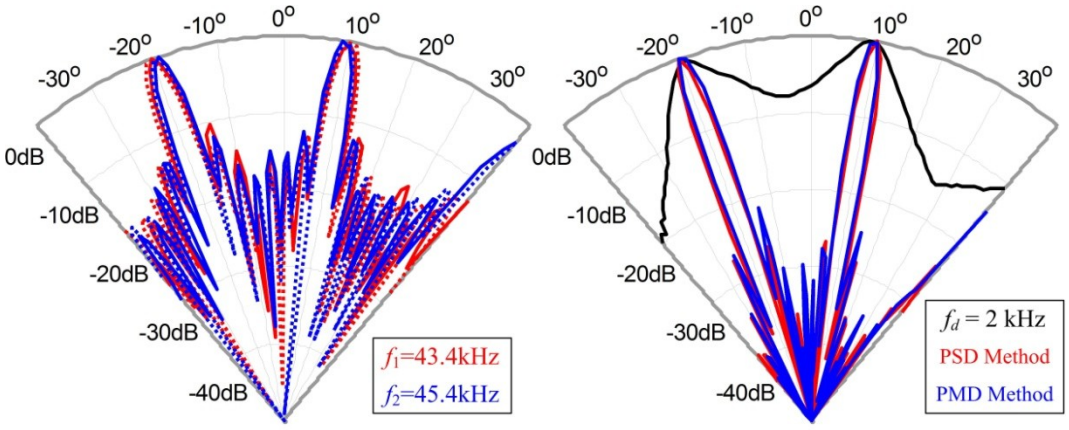

(a) PF Waves Generating DF Wave of 2 kHz

(b) DF Wave of 2 kHz Steered to -20° and 10°

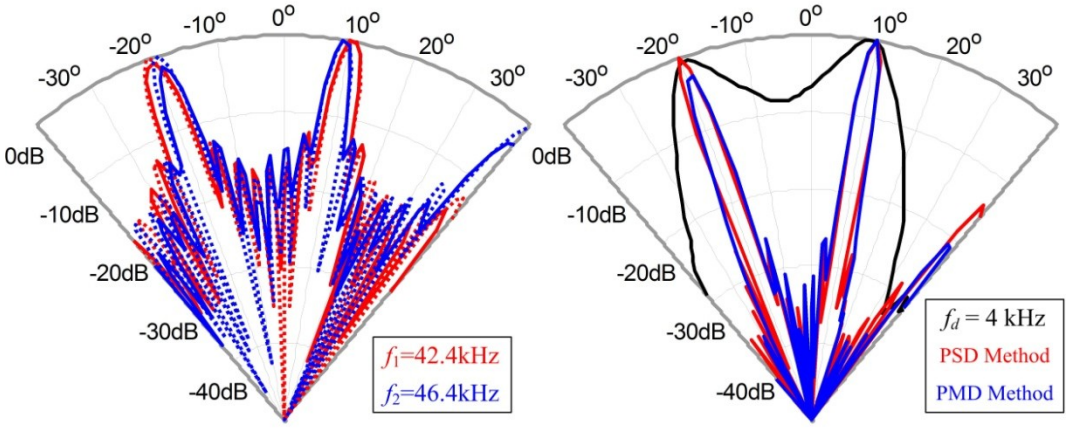

(c) PF Waves Generating DF Wave of 4 kHz

(d) DF Wave of 4 kHz Steered to -20° and 10°

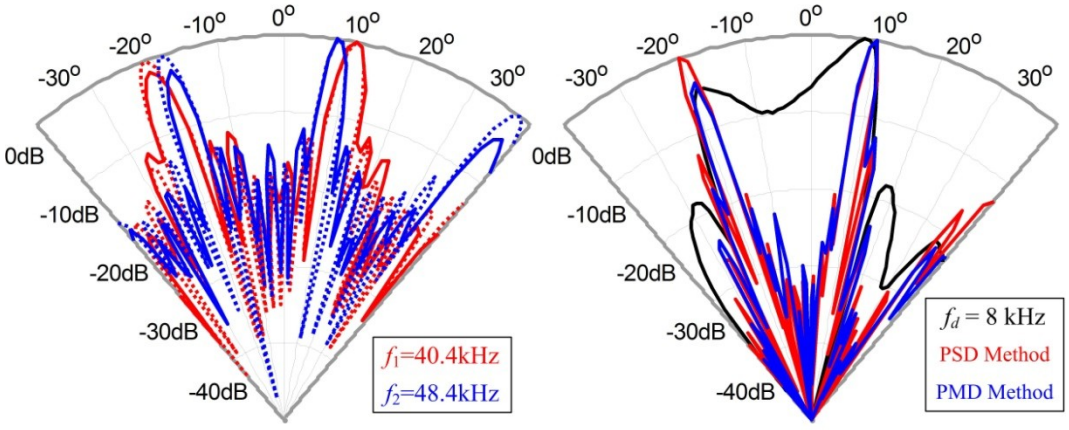

(e) PF Waves Generating DF Wave of 8 kHz

(f) DF Wave of 8 kHz Steered to -20° and 10°

Figure 5.17 Measured PF and DF beampatterns when the UTA consists of 8 channels with spacing of 1.5 cm and the dual beams are generated in the symmetric structure at -20° and 10°.

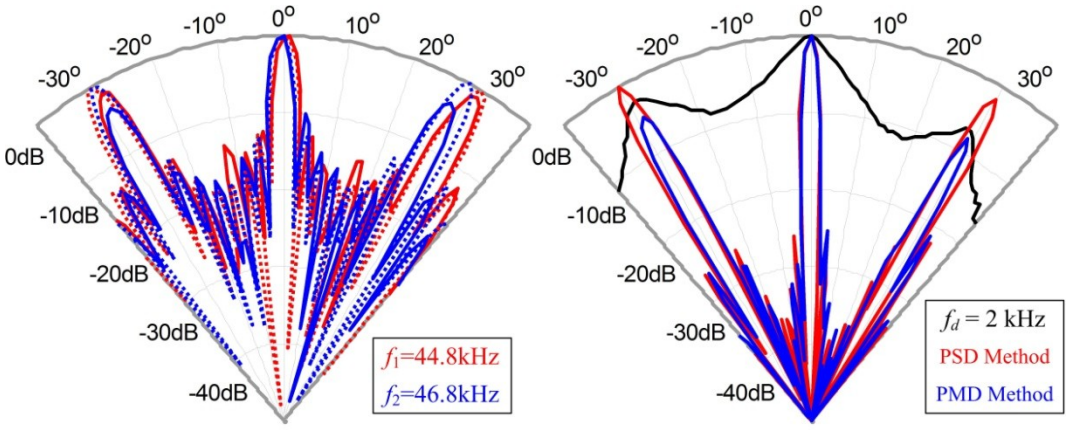

(a) PF Waves Generating DF Wave of 2 kHz

(b) DF Wave of 2 kHz Steered to -30° and 0°

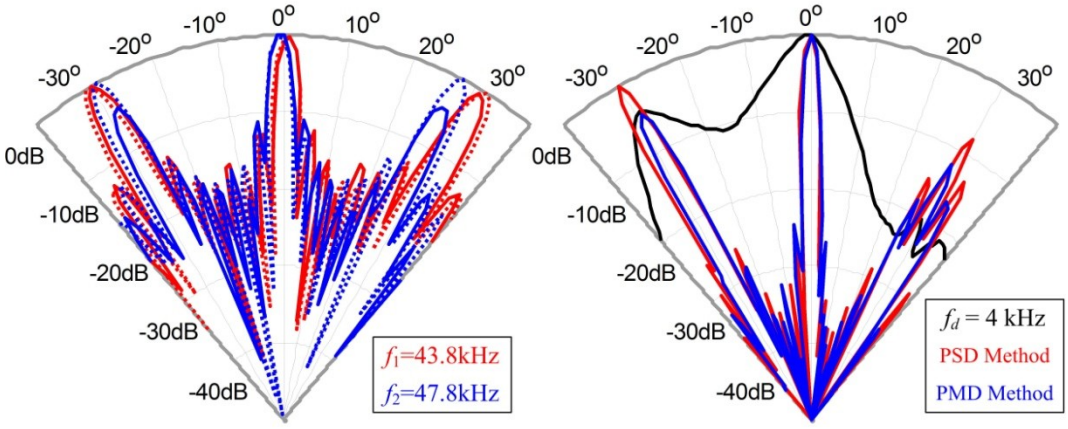

(c) PF Waves Generating DF Wave of 4 kHz

(d) DF Wave of 4 kHz Steered to -30° and 0°

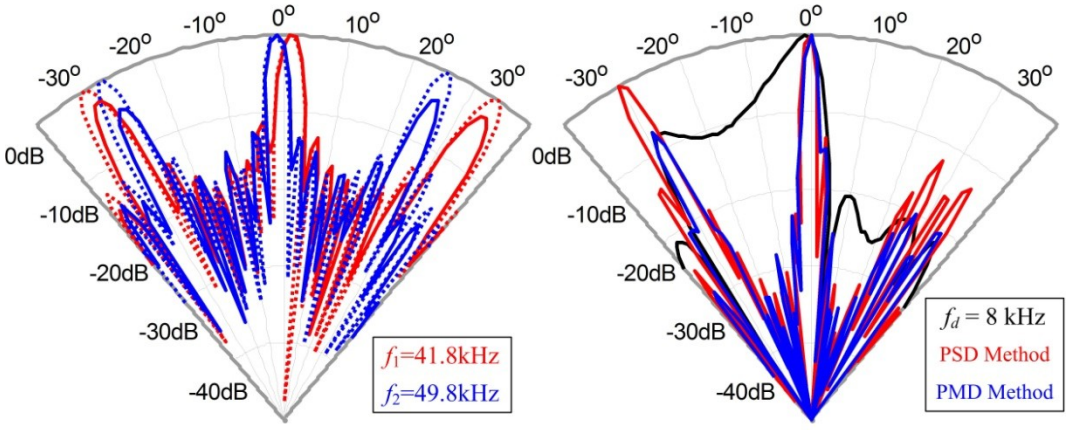

(e) PF Waves Generating DF Wave of 8 kHz

(f) DF Wave of 8 kHz Steered to -30° and 0°

Figure 5.18 Measured PF and DF beampatterns when the UTA consists of 8 channels with spacing of 1.5 cm and the dual beams are generated in the symmetric structure at -30° and 0°.

5.5 Conclusions

In this chapter, the feasibility of generating dual sound beams from a single steerable parametric loudspeaker without changing its hardware configuration was studied. A symmetric structure was proposed for dual-beamsteering. The spatial aliasing of the DF wave was exploited to generate the second beam that was resulted from the grating lobes of the PF waves. By adjusting the center frequency of the PF waves, the proposed symmetric structure was able to deliver identical audio content to any two directions with certain angular separation. Furthermore, the grating lobe elimination analysis was extended to the symmetrical structure. Design guidelines of the dual-beam generation were provided by considering the limited frequency bandwidth and the grating lobe elimination in the parametric loudspeaker.

Three cases were observed for an 8-channel UTA with equal weighting. When the spacing of the UTA is given by 1 cm (typical diameter of the ultrasonic transducer) and the operating frequency is from 30 kHz to 50 kHz, the separation between the dual beams of the DF wave ranges from 40° to 70° and grating lobes does not occur in the visible region between ±45°. When the spacing is extended to 1.5 cm (*i.e.* 1.75 times the wavelength of the PF wave at 40 kHz), the separation between the dual beams of the DF wave ranges from 26.5° to 45° and grating lobes are observed in the visible region between ±45° for the DF lower than 5% of the center frequency. The grating lobe elimination occurs for the DF wave ranging from 5% to 11.5% of the center frequency when the UTA consists of

8 channels and the equal weights are adopted.

Lastly, simulation and measurement results were presented to show that the proposed symmetric method effectively generated dual beams with different configurations of the UTA. It was also shown that the symmetric structure achieved higher and more consistent dual beams of the DF wave compared to the direct structure under the same power consumption.

Chapter 6
Product Directivity Models for the Parametric Loudspeaker

In the previous chapter, based on the product directivity principle, the simulated DF beampatterns are able to match the measured DF beampatterns with relatively high accuracies in the vicinities of their mainlobes and grating lobes. However, the matching accuracy drops significantly in the vicinities of most sidelobes. Hence, in this chapter, the theory behind the product directivity principle is revisited to demonstrate the relation between the PF and DF beampatterns. By accounting for the radii of the equivalent Gaussian sources, three modifications of the product directivity principle are proposed and given in (i) the advanced product directivity (APD) model, (ii) the exponential product directivity (EPD) model, and (iii) the combined product directivity (CPD) model. By using these proposed models, matching accuracies between the simulated and measured DF beampatterns are observed to be increased in the vicinities of the sidelobes

This chapter is organized as follows. The theory behind the product directivity principle is revisited. Three variants are derived and proposed in Section 6.1. The measured PF and DF beampatterns are compared with the simulated beampatterns based on the three variants of the product directivity principle in Section 6.2. An

envelope method is proposed and discussed in Section 6.3, which suggests using the envelope of the product directivity principle or its variants in simulation to model the relation between the PF and DF beampatterns. Finally, Section 6.4 summarizes the key findings of this chapter.

6.1 Product Directivity Models

The nonlinear effect produced by two sound beams whose axes intersect at nonzero angles is referred as scattering of sound by sound [DaH90]. The nonlinear interaction region is formed by the intersection of two PF beams. When Gaussian beams are assumed, a closed-form solution to the KZK equation shows that the far-field DF directivity is given by the product of the directivities of the Gaussian beams regardless of whether the PF sources are displaced or steered. This solution is known as the product directivity principle (or PD model). The PD model has been commonly used to predict the DF beampatterns of the steerable parametric loudspeaker in simulation. However, the simulated DF beampatterns usually do not match the measured DF beampatterns perfectly. In order to solve this practical problem, the theory behind the PD model is revisited to derive some modifications that are more applicable to the steerable parametric loudspeaker.

The following analysis is derived based on {Eqs. (20) and (24) in [DaH90]}. Two Gaussian beams of the PF waves are assumed to be concentric but steered to separate directions, as shown in Fig. 6.1. The function $\Gamma(\theta)$ is defined to show the relative strength of the scattered sound field and given by

$$\Gamma(\theta)=\frac{i\left[(z_1+z_2)\tan\theta-(z_1-z_2)\sin\theta_0\right]}{\sqrt{a_1^2+a_2^2}}, \tag{6.1}$$

where z_1 and z_2 are the Rayleigh distances of the Gaussian beams at the two PFs, respectively; $2\theta_0$ is the intersection angle of the two Gaussian beams. When $\Gamma(\theta)$ is sufficiently large ($\Gamma(\theta)>>1$), an explicit expression for the nonlinearly generated sound field can be obtained as

$$\begin{aligned} p_d(\theta,r)\sim\ & k_2k_da_1^2a_2^2\exp\left(ik_dr\tan^2\theta/2\right) \\ & \times\frac{1}{8z}\left\{D_1(\theta)D_2(\theta)E_1\left[\frac{ik_1k_2\left(a_1^2+a_2^2\right)\Gamma^2(\theta)}{2k_dr}\right]-\frac{D_s(\theta)}{\Gamma^2(\theta)}\right\}, \end{aligned} \tag{6.2}$$

where $p_d(\theta,r)$ is the complex pressure of the DF wave at angle θ and distance r; p_1 and p_2 are the on-source pressures of the two Gaussian beams; a_1 and a_2 are the radii of the two Gaussian beams; $D_1(\theta)$ and $D_2(\theta)$ are the directivities of the two Gaussian beams, given by (3.8); $D_s(\theta)$ is the directivity of the scattered sound; and $E_1(\bullet)$ is the exponential integral.

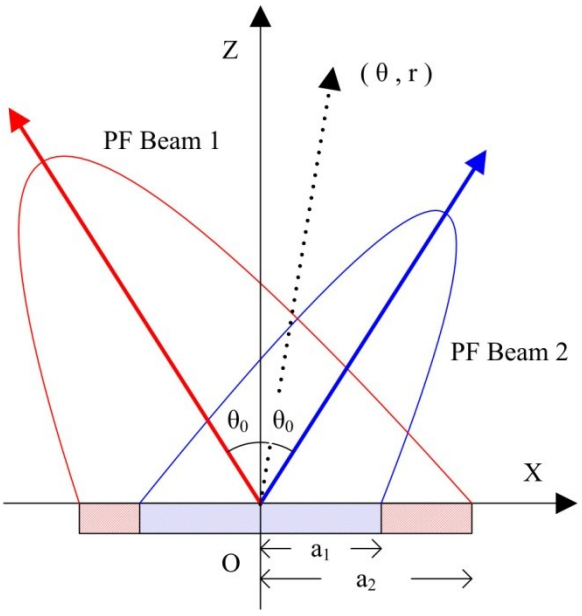

Figure 6.1 Geometry of two intersecting Gaussian beams.

Note that the exponential integral can be extended and approximated as

$$E_1(x) = \frac{\exp(-x)}{x} \sum_{n=0}^{N-1} \frac{n!}{(-x)^n} \approx \frac{\exp(-x)}{x}, \quad \forall |x| >> 1. \tag{6.3}$$

Furthermore, when x is purely imaginary and has large magnitude, (6.3) can be approximated by $|E_1(x)| \approx 1/x$. Using this approximation, it is obtained that

$$\left| E_1\left[\frac{ik_1 k_2 \left(a_1^2 + a_2^2\right) \Gamma^2(\theta)}{2k_d z} \right] \right| \approx \frac{2k_d z}{k_1 k_2 \left(a_1^2 + a_2^2\right) \left|\Gamma^2(\theta)\right|}. \tag{6.4}$$

Substitute (6.4) into (6.2), the absolute values on both sides of (6.4) give

$$\left| p_d(\theta, z) \right| \sim \frac{a_1^2 a_2^2}{\left(a_1^2 + a_2^2\right)} \frac{D_1(\theta) D_2(\theta)}{\left|\Gamma^2(\theta)\right|}. \tag{6.5}$$

As $\Gamma(\theta)$ is assumed to be sufficient large (referring to {Eq. (31) in [DaH90]}), $|\Gamma(\theta)|^2$ can be treated as a constant value when θ is limited within a small range. Hence, the APD model is proposed based on (6.5) for the DF wave generated from the two Gaussian beams, where the DF directivity is given by

$$D_{diff}(\theta) = \frac{a_1^2 a_2^2}{a_1^2 + a_2^2} p_1 D_1(\theta) p_2 D_2(\theta). \tag{6.6}$$

When two sine waves are used as the PF waves, the frequency components are similar to the modulated wave of the SSBAM. In the Berktay's far-field solution [Ber65b], the demodulated wave is proportional to the second-time derivative of the square of the envelope of the modulated wave. Thus, the contribution to the SPL generated by the parametric array is proportional to the square of the DF, *i.e.* f_d^2. In other words, the SPL of the DF wave increases by 12 dB per octave. However, in the numerical simulation and measurement carried out by Wygant *et al.* [WKW09], the results indicated that the SPL of the DF wave

increased by only 9 dB per octave, which corresponded to the frequency dependence of $f_d^{1.5}$. Hence, the SPL of the DF wave is suggested to be proportional to f_d^n, where n depends primarily on the ratio of the Rayleigh distance (*i.e.* the area of the emitter divided by the wavelength of the PF wave) to the absorption distance (*i.e.* half the reciprocal of the absorption coefficient at the PF). $n=2$ is a good approximation to the frequency dependence in (2.2), which is originally reported by Westervelt [Wes63]. However, $n=1$ gives a closer approximation to the frequency dependence for the case of highly nonlinear distortion, such as the solution obtained by Berktay and Leahy [BeL74] and the experimental results obtained by Vos *et al.* [VGV11].

Based on the aforementioned methodology, another modification to the PD model is proposed. This model is referred as the EPD model, and can be written as

$$D_{diff}(\theta)=f_d^n p_1 D_1(\theta) p_2 D_2(\theta), \tag{6.7}$$

where $1\le n\le 2$ is the tuning factor.

Similarly, as wavenumber is proportional to frequency, k_d^2 in (6.5) can be substituted by k_d^n. Thus, the CPD model combines the APD and EPD models, and derived as

$$D_{diff}(\theta)=f_d^n \frac{a_1^2 a_2^2}{a_1^2+a_2^2} p_1 D_1(\theta) p_2 D_2(\theta). \tag{6.8}$$

6.2 Measurement Results

The measurements are carried out using the setup introduced in Section 3.4.

The column configuration with spacing of 1 cm is adopted for the UTA, which is shown in Appendix B. The PF waves are measured at (a) 36 kHz, (b) 38 kHz, (c) 39 kHz, (d) 40 kHz, (e) 42 kHz, and (f) 44 kHz. When $H(\omega,\theta)$ in (3.9) is given by the measured PF beampatterns, the configurations of their equivalent Gaussian source arrays are obtained and shown in Fig. 6.2. The radii of Gaussian sources (in cm) are labeled next to their equivalent lobes. The Gaussian sources equivalent to the mainlobes and grating lobes are observed to have relatively smaller radii, due to their wider beamwidths compared to the sidelobes. At the troughs between two lobes, certain mismatches are observed. However, these mismatches are negligible, because they only occur when the normalized amplitudes of the lobes are lower than 0.1 (*i.e.* -20 dB). The least-squares curve fitting approach, expressed as (3.9), is proven to be adequate to derive the equivalent Gaussian source arrays matching the PF beampatterns of the steerable parametric loudspeaker.

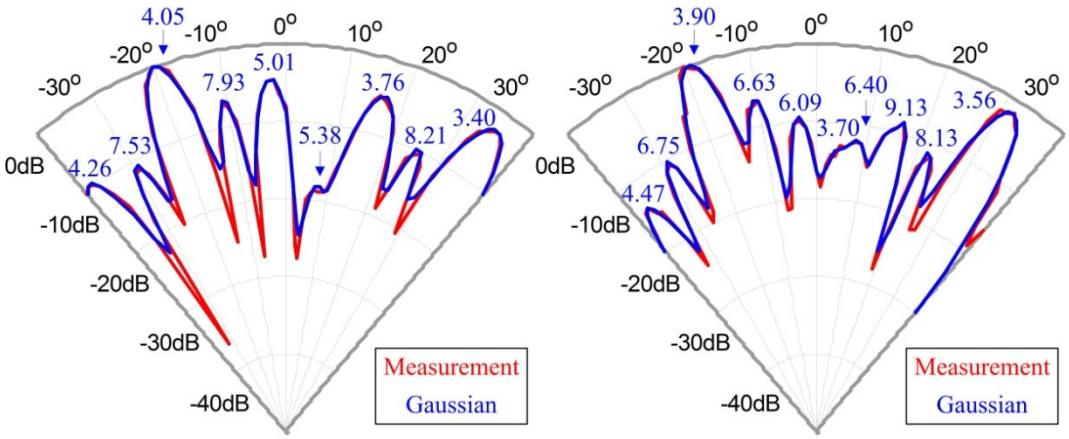

(a) PF Wave at 36 kHz

(b) PF Wave at 38 kHz

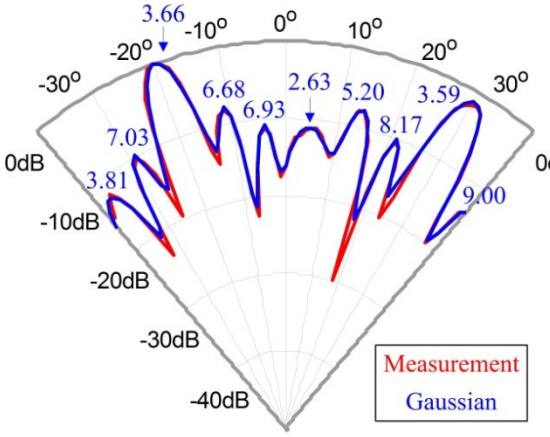

(c) PF Wave at 39 kHz

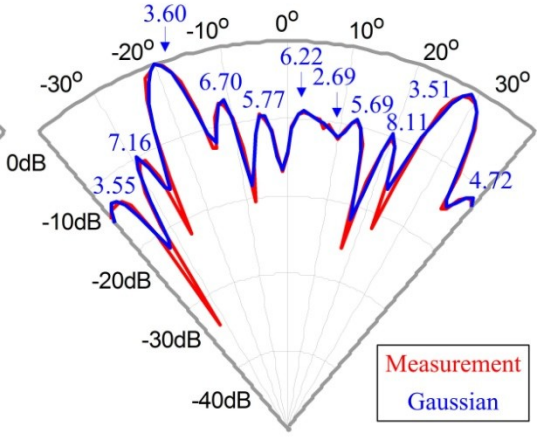

(d) PF Wave at 40 kHz

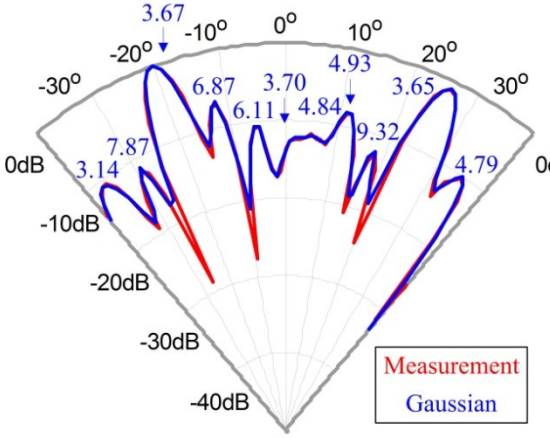

(e) PF Wave at 42 kHz

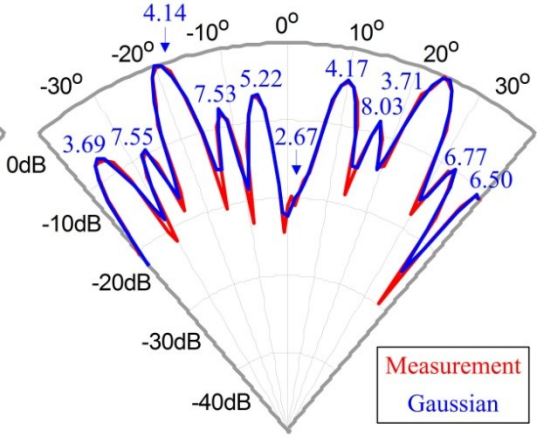

(f) PF Wave at 44 kHz

Figure 6.2 Measured PF beampatterns and beampatterns of their equivalent Gaussian source arrays, in which the radii of the Gaussian sources (in cm) are labeled next to the equivalent lobes.

From the aspect of complexity, the PD model can be readily applied, as long as the PF beampatterns are known. In contrast, the APD model requires an additional step to compute the configurations of the equivalent Gaussian source arrays of the measured PF beampatterns. Subsequently, the APD model is applied to every two Gaussian sources in the configurations and the computed sound fields are summed together to obtain the DF beampattern. Moreover, due to the fact that the EPD and CPD models introduce the tuning factor n in their expressions, the tuning factor has to be determined before the EPD and CPD models are applied. As mentioned in the previous section, n depends primarily on the ratio of the Rayleigh distance to the absorption distance. In our measurements, the PF waves are generated within a narrow band centered at 40 kHz. Thus, the absorption distance is assumed to be constant. However, for computing the Rayleigh distance, the intersection of two Gaussian sources is treated as the area of the emitter rather than considering the size of the UTA. Therefore, as the area of the emitter is proportional to the product of the radii of the two Gaussian sources, the tuning factor is proposed in the form of

$$n = \varepsilon a_1 a_2 + 1, \tag{6.9}$$

where ε is computed from the measured DF beampatterns at 8 kHz. For the EPD model, $\varepsilon = 39.4$; and for the CPD model, $\varepsilon = 7.8$. Hence, the EPD and CPD models are used to predict the DF beampatterns at 1 kHz and 4 kHz based on the determined turning factor.

The simulated beampatterns using different PD models (including the original

PD, APD, EPD, and CPD models) are compared with the measured beampatterns. The DF waves are generated at 1 kHz, 4 kHz, and 8 kHz, and their beampatterns are shown in Fig. 6.3, Fig. 6.4, and Fig. 6.5, respectively. The tuning factors for the EPD and CPD models are determined based on the measured beampatterns of the DF wave at 8 kHz. Thus, the simulated beampatterns using the EPD and CPD models when the DF wave is generated at 8 kHz are plotted for reference only in Fig. 6.5, but they are not applicable for comparison. Table 6.1 lists the normalized amplitudes of selected sidelobes (labeled as "S1", "S2", "S3", and "S4") and the grating lobe (labeled as "G") in the simulated and measured beampatterns. The measured beampattern is abbreviated as "MP" in figures and tables.

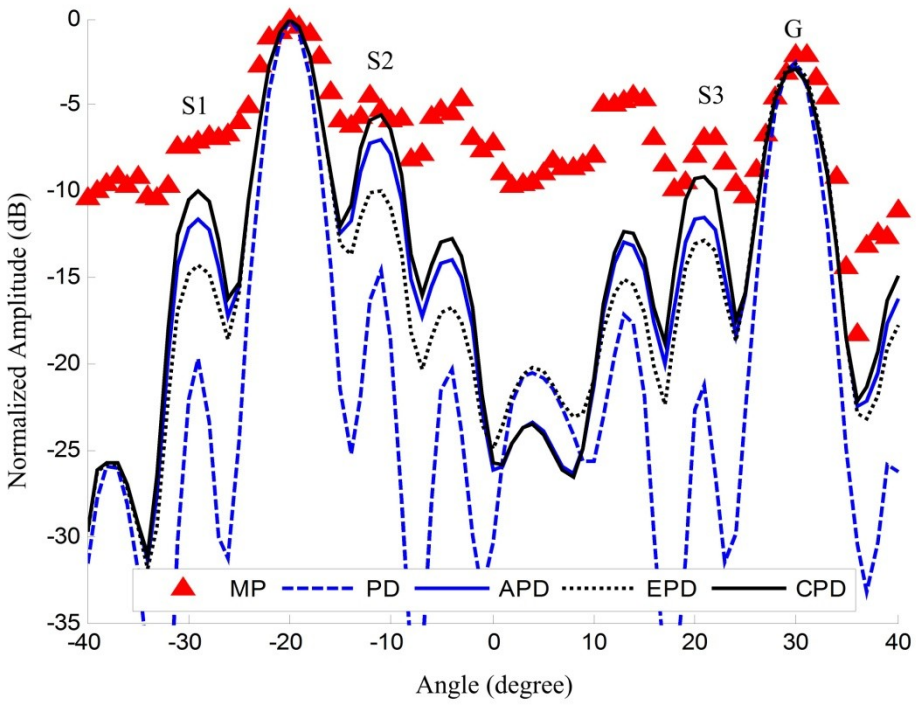

Figure 6.3 Comparison between the simulated beampatterns using the PD, APD, EPD, and CPD models versus the measured beampattern of the DF wave at 1 kHz.

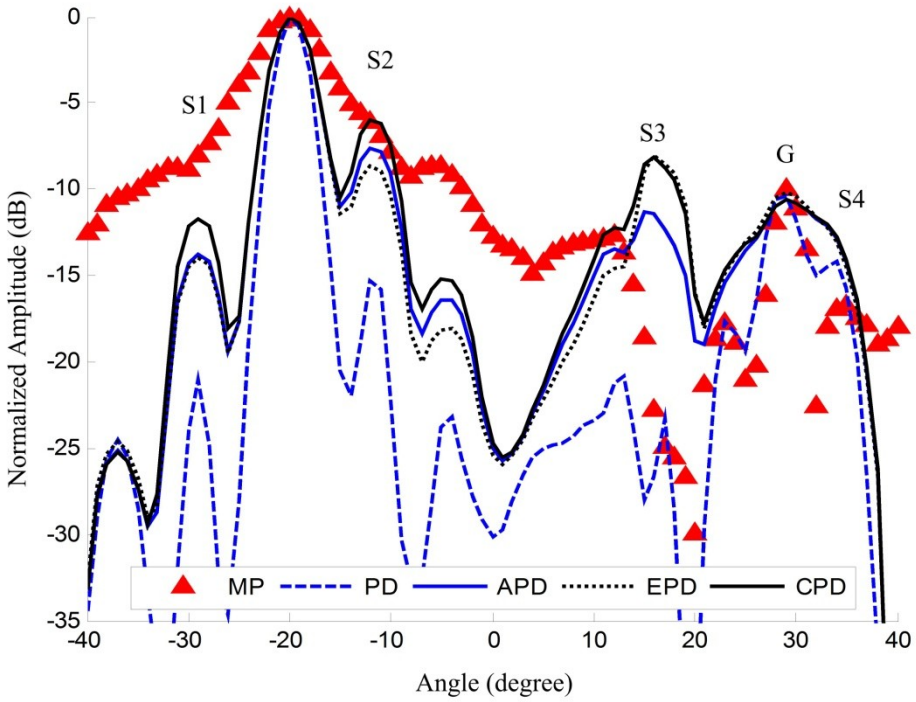

Figure 6.4 Comparison between the simulated beampatterns using the PD, APD, EPD, and CPD models versus the measured beampattern of the DF wave at 4 kHz.

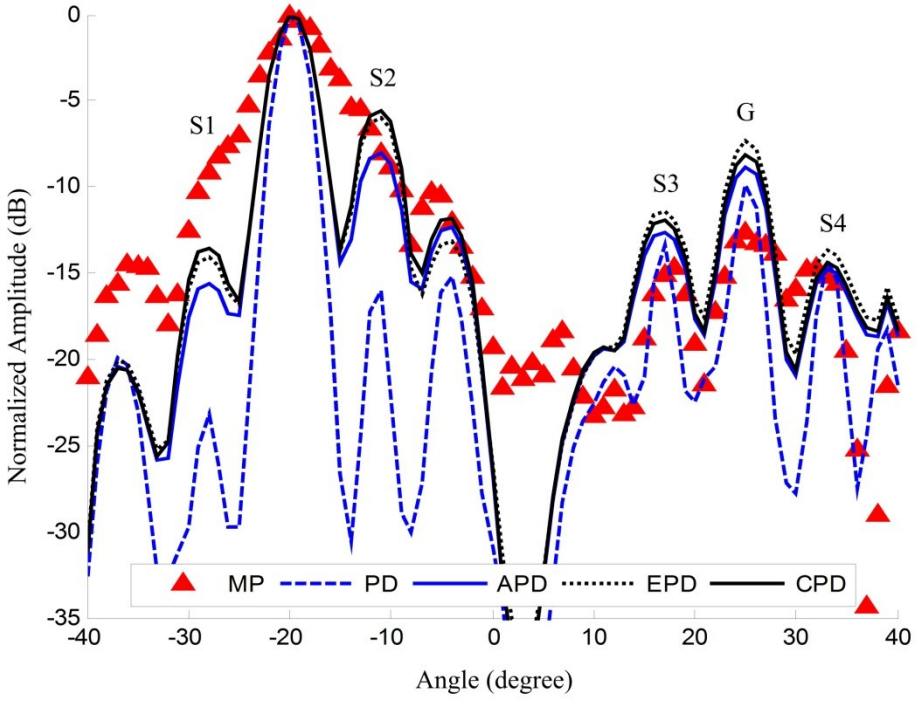

Figure 6.5 Comparison between the simulated beampatterns using the PD, APD, EPD, and CPD models versus the measured beampattern of the DF wave at 8 kHz.

Table 6.1 Normalized amplitudes of the grating lobes and selected sidelobes in the simulated beampatterns using the PD, APD, EPD, and CPD models versus those in the measured beampatterns of the DF waves.

1 kHz	S1 (-29°)	S2 (-12°)	S3 (21°)	G (30°)	
MP (dB)	-7.087	-4.46	-6.95	-2.087	
PD (dB)	-20.91	-15.94	-21.42	-3.317	
APD (dB)	-11.69	-7.387	-11.37	-2.864	
EPD (dB)	-14.19	-10.17	-12.36	-2.591	
CPD (dB)	-10	-6.012	-8.934	-2.894	
4 kHz	S1 (-29°)	S2 (-12°)	S3 (23°)	G (29°)	S4 (35°)
MP (dB)	-8.073	-6.127	-17.77	-9.983	-16.78
PD (dB)	-22.45	-14.81	-17.45	-9.577	-16.57
APD (dB)	-13.77	-7.595	-15.19	-9.466	-13.88
EPD (dB)	-13.79	-8.536	-14.58	-9.652	-14.51
CPD (dB)	-11.67	-5.957	-14.37	-9.409	-13.64
8 kHz	S1 (-28°)	S2 (-11°)	S3 (17°)	G (25°)	S4 (33°)
MP (dB)	-9.17	-8.07	-15.06	-12.66	-15.24
PD (dB)	-22.74	-16.06	-13.98	-10.74	-14.36
APD (dB)	-15.67	-8.036	-12.66	-8.822	-14.78

In Fig. 6.3, the simulated beampattern using the CPD model provides the best match to the measured beampattern in the vicinities of the three sidelobes labeled as "S1", "S2", and "S3". The simulated beampatterns using the APD and EPD models provide comparatively good matches to the measured beampattern in the vicinities of these three sidelobes as well. Significant improvements are observed when the simulated beampatterns using the three proposed models are compared with that using the original PD model in the vicinities of the sidelobes. However, in the vicinity of the grating lobe, the increase in matching accuracy is moderate, because the simulated beampattern using the PD model has already provided sufficiently good match to the measured beampattern.

In Fig. 6.4, the simulated beampattern using the CPD model provides the best match to the measured beampattern in the vicinities of the two sidelobes that are adjacent to the mainlobe and labeled as "S1" and "S2". The simulated beampattern using the PD model provides the best match to the measured beampattern in the vicinities of the other two sidelobes that are adjacent to the grating lobe and labeled as "S3" and "S4". The simulated beampatterns using the three proposed models have similar results in the vicinity of the grating lobe, which are not as accurate as that using the PD model in matching the measured beampattern.

Figure 6.5 shows the simulated and measured beampatterns of the DF wave at 8 kHz. As mentioned above, only the simulated beampatterns using the PD and APD models are included in the comparison. The simulated beampattern using the APD model provides a better match to the measured beampattern in the vicinities

of the three sidelobes labeled as "S1", "S2", and "S4". However, the one using the APD model provides a better match in the vicinities of the grating lobe and the sidelobes labeled as "S3".

It is seen from the above comparative results that the simulated beampatterns using the proposed models give better matches to the measured DF beampatterns in the vicinities of the sidelobes adjacent to the mainlobe. When the grating lobe elimination occurs, the simulated beampatterns using the PD model can accurately match the measured DF beampatterns in the vicinities of the grating lobes and the sidelobes adjacent to the grating lobes. However, the prediction of the eliminated grating lobe is not essential to the beampattern design of the steerable parametric loudspeaker. The simulated beampatterns using the CPD model are found to give the highest overall matching accuracy to the measured DF beampatterns, compared with the simulated beampatterns using the EPD model, which are only able to match the measured DF beampatterns accurately in the vicinities of the grating lobes. In the end, when the trade-off between matching accuracy and ease of use is considered, the APD model is recommended due to its better average matching performance with ease of application.

6.3 Discussion on Envelopes of the Product Directivity Models

The discussion in this section is motivated by some observations in previous measurements, particularly when the recording room is not perfectly anechoic for measurement over the combined frequency range of the PF and DF waves. Firstly,

the mainlobes' beamwidths were observed to be wider in the measured DF beampatterns than in the simulated DF beampatterns. Secondly, sidelobes occurred in the simulated DF beampatterns, but were rarely observed in the measured DF beampatterns. Thirdly, the simulated DF beampatterns matched the measured DF beampatterns more accurately at local peaks (including the peaks of the mainlobe, the grating lobes and the sidelobes), compared to other angular directions. Thus, from an engineering aspect, an envelope method, which uses the envelope of the PD model as the prediction of the DF beampattern, is proposed. This envelope method is applicable to all the proposed PD models as well. In particular, the envelope method targets to provide an improved estimation of the beamwidth of the mainlobe.

The theoretical basis of the envelope method is stated as below. The acoustic field produced by two Gaussian beams is known to consist of the scattered wave and the pumped wave [DaH90]. The scattered wave is generated entirely in the near-field and cannot be ignored until hundreds of Rayleigh distances away from the sources. However, the pumped wave continuously receives energy from the PF waves, and its beampattern is dependant only on the product directivity of the two Gaussian beams. In typical applications of the steerable parametric loudspeaker, the listener is only few meters away from the UTA. This distance is usually between the Rayleigh distance (less than 4 meters as shown in Fig. A.1) and the absorption distance (3 to 6 meters as shown in Fig. A.2). In this case, the scattered wave is generated and forms the acoustic field together with the pumped wave.

The PD model may not be adequate to approximate the DF beampattern generated from the two Gaussian beams. It was noted by Berntsen *et al.* [BTT89] that scattered SF wave was to be found in the angular region delimited by the axis of the PF beams, but the scattered DF wave was to be found outside that region. When the scattered wave cannot be spatially separated from the pumped wave, a broader mainlobe of the DF wave is expected. This explanation coincides with the measurement results obtained by Muir and Willette [MuW72] and is also reflected in Figs. 6.3-6.5. These measurement results show that the amplitudes of the local peaks derived by the PD model match the measured values accurately. This is probably due to the pumped wave that plays a dominating role on the axis of the PF beams. Moreover, since the sidelobes are rarely observed, the measured DF beampattern shows up as monotonic outside the local peaks, which is most likely due to the co-existence of the pumped and scattered waves.

The envelope method is applied in the simulation. New simulation results are obtained and compared with the same measurement results plotted in Figs. 6.3-6.5. The simulated DF beampatterns using the envelopes of the PD models (including the original PD, APD, EPD and CPD models) are compared with the measured DF beampattern at 1 kHz, 4 kHz, and 8 kHz. Their corresponding beampatterns are plotted in Fig. 6.6, Fig. 6.7, and Fig. 6.8, respectively. Table 6.2 lists the mainlobes' beamwidths in the simulated (before and after applying the envelope method) and measured beampatterns. In Fig. 6.6, the simulated beampattern using PD (Envelope) model provides the best match to the measured beampattern in the

vicinities of the mainlobe and the grating lobe. In Fig. 6.7, the simulated beampattern using the CPD (Envelope) model provides the best match to the measured beampattern in the vicinity of the mainlobe, while that using the PD (Envelope) model still gives a close match to the measured beampattern in the vicinity of the grating lobe. In Fig. 6.8, the simulated beampattern using the EPD (Envelope) model gives the best match to the measured beampattern in the vicinity of the mainlobe, and it is followed by that using the CPD (Envelope) model. In general, the envelope method improves the matches between the simulated and measured beampatterns. However, none of these models can be used to simulate the DF beampattern that is an exact prediction to the measured DF beampattern. Choosing a PD model in the design of steerable parametric loudspeaker remains a trade-off between matching accuracy and ease of use. The PD and APD models are preferred for the absence of tuning factors in their expressions. After applying the envelope method, the APD model outperforms the PD model in terms of the average matching performance. Thus, the APD (Envelope) model will be used to simulate the DF beampatterns in the next chapter.

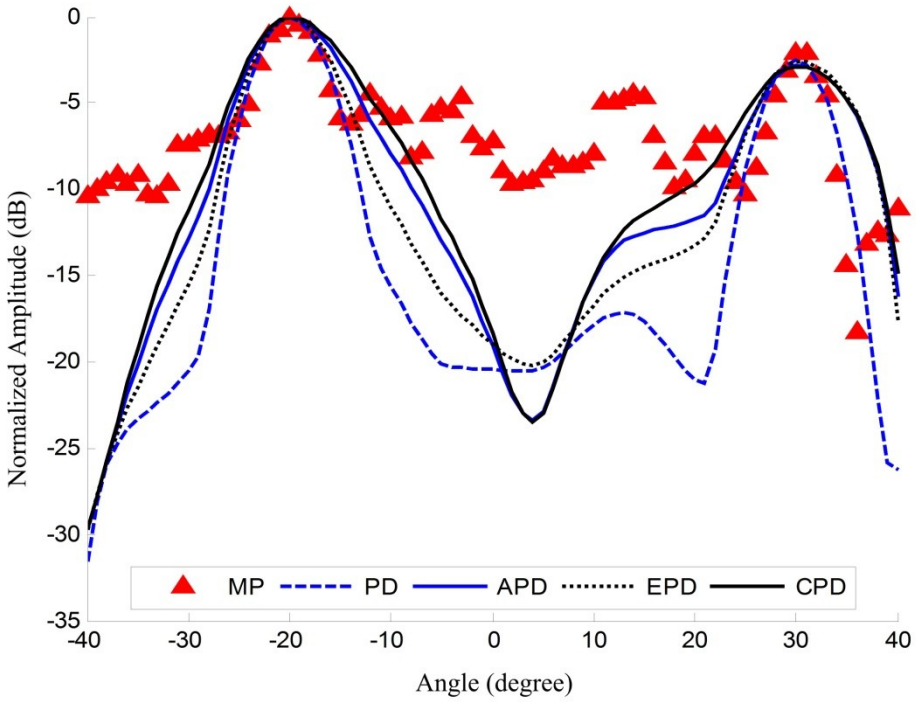

Figure 6.6 Comparison between the simulated beampatterns using the envelope method versus the measured beampattern of the DF wave at 1 kHz.

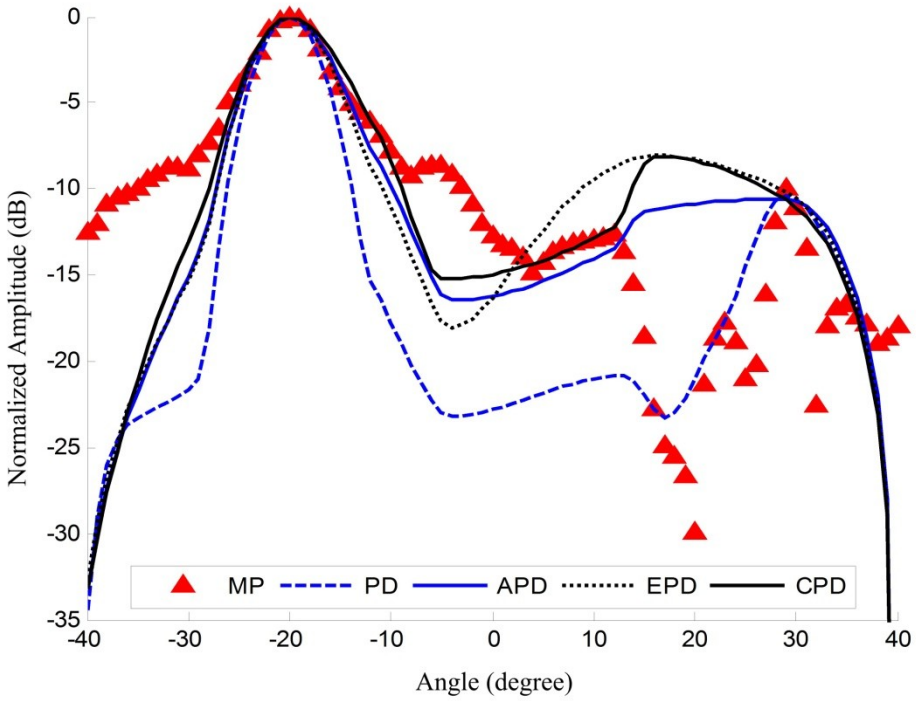

Figure 6.7 Comparison between the simulated beampatterns using the envelope method versus the measured beampattern of the DF wave at 4 kHz.

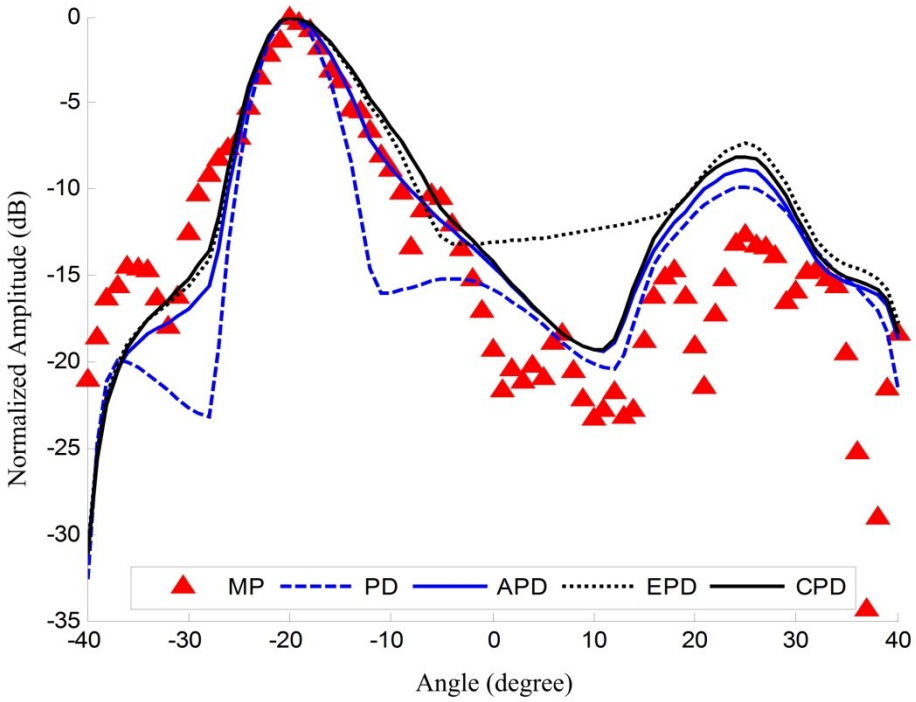

Figure 6.8 Comparison between the simulated beampatterns using the envelope method versus the measured beampattern of the DF wave at 8 kHz.

Table 6.2 6 dB beamwidths (in degree) of the mainlobes in the simulated beampatterns using different PD models and the envelope method versus those in the measured beampatterns of the DF waves.

Model (Method)	1 kHz	4 kHz	8 kHz
MP	10.08°	14.88°	13.98°
PD	5.55°	5.23°	5.83°
APD	6.34°	6.73°	6.22°
EPD	6.33°	6.72°	6.22°
CPD	6.34°	6.74°	6.22°
PD (Envelope)	10.69°	10.00°	9.30°
APD (Envelope)	13.98°	12.40°	11.91°
EPD (Envelope)	12.00 °	11.79°	13.93°
CPD (Envelope)	16.03°	14.04°	14.67°

6.4 Conclusions

In this chapter, three variants of the PD model were proposed, namely (i) the APD model, (ii) the EPD model, and (iii) the CPD model. The proposed variants of the PD model are based on the transformation of linear transducer array into an equivalent Gaussian source array. Thus, the radii of the equivalent Gaussian sources are taken into consideration in the proposed variants. In the comparison between simulation and measurement results, better predictions were obtained for

the DF beampatterns when using the proposed models. The proposed models outperformed the original PD model when being used to simulate the DF beampatterns in the vicinities of the sidelobes adjacent to the mainlobe. However, the PD model remains to be a good and simple model to be used in the vicinities of the eliminated grating lobes. The APD model is recommended for its good matching performance, and can be readily applied as soon as the PF beampatterns are known. Taking the environmental factors (such as the temperature and relative humidity of air) into consideration to achieve more accurate predictions, the CPD and EPD models require the tuning factors to be determined in advance using additional measurement results. In the discussion, the envelopes of the PD models were used to predict the DF beampatterns. The comparative results showed that the envelope method could improve the overall predictions of the DF beampatterns. By balancing the trade-off between accuracy and ease of use, the envelope of the APD model will be used to simulate the DF beampatterns in the following chapter.

Chapter 7
Analysis and Calibration of System Errors in the Parametric Loudspeaker

The spatial performance of the steerable parametric loudspeaker based on phased array techniques can be predicted through simulation in two steps: (1) to compute the PF beampatterns based on the UTA's configuration; (2) to simulate the DF beampatterns based on the computed PF beampatterns. In the previous chapter, the relation between the PF and DF beampatterns has been studied and some models have been proposed for the second step of the spatial performance simulation. Thus, in this chapter, the calibration method for the steerable parametric loudspeaker is carried out for the first step of the spatial performance simulation. A beamsteering structure is proposed for the steerable parametric loudspeaker to incorporate the spacing error, the weight error, the delay error, as well as the steering angle error caused by the channel directivity. The normalized amplitudes of the grating lobes are numerically analyzed for the DF wave when these four types of system errors are incurred in the PF waves. A combination of the Monte Carlo method and the nonlinear least-squares method is then proposed to calibrate a steerable parametric loudspeaker when its measured PF beampatterns are used as the working standard. Cross-validation of the calibration method is also

conducted and the mismatches between simulated and measured beampatterns are reduced for the PF waves as well as the DF waves after calibration.

This chapter is organized as follows. The proposed beamsteering structure and the analysis of system errors are presented in Section 7.1. It is followed by the description of the calibration algorithm for steerable parametric loudspeakers in Section 7.2. In Section 7.3, the calibration data is derived from the measurement results. The matching accuracy between the simulated and measured PF beampatterns is significantly improved after calibration. Using the APD (Envelope) model in simulation, the matching accuracy between the simulated and measured DF beampatterns is improved as well. Section 7.4 extends the spatial performance simulation from the case when two PF waves are used to generate the DF wave, to the cases when different preprocessing methods are applied for the steerable parametric loudspeaker. Section 7.5 concludes the main findings in this chapter.

7.1 Analysis of System Errors in the Parametric Loudspeaker

In practice, uncertainties exist in the positions of the ultrasonic transducers during the assembly of the UTA. The group of delays (or phases) and weights (or gains) applied to the UTA can deviate from the designed values, due to variable environmental conditions and inconsistent characteristics of the PZT transducers [JoD93]. Hence, it is impractical to calibrate the steerable parametric loudspeaker by examining each single transducer in the UTA. The proposed calibration method in this chapter categorizes the possible system errors into four types related to the

spacing, the weight, the delay, and the directivity of each channel.

7.1.1 Conventional array errors

A modified beamsteering structure is proposed for the analysis of the system errors, as shown in Fig. 7.1, where d_m is the spacing of the UTA, which includes the spacing error; $\hat{w}_m$ is the distorted weight of the m th channel; and $\hat{\tau}_m$ is the distorted delay amount of the m th channel, for $m = 0,\ 1,\ 2,\ \cdots$.

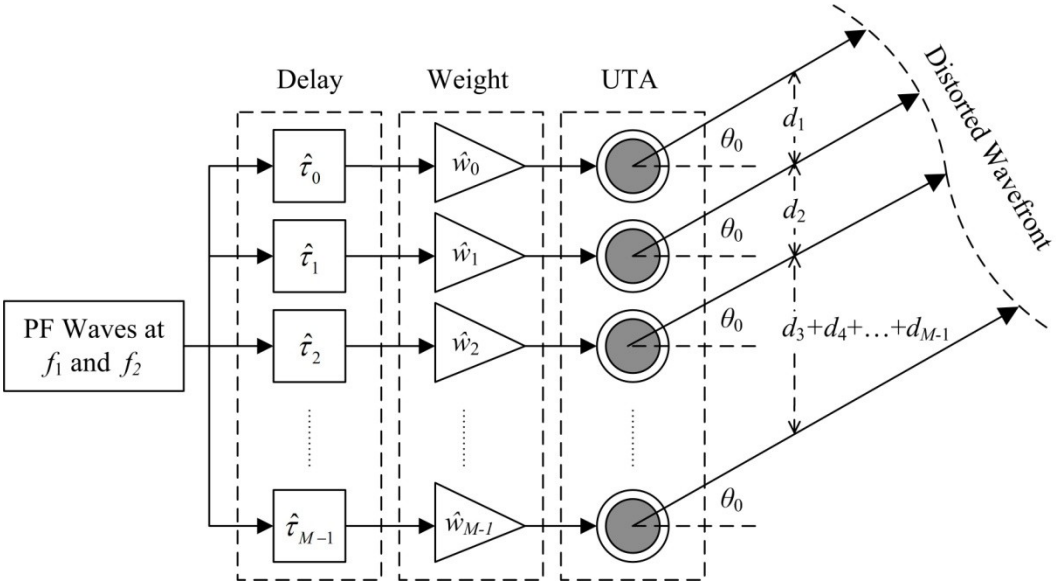

Figure 7.1 Structure of the steerable parametric loudspeaker where the spacing, weight, and delay errors are incurred.

It is also useful to note that the spacing error, the weight error and the delay error are not unique problems in the steerable parametric loudspeaker, but are also commonly found in other kinds of sensor arrays [JoD93]. For example, several calibration techniques were developed for the antenna arrays [AFW89, See94, GBE03, Kei11]. However, in the steerable parametric loudspeaker, the system errors cause direct distortions in the PF beampatterns, which subsequently result

in the distortions of the DF beampatterns. Since the analytical expressions of the DF beampattern are not analytically obtained, numerical simulations are carried out to evaluate the grating lobes in amplitude when system errors are incurred as illustrated in Fig. 7.1.

In the simulations, the UTA consists of 8 channels with the spacing of 1 cm. The PF waves are generated at symmetric frequencies with reference to the center frequency of 40 kHz, and the DF waves range from 0 to 20 kHz. Different types of system errors are simulated separately and generated based on the normal (or Gaussian) distribution with zero mean and variances decided by the limitations of the errors according to the empirical rule. As introduced in previous chapters, the grating lobe elimination occurs when the angular distance is sufficiently large. When the grating lobes of the PF waves are not far apart from each other, it results in the partial grating lobe elimination. Figure 7.2 shows the levels of grating lobe elimination when different levels of system errors are incurred in the steerable parametric loudspeaker. The grating lobe elimination is greatly weakened when the spacing errors increase, because the spacing errors affect the locations of the grating lobes of the PF waves, which are critical to the occurrence of grating lobe elimination. The delay errors degrade the level of grating lobe elimination more significantly than the spacing errors. When the limitations of the delay errors are set to 10% and 15%, the grating lobes are observed to achieve higher amplitudes than the mainlobes at certain DFs. In contrast, the grating lobe elimination is robust to the weights errors, because the weight errors only change the amplitudes

of the sidelobes of the PF waves.

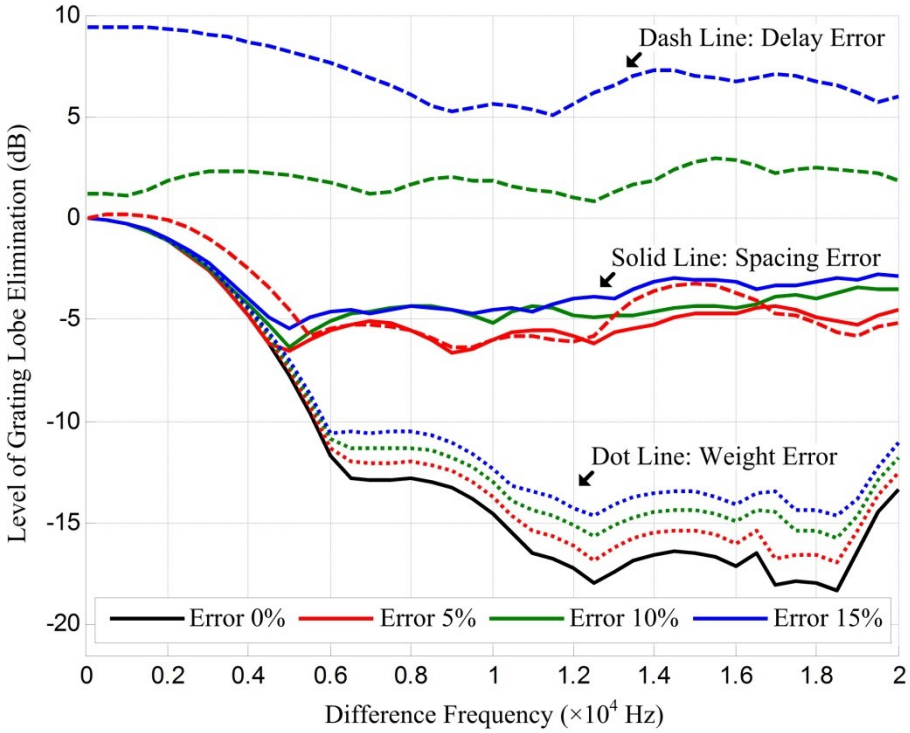

Figure 7.2 Levels of grating lobe elimination when system errors are incurred in the UTA with 8 channels and spacing of 1 cm.

7.1.2 Steering angle error

In practice, the typical bell-shaped channel directivity can be considered as an additional spatial filter to the PF beampatterns. This additional spatial filter results in steering angle errors in the PF and DF beampatterns. The steering angle error is defined as the difference between the desired steering angle and the actual steering angle. To simplify the analysis of the steering angle error, the channel directivity is modeled by the Gaussian directivity. Based on the product directivity principle, the DF beampattern is given by the product of four terms as follows:

$$D_{diff}(\theta) = D_G(\omega_1,\theta)H(\omega_1,\theta)D_G(\omega_2,\theta)H(\omega_2,\theta), \tag{7.1}$$

where $D_G(\omega,\theta)$ is the Gaussian directivity, given by (3.8); $H(\omega,\theta)$ is the beampattern of the PF wave, given by (3.10).

The actual steering angle is found at the location of nulls for the derivative of the DF beampattern with respect to θ near the desired steering angle. Since the steering angle error is relatively small, it is approximated that the amplitude of the PF beampattern at the actual steering angle θ_{ac} is close to the amplitude at the desired steering angle, *i.e.* $H(\omega,\theta_{ac}) \approx H(\omega,\theta_0)$. Furthermore, assuming that equal weights are used in the UTA and the number of channels is even, the derivative of (7.1) can be approximated by

$$\begin{aligned}\frac{\partial D_{diff}(\theta)}{\partial\theta} \cong \exp\left(-\frac{\omega_1^2+\omega_2^2}{4c_0^2}a^2\tan^2\theta\right) \\ \times\left[\frac{\partial H(\omega_1,\theta)}{\partial\theta}+\frac{\partial H(\omega_2,\theta)}{\partial\theta}-\frac{\omega_1^2+\omega_2^2}{4c_0^2}a^2\tan\theta\sec^2\theta\right].\end{aligned} \tag{7.2}$$

For arbitrary small angle, $\sin\varphi \approx \varphi$ is valid. Since the steering angle error is relatively small, *i.e.* $\sin\theta_{ac} - \sin\theta_0 \approx 0$, the derivative of the PF beampattern with respect to θ can be simplified to

$$\frac{\partial H(\omega,\theta)}{\partial\theta} = -2\sum_{m=1}^{\frac{M}{2}}\left[\left(m-\frac{1}{2}\right)^2\omega^2\frac{d^2}{c_0^2}\cos\theta\left(\sin\theta-\sin\theta_0\right)\right]. \tag{7.3}$$

By substituting (7.3) into (7.2) and setting the right-hand side of (7.2) to zero, the implicit formula for estimating the actual steering angle θ_{ac} is obtained as

$$\sin\theta_0 = \sin\theta_{ac}\left(1+\frac{6a^2}{\left(M^2-1\right)d^2\cos^4\theta_{ac}}\right). \tag{7.4}$$

Equation (7.4) shows that the steering angle error is frequency-invariant due to the absence of the frequency angular terms. It is also observed that the steering

angle error increases: (i) when lesser channels are used in the UTA; (ii) when the absolute value of the steering angle increases; (iii) when the channel directivity is relatively sharper (*i.e.* the radius of the Gaussian source that models the channel directivity increases).

The steering angle errors are simulated and plotted in Fig. 7.3 for different numbers of channels when equal weights are used in the UTA. The radius of the Gaussian source is set to 2.5 mm, which leads to the channel directivity having a 3dB-beamwidth of 65^{o} at 40 kHz. In particular, when there are 4 channels in the UTA with spacing of 1 cm and the desired steering angle is 20°, the steering angle error is estimated to be 0.64°, which corresponds to a constant of 3.15% delay error to each channel. When there are 8 channels in the UTA with spacing of 0.5 cm and the desired steering angle is 20°, the steering angle error is estimated to be 0.61°, which corresponds to a constant of 3% delay error to each channel.

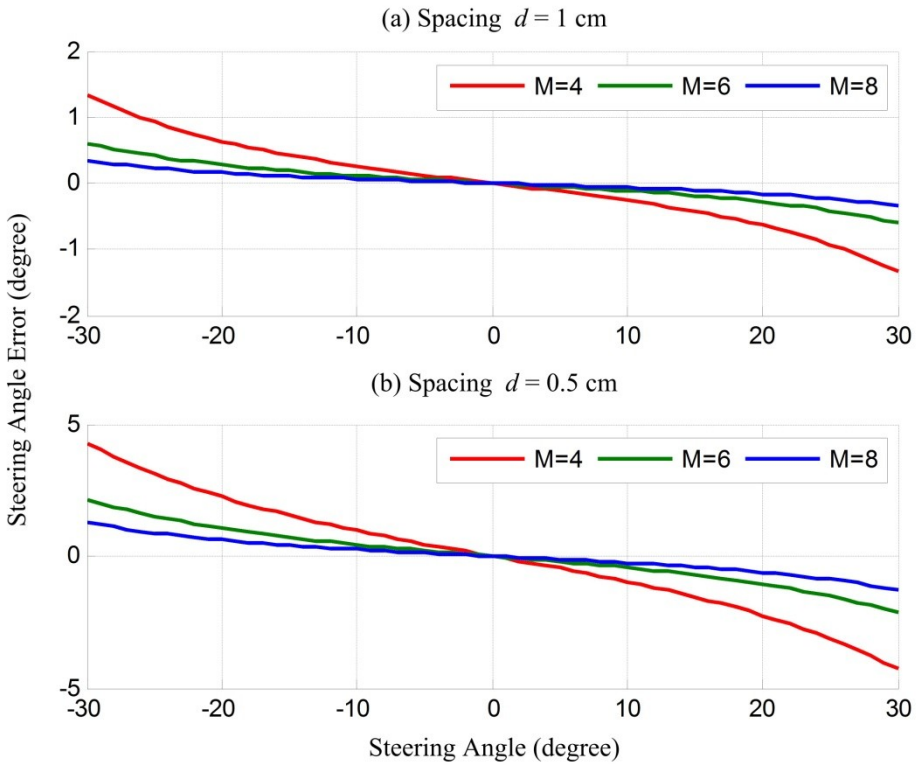

Figure 7.3 Steering angle errors for $M = 4,\ 6,$ and 8 channels in the UTA with spacing of (a) 1 cm and (b) 0.5 cm when equal weights are adopted.

7.2 Calibration Method for the Steerable Parametric Loudspeaker

The proposed calibration method of the steerable parametric loudspeakers is based on the beamsteering structure, as shown in Fig. 7.1. Hence, the distorted PF beampattern is given by

$$\tilde{I} \qquad \sum_{m=0}^{M-1} \delta_W^m w_m \exp\left[j\delta_D^m m\omega \frac{d}{c_0}\left(\sin\theta - \delta_P^m \sin\theta_0\right)\right], \tag{7.5}$$

where δ_W^m is the weight distortion factor, representing the distortion of weight for the m th channel. The weight of each channel is given by $\hat{w}_m = \delta_W^m w_m$. δ_D^m is the spacing distortion factor, representing the distortion of spacing for the m th

channel. The spacing between neighboring channels is given by $\hat{d}_m = \delta_D^m md$. δ_P^m is the delay distortion factor for the m th channel. Hence, the distorted delay amount of the m th channel is given by

$$\tau_m = \frac{\delta_D^m md}{c} \delta_P^m \sin\theta_0. \tag{7.6}$$

In (7.5), there are $3M$ unknown factors. The estimations of these distortion factors are obtained by minimizing the mismatch between the measured directivity H_M and the distorted PF beampattern given by (7.5). This procedure is described as

$$\left[\delta_W^m, \delta_D^m, \delta_P^m\right] = \arg\min \sum_{\theta} \left| H_M(\omega, \theta) - \tilde{I} \right. \tag{7.7}$$

The optimization problem in (7.7) is over parameterized, since the beamsteering structure in Fig. 7.1 selects three types of system errors to represent any possible distortion in the steerable parametric loudspeaker. Generally, (7.7) is not able to be solved analytically.

Alternatively, an optimization approach is presented in Fig. 7.4 that combines the Monte Carlo method and the nonlinear least-squares method. It is noted that the spacing and weight distortion factors are independent of the PF wave, but the phase distortion factors are changing with the PF. Hence, in the first step, initial estimations of the spacing and weight distortion factors are generated from two random vector generators with the same uniform distribution within the range from 0.85 to 1.15. This range is determined from the simulation results in Fig. 7.2. Peak signal to noise ratio (PSNR) is adapted to evaluate the mismatch between the simulated and measured beampattern. The measured beampatterns are considered

as the original signal, and the simulated beampatterns (before and after calibration) are treated as the noisy approximation of the original signal. Therefore, the PSNR used in this chapter is defined as

$$PSNR = -20\log_{10}\left(\frac{1}{L}\sum_{\theta}\left|H_M(\omega,\theta) - \tilde{I}\right.\right. \qquad (7.8)$$

where L is the number of points in each measured beampattern. To improve the PSNR value, *i.e.* to get a more accurate match to the measured beampattern, this first step is done iteratively. A large number of iterations are apparently required to achieve a set of good calibration data. The loop only terminates when the PSNR value has not improved over the latest 10^6 iterations. In the next step, when the optimized estimations of the spacing and weight distortion are obtained, the phase distortion factors are solved for each PF by the nonlinear least-squares method.

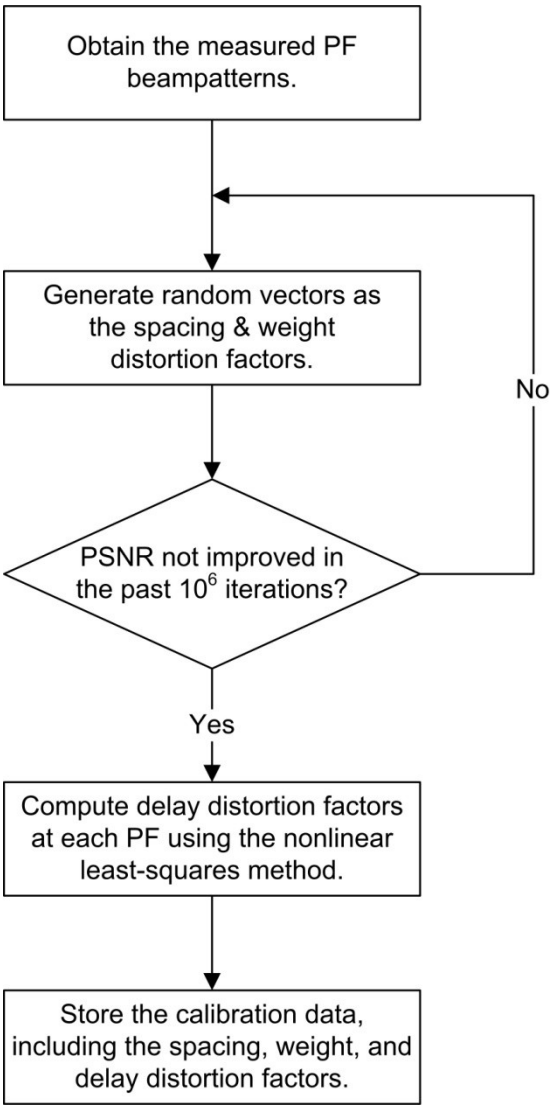

Figure 7.4 Flow chart of the proposed calibration method, which is a combination of the Monte Carlo method and the nonlinear least-squares method.

7.3 Measurement Results

The measurement setup is introduced in Section 3.4 and Appendixes. The PF beampatterns are measured at frequency pairs of (39.75 & 40.25) kHz, (39.5 & 40.5) kHz, (39 & 41) kHz, (38 & 42) kHz, and (36 & 44) kHz. Therefore, the DF beampatterns are measured correspondingly at 0.5 kHz, 1 kHz, 2 kHz, 4 kHz, and

8 kHz. In each measurement, the mainlobes are steered three times to 0°, 10° and 20°. The proposed calibration algorithm is applied to all the measured PF beampatterns except those obtained at 39 kHz and 41 kHz, because this pair of PF waves is reserved for cross-validation. The spacing and weight factors are listed in Table 7.1, and the delay distortion factors are listed in Table 7.2. Moreover, the delay distortion factors at 39 kHz and 41 kHz are derived from polynomial curve fitting based on the calibration data of the other PF waves. Their results are listed in Table 7.3.

Table 7.1 Calibration data of the weight and spacing distortion factors.

	1	2	3	4	5	6	7	8
δ_W^m	0.0167	0.1407	0.1376	-0.1313	-0.1285	-0.0685	-0.0536	-0.0474
δ_D^M	-0.0004	-0.0619	0.0288	0.0738	0.0091	0.0036	0.0725	0.0230

Table 7.2 Calibration data of the phase distortion factors for the PF waves at (39.75 & 40.25) kHz, (39.5 & 40.5) kHz, (38 & 42) kHz, and (36 & 44) kHz.

(kHz)	1	2	3	4	5	6	7	8
36	-0.0190	-0.0714	-0.0332	-0.1500	-0.1500	0.1338	0.0725	0.0086
38	0.0045	-0.0714	0.0117	-0.1379	-0.1395	0.0226	0.0514	-0.0090
39.5	0.0176	-0.0035	-0.0021	0.0508	0.0630	-0.0447	0.0255	-0.0280
39.75	0.0226	-0.0320	0.1284	0.0164	0.1416	-0.0838	0.0098	-0.0099
40.25	0.0433	0.0139	0.1121	0.1500	0.1500	-0.1073	-0.0116	-0.0301
40.5	0.0238	0.0024	0.1143	0.0274	0.1344	-0.0748	0.0077	0.0042
42	0.0120	-0.0162	0.0048	0.1100	0.0800	0.0924	0.0347	-0.0115
44	0.0166	-0.0327	-0.0103	0.0749	0.0163	0.0026	-0.0164	-0.0162

Table 7.3 Interpolated phase distortion factors for the PF waves at (39 & 41) kHz.

(kHz)	1	2	3	4	5	6	7	8
39	0.0176	-0.0239	0.0607	-0.0294	0.0107	-0.0505	0.0271	-0.0192
41	0.0304	-0.0216	0.0744	0.1235	0.1748	-0.0564	-0.0026	-0.0046

Using the calibration data, the calibrated PF beampatterns at 39 kHz and 41 kHz are obtained and plotted in Fig. 7.5(a) and Fig. 7.5(b), respectively. These calibrated PF beampatterns are compared with the measured beampatterns and the uncalibrated beampatterns for the purpose of cross-validation. The measured DF

beampattern at 2 kHz is also compared with the simulated beampatterns using the PD model and the APD (Envelope) model, as shown in Fig. 7.6(a) and 7.6(b), respectively. The matching accuracy is significantly improved after calibration in the vicinities of the grating lobe and the sidelobes. Due to the improvement in predicting the locations of grating lobes of the PF waves, the amplitude of grating lobe of the DF wave is more accurately predicted as well. The APD (Envelope) model shows a better performance in predicting the beamwidths of the mainlobe and the grating lobe compared to the PD model. Through this cross validation, the proposed calibration method has proven to be effective in solving the system errors in the steerable parametric loudspeaker.

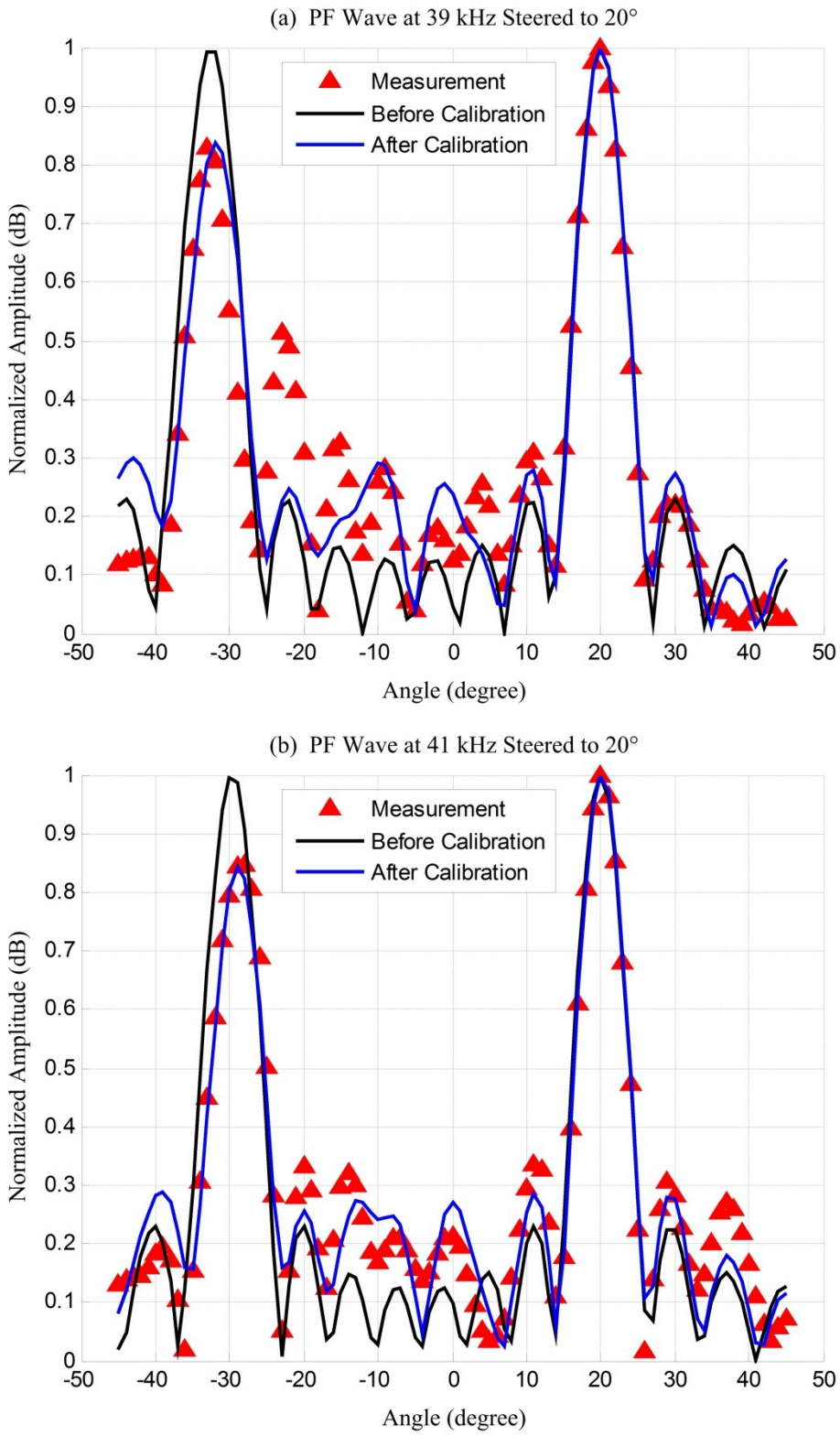

Figure 7.5 Comparison between the simulated (before and after calibration) and measured PF beampatterns at (a) 39 kHz and (b) 41 kHz, when their mainlobes are steered to 20°.

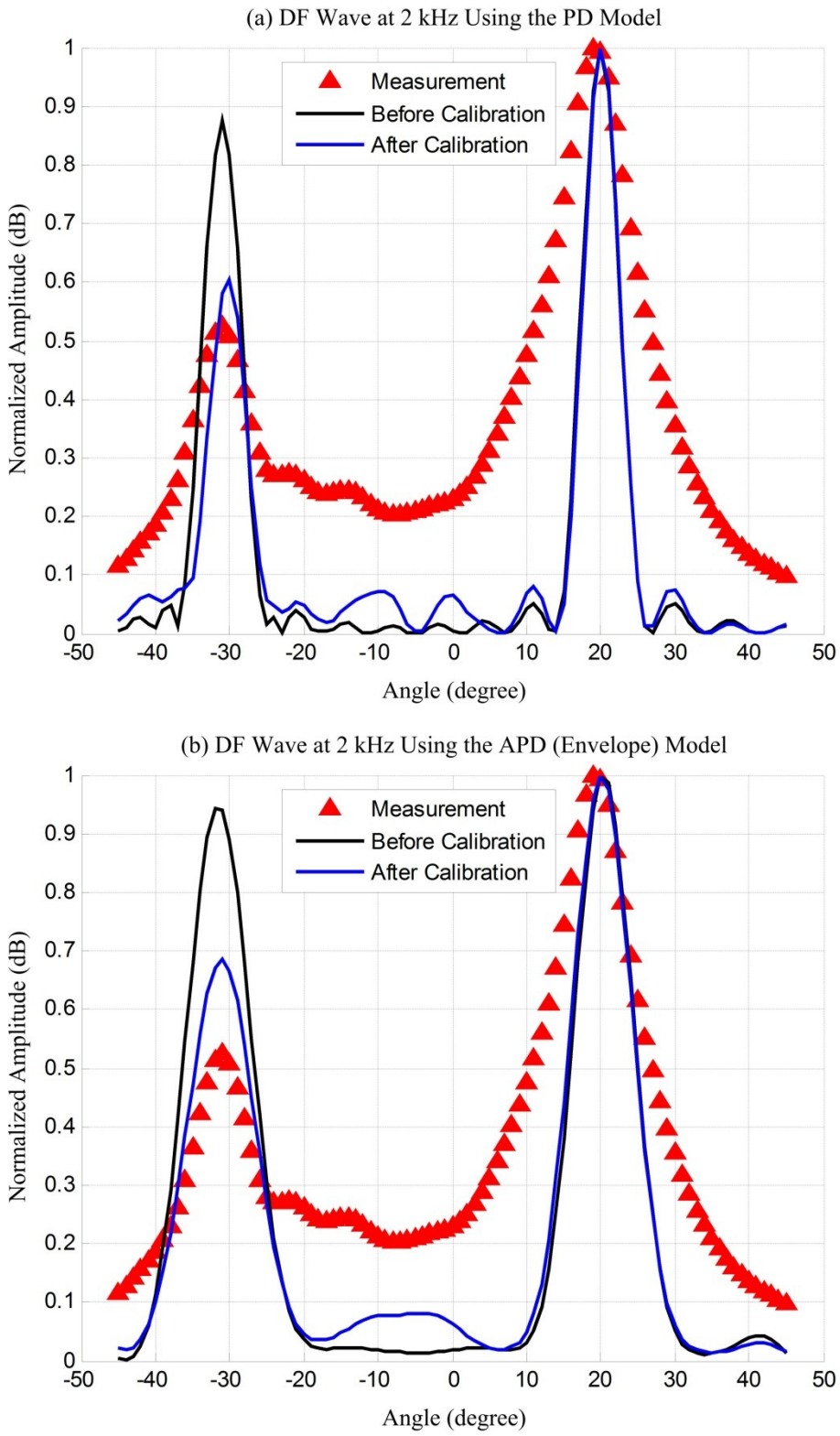

Figure 7.6 Comparison between the simulated (before and after calibration) and measured DF beampatterns at 2 kHz, when (a) the PD model and (b) the APD (Envelope) model are applied in the simulations.

A detailed comparison before and after calibration is illustrated in Fig. 7.7 and Fig. 7.8 for the PF and DF beampatterns in terms of PSNR, respectively. The DF beampatterns are simulated based on the APD (Envelope) model. The PSNR value of all the PF beampatterns is 19.72 dB. This value is improved to 22.37 dB after calibration. An exceptional case that the PSNR value drops after calibration is noted in Fig. 7.8(a), when the PF wave is generated at 38 kHz and steered to 0°. This observation is possibly due to the global objective function employed in the proposed calibration method, which may occasionally result in lower PSNR value.

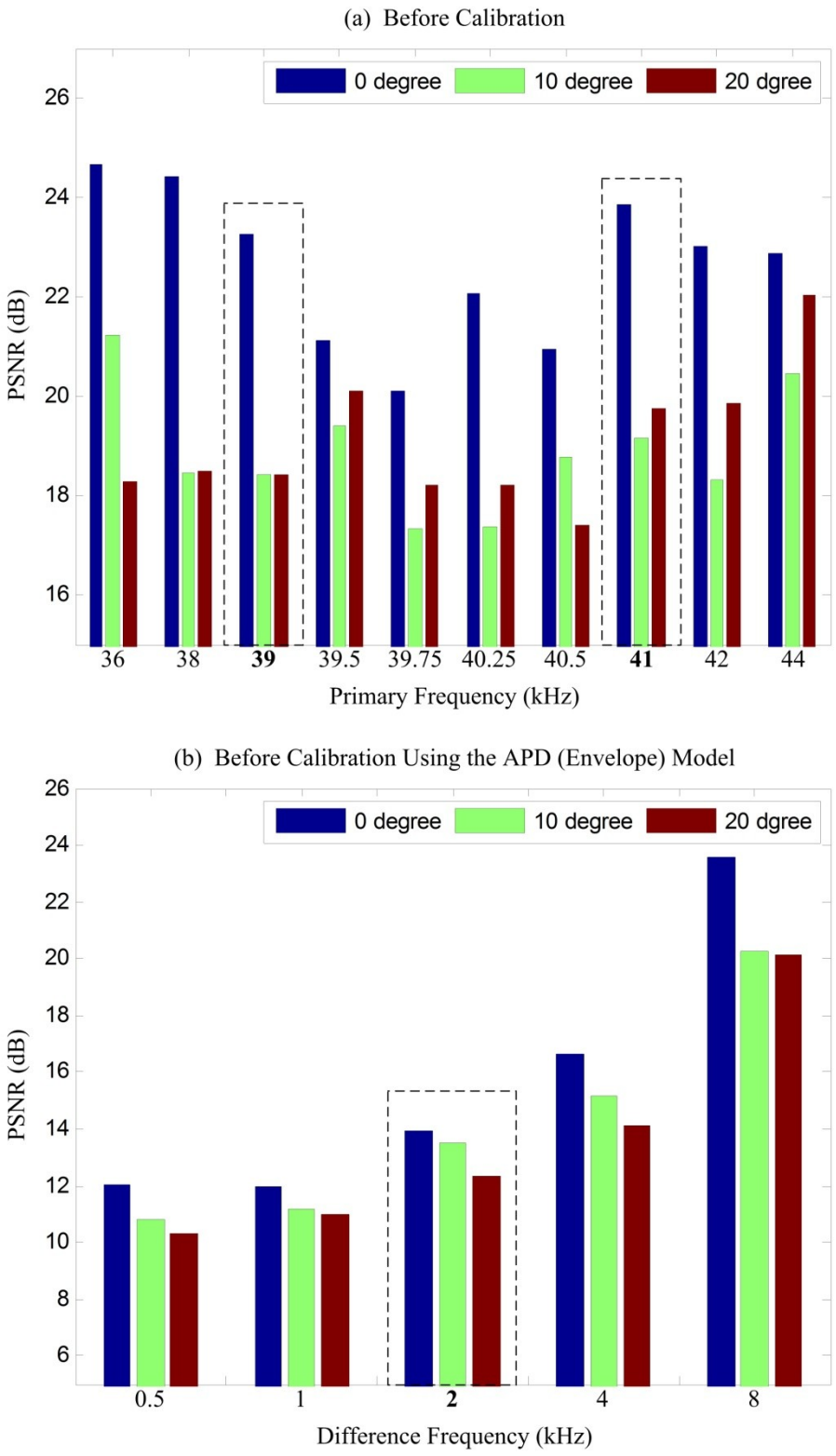

Figure 7.7 PSNR values of the simulated (a) PF and (b) DF beampatterns before calibration (the cross-validation results are highlighted in the dashed rectangles).

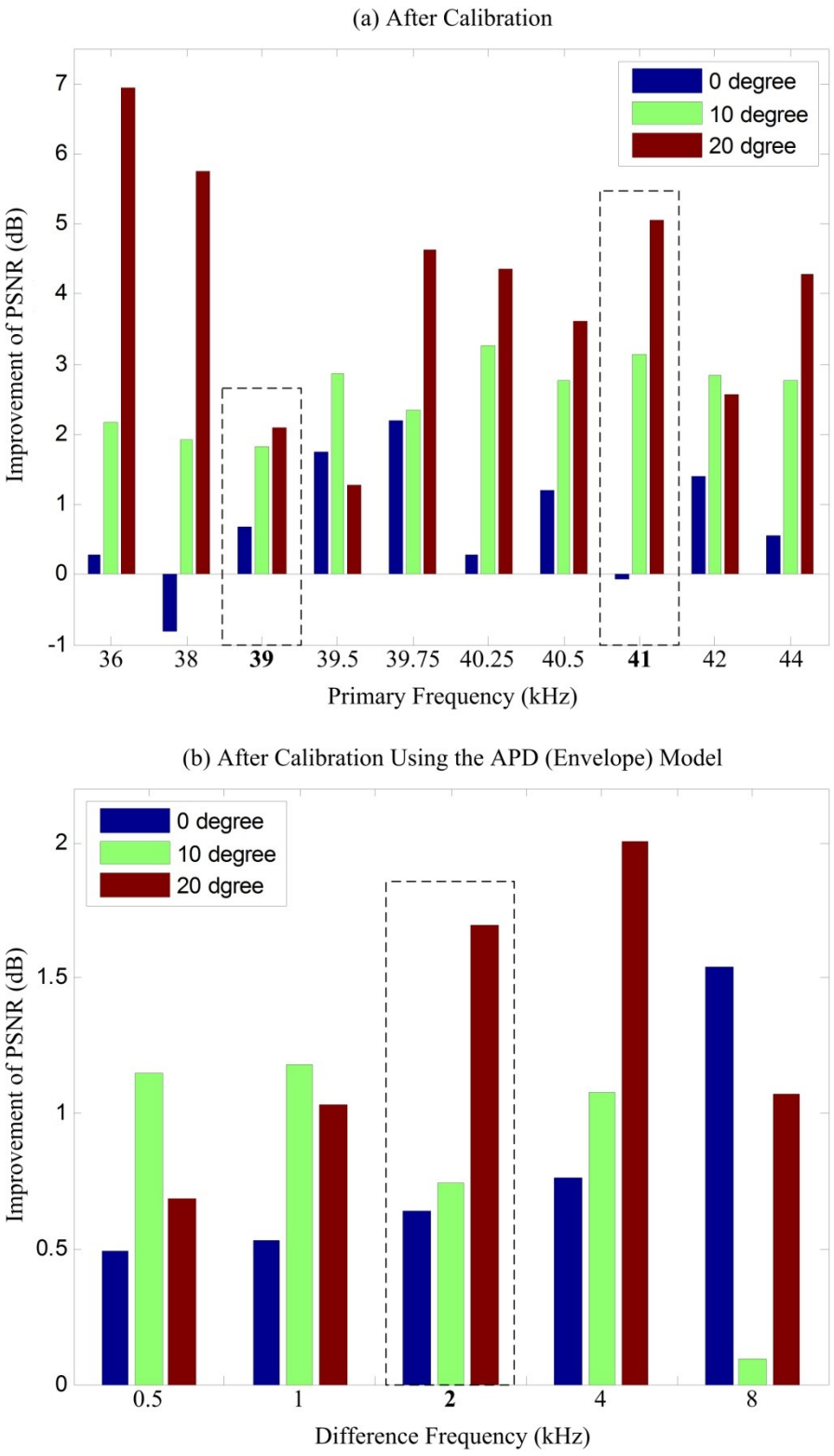

Figure 7.8 Improvement of PSNR values of the (a) PF and (b) DF beampatterns after calibration (the cross-validation results are highlighted in the dashed rectangles).

7.4 Discussion on Applying the Calibration Data with Different Preprocessing Techniques

Until now, the investigations reported in this thesis are conducted when only two PF waves are generated. However, preprocessing methods are required in the parametric loudspeaker to reduce the harmonic distortions. Section 3.2 has shown that AM preprocessing methods, including the DSBAM, the SRAM, the LSBAM and the USBAM, are applicable in the structure shown in Fig. 3.4. In this section, the DF beampatterns are computed in simulation when preprocessing methods are applied in the parametric loudspeaker.

The envelope functions of the DSBAM is given by

$$f_{DSBAM}(t) = 1 + \cos \omega_d t. \tag{7.9}$$

The modulated wave is given by the product of the carrier wave and the envelope function, *i.e.*

$$\begin{aligned} f_{DSBAM}(t)\cos \omega_c t &= \frac{1}{2}\cos(\omega_c - \omega_d)t + \cos \omega_c t + \frac{1}{2}\cos(\omega_c + \omega_d)t \\ &= \frac{1}{2}\left[\cos(\omega_c - \omega_d)t + \cos \omega_c t\right] + \frac{1}{2}\left[\cos \omega_c t + \cos(\omega_c + \omega_d)t\right]. \end{aligned} \tag{7.10}$$

Equation (7.10) shows that the modulated wave of the DSBAM consists of three PF waves, and they can be divided into two pairs of ($\omega_c - \omega_0$ & ω_c) and (ω_c & $\omega_c + \omega_0$). Thus, the directivity of the parametric loudspeaker using the DSBAM can be simulated by adding the two DF beampatterns, which are resultant from these two pairs of PF waves.

Similarly, the envelope functions of the SRAM is given by

$$f_{SRAM}(t)=\sqrt{1+\cos\omega_d t}. \tag{7.11}$$

The Taylor expansion of (7.11) function up to the forth order is obtained as

$$f_{SRAM}(t)\approx 1+\frac{1}{2}\cos\omega_d t-\frac{1}{8}\cos^2\omega_d t+\frac{1}{16}\cos^3\omega_d t-\frac{5}{128}\cos^4\omega_d t. \tag{7.12}$$

Using the double-angle and tri-angle formulae, (7.12) is manipulated as

$$f_{SRAM}(t)\approx \frac{945}{1024}+\frac{35}{64}\cos\omega_d t-\frac{21}{256}\cos 2\omega_d t+\frac{1}{64}\cos 3\omega_d t-\frac{5}{1024}\cos 4\omega_d t. \tag{7.13}$$

Thus, the modulated wave of the SRAM is given by

$$\begin{aligned} f_{SRAM}(t)\cos\omega_c t=&\frac{35}{128}\cos(\omega_c-\omega_d)t+\frac{35}{128}\cos(\omega_c+\omega_d)t-\frac{21}{512}\cos(\omega_c-2\omega_d)t\\ &-\frac{21}{512}\cos(\omega_c+2\omega_d)t+\frac{1}{128}\cos(\omega_c-3\omega_d)t+\frac{1}{128}\cos(\omega_c+3\omega_d)t\\ &-\frac{5}{2048}\cos(\omega_c-4\omega_d)t-\frac{5}{2048}\cos(\omega_c+4\omega_d)t+\frac{945}{1024}\cos\omega_c t. \end{aligned} \tag{7.14}$$

Equation (7.14) shows that the modulated wave of the SRAM consists of nine PF waves, and they can be divided into 8 pairs of (ω_c & $\omega_c\pm h\omega_0$) for $h=1,2,3,4$.

The modulated wave of the SRAM is given as

$$\begin{aligned} f_{SRAM}(t)\cos\omega_c t=&\frac{35}{128}\left[\cos(\omega_c-\omega_d)t+\cos\omega_c t\right]+\frac{35}{128}\left[\cos\omega_c t+\cos(\omega_c+\omega_d)t\right]\\ &-\frac{21}{512}\left[\cos(\omega_c-2\omega_d)t+\cos\omega_c t\right]-\frac{21}{512}\left[\cos\omega_c t+\cos(\omega_c+2\omega_d)t\right]\\ &+\frac{1}{128}\left[\cos(\omega_c-3\omega_d)t+\cos\omega_c t\right]+\frac{1}{128}\left[\cos\omega_c t+\cos(\omega_c+3\omega_d)t\right]\\ &-\frac{5}{2048}\left[\cos(\omega_c-4\omega_d)t+\cos\omega_c t\right]-\frac{5}{2048}\left[\cos\omega_c t+\cos(\omega_c+4\omega_d)t\right]\\ &+\frac{458}{1024}\cos\omega_c t. \end{aligned} \tag{7.15}$$

Thus, the directivity of the parametric loudspeaker using the SRAM can be simulated by adding eight DF beampatterns together, which are resultant from the

eight pairs of PF waves in (7.15).

The directivity of the parametric loudspeakers using the LSBAM and the USBAM can be easily simulated based on the equations in Table 3.1, because only two PF waves are transmitted to generate the DF wave. Hence, comparisons among four AM preprocessing methods of the LSBAM, the USBAM, the DSBAM, and the SRAM is carried out. Since the steering angle is fixed at 0°, the phase distortion factors are not applicable. For this reason, only the calibration data of the weight and spacing distortion factors are taken into account, which are listed in Table 7.1. The unspecified settings are same as those used in Section 7.3. Thus, the directivities of the parametric loudspeakers using the LSBAM and the USBAM are plotted in Fig. 7.9(a) and Fig 7.9(b), respectively. The directivities of the parametric loudspeakers using the DSBAM and the SRAM are plotted in Fig 7.10(a) and Fig 7.10(b), respectively.

In Fig. 7.9, it is noted that the spatial aliasing is more severe in the parametric loudspeaker using the USBAM than that using the LSBAM. This is because the frequency components in the modulated wave of the USBAM are higher than those in the LSBAM and higher frequency requires higher non-aliasing sampling rate. In Fig. 7.10(a), the simulated beampatterns of the parametric loudspeaker using the DSBAM are given by the average of those using the LSBAM and the USBAM, which has been proven by (7.10). As shown in Fig. 7.10(b), the parametric loudspeaker using the SRAM achieves a nearly constant beamwidth and no occurrences of spatial aliasing. The above interesting findings remain to be

validated through measurement in the future work.

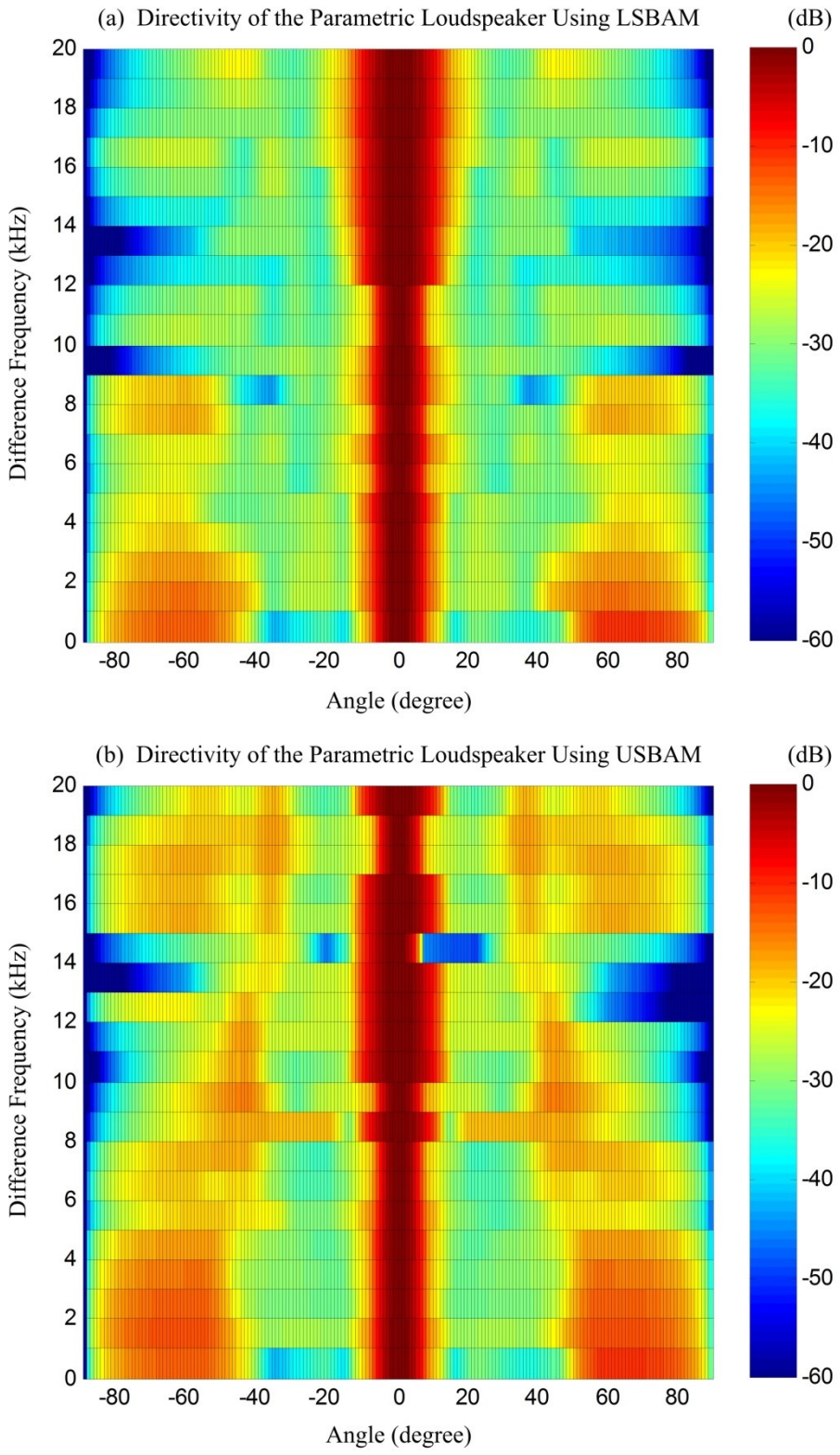

Figure 7.9 Directivities of the parametric loudspeakers using (a) the LSBAM and (b) the USBAM in simulations based on the calibration data and the APD (Envelope) model.

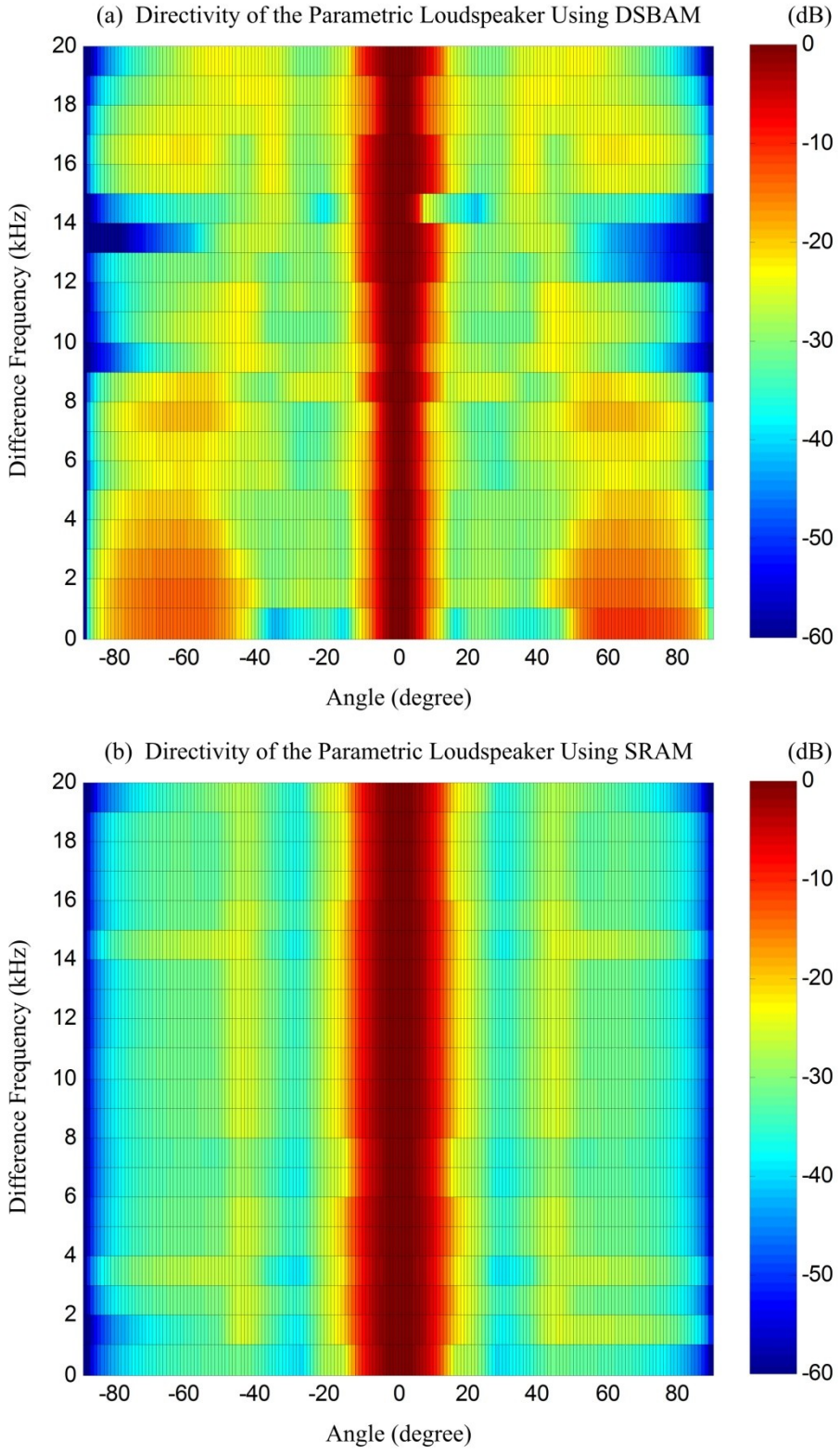

Figure 7.10 Directivities of the parametric loudspeakers using (a) the DSBAM and (b) the SRAM in simulations based on the calibration data and the APD (Envelope) model.

7.5 Conclusions

In this chapter, a new beamsteering structure was proposed for the steerable parametric loudspeakers, incorporating four types of system errors. Based on the proposed beamsteering structure, the calibration method was designed as a combination of the Monte Carlo method and the nonlinear least-squares method. Using the measured PF beampatterns of a steerable parametric loudspeaker as the input, this calibration method solved the calibration data of the spacing, weight, and delay distortion factors. Hence, these calibration data can be used to simulate the PF beampatterns, which accurately match the actual PF beampatterns. The DF beampatterns can then be simulated using the envelope of the APD model. The cross validation showed improved matching accuracy between the measured and simulated DF beampatterns, before and after calibration. In particular, the locations of the grating lobes were more accurately predicted after calibration, which were related to occurrences of the grating lobe elimination in the design of steerable parametric loudspeakers. An attempt to simulate the directivity of the parametric loudspeakers using AM preprocessing methods was reported. The modulated waves of the DSBAM and the SRAM were divided into several pairs of the PF waves. Thus, the directivity of the parametric loudspeaker using the DSBAM and the SRAM were simulated by adding the DF beampatterns resulted from every pair of the PF waves. The simulation results showed that the parametric loudspeaker using the SRAM achieved the best spatial performance with a nearly constant beamwidth and no occurrence of spatial aliasing.

Chapter 8
Conclusions and Future Works

8.1 Conclusions

The parametric loudspeakers are advantageous in transmitting highly directional sound beams in air. By applying phased array techniques to the parametric loudspeaker, the sound beams are able to be controlled and steered electronically and become suitable for various new applications. Being different from the conventional loudspeaker array, where the theoretical framework has been well established, the development of a steerable parametric loudspeaker still faces many underexplored issues. Thus, the steerable parametric loudspeaker based on the phased array techniques was investigated in this thesis on five aspects.

Firstly, it was verified to be feasible to apply phased array techniques in the parametric loudspeaker to achieve the directivity control of the sound beams. By adjusting the delay amounts of the PF waves, a theoretical derivation showed that the delay amount of the generated DF wave changed correspondingly. Hence, two beamsteering structures were proposed for the analysis involving only two PF wave and the implementation where preprocessing methods were applied. In order to build up a simulation framework that is used throughout this thesis, a transformation from a UTA to its equivalent Gaussian source array was proposed.

In the equivalent Gaussian source array, the product directivity principle was validated in the entire angular range (within ±90°) of the steerable parametric loudspeaker.

Secondly, a unique property was observed in the simulation and measurement results that the non-aliasing spacing of the steerable parametric loudspeaker could be extended to one and a half times the wavelength of the lower PF wave due to the grating lobe elimination. The occurrence of grating lobe elimination was found to be dependent on the configuration of the UTA and the frequency range of the DF waves. In general, to use more channels in the UTA results in a wider range of the grating lobe elimination. The measurement results validated the grating lobe elimination to be effective in the column and block configurations. In comparison, the column configuration allows better beamsteering capability, while the block configuration leads to a sharper mainlobe but with a trade-off of narrower range of the steering angle.

Thirdly, dual beams were generated from the steerable parametric loudspeaker without changing the hardware configuration. Besides the first DF beam generated from the mainlobes of the PF waves, the second DF beam was generated from the grating lobes of the PF waves. Therefore, the angular separation of the dual beams could be adjusted by the center frequency of the PF waves. The analysis of grating lobe elimination was extended to the dual-beam generation. Both simulation and measurement results showed that the proposed method effectively generated dual beams with different configurations of the UTA.

Fourthly, the relation between the PF and DF beampatterns was revisited. Three variants of the PD models were derived, and the envelope method was also discussed. Based on the comparison between simulation and measurement results, all the proposed models outperform the original PD model in the vicinities of the sidelobes adjacent to the mainlobe of the DF wave. When grating lobe elimination occurs, the PD model can be used to simulate the DF beampattern, which provides accurate predictions in the vicinities of the grating lobe and sidelobes adjacent to the grating lobe. When additional measurement results are available to determine the tuning factors, the CPD and EPD models achieve more accurate predictions by taking the environmental factors into consideration. By balancing the trade-off between accuracy and ease of use, the envelope of the APD model is recommended. The envelope method is also suggested to be applied in all the PD models to improve the overall predictions of the DF beampatterns.

Lastly, the system errors were solved in the steerable parametric loudspeaker by the proposed calibration method. Based on selected measured PF beampatterns, a combination of the Monte Carlo method and the nonlinear least-squares method was used to obtain the spacing, weight and delay distortion factors. The distortion factors can be applied in future simulations of the PF beampatterns to provide the spatial performance of the calibrated UTA. Applying the envelope method in the PD models, the DF beampatterns can be subsequently simulated to estimate the amplitudes and beamwidths of the mainlobe, grating lobes, and even sidelobes in the design of the steerable parametric loudspeaker using the same UTA.

8.2 Future works

Through the investigations of the steerable parametric loudspeaker reported in this thesis, several interesting extensions can be explored in the future, which are suggested as follows:

Firstly, almost all the analyses and measurements reported in this thesis were conducted with two PF waves being transmitted from the UTA to generate a sine DF wave. This frequency formation of the PF waves is similar to the modulated wave of the SSBAM when the modulating wave is a sine wave. Other preprocessing methods, such as the DSBAM and the SRAM, are applicable to the beamsteering structure proposed in Fig. 3.4. A preliminary analysis on the spatial performances of steerable parametric loudspeakers using the DSBAM and the SRAM has been reported in Section 7.4. However, detailed analyses of spatial aliasing and experimental measurements have yet to be carried out. In addition, instead of the current interest in finding out the DF beampattern, it is of interest to investigate the spatial characteristics of the higher harmonics that are produced as a by-effect of the parametric array.

Secondly, the main focus of this thesis is on the understanding of the steerable parametric loudspeaker when the DF wave is simplified as a sine wave. It can be extended to the generation of a steerable wideband sound beam. The difficulty of such a wideband implementation is the introduction of the inter-modulation effect, which must be carefully treated and verified through measurement. A band-limited white noise ranges from 500 Hz to 8 kHz can be selected as the test signal, and

preprocessing methods and phased array techniques described in this thesis can be carried out. A real-time implementation platform is suggested for the steerable parametric loudspeakers with the wideband generation.

Thirdly, although a few directivity models are proposed and validated in this thesis, discrepancies are commonly observed between the results obtained from measurements and simulations. Scientifically, a more accurate acoustic model is still preferred for evaluating spatial performances of the steerable parametric loudspeaker. Similar to the KZK equation used for the development of preprocessing methods, such an acoustic model should consider sound pressures of the PF waves, distance from the source to the observation point, and acoustical coefficients. The acoustical coefficients are closely affected by the environment, and some of them are frequency-dependant such as the absorption coefficient. Thus, this future acoustic model can become a good guideline for both theoretical derivations and practical implementations of the steerable parametric loudspeaker.

Lastly, the directivity of the steerable parametric loudspeaker is able to be designed with the inversed acoustic model. A directional microphone or an array of microphones can be deployed to monitor the sound field generated from the steerable parametric loudspeaker, and thus an adaptive feedback system can be proposed to adjust the directivity of the steerable sound beam according to the environment. This adaptive system can be further incorporated with ultrasound localization methods, such as the time reversal technique, to detect the targeted listener and implement a personal audio system with tracking capability.

Author's Publications

Journal

[ShG10a] C. Shi and W. S. Gan, "Development of a parametric loudspeaker: A novel directional sound generation technology," *IEEE Potentials*, vol. 29, no. 6, pp. 20-24, November 2010.

[ShG11] C. Shi and W. S. Gan, "Grating lobe elimination in steerable parametric loudspeaker," *IEEE Transactions on Ultrasonics, Ferroelectrics, and Frequency Control*, vol. 58, no. 2, pp. 437-450, February 2011.

[ShG12a] C. Shi and W. S. Gan, "Product directivity models for parametric loudspeakers," *Journal of the Acoustical Society of America*, vol. 131, no. 3, pp. 1938-1945, March 2012.

[ShG12b] C. Shi and W. S. Gan, "Analysis and calibration of system errors in steerable parametric loudspeakers," *Applied Acoustics*, vol. 73, no. 12, pp. 1263–1270, December 2012.

Conference

[SGC11] C. Shi, W. S. Gan, and Y. K. Chong, "Calibration of parametric

acoustic array," in *Proceedings of 8th International Conference on Information, Communications and Signal Processing*, Singapore, December 2011.

[ShG10b] C. Shi and W. S. Gan, "On grating lobe elimination of difference frequency in parametric loudspeaker," in *Proceedings of 2010 Asia Pacific Signal and Information Processing Association (APSIPA) Annual Summit and Conference*, Singapore, December 2010.

[ShG12c] C. Shi and W. S. Gan, "Modeling the directivity of parametric loudspeaker," in *Proceedings of 19th International Symposium on Nonlinear Acoustics*, Tokyo, Japan, May 2012.

[ShG13] C. Shi and W. S. Gan, "Steerable parametric loudspeaker with preprocessing methods," in *Proceedings of the 21st International Congress on Acoustics*, Montreal, Canada, June 2013.

[SMG13] C. Shi, H. Mu, and W. S. Gan, " A psychoacoustical preprocessing technique for virtual bass enhancement of the parametric loudspeaker," in *Proceedings of the 38th International Conference on Acoustics, Speech, and Signal Processing*, Vancouver, Canada, May 2013.

[STG13] C. Shi, E. L. Tan, and W. S. Gan, "Hybrid immersive three-dimensional sound reproduction system with steerable parametric loudspeakers," in *Proceedings of the 21st International Congress on Acoustics*, Montreal, Canada, June 2013.

References

[ABC09] M. Ardid, M. Bou-Cabo, F. Camarena, V. Espinosa, G. Larosa, J. A. Martinez-Mora, and M. Ferri, "Use of parametric acoustic sources to generate neutrino-like signals," *Nuclear Instruments and Methods in Physics Research Section A: Accelerators, Spectrometers, Detectors and Associated Equipment*, vol. 604, no. 1-2, pp. S208-S211, June 2009.

[ABT84] S. I. Aanonsen, T. Barkve, J. N. Tjøtta, and S. Tjøtta, "Distortion and harmonic generation in the nearfield of a finite amplitude sound beam," *Journal of the Acoustical Society of America*, vol. 75, no. 3, pp. 749-768, March 1984.

[AFW89] H. M. Aumann, A. J. Fenn, and F. G. Willwerth, "Phased array antenna calibration and pattern prediction using mutual coupling measurements," *IEEE Transactions on Antennas and Propagation*, vol. 37, no. 7, pp. 844-850, July 1989.

[AKH08] M. Akiyama, T. Kamakura, and C. Hedburg, "Parametric sound fields by phase-cancellation excitation of primary waves," in *Proceedings of the 18th International Symposium on Nonlinear Acoustics*, Stockholm, Sweden, July 2008, pp. 30-33.

[AKK91] K. Aoki, T. Kamakura, and Y. Kumamoto, "Parametric loudspeaker: Characteristics of acoustic field and suitable modulation of carrier ultrasound," *Electronics and Communications in Japan (Part III: Fundamental Electronic Science)*, vol. 74, no. 9, pp. 76–82, 1991.

[AKK94] K. Aoki, T. Kamakura, Y. Kumamoto, "A parametric loudspeaker: Applied examples," *Electronics and Communications in Japan (Part III: Fundamental Electronic Science)*, vol. 77, no. 1, pp. 64-74, 1994.

[ALH93] M. A. Averkiou, Y. S. Lee, and M. F. Hamilton, "Self-demodulation of amplitude- and frequency-modulated pulses in a thermoviscous fluid," *Journal of the Acoustical Society of America*, vol. 94, no. 5, pp. 2876-2883, November 1993.

[AMH05] A. Achanta, M. McKenna, J. Heyman, "Nonlinear acoustic concealed weapons detection," in *Proceedings of the 34th Applied Imagery and Pattern Recognition Workshop*, Washington, USA, December 2005, pp. 21-27.

[ARP97] M. A. Averkiou, D. N. Roundhill, and J. E. Powers, "A new imaging technique based on the nonlinear properties of tissues," in *Proceedings of the 1997 IEEE Ultrasonics Symposium*, Toronto, Canada, October 1997, pp. 1561-1566.

[ATT12] S. Aoki, M. Toba, and N. Tsujita, "Sound localization of stereo

reproduction with parametric loudspeakers," *Applied Acoustics*, vol. 73, no. 12, pp. 1289-1295, December 2012.

[Bar72] J. F. Bartram, "A useful analytical model for the parametric acoustic array," *Journal of the Acoustical Society of America*, vol. 52, no. 3B, pp. 1042-1044, September 1972.

[BeA69] H. O. Berktay and C. A. Al-Temimi, "Virtual arrays for underwater reception," *Journal of Sound and Vibration*, vol. 9, no. 2, pp. 295-307, March 1969.

[BeB60] J. L. S. Bellin and R. T. Beyer, "Scattering of sound by sound," *Journal of the Acoustical Society of America*, vol. 32, no. 3, pp. 339-341, March 1960.

[BeB62] J. L. S. Bellin and R. T. Beyer, "Experimental investigation of an end-fire array," *Journal of the Acoustical Society of America*, vol. 34, no. 8, pp. 1051-1054, August 1962.

[BeB75] M. B. Bennett and D. T. Blackstock, "Parametric array in air," *Journal of the Acoustical Society of America*, vol. 57, no. 3, pp. 562-568, March 1975.

[BeL74] H. O. Berktay and D. J. Leahy, "Farfield performance of parametric transmitters," *Journal of the Acoustical Society of America*, vol. 55, no. 3, pp. 539-546, March 1974.

[Ber65a] H. O. Berktay, "Nonlinear interaction of two sound beams," *Journal of the Acoustical Society of America*, vol. 38, no. 3, pp.

480-481, September 1965.

[Ber65b] H. O. Berktay, "Parametric amplification by the use of acoustic nonlinearities and some possible applications," *Journal of Sound and Vibration*, vol. 2, no. 4, pp. 462-470, October 1965.

[Ber65c] H. O. Berktay, "Parametric amplification by the use of acoustic nonlinearities and some possible applications," *Journal of Sound and Vibration*, vol. 2, no. 4, pp. 462-470, October 1965.

[Bey98] R. T. Beyer, "The parameter B/A," in *Nonlinear Acoustics*, edited by M. F. Hamilton and D. T. Blackstock, Eds. San Diego: Academic Press, 1998, pp. 25-39.

[BMK09] D. G. Browning, M. B. Moffett, and W. L. Konrad, "Parametric acoustic array development at the US Navy's New London, Connecticut laboratory," *Journal of the Acoustical Society of America*, vol. 125, no. 4, pp. 2687-2687, April 2009.

[BKS08] M. Barbagallo, M. Kleiner, and A. Sarti, "Modulation and demodulation of steerable ultrasound beams for audio transmission and rendering," in *Proceedings of the 11th International Conference on Digital Audio Effects*, Espoo, Finland, September 2008, pp. 227-232.

[BrK12] Brüel & Kjær, "Condenser microphone cartridges," [Online] http://www.bksv.com/doc/Bp0100.pdf (Accessed 30 Jun 2012).

[Bro96] K. Brown, "Acoustic imaging sound dome," United States Patent

5532438, July 2, 1996.

[BTT89] J. Berntsen, J. N. Tjøtta, and S. Tjøtta, "Intersection of sound waves. Part IV: Scattering of sound by sound," *Journal of the Acoustical Society of America*, vol. 86, no. 5, pp. 1968-1983, November 1989.

[BWB60] J. L. S. Bellin, P. J. Westervelt, and R. T. Beyer, "Experimental investigation of a parametric end-fire array," *Journal of the Acoustical Society of America*, vol. 32, no. 7, pp. 935, July 1960.

[BWT72] G. R. Barnard, J. G. Willette, J. J. Truchard, and J. A. Shooter, "Parametric acoustic receiving arrays," *Journal of the Acoustical Society of America*, vol. 52, no. 5B, pp. 1437-1441, November 1972.

[BZH05] L. A. Brooks, A. C. Zander, and C. H. Hansen, "Investigation into the feasibility of using a parametric array control source in an active noise control system," in *Proceedings of Acoustics 2005*, Busselton, Australia, November 2005, pp. 39-45.

[ChS81] N. P. Chotiros and B. V. Smith, "A theoretical and experimental study of the behaviour of a parametric array in a random medium," *Journal of Sound and Vibration*, vol. 74, no. 3, pp. 395-410, February 1981.

[CHX05] M. Chen, D. G. Huang, L. M. Xu, T. Y. Hu, and Y. Wang, "Research on a novel audio beam loudspeaker based digital signal

processor," in *Proceedings of the 2005 IEEE International Conference on Mechatronics and Automation*, Niagara Falls, Canada, July 2005, pp. 466-470.

[Cos05] P. J. Costianes, "An overview of concealed weapons detection for homeland security," in *Proceedings of the 34th Applied Imagery and Pattern Recognition Workshop*, Washington, United States, December 2005, pp. 1-5.

[CrN01] J. J. Croft and J. O. Norris, "Theory, history, and the advancement of parametric loudspeakers: A technology review," American Technology Corporation, White paper, Part # 98-10006-1100 Rev. E, 2001.

[CSN03] J. J. Croft, M. E. Spencer, and J. O. Norris, "Modulator processing for a parametric speaker system," United States Patent 6584205B1, June 24, 2003.

[CSW88] A. Cai, J. A. Sun, and G. Wade, "Adapting parametric acoustic arrays for tomographic imaging," *Ultrasonic Imaging*, vol. 10, no. 3, pp. 196-203, July 1988.

[CZW96] R. F. W. Coates, M. Zheng, and L. Wang, "BASS 300 PARACOM: A model underwater parametric communication system," *Journal of Oceanic Engineering*, vol. 21, no. 2, pp. 225-232, April 1996.

[DaH90] C. M. Darvennes and M. F. Hamilton, "Scattering of sound by sound from two Gaussian beams," *Journal of the Acoustical*

Society of America, vol. 87, no. 5, pp. 1955-1964, May 1990.

[Din00] D. Ding, "A simplified algorithm for the second-order sound fields," *Journal of the Acoustical Society of America*, vol. 108, no. 6, pp. 2759-2764, December 2000.

[DSL96] D. Ding, Y. Shui, J. Lin, and D. Zhang, "A simple calculation approach for the second harmonic sound field generated by an arbitrary axial-symmetric source," *Journal of the Acoustical Society of America*, vol. 100, no. 2, pp. 727-733, August 1996.

[Gad05] M. C. Gadsby, "Acoustic beam-forming," Final Year Project Report, School of Electrical Engineering and Computer Science, University of Newcastle, Callaghan, Australia, June 2005.

[Gan12] W. S. Gan, "Directional audio projection: How DSP techniques can be used to create directional audio beam?" presented at the special lecture organized by IEEE Student Branch at Kansai University, Osaka, Japan, March 2012.

[GBE03] I. J. Gupta, J. R. Baxter, S. W. Ellingson, H. G. Park, H. S. Oh, and M. G. Kyeong, "An experimental study of antenna array calibration", *IEEE Transactions on Antennas and Propagation*, vol. 53, no. 3, pp. 664-667, March 2003.

[GCS89] J. Y. Guigne, V. H. Chin, and S. M. Solomon, "Acoustic attenuation measurements using parametric arrays," *Ultrasonics*, vol. 27, no. 5, pp. 297-301, September 1989.

[Gre10] R. Greff, "The use of parametric arrays for transaural applications," in *Proceedings of the 20th International Congress on Acoustics*, Sydney, Australia, August 2010, no. 717, pp. 1-5.

[GRH91] J. Y. Guigne, N. Rukavina, P. H. Hunt, and J. S. Ford, "An acoustic parametric array for measuring the thickness and stratigraphy of contaminated sediments," Journal of Great Lakes Research, vol. 17, no. 1, pp. 120-131, 1991.

[GrK10] G. Grelowska and E. Kozaczka, "Characterization of local seabed properties using parametric echosounder," in *Proceedings of the 17th International Congress on Sound and Vibration*, Cairo, Egypt, July 2010, paper 884, pp. 1-7.

[GTK11] W. S. Gan, E. L. Tan, and S. M. Kuo, "Audio Projection," *IEEE Signal Processing Magazine*, vol. 28, no. 1, pp. 43-57, January 2011.

[GYK12] W. S. Gan, J. Yang, and T. Kamakura, "A review of parametric acoustic array in air," *Applied Acoustics*, vol. 73, no. 12, pp. 1211-1219, December 2012.

[GYT06] W. S. Gan, J. Yang, K. S. Tan, and M. H. Er, "A digital beamsteerer for difference frequency in a parametric array," *IEEE Transactions on Audio, Speech, and Language Processing*, vol. 14, no. 3, pp. 1018-1025, May 2006.

[HaB00] D. I. Havelock and A. J. Brammer, "Directional loudspeakers using

sound beams," *Journal of the Audio Engineering Society*, vol. 48, no. 10, pp. 908-916, October 2000.

[HAH05] J. Heyman, A. Achanta, M. Hinders, K. Rudd, and P. Costianes, "Nonlinear acoustic concealed weapons detection (CWD)," in *Automatic Target Recognition XV (Proceedings of SPIE 5807)*, Orlando, United States, May 2005, pp. 162-169.

[HaM98] M. F. Hamilton and C. L. Morfey, "Model equations," in *Nonlinear Acoustics*, edited by M. F. Hamilton and D. T. Blackstock, Eds. San Diego: Academic Press, 1998, pp. 41-63.

[Ham98] M. F. Hamilton, "Sound beams," in *Nonlinear Acoustics*, edited by M. F. Hamilton and D. T. Blackstock, Eds. San Diego: Academic Press, 1998, pp. 233-261.

[HaR05] R. W. Haupt and K. D. Rolt, "Standoff acoustic laser technique to locate buried land mines," *Lincoln Laboratory Journal*, vol. 15, no. 1, pp. 3-22, 2005.

[Hin99] P. C. Hines, "Quantifying seabed properties in shelf waters using a parametric sonar," *Measurement Science and Technology*, vol. 10, no. 12, pp. 1127–1134, December 1999.

[HiR09] M. K. Hinders and K. E. Rudd, "Acoustic parametric array for identifying standoff targets," in *Review of Progress in Quantitative Nondestructive Evaluation Volume 29 (AIP Conference Proceedings Volume 1211)*, Kingston, RI, USA, July 2009, pp.

1757-1764.

[HMN09] K. Hirokawa, M. Morise, and T. Nishiura, "The fundamental design of reflective audio spot utilizing ultrasound loudspeaker," in *Proceedings of the 10th Western Pacific Acoustics Conference*, Beijing, China, September 2009, no. 126, pp. 1-6.

[HRO98] P. C. Hines, W. C. Risley, and M. P. O'Connor, "A wide-band sonar for underwater acoustics measurements in shallow water," in *Proceedings of OCEANS' 98 Volume 3*, Nice, France, September 1998, pp. 1558-1562.

[InP56] U. Ingard and D. C. Pridmore-Brown, "Scattering of sound by sound," *Journal of the Acoustical Society of America*, vol. 28, no. 3, pp. 367-369, May 1956.

[IsH02] I. Ishimaru and R. Hyoudou, "Sound focusing technology using parametric effect with beat signal," in *Proceedings of the 2002 IEEE International Workshop on Robot and Human Interactive Communication*, Berlin, Germany, September 2002, pp. 277-281.

[IYI07] K. Ishii, Y. Yamamoto, M. Imai, and K. Nakadai, "A navigation system using ultrasonic directional speaker with rotating base," in *Lecture Notes in Computer Science 4558*, Springer, 2007, pp. 526-535.

[JBG10] R. Johannes, J. W. Beh, W. S. Gan, and E. L. Tan, "Investigation of 3D audio rendering with parametric array loudspeakers," in

Proceedings of the 128th Convention of the Audio Engineering Society, London, UK, May 2010, paper 7975, pp. 1-15.

[JiG12] W. Ji and W. S. Gan, "Identification of a parametric loudspeaker system using an adaptive Volterra filter," *Applied Acoustics*, vol. 73, no. 12, pp. 1251-1262, December 2012.

[JGJ10] W. Ji, W. S. Gan, and P. Ji, "Theoretical and experimental comparison of amplitude modulation techniques for parametric," in *Proceedings of the 128th Convention of the Audio Engineering Society*, London, United Kingdom, May 2010, paper 8006, pp. 1-10.

[JGT10] P. Ji, W. S. Gan, E. L. Tan, and J. Yang, "Performance analysis on recursive single-sideband amplitude modulation for parametric loudspeakers," in *Proceedings of the 2010 IEEE International Conference on Multimedia and Expo*, Singapore, July 2010, pp. 748-753.

[JLW12] P. Ji, W. Liu, S. Wu, J. Yang, and W. S. Gan, "An alternative method to measure the on-axis difference-frequency sound in a parametric loudspeaker without using an acoustic filter," *Applied Acoustics*, vol. 73, no. 12, pp. 1244-1250, December 2012.

[JoD93] D. H. Johnson and D. E. Dudgeon, "Beamforming," in *Array Signal Processing: Concepts and Techniques*, edited by D. H. Johnson and D. E. Dudgeon, Eds. New Jersey: Prentice Hall, 1993,

pp. 111–198.

[JoG09] R. Johannes and W. S. Gan, "3D sound effects with transaural audio beam projection," in *Proceedings of the 10th Western Pacific Acoustics Conference*, Beijing, China, September 2009, paper 244, pp. 1-8.

[JSC11] Y. Jing, D. Shen, and G. T. Clement, "Verification of the Westervelt equation for focused transducers," *IEEE Transactions on Ultrasonics, Ferroelectrics, and Frequency Control*, vol. 58, no. 5, pp. 1097-1101, May 2011.

[JTC11] Y. Jing, M. Tao, and G. T. Clement, "Evaluation of a wave-vector-frequency-domain method for nonlinear wave propagation," *Journal of the Acoustical Society of America*, vol. 129, no. 1, pp. 32-46, January 2011.

[JTG11a] P. Ji, E. L. Tan, W. S. Gan, and J. Yang, "A comparative analysis of preprocessing methods for the parametric loudspeaker based on the Khokhlov-Zabolotskaya-Kuznetsov equation for speech reproduction," *IEEE Transactions on Audio, Speech, and Language Processing*, vol. 19, no. 4, pp. 937-946, May 2011.

[JTG11b] W. Ji, E. L. Tan, and W. S. Gan, "Baseband distortion modeling for a parametric loudspeaker system using Volterra kernels ," in *Proceedings of the 3rd Annual Summit and Conference of Asia Pacific Signal and Information Processing Association*, Xi'an,

China, October 2011.

[JuK10] H. S. Ju and Y. H. Kim, "Near-field characteristics of the parametric loudspeaker using ultrasonic transducers," *Applied Acoustics*, vol. 71, no. 9, pp. 793-800, September 2010.

[JYG09] P. Ji, J. Yang, and W. S. Gan, "The investigation of localized sound generation using two ultrasound beams," *IEEE Transactions on Ultrasonics, Ferroelectrics and Frequency Control*, vol. 56, no. 6, pp. 1282-1287, June 2009.

[JYT07] P. Ji, C. Ye, and J. Tian, "Development of a directional loudspeaker system for sound reproduction," in *Proceedings of the 2007 IEEE International Conference on Multimedia and Expo*, Beijing, China, July 2007, pp. 591-594.

[KAA04] T. Kamakura, M. Akiyama, and K. Aoki, "A higher-order parabolic equation for describing nonlinear propagation of ultrasound beams," *Acoustical Science and Technology*, vol. 25, no. 2, pp. 163-165, 2004.

[KAK91] T. Kamakura, K. Aoki, and Y. Kumamoto, "Suitable modulation of the carrier ultrasound for a parametric loudspeaker," *ACUSTICA*, vol. 73, no. 4, pp. 215-217, 1991.

[KAS06] T. Kamakura, K, Aoki, and S. Sakai, "A highly directional audio system using a parametric array in air," in *Proceedings of the 9th Western Pacific Acoustics Conference*, Seoul, Korea, June 2006.

[KaS08] T. Kamakura and S. Sakai, "Practical development of directive sound system: Examinations from various research fields," *Fundamentals Review*, vol. 1, no. 3, pp. 37-43, August 2008.

[KCD00] L. Kopp, D. Cano, E. Dubois, L. Wang, B. Smith, and R. F. W. Coates, "Potential performance of parametric communications," *IEEE Journal of Oceanic Engineering*, vol. 25, no. 3, pp. 282-295, July 2000.

[Kei11] W. P. M. N. Keizer, "Fast and accurate array calibration using a synthetic array approach", *IEEE Transactions on Antennas and Propagation*, vol. 59, no. 11, pp. 4115-4122, November 2011.

[KGC04] F. A. Karnapi, W. S. Gan, and Y. K. Chong, "FPGA implementation of parametric loudspeaker system," *Microprocessors and Microsystems*, vol. 28, no. 5-6, pp. 261-272, August 2004.

[KGE02] F. A. Karnapi, W. S. Gan, and M. H. Er, "Method to enhance low frequency perception from a parametric array loudspeaker," in *Proceedings of the 112th Convention of the Audio Engineering Society*, Munich, Germany, May 2002.

[KGK10] E. Kozaczka, G. Grelowska, and S. Kozaczka, "Sounding of the seabed of the gulf of Gdansk by the means of the parametric sonar," in *Proceedings of the 17th International Congress on Sound and Vibration*, Cairo, Egypt, July 2010, paper 1052, pp. 1-8.

[KHA89] T. Kamakura, N. Hamada, K. Aoki, and Y. Kumamoto, "Nonlinearly generated spectral components in the nearfield of a directive sound source," *Journal of the Acoustical Society of America*, vol. 85, no. 6, pp. 2331-2337, June 1989.

[KHT11] K. Kimura, O. Hoshuyama, T. Tanikawa, and M. Hirose, "VITA: Visualization system for interaction with transmitted audio signals," in *ACM SIGGRAPH 2011 Posters*, Vancouver, Canada, August 2011, no. 54, p. 1.

[KIC85] T. Kamakura, K. Ikegaya, and I. M. Chou, "Nonlinear interactions of finite amplitude and weak subharmonic plane waves: Phase-dependent parametric amplification," *Journal of the Acoustical Society of Japan (E)*, vol. 6, no. 3, pp. 155-160, July 1985.

[KiK02] Y. W. Kim and S. I. Kim, "Novel preprocessing technique to improve harmonic distortion in airborne parametric array," in *Proceedings of the 6th International Conference on Signal Processing*, Beijing, China, August 2002, pp. 1815-1818.

[KiS02] W. Kim and V. W. Sparrow, "Audio application of the parametric array implementation through a numerical model," in *Proceedings of the 113th Convention of the Audio Engineering Society*, Los Angeles, United States, October 2002, paper 5652, pp. 1-16.

[KMN10] S. Kurimoto, M. Morise, and T. Nishiura, "The suppression for undesired reflection towards audio spot," in *Proceedings of the 20th International Congress on Acoustics*, Sydney, Australia, August 2010, paper 958, pp. 1-5.

[KNA09] T. Kamakura, H. Nomura, M. Akiyama, and S. Sakai, "Spatial phase-inversion technique for generating parametric sounds," in *Proceedings of the 16th International Congress on Sound and Vibration*, Krakow, Poland, July 2009, paper 87, pp. 1-8.

[KoI11] T. Komatsuzaki and Y. Iwata, "Active noise control using high-directional parametric loudspeaker," *Journal of Environment and Engineering*, vol. 6, no. 1, pp. 140-149, 2011.

[KPH98] T. D. Kite, J. T. Post, and M. F. Hamilton, "Parametric array in air distortion reduction by preprocessing," in *Proceedings of the 16th International Congress on Acoustics*, Seattle, United States, June 1998.

[KPZ06] M. R. F. Kidner, C. Petersen, A. C Zander, and C. H. Hansen, "Feasibility study of localised active noise control using an audio spotlight and virtual sensors," in *Proceedings of Acoustics 2006*, Christchurch, New Zealand, November 2006, pp. 55-61.

[Kri77] J. Kritz, "Parametric array Doppler sonar," *IEEE Journal of Oceanic Engineering*, vol. 2, no. 2, pp. 190-200, April 1977.

[KSL00] G. Kaduchak, D. N. Sinha, D. C. Lizon, and M. J. Kelecher, "A non-contact technique for evaluation of elastic structures at large stand-off distances applications to classification of fluids in steel vessels," *Ultrasonics*, vol. 37, no. 8, pp. 531-536, January 2000.

[KSN08] T. Kamakura, S. Sakai, H. Nomura, and M. Akiyama, "Parametric audible sounds by phase-cancellation excitation of primary waves," in *Proceedings of Acoustics 2008*, Paris, France, June 2008, pp. 4367-4372.

[KSS06] H. J. Kim, L. W. Schmerr, and A. Sedov, "Generation of the basis sets for multi-Gaussian ultrasonic beam models: An overview," *Journal of the Acoustical Society of America*, vol. 119, no. 4, pp. 1971-1978, April 2006.

[KTK92] T. Kamakura, M. Tani, Y. Kumamoto, and K. Ueda, "Harmonic generation in finite amplitude sound beams from a rectangular aperture source," *Journal of the Acoustical Society of America*, vol. 91, no. 6, pp. 3144-3151, June 1992.

[Kuz71] V. P. Kuznetsov, "Equations of nonlinear acoustics," *Soviet Physics - Acoustics*, vol. 16, pp. 467-470, 1971.

[KYI84] T. Kamakura, M. Yoneyama, and K. Ikegaya, "Developments of parametric loudspeaker for practical use," in *Proceedings of the 10th International Symposium on Nonlinear Acoustics*, Kobe,

Japan, 1984, pp. 147-150.

[KZH06] M. R. F. Kidner, A. C. Zander, and C. H. Hansen "Active control of sound using a parametric array," in *Proceedings of ACTIVE 2006*, Adelaide, Australia, September 2006, pp. 1-12.

[LBP11] C. H. Lee, J. Bae, D. G. Paeng, J. Lee and S. Kim, "Digital beamsteering system using acoustic transducer array," *Journal of the Acoustical Society of America*, vol. 129, no. 4, p. 2675, April 2011.

[Lee93] Y. S. Lee, "Numerical solution of the KZK equation for pulsed finite amplitude sound beams in thermoviscous fluids," Doctor of Philosophy Dissertation, The University of Texas, Austin, United States, 1993.

[LeG06] K. C. M. Lee and W. S. Gan, "Bandwidth-efficient recursive pth-order equalization for correcting baseband distortion in parametric loudspeakers," *IEEE Transactions on Audio, Speech, and Language Processing*, vol. 14, no. 2, pp. 706-710, March 2006.

[Lie02] Y. H. Liew, "Signal processing techniques for sound reproduction in parametric arrays," Master of Engineering Thesis, Nanyang Technological University, Singapore, 2002.

[LiH10] D. Li and D. Huang, "Investigation of directional audio system

based on ultrasonic modulation," in *Proceedings of the 2010 IEEE International Conference on Mechatronics and Automation*, Xi'an, China, August 2010, pp. 861-865.

[LKM06] H. Lee, D. Kang, and W. Moon, "Microelectromechanical-systems -based parametric transmitting array in air: Application to the ultrasonic ranging transducer with high directionality," in *Proceedings of SICE-ICASE International Joint Conference 2006*, Busan, Korea, October 2006, pp. 1081-1084.

[LKM07] H. Lee, D. Kang, and W. Moon, "Design and fabrication of the high directional ultrasonic ranging sensor to enhance the spatial resolution," in *Proceedings of the 14th International Conference on Solid-State Sensors, Actuators and Microsystems*, Lyon, France, June 2007, pp. 1303-1306.

[LKM09] H. Lee, D. Kang, and W. Moon, "A micro-machined source transducer for a parametric array in air," *Journal of the Acoustical Society of America*, vol. 125, no. 4, pp. 1879-1893, April 2009.

[LKS11a] S. Lee, T. Katsuura, and Y. Shimomura, "Effects of parametric speaker sound on physiological functions during mental task," *Journal of Physiological Anthropology*, vol. 30, no. 1, pp. 9–14, February 2011.

[LKS11b] S. Lee, T. Katsuura, and Y. Shimomura, "Verification of endocrinological functions at a short distance between parametric

speakers and the human body," *Activitas Nervosa Superior Rediviva*, vol. 53, no. 4, pp. 187–193, 2011.

[LKT10] S. Lee, T. Katsuura, T. Towatari-Ueno, and Y. Shimomura, "The effects of parametric speaker sound on salivary hormones," *Activitas Nervosa Superior Rediviva*, vol. 52, no. 2, pp. 119-124, 2010.

[LVE96] G. Loubet, F. Vial, A. Essebbar, L. Kopp, and D. Cano, "Parametric transmission of wide-band signals," in *Proceedings of OCEANS' 96 Volume 2*, Fort Lauderdale, United States, September 1996, pp. 839-844.

[LXX11] X. Li, L. Xu, and L. Xu, "Audio near-distance directional loudspeaker technology for portable multimedia devices," in *Proceedings of the 2011 IEEE International Conference on Mechatronics and Automation*, Beijing, China, August 2011, pp. 727-731.

[LYG02] K. C. M. Lee, J. Yang, W. S. Gan, and M. H. Er, "Modeling nonlinearity of air with Volterra kernels for use in a parametric array loudspeaker," in *Proceedings of the 112th Convention of the Audio Engineering Society*, Munich, Germany, May 2002, paper 5653, pp. 1-6.

[LYM06] S. Liu, W. Yao, J. Meng, L. Xu, and M. Chen, "Hardware design of signal processing for a novel audio beam loudspeaker based on

DSP," in *Proceedings of the 1st IEEE Conference on Industrial Electronics and Applications*, Singapore, May 2006, pp. 1-4.

[MaS10] T. Masayoshi and A. Shigeaki, "Stereo reproduction using parametric loudspeakers," in *Proceedings of the 20th International Congress on Acoustics* Sydney, Australia, August 2010, paper 262, pp. 1-4.

[MBK71] R. H. Mellen, D. G. Browning, and W. L. Konrad, "Parametric sonar transmitting array measurements," *Journal of the Acoustical Society of America*, vol. 49, no. 3B, pp. 932-935, March 1971.

[MBK07] T. Miyachi, J. J. Balvig, W. Kisada, K. Hayakawa, and T. Suzuki, "A quiet navigation for safe crosswalk by ultrasonic beams," in *Lecture Notes in Computer Science 4694*, Springer, 2007, pp. 1049-1057.

[MBK10] T. Miyachi, J. J. Balvig, W. Kisada, K. Hayakawa, and T. Suzuki, "A navigation system with ultrasonic beams for reliable connection of sustainable transports," in *Proceedings of the 12th International Conference on Mobility and Transport for Elderly and Disabled Persons*, Hong Kong, China, June 2010.

[MBM06] T. Miyachi, J. J. Balvig, and J. Moriyama, " An expansion of space affordance by sound beams and tactile indicators," in *Lecture Notes in Computer Science 4252*, Springer, 2006, pp. 603-610.

[Mer75] H. M. Merklinger, "Improved efficiency in the parametric

transmitting array," *Journal of the Acoustical Society of America*, vol. 58, no. 4, pp. 784-787, October 1975.

[Mer09] T. Merkel, "How to receive sound through ultrasound: The interaction between ultrasonic and audio waves in the air", in *Proceedings of the 16th International Congress on Sound and Vibration*, Krakow, Poland, July 2009, paper 258, pp. 1-6.

[MIT10] M. Morise, D. Ikefuji, H. Tujii, K. Hirokawa, and T. Nishiura, "A design of reflective audio spot with reflective objects," in *Proceedings of the 20th International Congress on Acoustics*, Sydney, Australia, August 2010, no. 755, pp. 1-4.

[MKK02] H. Mizoguchi, T. Kanamori, S. Kagami, K. Hiraoka, M. Tanaka, T. Shigehara, and T. Mishima, "Implementation of invisible messenger system to whisper in a person's ear remotely by integrating visual face tracking and speaker array," in *Proceedings of 2002 IEEE International Conference on Systems, Man and Cybernetics*, Yasmine Hammamet, Tunisia, October 2002, no. WA2N4, pp. 1-5.

[MoM77] M. B. Moffett and R. H. Mellen, "Model for parametric acoustic sources," *Journal of the Acoustical Society of America*, vol. 61, no. 2, pp. 325-337, February 1977.

[MoM81] M. B. Moffett and R. H. Mellen, "Effective lengths of parametric acoustic sources," *Journal of the Acoustical Society of America*,

vol. 70, no. 5, pp. 1424-1426, 1981.

[MRB98] O. B. Matar, J. P. Remenieras, C. Bruneel, A. Roncin, and F. Patat, "Noncontact measurement of vibration using airborne ultrasound," *IEEE Transactions on Ultrasonics, Ferroelectrics, and Frequency Control*, vol. 45, no. 3, pp. 626-633, May 1998.

[MSH11] J. Mendoza-Lopes, S. Sanchez-Solano, and J. L. Huertas-Diaz, "Characterization and modeling of piezoelectric integrated micro speakers for audio acoustic actuation," *World Academy of Science, Engineering and Technology*, vol. 58, pp. 183-189, October 2011.

[MuB69] T. G. Muir and J. E. Blue, "Experiments on the acoustic modulation of large-amplitude waves," *Journal of the Acoustical Society of America*, vol. 46, no. 1b, pp. 227-232, July 1969.

[Mur09] Murata, "Ultrasonic sensor application manual," [Online] http://www.murata.com/products/catalog/pdf/s15e.pdf (Accessed 30 Jun 2012).

[MuW72] T. G. Muir and J. G. Willette, "Parametric acoustic transmitting arrays," *Journal of the Acoustical Society of America*, vol. 52, no. 5B, pp. 1481-1486, November 1972.

[MWB70] M. B. Moffett, P. J. Westervelt, and R. T. Beyer, "Large amplitude pulse propagation: A transient effect," *Journal of the Acoustical Society of America*, vol. 47, no. 5B, pp. 1473-1474, May 1970.

[MWB71] M. B. Moffett, P. J. Westervelt, and R. T. Beyer, "Large amplitude

pulse propagation: A transient effect II," *Journal of the Acoustical Society of America*, vol. 49, no. 1B, pp. 339-343, January 1971.

[NaT65] J. Naze and S. Tjøtta, "Nonlinear interaction of two sound beams," *Journal of the Acoustical Society of America,* vol. 37, no. 1, pp. 174-175, January 1965.

[NaT05] K. Nakadai and H. Tsujino, "Towards new human-humanoid communication Listening during speaking by using ultrasonic directional speaker," in *Proceedings of the 2005 IEEE International Conference on Robotics and Automation*, Barcelona, Spain, April 2005, pp. 1483-1488.

[NHC86] Y. Nakagawa, W. Hou, A. Cai, N. Arnold, G. Wade, M. Yoneyama, and M. Nakagawa, "Nonlinear parameter imaging with finite-amplitude sound waves," in *Proceedings of the 1986 IEEE Ultrasonics Symposium*, Williamsburg, United States, November 1986, pp. 901-904.

[NHK12] H. Nomura, C. M. Hedberg, and T. Kamakura, "Numerical simulation of parametric sound generation and its application to length-limited sound beam," *Applied Acoustics*, vol. 73, no. 12, pp. 1231-1238, December 2012.

[Nic71] R. H. Nichols, "Finite amplitude effects used to improve echo sounder," *Journal of the Acoustical Society of America*, vol. 50, no. 4A, pp. 1086-1087, October 1971.

[Nip12] Nicera, "Parametric speaker," [Online] http://www.nicera.co.jp/pro/ut/ut-04e.html (Accessed 30 Jun 2012).

[NOS09] K. Nakamura, H. Ogura, and T. Sugimoto, "Direct visualization of high-intensity focused ultrasonic field using light-emitting diodes and piezoelectric elements," *Acoustical Imaging*, vol. 29, no. 5, pp. 309-316, 2009.

[NWN08] Y. Nakatani, D. Watanabe, and M. Nakatani, "Disaster evacuation support system for visitors," in *Proceedings of IADIS International Conference Intelligent Systems and Agents 2008*, Amsterdam, Netherlands, July 2008, pp. 127-134.

[NYN06] Y. Nakashima, T. Yoshimura, N. Naka, and T. Ohya, "Prototype of mobile super directional loudspeaker," *NTT DoCoMo Technical Journal*, vol. 8, no. 1, pp. 25-32, June 2006.

[NYO05] Y. Nakashima, T. Yoshimura, and T. Ohya, "Prototype of parametric array loudspeaker on mobile phone and its acoustical characteristics," in *Proceedings of the 118th Convention of the Audio Engineering Society*, Barcelona, Spain, May 2005, paper 6521, pp. 1-6.

[OlL06a] D. Olszewski and K. Linhard, "Optimum array configuration for parametric ultrasound loudspeakers using standard emitters ," in *Proceedings of Interspeech 2006*, Pittsburgh, United States, September 2006, pp. 657-660.

[OlL06b] D. Olszewski and K. Linhard, "Highly directional multi-beam audio loudspeaker," in *Proceedings of Interspeech 2006*, Pittsburgh, United States, September 2006, pp. 2630-2633.

[OlL06c] D. Olszewski and K. Linhard, "Imperfections of parametrically generated sound beams caused by reflexions ," in *Proceedings of Symposium on Ultrasonic Electronics Volume 27*, November 2006, Nagoya, Japan, pp. 335-336.

[Ols06] D. Olszewski, "Optimum carrier frequency for ultrasound loudspeaker," in *Proceedings of Symposium on Ultrasonic Electronics Volume 27*, Nagoya, Japan, November 2006, pp. 337-338.

[Ols09] D. Olszewski, "Targeted Audio," in *Computers in the Human Interaction Loop: Perceptual Technologies*, Springer, 2009, pp. 133-141.

[OMW03] M. Okamoto, M. Miyoshi, and Y. Watanabe, "Acoustic nonlinear effect on auricular cartilage vibrated with amplitude-modulated ultrasound," *Japanese Journal of Applied Physics*, vol. 42, no. 5B, pp. 2918-2922, May 2003.

[OPL05] D. Olszewski, F. Prasetyo, and K. Linhard, "Steerable highly directional audio beam loudspeaker," in *Proceedings of Interspeech 2005*, Lisbon, Portugal, September 2005, pp. 137-140.

[Ost09] L. A. Ostrovsky, "Research on parametric arrays in Russia:

Historical perspective," *Journal of the Acoustical Society of America*, vol. 125, no. 4, pp. 2688-2688, April 2009.

[Pom99] F. J. Pompei, "The use of airborne ultrasonics for generating audible sound beams," *Journal of the Audio Engineering Society*, vol. 47, no. 9, pp. 726-731, September 1999.

[Pom02] F. J. Pompei, "Sound from ultrasound: The parametric array as an audible sound source," Doctor of Philosophy Dissertation, Massachusetts Institute of Technology, United States, 2002.

[PoW02] F. J. Pompei and S. C. Wooh, "Phased array element shapes for suppressing grating lobes," *Journal of the Acoustical Society of America*, vol. 111, no. 5, pp. 2040-2048, May 2002.

[PRH10] G. Phanomchoeng, R. Rajamani, and J. Hourdos, "Directional sound for long-distance auditory warnings from a highway construction work zone," *IEEE Transactions on Vehicular Technology*, vol. 59, no. 5, pp. 2266-2276, June 2010.

[Rit06] A. Ritty, "Directional loudspeaker using a parametric array," *Acta Polytechnica*, vol. 46, no. 4, pp. 47-48, 2006.

[RoM02] Y. Roh and C. Moon, "Design and fabrication of an ultrasonic speaker with thickness mode piezoceramic transducers," *Sensors and Actuators A: Physical*, vol. 99, no. 3, pp. 321–326, June 2002.

[RuH08] K. E. Rudd and M. K. Hinders, "Simulation of incident nonlinear sound beam and 3D scattering from complex targets," *Journal of*

Computational Acoustics, vol. 16, no. 3, pp. 427-445, September 2008.

[SaK08] S. Sakai and T. Kamakura, "Dynamic single sideband modulation for realizing parametric loudspeaker," in *Proceedings of the 18th International Symposium on Nonlinear Acoustics*, Stockholm, Sweden, July 2008, paper 1022, pp. 613-616.

[See94] C. M. S. See, "Sensor array calibration in the presence of mutual coupling and unknown sensor gains and phases", *Electronics Letter*, vol. 30, no. 5, pp. 373-374, March 1994.

[SKI12] Y. Sugibayashi, S. Kurimoto, D. Ikefuji, M. Morise, and T. Nishiura, "Three-dimensional acoustic sound field reproduction based on hybrid combination of multiple parametric loudspeakers and electrodynamic subwoofer," *Applied Acoustics*, vol. 73, no. 12, pp. 1282-1288, December 2012.

[SMN10] Y. Sugibayashi, M. Morise, and T. Nishiura, "The steering for distance perception with reflective audio spot," in *Proceedings of the 20th International Congress on Acoustics*, Sydney, Australia, August 2010, no. 759, pp. 1-6.

[STM08] K. Shinagawa, H. Takemura, and H. Mizoguchi, "Sound spot generation and evaluation by a large scale panel loudspeaker array," in *Proceedings of 2008 IEEE International Conference on Systems, Man and Cybernetics*, Singapore, October 2008, pp.

1164-1168.

[SvO05] G. Svanfeldt, D. Olszewski, "Perception experiment combining a parametric loudspeaker and a synthetic talking head," in *Proceedings of Interspeech 2005*, Lisbon, Portugal, September 2005, pp. 1721-1724.

[SYG03] K. Sha, J. Yang, and W. S. Gan, "A complex virtual source approach for calculating the diffraction beam field generated by a rectangular planar source," *IEEE Transactions on Ultrasonics, Ferroelectrics, and Frequency Control*, vol. 50, no. 7, pp. 890-897, July 2003.

[Tan04] K. S. Tan, "Array signal processing for parametric array," Master of Engineering Thesis, Nanyang Technological University, Singapore, 2004.

[TaG12] E. L. Tan and W. S. Gan, "Reproduction of immersive sound using directional and conventional loudspeakers," *Journal of the Acoustical Society of America*, vol. 131, no. 4, p. 3215, April 2012.

[TaT09a] N. Tanaka and M. Tanaka, "Active noise control using a steerable parametric array loudspeaker," in *Proceedings of ACTIVE 2009*, Ottawa, Canada, August 2009, paper 588, pp. 1-12.

[TaT09b] R. Tachi and N. Tanaka, "Active noise control using acoustic wave reflection of parametric speaker," in *Proceedings of the 13th Asia Pacific Vibration Conference*, Christchurch, New Zealand,

November 2009, pp. 1-7.

[TaT10a] N. Tanaka and M. Tanaka, "Active noise control using a steerable parametric array loudspeaker," *Journal of the Acoustical Society of America*, vol. 127, no. 6, pp. 3526-3537, June 2010.

[TaT10b] N. Tanaka and M. Tanaka, "Active noise control using a parametric array loudspeaker," in *Proceedings of the 17th International Congress on Sound and Vibration*, Cairo, Egypt, July 2010, no. 598, pp. 1-8.

[TaT11] N. Tanaka and M. Tanaka, "Mathematically trivial control of sound using a parametric beam focusing source," *Journal of the Acoustical Society of America*, vol. 129, no. 1, pp. 165-172, January 2011.

[TaY10] S. Takeoka and Y. Yamasaki, "Acoustic projector using directivity controllable parametric loudspeaker array," in *Proceedings of the 20th International Congress on Acoustics*, Sydney, Australia, August 2010, paper 921, pp. 1-5.

[TGJ08] E. L. Tan, W. S. Gan, P. Ji, and J. Yang, "Distortion analysis and reduction for the parametric array," in *Proceedings of the 124th Convention of the Audio Engineering Society*, no. 7426, Amsterdam, Netherlands, May 2008, pp. 1-6.

[TGY03] K. S. Tan, W. S. Gan, J. Yang, and M. H. Er, "Constant beamwidth beamformer for difference frequency in parametric array," in

Proceedings of the 2003 International Conference on Multimedia and Expo, Baltimore, United States, July 2003, vol. 2, pp. 593-596.

[TGY04] K. S. Tan, W. S. Gan, J. Yang, and M. H. Er, "An efficient digital beamsteering system for difference frequency in parametric array," in *Proceedings of the 2004 IEEE International Conference on Acoustics, Speech, and Signal Processing*, Montreal, Canada, May 2004, vol. 2, pp. 193-196.

[TGY08] E. L. Tan, W. S. Gan, and J. Yang, "Preprocessing Techniques for Parametric Loudspeakers," in *Proceedings of the 1st International Conference on Audio, Language and Image Processing*, Shanghai, China, July 2008, pp. 1204-1208.

[TJG10] E. L. Tan, P. Ji, and W. S. Gan, "On preprocessing techniques for bandlimited parametric loudspeakers," *Applied Acoustics*, vol. 71, no. 5, pp. 486-492, May 2010.

[TKM04] Y. Tamai, S. Kagami, H. Mizoguchi, Y. Amemiya, K. Nagashima, and T. Takano, "Sound spot generation by 128-channel surrounded speaker array," in *Proceedings of 2004 IEEE Sensor Array and Multichannel Signal Processing Workshop*, Sitges, Spain, July 2004, pp. 542-546.

[TSG12] E. L. Tan, C. Shi, and W. S. Gan, "Improving hearing impairment using audio beam system," United States Provisional Patent, 2012.

[Tod05] M. Toda, "New type of acoustic filter using periodic polymer

layers for measuring audio signal components excited by amplitude-modulated high-intensity ultrasonic waves," *Journal of the Audio Engineering Society*, vol. 53, no. 10, pp. 930-941, October 2005.

[VBG98] A. L. Vyas, V. S. Balaji Raj, and R. G. Gupta, "Design considerations of parametric arrays," in *Proceedings of the 1998 International Symposium on Underwater Technology*, Tokyo, Japan, April 1998, pp. 98-102.

[VGV11] H. J. Vos, D. E. Goertz, A. F. W. van der Steen, and N. de Jong, "Parametric array technique for microbubble excitation," *IEEE Transactions on Ultrasonics, Ferroelectrics and Frequency Control*, vol. 58, no. 5, pp. 924-934, May 2011.

[VKT00] V. A. Voronin, T. N. Kutsenko, and S. P. Tarasov, "Formation of the directional pattern of a parametric array," *Acoustical Physics*, vol. 46, no. 6, pp. 737-739, November 2000.

[WCL07] Y. Wang, M. Chen, H. Li, and Z. Zhou, "Defining the parameters of truncated square-rooting DSB for parametric loudspeaker," in *Proceedings of the 2007 IEEE International Conference on Mechatronics and Automation*, Harbin, China, August 2007, pp. 1689-1693.

[WeB88] J. J. Wen and M. A. Breazeale, "A diffraction beam field expressed as the superposition of Gaussian beams," *Journal of the Acoustical*

Society of America, vol. 83, no. 5, pp. 1752–1756, May 1988.

[WEL07] A. Wright, A. Evans, A. Linney, and M. Lincoln, "The listening room: A speech-based interactive art installation," in *Proceedings of the 15th international conference on Multimedia*, Augsburg, Germany, September 2007, pp. 681-690.

[Wes57a] P. J. Westervelt, "Scattering of sound by sound," *Journal of the Acoustical Society of America,* vol. 29, no. 2, pp. 199-203, February 1957.

[Wes57b] P. J. Westervelt, "Scattering of sound by sound," *Journal of the Acoustical Society of America,* vol. 29, no. 8, pp. 934-935, August 1957.

[Wes60] P. J. Westervelt, "Parametric end-fire array," *Journal of the Acoustical Society of America,* vol. 32, no. 7, pp. 934-935, July 1960.

[Wes63] P. J. Westervelt, "Parametric acoustic array," *Journal of the Acoustical Society of America*, vol. 35, no. 4, pp. 535-537, April 1963.

[WKW09] I. O. Wygant, M.Kupnik, J. C. Windsor, W. M. Wright, M. S. Wochner, G. G. Yaralioglu, M. F. Hamilton, and B. T. Khuri-Yakub, "50 kHz capacitive micromachined ultrasonic transducers for generation of highly directional sound with parametric arrays," *IEEE Transactions on Ultrasonics,*

Ferroelectrics, and Frequency Control, vol. 56, no. 1, pp. 193-203, January 2009.

[WLX09] Y. Wang, X. Li, L. Xu, and L. Xu, "SSB modulation of the ultrasonic carrier for a parametric loudspeaker," in *Proceedings of the 2009 International Conference on Electronic Computer Technology*, Macau, February 2009, pp. 669-673.

[WSM05] K. van Wijk, J. A. Scales, T. D. Mikesell, and J. R. Peacock, "Toward noncontacting seismology," *Geophysical Research Letters*, vol. 32, no. 1, pp. L01308.1-L01308.4, January 2005.

[WWH12] S. Wu, M. Wu, C. Huang, and J. Yang, "FPGA-based implementation of steerable parametric loudspeaker using fractional delay filter," *Applied Acoustics*, vol. 73, no. 12, pp. 1271-1281, December 2012.

[WXC08] Y. Wang, L. Xu, M. Chen, L. Xu, C. Yang, and J. Ma, "The nonlinear distortion of directional loudspeaker, " in *Proceedings of the 1st International Conference on Audio, Language and Image Processing*, Shanghai, China, July 2008, pp. 17-21.

[YFK83] M. Yoneyama, J. Fujimoto, Y. Kawamo, and S. Sasabe, "The audio spotlight: An application of nonlinear interaction of sound waves to a new type of loudspeaker design," *Journal of the Acoustical Society of America*, vol. 73, no. 5, pp. 1013-1020, May 1983.

[YGT05] J. Yang, W. S. Gan, K. S. Tan, and M. H. Er, "Acoustic

beamforming of a parametric speaker comprising ultrasonic transducers," *Sensors and Actuators A: Physical*, vol. 125, no. 1, pp. 91-99, October 2005.

[YHW11] T. Yang, D. Huang, Y. Wang, and M. Chen, "Directivity analysis of transducer array of acoustic directional dispersing device," in *Proceedings of the 2011 IEEE International Conference on Mechatronics and Automation*, Beijing, China, August 2011, pp. 2317-2321.

[YJG07] J. Yang, P. Ji, and W. S. Gan, "Distortion reduction for parametric loudspeaker," in *Proceedings of the 19th International Congress on Acoustics*, Madrid, Spain, September 2007, pp. 1-6.

[YSG04] J. Yang, K. Sha, W. S. Gan, J. Tian, "A fast field scheme for the parametric sound radiation from rectangular aperture source," *Chinese Physics Letters*, vol. 21, no. 1, pp. 110-113, January 2004.

[YSG05] J. Yang, K. Sha, W. S. Gan, and J. Tian, "Modeling of finite-amplitude sound beams: Second order fields generated by a parametric loudspeaker," *IEEE Transactions on Ultrasonics, Ferroelectrics, and Frequency Control*, vol. 52, no. 4, pp. 610-618, April 2005.

[YTG05] J. Yang, K. S. Tan, W. S. Gan, M. H. Er, and Y. H. Yan, "Beamwidth control in parametric acoustic array," *Japanese Journal of Applied Physics*, vol. 44, no. 9A, pp. 6817–6819,

September 2005.

[ZaK69] E. A. Zabolotskaya and R. V. Khokhlov, "Quasi-plane waves in the nonlinear acoustics of confined beams," *Soviet Physics - Acoustics*, vol. 15, pp. 35-40, 1969.

[ZCG01] D. Zhang, X. Chen, and X. Gong, "Acoustic nonlinearity parameter tomography for biological tissues via parametric array from a circular piston source: Theoretical analysis and computer simulations," *Journal of the Acoustical Society of America*, vol. 109, no. 3, pp. 1219-1225, March 2001.

[ZGZ02] D. Zhang, X. Gong, and B. Zhang, "Second harmonic sound field after insertion of a biological tissue sample," *Journal of the Acoustical Society of America*, vol. 111, no. 1, pp. 45-48, January 2002.

[ZhC98] M. Zheng and R. F. W. Coates, "The angular response of a parametric array: Analytical solution," *Journal of Sound and Vibration*, vol. 209, no. 3, pp. 493-503, January 1998.

[ZhW99] M. Zheng and L. S. Wang, "The angular response of a parametric array: General numerical solution," *Journal of Sound and Vibration*, vol. 228, no. 1, pp. 177-197, November 1999.

Appendix A Rayleigh Distance and Absorption Distance of the Parametric Loudspeaker

Rayleigh distance is plotted in Fig. A.1 with respect to the number of transducer used in the UTA, when the PF wave is generated at 40 kHz and the speed of sound is estimated at 344.21 m/s (when the room temperature is 20℃). Since the Rayleigh distance is proportional to the emitter size, it is proportional to the number of transducers and the transducer size in the UTA. When 200 transducers with an individual diameter of 10mm are grouped and configured in the UTA, the Rayleigh distance of the parametric loudspeaker does not exceed 4 meters.

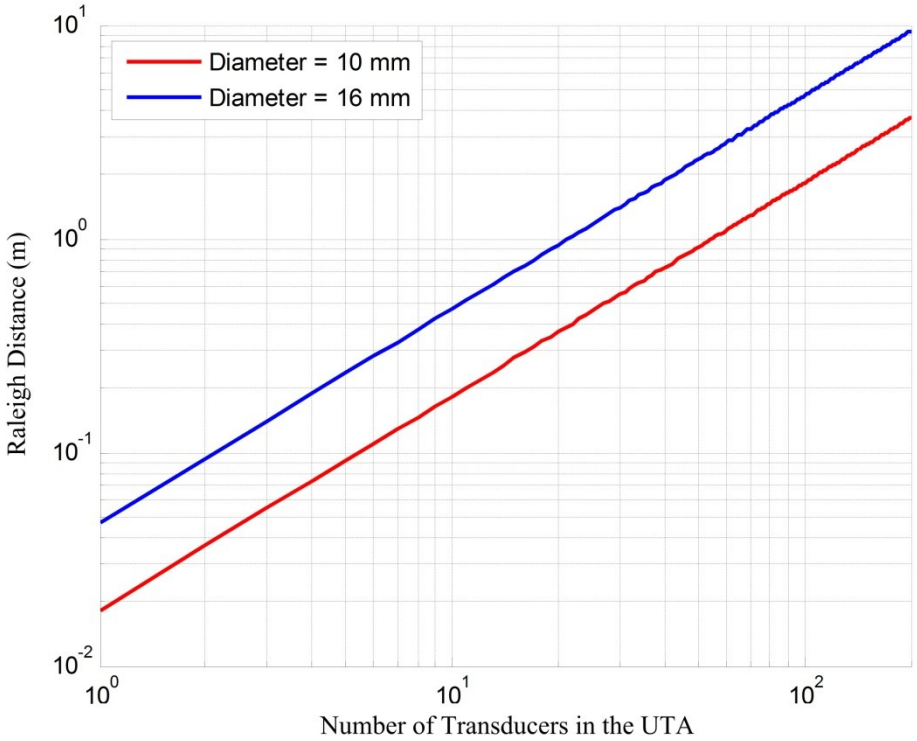

Figure A.1 Rayleigh distance of the parametric loudspeaker.

Absorption distance is plotted in Fig. A.2 with respect to the relative humidity, when the PF wave is generated at 40 kHz and the room temperature ranges from 20℃ to 40℃. When the room temperature is 20℃, the absorption distance decreases until the relative humidity increases to 50%, and maintains an almost constant level after the relative humidity reaches 50%. When the relative humidity is 50%, the absorption distance ranges from 3 to 4 meters and does not change significantly with the room temperature. Generally, the absorption distance ranges from 3 to 6 meters in the normal room condition.

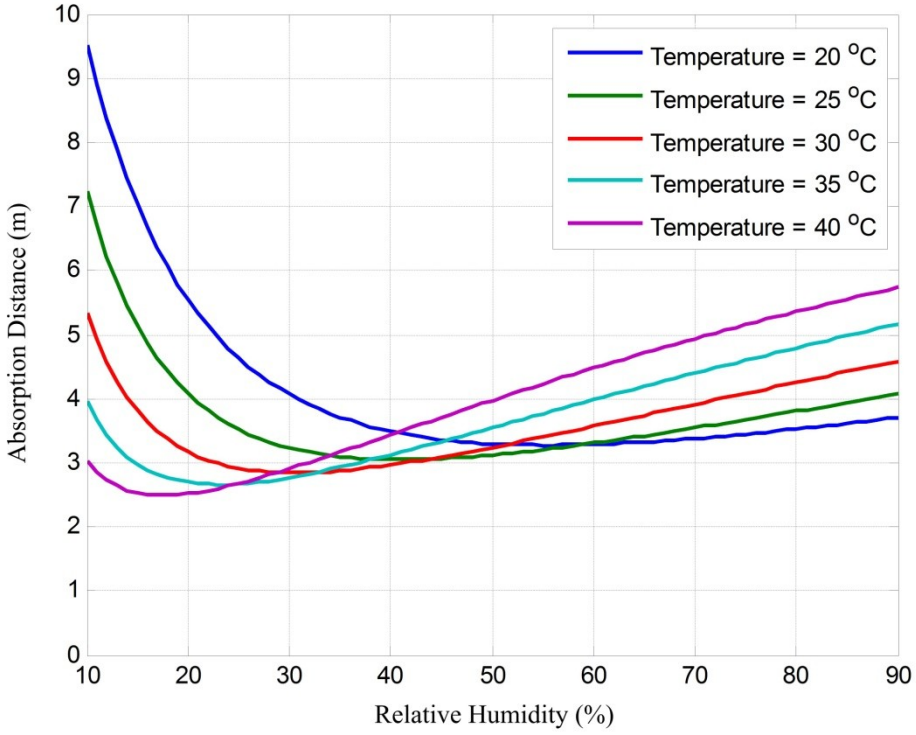

Figure A.2 Absorption distance of the parametric loudspeaker.

Appendix B Configurations of the UTAs in the Measurements

Four configurations of the UTA are built up for the measurements reported in this thesis. The layout of the block configuration is shown in Fig. B.1 and the photos of all the four configurations are shown in Fig. B.2. In every configuration, four PZT transducers are connected in serial and driven by one output channel of the NI PCI-6733 board as mentioned in Section 3.4.

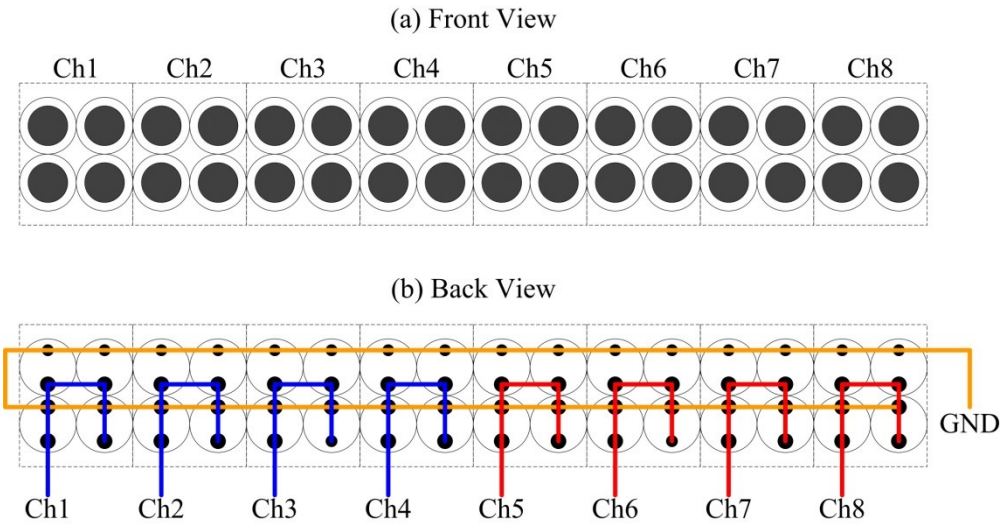

Figure B.1 (a) Front view and (b) back view of the block configuration of the UTA.

(a) Column Configuration (d = 1 cm)

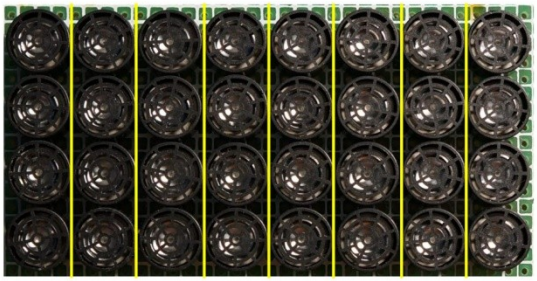

(b) Column Configuration (d = 1.25 cm)

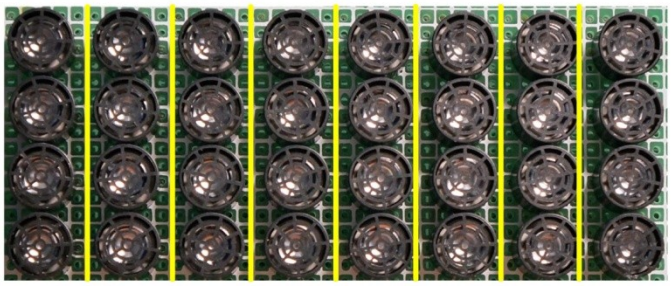

(c) Column Configuration (d = 1.5 cm)

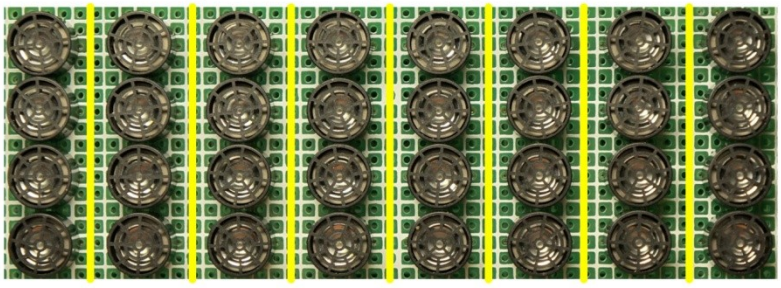

(d) Block Configuration (d = 2 cm)

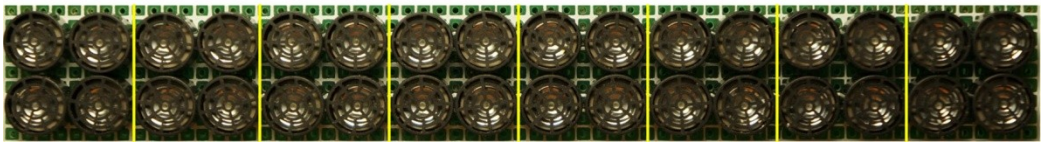

Figure B.2 Configurations of the UTAs: (a) column configuration with spacing of 1 cm; (b) column configuration with spacing of 1.25 cm; (c) column configuration with spacing of 1.5 cm; (d) block configuration with spacing of 2 cm.

Appendix C LabVIEW Program for the Steerable Parametric Loudspeaker

The beamsteering structure shown in Fig. 3.3 is implemented in LabVIEW 2009. This program allows users to adjust the settings of the two PF waves, the spacing of the UTA, the speed of sound, and the intended steering angle. Figure C.1 shows that the eight channels of the UTA are uniformly spaced and equally weighted, but delayed by different amounts in the LabVIEW program to achieve beamsteering. Figure C.2 provides block diagram of this LabVIEW program.

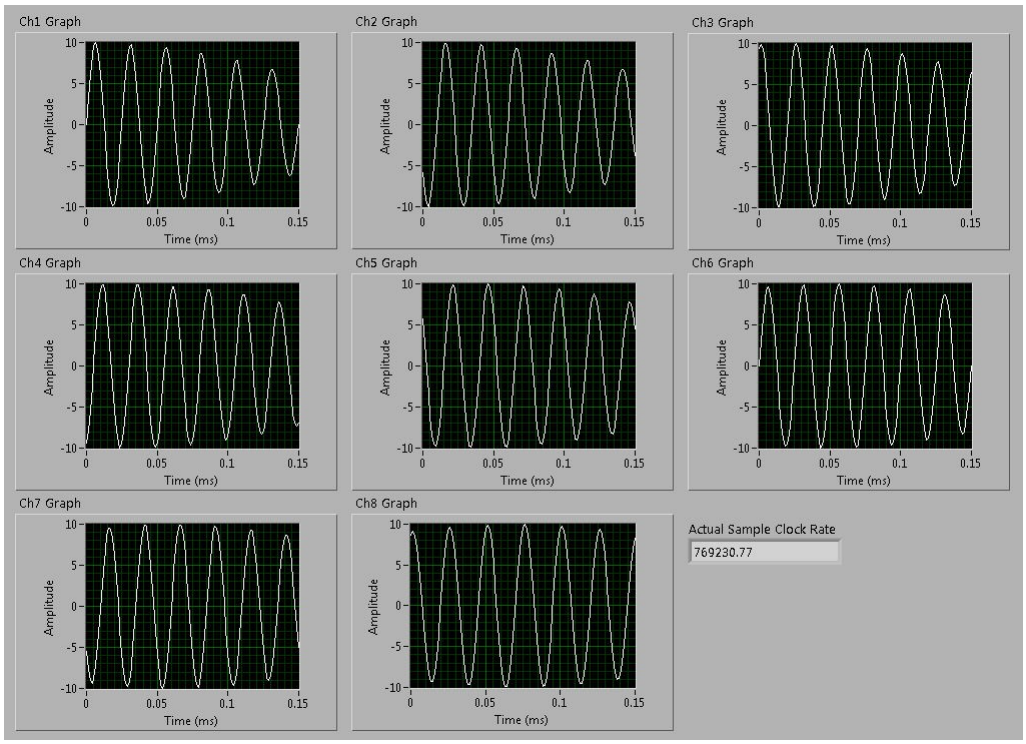

Figure C.1 Front panel of the LabVIEW program for the steerable parametric loudspeaker.

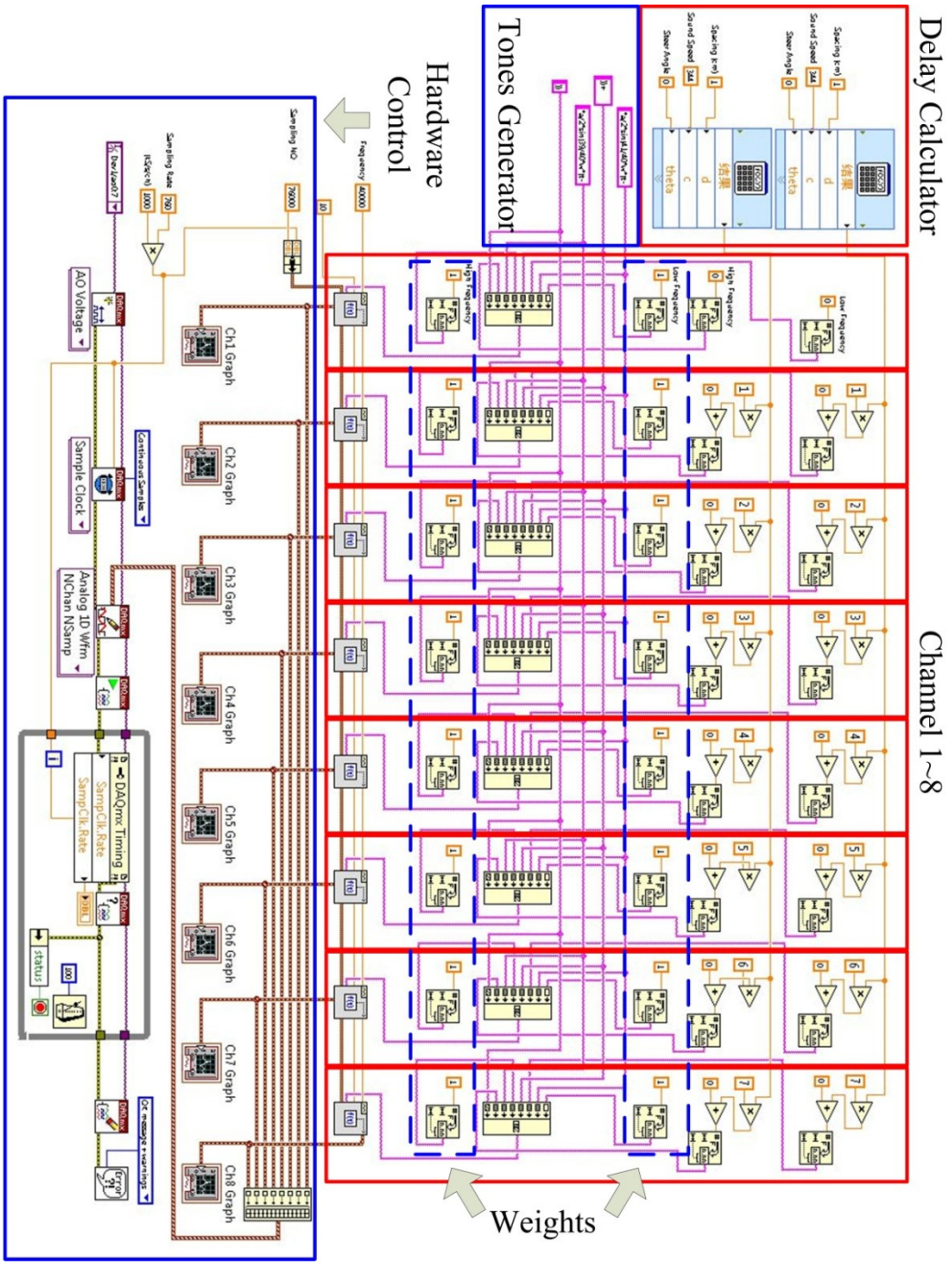

Figure C.2 Block diagram of the LabVIEW program for the steerable parametric loudspeaker.

Appendix D Photos of the Measurement Setups

Three photos taken during the measurements reported in this thesis are presented. The measurement rooms in the School of Electrical and Electronic Engineering (EEE) and in the School of Mechanical and Aerospace Engineering (MAE) are shown in Fig. D.1 and Fig. D.2, respectively. Both rooms are 5 meters in length, but the room in the school of MAE is wider and higher. Controllers are always installed in the control room, which is outside the anechoic chamber, to isolate noises caused by the fans of the controllers.

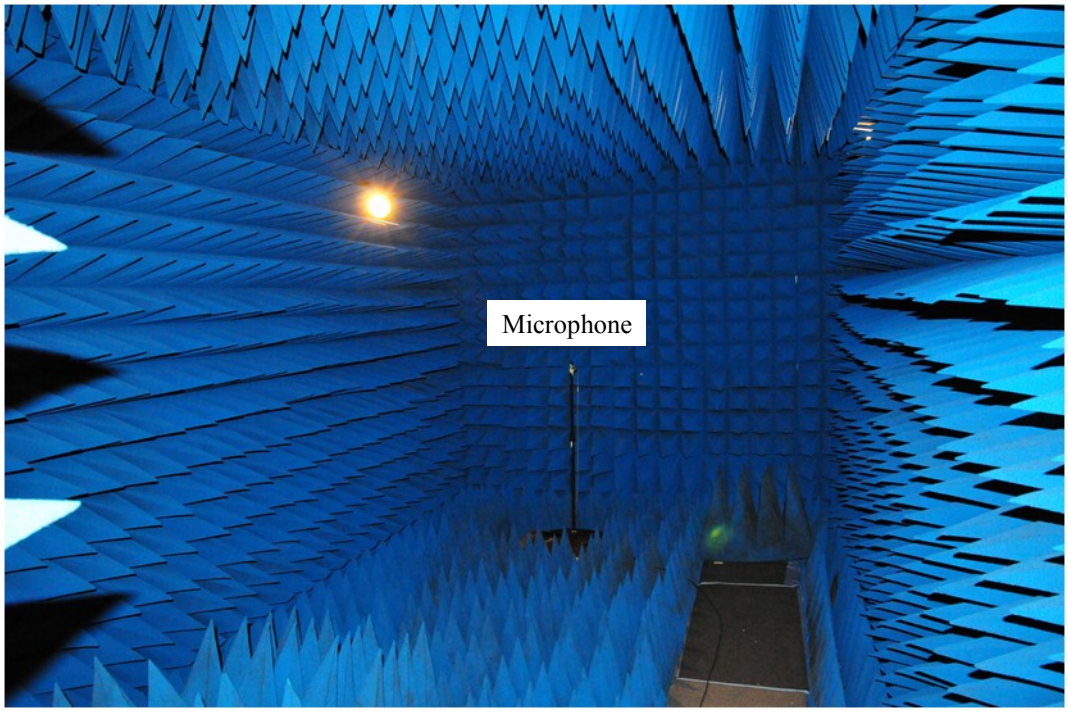

Figure D.1 Measurement room in the School of Electrical and Electronic Engineering, Nanyang Technological University.

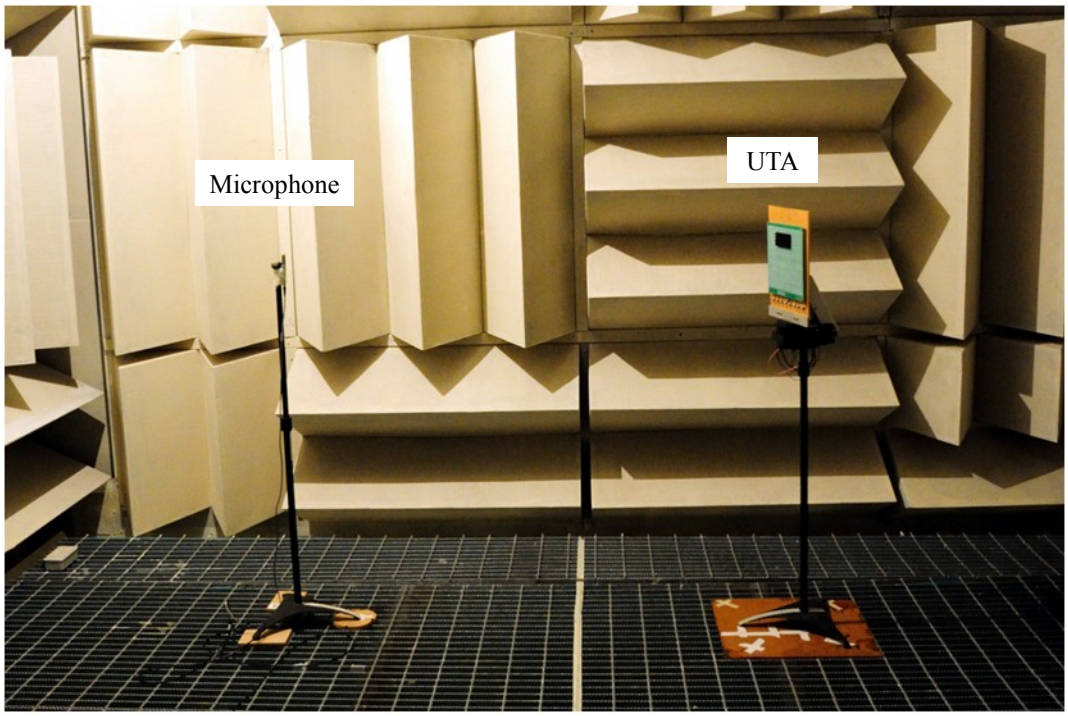

Figure D.2 Measurement room in the School of Mechanical and Aerospace Engineering, Nanyang Technological University.

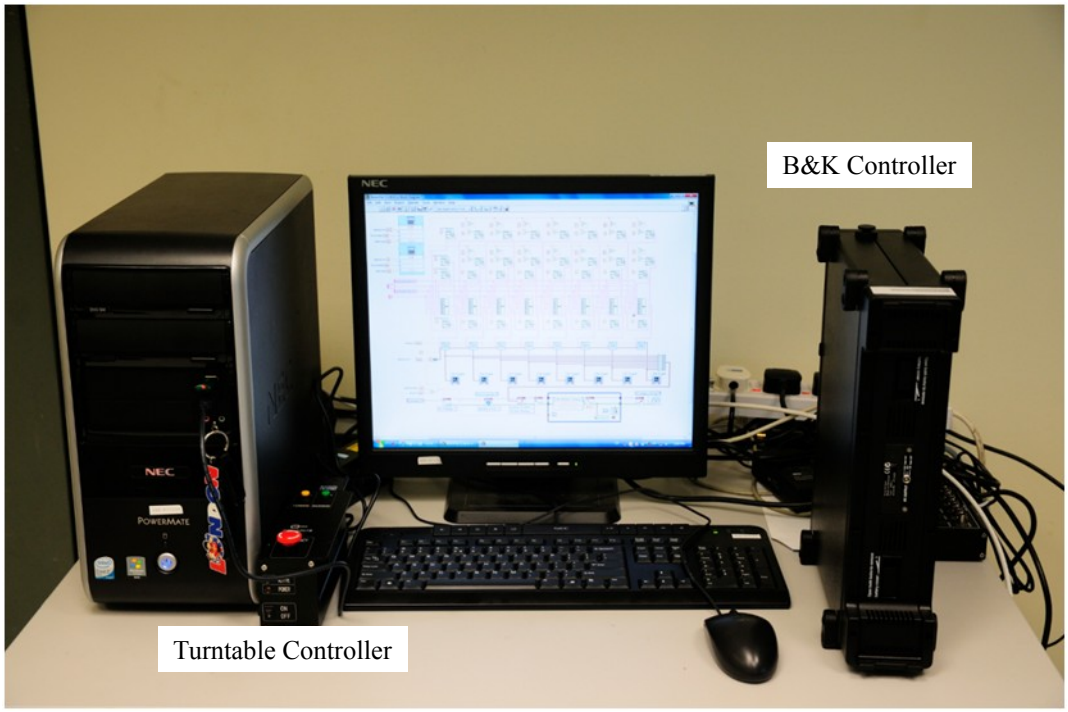

Figure D.3 Measurement setup in the control room (outside the anechoic chamber).